Recyclable Photocatalysts for Oil Sands Process-Affected Water Treatment

by

Timothy Michael Carter Leshuk

A thesis
presented to the University of Waterloo
in fulfillment of the
thesis requirement for the degree of
Doctor of Philosophy
in
Chemical Engineering (Nanotechnology)

Waterloo, Ontario, Canada, 2018

Examining Committee Membership

The following served on the Examining Committee for this thesis. The decision of the Examining Committee is by majority vote.

External Examiner	Edgar J. Acosta Professor
Supervisor(s)	Frank Gu Associate Professor
Internal Member	William A. Anderson Professor
Internal Member	Neil McManus Research Assistant Professor
Internal-external Member	Neil R. Thomson Professor

Author's Declaration

This thesis consists of material all of which I authored or co-authored: see Statement of Contributions included in the thesis. This is a true copy of the thesis, including any required final revisions, as accepted by my examiners.

I understand that my thesis may be made electronically available to the public.

Statement of Contributions

Chapter 2 of this thesis is adapted from a previously published book chapter co-authored by myself and my supervisor, Dr. Frank Gu.

Chapter 3 of this thesis is adapted from a previously published article co-authored by myself, a co-op student, Mr. Timothy Wong, a Ph.D. student, Mr. Stuart Linley, Mr. Kerry M. Peru of Environment & Climate Change Canada, Dr. John V. Headley of Environment & Climate Change Canada, and my supervisor, Dr. Frank Gu. T.L. conceived and designed the experiments; T.L. and T.W. performed the majority of the experiments, and S.L. performed the 09/2014 photocatalytic test; K.M.P. performed the HRMS measurements; T.L. analyzed the data, prepared the figures, and wrote the paper; K.M.P. and J.V.H. aided with interpretation and presentation of the HRMS data, and provided critical feedback on the manuscript; F.G. supervised the project, contributed reagents, materials, analysis tools, and critically reviewed the paper.

Chapter 4 of this thesis is adapted from a previously published article co-authored by myself, a co-op student, Mr. Diogo de Oliveira Livera, Mr. Kerry M. Peru of Environment & Climate Change Canada, Dr. John V. Headley of Environment & Climate Change Canada, a co-op student, Ms. Sucharita Vijayaraghavan, a co-op student, Mr. Timothy Wong, and my supervisor, Dr. Frank Gu. T.L. conceived and designed the experiments, with the exception of the protocols for the NBT and TA radical probe assays, which were developed by D.d.O.L.; D.d.O.L. and T.L. performed the experiments, S.V. and T.W. performed the photocatalytic tests contributing to Figure 36 and Figure 19, respectively; K.M.P. performed the HRMS measurements; T.L. analyzed the data, prepared the figures, and wrote the paper; K.M.P. and J.V.H. provided the Industry B OSPW sample, aided with interpretation and presentation of the HRMS data, and provided critical feedback on the manuscript; F.G. supervised the project, contributed reagents, materials, analysis tools, and critically reviewed the paper.

Chapter 5 of this thesis is adapted from a previously published article co-authored by myself, a Ph.D. student, Mr. Andrew B. Holmes, a co-op student, Mr. Duleeka Ranatunga, a Ph.D. student, Mr. Paul Z. Chen, a co-op student, Ms. Yunsheng Jiang, and my supervisor, Dr. Frank Gu. T.L. conceived of the presented idea, designed the MF particles, and conceived and designed the experiments, with input from A.B.H. on the protocol for the flocculation experiments; T.L. and A.B.H. performed the experiments; A.B.H. developed the protocols for and performed the FGDW PC test, and Se analysis; D.R. performed the synthesis of some MF samples; P.Z.C. developed the protocol for and synthesized the Au NPs; Y.J. performed the synthesis of the Ag, Pd, and Pt NPs; T.L. analyzed the data, prepared the figures, and wrote the paper, with support of A.B.H.; F.G. supervised the project, contributed reagents, materials, analysis tools, and critically reviewed the paper.

Chapter 6 of this thesis is adapted from a previously published article co-authored by myself, a M.A.Sc. student, Mr. Harish Krishnakumar, a co-op student, Mr. Diogo de Oliveira Livera, and

my supervisor, Dr. Frank Gu. T.L. conceived of the presented idea, and conceived and designed the experiments; T.L. and H.K. synthesized the floating photocatalysts; H.K. and D.d.O.L. performed the experiments; T.L. analyzed the data and wrote the paper; F.G. encouraged T.L. to consider passive OSPW remediation solutions, supervised the project, contributed reagents, materials, analysis tools, and critically reviewed the paper.

Chapter 7 of this thesis is adapted from a paper that has been submitted for publication, co-authored by myself, Mr. Kerry M. Peru of Environment & Climate Change Canada, a co-op student, Mr. Diogo de Oliveira Livera, a co-op student, Mr. Austin Tripp, a co-op student, Mr. Patrick Bardo, Dr. John V. Headley of Environment & Climate Change Canada, and my supervisor, Dr. Frank Gu. T.L. conceived and designed the experiments; K.M.P. performed the HRMS measurements; D.d.O.L. and A.T. performed the experiments contributing to Figures 69-71; A.T. and P.B. performed the synthesis of the BPCs; P.B. and T.L. performed the main photocatalytic test; T.L. analyzed the data, prepared the figures, and wrote the paper; J.V.H. encouraged T.L. and F.G. to investigate photocatalytic treatment of OSPW BEO and NEO; K.M.P. and J.V.H. aided with interpretation and presentation of the HRMS data, and provided critical feedback on the manuscript; F.G. supervised the project, contributed reagents, materials, analysis tools, and critically reviewed the paper.

Abstract

One of the largest environmental challenges faced by Canada is the cleanup and reclamation of land and water impacted by mining operations in the Athabasca oil sands. The persistence of toxicity associated with the soluble naphthenic organic compounds (NOCs) of oil sands process-affected water (OSPW) implies that a treatment solution may be necessary to enable safe return of this water to the environment, and the industry is currently exploring passive (*i.e.*, no energy or chemical input) remediation solutions. Among the methods investigated for OSPW treatment, advanced oxidation processes (AOPs) have been shown to be particularly effective for degrading NOCs and reducing OSPW toxicity. However, AOPs are chemically and energy intensive, and are generally considered impractically expensive to meet the scale of treatment required. Solar photocatalysis is a powerful AOP with the potential for passive treatment, however the separation and recycling of nanoparticle photocatalysts remains a key barrier to implementation.

This thesis focuses on evaluating photocatalytic treatment of NOCs in OSPW, and the development of composite materials to facilitate separation and recycling of nanoparticle photocatalysts. Solar photocatalysis over TiO_2 was found to degrade OSPW naphthenic acids (NAs) through superoxide-dependent oxidative mineralization. The important water and process parameters affecting the rate of photocatalytic treatment were elucidated, and an empirical model was proposed to predict OSPW treatment kinetics in different tailings ponds. Magnetic flocculation was developed as a new paradigm for magnetic nanoparticle capture, and demonstrated to efficiently recycle colloidally dispersed TiO_2 nanoparticles in a closed-loop process. Floating photocatalysts were also synthesized to adapt the photocatalytic process towards a passive deployment paradigm, by immobilizing TiO_2 nanoparticles onto buoyant glass microspheres. Floating photocatalysts were demonstrated to preferentially treat OSPW base- and neutral-extractable organics and priority toxic naphthenic organic classes of concern.

Firstly, photocatalysis with TiO_2 was evaluated for the first time in raw OSPW under natural sunlight. One day of photocatalytic treatment under natural sunlight eradicated acid-extractable organics (AEO) from raw OSPW, and acute toxicity of the OSPW toward *Vibrio fischeri* was eliminated. Nearly complete mineralization of organic carbon was achieved within 1-7 day equivalents of sunlight exposure, and degradation was shown to proceed through a superoxide-mediated oxidation pathway. High resolution mass spectrometry (HRMS) analysis of oxidized intermediate compounds indicated preferential degradation of the heavier and more cyclic NAs (higher number of double bond equivalents), which are the most environmentally persistent fractions. The photocatalyst was shown to be recyclable for multiple uses, and thus solar photocatalysis was concluded to be a promising "green" AOP for OSPW treatment.

Further studies focused on factors affecting the kinetics of photocatalytic AEO degradation in OSPW. The rate of photocatalytic treatment varied significantly in two different OSPW sources, which could not be accounted for by differences in AEO composition, as studied by HRMS. The effects of inorganic water constituents were investigated using factorial and response surface

experiments, which revealed that hydroxyl ($HO^{\bullet}$) radical scavenging by iron (Fe^{3+}) and bicarbonate (HCO_3^-) inhibited the NA degradation rate. The effects of NA concentration and temperature on the treatment kinetics were also evaluated in terms of Langmuir-Hinshelwood and Arrhenius models; pH and temperature were identified as weak factors, while dissolved oxygen (DO) was critical to the photo-oxidation reaction. Accounting for all of these variables, a general empirical kinetic expression was proposed, enabling prediction of photocatalytic treatment performance in diverse sources of OSPW.

Considering the challenge of TiO_2 nanoparticle separation from colloidal dispersions, magnetic flocculation was developed as a new approach to nanoparticle recovery. Flocculant polymers were coated onto magnetic nanoparticles ($Fe_3O_4@SiO_2$) to prepare reusable magnetic flocculants (MFs). When added to colloidal nanoparticle dispersions, MFs aggregate with the suspended nanoparticles to form magnetically responsive flocs, which upon separation can be reversibly deflocculated for nanoparticle release, and reuse in a closed loop process. High separation efficiency was attained in a variety of nanoparticle suspensions, including Au, Ag, Pd, Pt, and TiO_2, stabilized by different coatings and surface charge. The MFs were shown to be recyclable for photocatalytic treatment of naphthenic acids in oil sands process-affected water (OSPW) and selenium in flue gas desulfurization wastewater (FGDW). Magnetic flocculation thus represents a general platform and alternative paradigm for nanoparticle separation, with potential applications in water treatment and remediation of nanoparticle pollution.

As an alternative passive catalyst recycling strategy, floating photocatalysts (FPCs) were prepared by immobilizing TiO_2 on glass microbubbles, such that the composite particles float at the air-water interface for passive solar photocatalysis. The FPCs were demonstrated to outperform P25 TiO_2 nanoparticles in degrading AEO in raw OSPW under natural sunlight and gentle mixing conditions. The FPCs were also found to be recyclable for multiple uses through simple flotation and skimming. Thus the concept of a potentially passive or semi-passive AOP for OSPW treatment was demonstrated for the first time.

Finally, OSPW treatment using FPCs was evaluated under a petroleomics paradigm: chemical changes across acid-, base- and neutral-extractable organic fractions were tracked throughout the treatment with both positive and negative ion mode HRMS. Transformation of OS^+ and NO^+ classes of concern in the earliest stages of the treatment, along with preferential degradation of high carbon-numbered O_2^- acids, suggest that photocatalysis may detoxify OSPW with higher efficiency than previously thought, given that the majority of the toxicity of OSPW is currently understood to derive from a subset of such toxic classes, comprising only a minority of the total NOCs.

Overall, this thesis advances the understanding of the photocatalytic treatment of OSPW, as well as separation processes for nanoparticle photocatalysts. Combining a sunlight-driven, chemical-oxidant-free catalytic oxidation process with a low-energy, membrane-free catalyst separation and recovery technique may represent a promising strategy to adapt advanced oxidation process (AOP) technology for the passive treatment of OSPW, or other remote mining-impacted waters.

Acknowledgements

Firstly, I wish to express my deepest gratitude to my supervisor, Professor Frank Gu, for his care, support, and guidance throughout my Ph.D. studies, his research training and mentorship, and his boundless support, encouragement, and motivation. I consider myself extremely fortunate to have met Prof. Gu, and consider it my true privilege to have studied under him all these years. He has had the single largest influence on the trajectory of my career of anyone in my life, and has not only shaped and guided my growth as an independent researcher, but also inspired my future professional ambitions. Prof. Gu has been an extremely dedicated and endlessly supportive supervisor, advisor, and mentor, and I will be forever grateful for the time I spent in his lab.

I also wish to thank my thesis committee members, Professor William Anderson, Professor Neil McManus, and Professor Neil Thomson, for their constructive comments, guidance, and encouragement of my research. I am also very grateful to my external committee member, Professor Edgar Acosta, for participating in my thesis defense, and providing constructive comments.

I am very grateful for the support, encouragement, and guidance provided by Dr. Arthur Carty throughout my studies in the Waterloo Institute for Nanotechnology (WIN). I am also very thankful for his generous support of the WIN Graduate Student Society.

I also wish to acknowledge the help and support I received from various research groups and individuals in carrying out various experiments described herein. I wish to thank Howard Siu and Jenn Coggan, University of Waterloo, for the use of their FTIR spectrometer and probe sonicator, and Professor Pu Chen, Department of Chemical Engineering, University of Waterloo, for the use of his fluorimeter. I would also like to thank Professor Shirley Tang and Louis Cheung, Department of Chemistry, University of Waterloo, for the use of their tube furnace. I am also grateful to Professor Juewen Liu, Department of Chemistry, University of Waterloo, for allowing use of his zeta potential analyzer. I would also like to thank Professor Linda Nazar and Dr. Guerman Popov, Department of Chemistry, University of Waterloo, for assistance with XRD analysis. I also wish to thank Professor Tong Leung and Liyan Zhao, Department of Chemistry, University of Waterloo, for assistance with the XPS analysis. I would also like to thank Professor Tong Leung, Marwa Abd-Ellah and Dr. Nafiseh Moghimi, Department of Chemistry, University of Waterloo, for assistance with the SEM and EDX analysis, as well as David Wulff, Department of Chemical Engineering, University of Waterloo, for assistance with the SEM analysis. I am also grateful to John Tse, Nanotechnology Engineering, University of Waterloo, for assistance with the BPC recyclability study. I would also like to express my gratitude to Shell Canada for providing OSPW samples for these experiments.

I am extremely grateful for the help and support of the other members of my research group, who have helped brainstorm, troubleshoot experiments and encouraged me on countless occasions. I am especially grateful to the co-op students I have had the privilege to work with throughout my

Ph.D. studies, without whose tireless efforts in the lab, this research would not have been possible: Diogo de Oliveira Livera, Timothy Wong, Duleeka Ranatunga, Sucharita Vijayaraghavan, Austin Tripp, Yunsheng Jiang, Patrick Bardo, Michelle Si, Adam Calvert, Savannah Knorr, Jordan van Wyk, Alyssha Schneider-Yamamura, Nicholas Calen, Lisa Krygsman, Michael Johnson, William McLaren, Sukrit Rajpal, Rosa Chen, Don Tu, Iason Giannis, Adrian Kong, Brooks MacLachlan, Myung-Sik Kim, Zi Qi Chen, Matthew Lam, Gregory Lazaris, Corin Seelmann, and Danielle Smith. I am further grateful to all of my fellow graduate students in the research group: Stuart Linley, Zac Young, Andrew Holmes, Michelle Si, Harish Krishnakumar, Sandy Liu, Paul Chen, Mohit Verma, David Wulff, Noor Bahsoun, Mostafa Saquib, Aaminah Ahmad, Sukrit Rajpal, Lori Pollit, Jeff Watchorn, Mahtab Roshandel, Jacob Rogowski, Sarah LeBlanc, Erin Bedford, Peter Lin, Jiang Xu, and Drew Davidson.

I would like to express my sincere gratitude to the University of Waterloo's staff and administrators for their help in facilitating this project, and providing a productive work environment for research success. I wish to thank Chris Kleven for the numerous times he helped move and set-up experimental apparatuses; Ken Gosselink, Jerry Hutten, Les Van Dongen and Michael Pereira for their assistance in arranging locations around campus to conduct experiments; the Waterloo Institute for Nanotechnology (WIN) team, Directors Arthur Carty and Sushanta Mitra, Caroline Brooks, Lisa Pokrajac, Ivy Tjendra, Jisu Kwon, and Alain Francq; the Department of Chemical Engineering staff, Liz Bevan, Judy Caron, Pauline Ferfolja, Rose Guderian, Ingrid Sherrer, Tom Dean, Ralph Dickhout, and Bert Habicher; Tony Bairos, Trevor Beatson, their teams, and all the staff at Central Stores for help moving, shipping, and storing large quantities of OSPW; as well as the University's custodial staff and Plant Ops support staff.

I am forever thankful for my family and friends, and their endless support, compassion, encouragement, and faith in me throughout my academic studies.

Finally, I gratefully acknowledge the financial support provided to me throughout my Ph.D. studies: the Natural Sciences and Engineering Research Council of Canada (NSERC) Vanier Canada Graduate Scholarship, the NSERC Toward Environmentally Responsible Resource Extraction Network (TERRE-NET), Ontario Graduate Scholarship, the WIN Nanofellowship, the University of Waterloo (UW) President's Graduate Scholarship, the Engineering Graduate Scholarship, and UW Graduate Research Studentship. I wish to thank the Government of Ontario and Canada, and Canadian taxpayers, for their support for research and innovation.

Dedication

To my mother, father, and sister.

Table of Contents

List of Figures

List of Tables

List of Abbreviations

AEO	Acid extractable organics
AOP	Advanced oxidation process
BEO	Base extractable organics
BET	Brunauer–Emmett–Teller (adsorption theory)
BOD	Biochemical oxygen demand
BPC	Buoyant photocatalyst
CF	Coagulation & flocculation
COCs	Naphthenic organic classes of concern
COD	Chemical oxygen demand
DLS	Dynamic light scattering
EDX	Energy dispersive x-ray spectroscopy
ESI	Electrospray ionization
ESI(-) MS	Negative ion mode ESI mass spectrometry
ESI(+) MS	Positive ion mode ESI mass spectrometry
FGDW	Flue gas desulfurization wastewater
FPC	Floating photocatalyst
FTIR	Fourier transform infrared spectroscopy
GMB	Glass microbubble
HGM	Hollow glass microsphere
HRMS	High resolution mass spectrometry
ICPMS	Inductively coupled plasma mass spectrometry
LbL	Layer-by-layer
MF	Magnetic flocculant or magnetic flocculation
MS	Mass spectrometry
NAs	Naphthenic acids, of the general formula $C_cH_{2c+Z}O_2$
NEO	Neutral extractable organics
NOCs	Naphthenic organic compounds, of general formula $C_cH_{2c+Z}N_nO_oS_s$
NOM	Natural organic matter

OSPW	Oil sands process-affected water
PC	Photocatalysis, photocatalyst, or photocatalytic
SEM	Scanning electron microscopy
SPION	Superparamagnetic iron oxide nanoparticle
TDS	Total dissolved solids
TEM	Transmission electron microscopy
TGA	Thermogravimetric analysis
TOC	Total organic carbon
TSS	Total suspended solids
WET	Whole effluent toxicity
XPS	X-ray photoelectron spectroscopy
XRD	X-ray diffraction

Chapter 1
General Introduction

1.1 Overview

One of the largest environmental challenges faced by Canada is the cleanup and reclamation of land and water impacted by mining operations in the Athabasca oil sands. The Clark process used for extraction of bitumen in Canada's oil sands generates large volumes of water as a by-product, referred to as oil sands process-affected water (OSPW), which is stored on site in tailings ponds for water recycling. The oil sands mining companies are obligated to eventually return this water to the environment,[1–3] but currently are operating on a zero-discharge policy, due in part to the water's toxicity, which is primarily attributed to dissolved bitumen-derived organics.[4–7] Fractions of these organics are highly persistent,[8,9] and remain potently toxic even after decades of aging.[10] Thus treatment of OSPW may be required to enable safe discharge, and the industry is currently exploring passive (*i.e.*, no energy or chemical input) remediation solutions.[11]

OSPW is a complex saline solution containing high concentrations of suspended clays, dissolved organic compounds, trace heavy metals, and residual bitumen and solvents. A primary source of OSPW toxicity has been attributed to the naphthenic organic compounds (NOCs), including naphthenic acids (NAs), which are structurally diverse alkyl-branched acyclic and cycloaliphatic carboxylic acids with the conventional formula $C_nH_{2n+z}O_2$ (where z is a negative even integer related to the number of rings and double bonds).[12,13]

Among the methods investigated for OSPW treatment, advanced oxidation processes (AOPs) have been shown to be particularly effective for degrading NAs and reducing OSPW toxicity.[14–18] Unfortunately, AOPs are typically chemically intensive, requiring oxidant dosing of the contaminated water (*e.g.*, with O_3,[16] H_2O_2,[15] $S_2O_8^{2-}$,[19] OCl^-,[20] or FO_4^{2-}[21]), or require significant input of electrical power (e.g., to generate O_3 or UV light), and thus are conventionally considered to by operationally expensive. Furthermore, considering the infrastructure requirements to implement AOPs, they remain essentially the opposite of the passive treatment solution sought by industry, and thus despite their proven efficacy for OSPW treatment at the bench-scale, conventional AOPs may be impractical to deploy to remote mining locations or to truly address the scale of OSPW treatment required.

Photocatalysis over TiO_2 is an extremely powerful AOP that has been proven to eliminate a broad spectrum of organic pollutants in wastewaters. In aqueous suspension, photocatalysts absorb light to generate highly reactive free radicals, such as hydroxyl and superoxide radicals, which are capable of mineralizing even recalcitrant organic contaminants.[22,23] TiO_2 is a low-cost, earth abundant, and chemically stable photocatalytic material which, in principle, can be recovered and reused over multiple treatment cycles. Using sunlight as an abundant free energy source, and given the ability of the photocatalyst to be recycled without the need for continuous

chemical amendment of the water, photocatalysis may not suffer from the same limitations of cost and scale as other AOPs, and may instead share some advantages of passive treatment processes. Given these advantages, it was hypothesized that solar photocatalysis may be a promising technology for treating the organic constituents of OSPW, provided a means of recovering or recycling the photocatalytic material could be developed.

For photocatalytic water treatment, the most efficient implementations involve dispersion of nanoparticle photocatalysts into the contaminated water as a slurry.[22,24,25] Nanoparticle recovery after the treatment process is essential not only for reuse of the catalyst, but also to prevent nanoparticle contamination of the treated effluent. Unfortunately, nanoparticle separation challenges have proven a critical hurdle to practical application of this promising treatment technology.[26–28]

Therefore this thesis sought to evaluate the potential of photocatalysis to treat the naphthenic organic compounds in OSPW, as well as apply nanotechnology engineering principles to develop composite materials and catalyst recycling systems to enable practical deployment. Firstly, the potential of heterogenous photocatalysis over TiO_2 nanoparticles to mineralize naphthenic organics in raw OSPW under natural sunlight was established. The kinetics of photocatalytic OSPW treatment was further studied in different sources of OSPW, and the effect of key process variables was used to propose an empirical kinetics model. Flocculation and magnetic separation concepts were combined to develop a magnetic flocculation platform as a reusable system for slurry nanoparticle recycling. TiO_2 nanoparticles were also immobilized onto buoyant microspheres as a passive deployment system for OSPW treatment, and application of these floating photocatalysts were thoroughly investigated under a petroleomics paradigm.

1.2 Research Objectives

The overall objective of this research project was to develop a recyclable photocatalytic solution for OSPW treatment. The ability of TiO_2 nanoparticle heterogeneous photocatalysis to feasibly operate in raw OSPW under natural sunlight and affect oxidative degradation of naphthenic organics was first established. The effect of important water and process factors on the treatment kinetics were then further studied to establish key parameters towards the eventual design of scaled OSPW treatment systems. Finally, magnetic and flotation-based recovery systems were developed as solutions for nanoparticle photocatalyst recycling.

The specific objectives of the study are as follows:

1. Demonstrate the ability of solar photocatalysis over TiO_2 nanoparticles to oxidize naphthenic acids in raw OSPW
    - Investigate degradation of naphthenic acids by the conventional FTIR analytical method
    - Determine extent of organics mineralization throughout the treatment process
    - Confirm oxidative reaction pathway

2. Determine the effect of key process and operating parameters on the kinetics of photocatalytic OSPW treatment
    - Determine photocatalytic treatment kinetics of OSPW from different industrial suppliers
    - Determine the impact of specific inorganic constituents, organics concentration, temperature, pH, and dissolved oxygen on the OSPW treatment rate
    - Develop an empirical kinetics model for photocatalytic OSPW treatment
3. Develop reusable magnetic flocculants (MFs) for photocatalyst nanoparticle separation and recycling
    - Synthesize polyelectrolyte-coated Fe_3O_4@SiO_2 nanoparticles as MFs
    - Characterize the material properties of the synthesized MFs
    - Determine physical mechanism of magnetic flocculation, and optimize TiO_2 nanoparticle separation
    - Demonstrate reusable performance of the MFs in a closed-loop process
4. Develop buoyant photocatalyst composite particles for passive photocatalyst separation and recycling
    - Synthesize TiO_2 nanoparticle-coated hollow glass microspheres as buoyant photocatalysts (BPCs)
    - Determine BPC OSPW treatment kinetics relative to slurry TiO_2 nanoparticles under gentle mixing conditions
5. Demonstrate the treatment of OSPW acid-, base- and neutral-extractable organics with buoyant photocatalysts (BPCs) under a petroleomics paradigm
    - Develop a new silica-binder formulation for anchoring TiO_2 nanoparticles to hollow glass microsphere supports
    - Determine kinetics of the BPCs to degrade acid-, base- and neutral-extractable organics in OSPW
    - Investigate degradation of specific naphthenic organic classes of concern during the photocatalytic treatment process

1.3 Thesis Outline

The thesis is composed of eight chapters: the introduction, a literature review, five experimental research-based chapters, and a final chapter summarizing the conclusions and recommendations for future research.

Chapter 1 introduces the context of the thesis, the motivating challenges, scope of work, research hypothesis, and specific research objectives.

Chapter 2 reviews the literature regarding the fundamentals of magnetic separation processes for nanoparticle recovery, within the context of water treatment. The fundamental magnetic properties and forces relating to magnetophoretic phenomena are presented, and the importance of many-particle interactions (*i.e.*, cooperative magnetophoresis) in magnetic nanoparticle

separation is highlighted. The implications of these principles for engineering of magnetically-separable nanoparticles for water treatment is discussed.

Chapter 3 evaluates the potential of heterogeneous photocatalysis over TiO_2 to degrade organic compounds in OSPW under natural sunlight. One day of photocatalytic treatment eliminates acid extractable organics, while nearly complete mineralization of organic carbon is achieved with sufficient solar exposure, and degradation is shown to proceed through a superoxide-mediated oxidation pathway. This chapter establishes the potential of solar photocatalysis as an OSPW treatment solution.

Chapter 4 builds upon the results of Chapter 3 by applying the photocatalytic treatment process to OSPW received from different oil sands industrial suppliers. The starkly different treatment kinetics between the two OSPW sources motivates a statistical investigation of the causative factors, and specific inorganic constituents are identified as deleterious elements. To deepen the understanding of potential factors affecting OSPW treatment kinetics, the role of organics concentration, temperature, pH, and dissolved oxygen on the OSPW treatment rate are also established. This chapter presents a kinetics model for OSPW treatment using slurried TiO_2 nanoparticles, which provides a basis to understand the important water and process parameters affecting the photocatalytic treatment process.

Chapter 5 demonstrates the synthesis of reusable magnetic flocculant (MF) nanoparticles for the capture, separation, and recycling of nanoparticles such as TiO_2 photocatalysts. While previous chapters demonstrated the performance of photocatalysis to treat OSPW, TiO_2 nanoparticle slurries are prohibitive to implement due to the challenge of capturing free nanoparticles. Therefore this chapter optimizes a membrane-free closed-loop system for flocculation, magnetic separation, and release of TiO_2 nanoparticles, and demonstrates recyclable OSPW treatment using this system.

Chapter 6 demonstrates buoyant photocatalyst composite particles as a proof-of-concept deployment method for potentially passive OSPW treatment. While the MF system of Chapter 5 demonstrated a novel method for magnetic recycling of photocatalysts, the multi-step separation process and magnetic equipment requirements disqualify it as a “passive” process as sought by the oil sands industry. This chapter evaluates simple flotation as an alternate catalyst separation technique that aligns with a passive treatment paradigm, and demonstrates promising treatment performance under gentle mixing conditions.

Chapter 7 revisits the concept of buoyant photocatalysts (BPCs), and implements an alternate synthesis technique using mesoporous silica as a binder to coat the TiO_2 nanoparticles onto the buoyant supports. The treatment of OSPW with BPCs is comprehensively investigated with high-resolution mass spectrometry from a petroleomic perspective, to gain a holistic insight into the various chemical transformations occurring to the complex mixture of OSPW naphthenic organics during photocatalytic treatment. This chapter demonstrates that photocatalysis preferentially treats naphthenic organics classes of concern well before full mineralization of

organics, and suggests that only relatively short solar exposures may be needed to photocatalytically detoxify OSPW.

Finally, Chapter 8 highlights the overall conclusions drawn from the research in the preceding chapters, and presents recommendations for future work building on these findings. A number of these recommendations are towards strategies to increase the photocatalytic treatment efficiency, through either materials engineering approaches or combined treatment processes (*e.g.*, adsorption, biodegradation), while the other recommendations are directed at key steps towards developing the technology for practical deployment.

Chapter 2
Literature Review*

2.1 Summary

Nanoparticle colloidal dispersions are highly promising for use in water purification, but practical and cost-effective options to separate the dispersed nanoparticles from the treated water remain a critical roadblock to industrial adoption. Magnetic separation of superparamagnetic nanoparticles from water for recycling and reuse has the potential to be an efficient, practical, and low-cost slurry-type water treatment method. In this chapter we review the fundamental theory and concepts of magnetic nanoparticle separations.

2.2 Introduction

Nanotechnologies based on magnetic separations show huge promise in the field of water treatment and purification, and magnetic nanomaterials are being heavily researched for scrubbing water of a wide variety of contaminants. This chapter is primarily focused on the magnetic separation or recovery of nanoscale particles from a colloidal dispersion or slurry, and their use in water purification, with the potential for recyclability. Slurry-type water treatment technologies involving colloidal particles show distinct advantages compared with other treatment methodologies, such as the use of membranes, flocculation, or chemical methods such as chlorination. The concept of a slurry is the dispersion of (nano)particles throughout the volume of contaminated water to be treated, purifying the water using these dispersed particles, and then recovering them afterwards from the treated water (potentially for reuse/recycling of the particles in subsequent rounds of treatment). Such a nano-colloid allows a huge specific surface area to be mobilized and dispersed throughout the water volume in an energy-efficient manner, allowing for easy mixing of the particles with the polluted water (due to the enhanced diffusion coefficients of fine particles) and efficient mass transfer with the target contaminants, which has the potential to exhibit superior treatment kinetics at lower applied energy and cost compared to membrane technology for example. If the nanoparticles can be reused multiple times, this only adds to the cost savings. Nanoparticles in a slurry formulation can treat water through adsorption or chelation of contaminants, catalytic degradation, flocculation, or other means dependent on

* This chapter is adapted from a previously published book chapter: Leshuk, T.; Gu, F. Magnetically Recyclable Nanomaterials for Water Treatment. In *Nanotechnology for Water Treatment and Purification*; Hu, A., Apblett, A., Eds.; Lecture Notes in Nanoscale Science and Technology; Springer, 2014; Vol. 22.

accessible surface area of the colloidal particles. Furthermore, magnetic nanoparticles can be used as the support or substrate for any conventional water treatment materials; similarly, composite materials containing a magnetic component can be used as magnetically active particles.

An obvious and critical concern when using nanoparticle slurries however is the difficulty in fully recovering the nanoparticles from the water in a cost-efficient manner. Indeed, due to concerns of nanotoxicology or environmental release of "nanopollutants," it is imperative to avoid leaving any residual nanoparticles in the final treated water, which is why having a fast and cost-effective method to recover the nanoparticles from dispersion is essential. The basic concept of magnetic separation is that when a magnet or magnetic field gradient is applied to a slurry of magnetic nanoparticles in the treated water, the particles will move towards the magnet for collection, resulting in nanoparticle-free treated water for discharge. Using permanent magnets for the separation step is also low energy and cost efficient. Thus the magnetic separation paradigm has the potential to enable efficient and cheap water purification, with the ability to address many of the same water contaminants treated by conventional means, but without requiring the use of chemical additives (which can be relatively expensive or leave degradation by-products in the treated water). Magnetic separations for water treatment purposes could be envisioned to be applied at an industrial or civic scale, for the purification of industrial effluent or drinking water; for environmental cleanup; in niche applications such as aerospace; or in point-of-use processes where more advanced water treatment infrastructure is nonexistent. Indeed, it should be emphasized that magnetic separation technology has already been extensively employed in industry (*e.g.*, mining, food quality control, etc.).[29,30]

Conceptually, the process of magnetic separation is easily envisaged – many of us have played with magnets and iron filings as children, and the principle seems clear and concrete: magnetic particles simply move towards a magnet. Indeed, several recent reviews on magnetically recyclable particles make a similar assumption that simply by virtue of their magnetic nature, magnetic particles will be automatically separated from dispersion upon application of a magnetic field.[31,32] In actuality however, magnetic separation of particles from a suspension involves complex physics, and magnetic separability is far from guaranteed, but rather depends on the nature of the magnetic materials used, the concentration of particles and their colloidal stability, the magnitude of magnetic field gradients, among many other variables. The purpose of this section is to introduce some of the physics governing magnetophoretic phenomena, and considerations to be taken into account when designing magnetic separations.

2.3 Magnetism and Magnetization

In the context of nanotechnology for water treatment, we are primarily interested in nanoparticles of magnetic materials, or nanomaterials and composites comprised of such particles, due to their small size and high specific surface area. Therefore the following discussion will relate primarily to ultrafine particles of magnetic materials, and is drawn from references.[33–36]

For magnetic separations in a water treatment, oxide nanoparticles are typically used, as fine metallic particles are highly reactive in aqueous environments and oxidize readily under environmental conditions, which would lead to variable or unpredictable magnetic properties as the particles oxidize over time. Iron oxides have been especially studied and implemented as magnetic nanomaterials due to economic considerations (iron is cheap and abundant, compared to cobalt for example, or rare earth elements), their relatively low toxicity and low environmental threat, along with their ease of synthesis and well-understood chemistry.

The iron ion possesses a strong magnetic moment due to the unpaired spin magnetic moments of its valence electrons. In crystals containing iron, these permanent atomic magnetic moments can align or orient themselves with respect to each other in various arrangements, giving rise to paramagnetic, ferromagnetic, antiferromagnetic, or ferrimagnetic materials (Figure 1). In a paramagnetic material, the individual atomic magnetic moments are randomly oriented in the absence of a magnetic field, irrespective of temperature, giving the bulk material a net magnetic moment of zero (Figure 1a). On application of an external magnetic field however, some of the atomic moments will align in the direction of the field, imparting a small net magnetic moment to the material, which disappears on removal of the external field. In a ferromagnetic crystal, the atomic magnetic moments are aligned parallel with each other even in the absence of an applied field (Figure 1b), while in an antiferromagnetic crystal the moments are aligned but in opposite directions (Figure 1c), cancelling each other out and rendering a net zero magnetic moment to the material as a whole. A ferrimagnetic material is similar to an antiferromagnetic material, but where the antiparallel magnetic moments are of different magnitudes (Figure 1d), and thus the material retains a net magnetic moment, behaving like a ferromagnet.

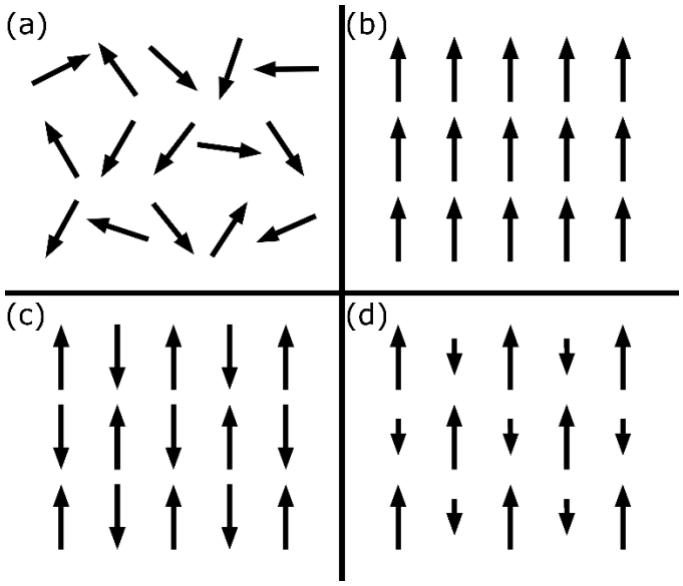

Figure 1. Simple schematic of the alignment of atomic magnetic domains in different magnetic materials: (a) paramagnetic, (b) ferromagnetic, (c) antiferromagnetic, and (d) ferrimagnetic. Figure adapted from.[36]

Thermal energy typically alignment of these atomic magnetic moments, and the ordered alignment breaks down above a certain temperature, namely the Curie temperature $\boldsymbol{T_C}$ for ferromagnetic and ferrimagnetic materials, or the Néel temperature $\boldsymbol{T_N}$ for antiferromagnetic materials, above which temperatures the magnetic moments of the materials are randomly oriented like a paramagnetic material, retaining no net magnetic moment.

A bulk ferromagnetic material is comprised of multiple microscopic magnetic domains, where the atomic magnetic moments within each domain are aligned with each other (as in Figure 1b), but not necessarily with adjacent domains. Crystal grain boundaries delineate magnetic domains in a polycrystalline material, although a single crystal grain can be composed of multiple magnetic domains.

The magnetization of a material $\boldsymbol{M}$ is defined as its net magnetic moment per unit volume, and is the sum of the individual magnetic moments composing the material, per unit volume. On a bulk scale, the magnetization of a material is thus the sum of the magnetization of the constituent magnetic domains, while on the microscopic level of the domains, the magnetization is the sum of the atomic magnetic moments in that domain. Within a single domain, due to the alignment of all the atomic magnetic moments (in a ferromagnet), the magnetization of the material is saturated at a maximum value $\boldsymbol{M_s}$ (in the direction of the alignment of the atomic moments), which is limited by the magnitude of the atomic moments and their arrangement and packing within the crystal lattice. Thus M_s is a material-specific property, dependent on the atomic composition and crystal structure of the particular material. However, on the bulk scale again, the net magnetization of a ferromagnetic material can be zero, as all the domain magnetic

moments within the material, despite being each magnetized at M_s, can be oriented in random directions, cancelling each other out.

On application of an external magnetic field $\boldsymbol{H}$, the magnetization of the material can be altered, producing a magnetization curve (Figure 2). Starting from zero, the magnetization of a bulk ferromagnetic material increases with H until a saturation value of M_s is reached. This process corresponds to the reorientation and alignment of the individual domain moments composing the material in the direction of the externally applied field, converting a multi-domain material to effectively a single domain (alignment of all microscopic domains). Thus M_s is naturally reached when all the domains, each magnetized at M_s, are oriented in the same direction. Thus magnetization of a material does not alter the magnitude of magnetization in any domain, but rather the direction of their magnetization.

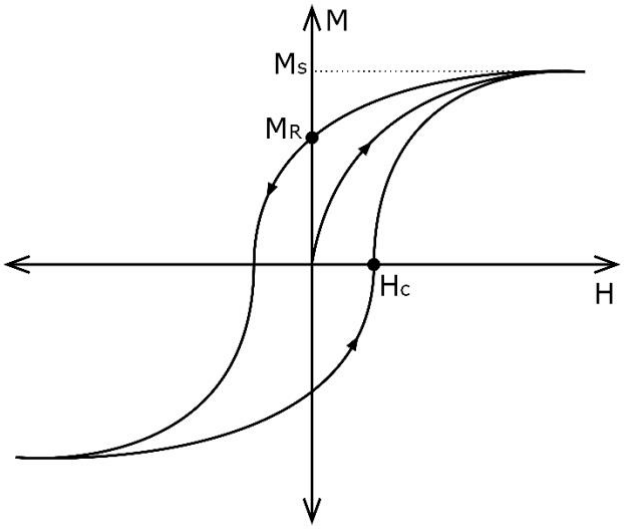

Figure 2. Magnetization curve of a typical ferromagnetic material, adapted from.[33]

However, when H is removed, the magnetization of the material does not return to net zero, since the magnetic domains do not all return to their original random orientations, but rather some remain aligned with each other in the previous direction of H. This residual magnetization, $\boldsymbol{M_R}$, is called the remanence. To reduce the net magnetization of the material M_R back to zero, an externally applied field of magnitude $\boldsymbol{H_C}$ must be applied in the opposite direction of M_R, where H_C is called the coercivity. This effect leads to hysteresis in the magnetization curve. The susceptibility of the material is the relation between H and M, where the differential susceptibility $\boldsymbol{\chi_d} = dM/dH$, with an initial susceptibility $\boldsymbol{\chi_0}$ given by the value of χ_d at $M = 0$, *i.e.*, the slope of the magnetization curve at the origin.

Magnetite (Fe_3O_4) and maghemite (γ-Fe_2O_3) are common magnetic iron oxides, and are ferrimagnetic at room temperature, with T_C of 850 K (although T_C is difficult to measure for maghemite, as it is unstable at high temperatures, irreversibly transforming to hematite at ~670

K). Magnetite contains a 2:1 ratio of Fe^{3+}:Fe^{2+} ions, where maghemite is the typical oxidation product of magnetite, produced through removal of the Fe^{2+} ions from the magnetite crystal lattice. Both materials have an average susceptibility of ~3 (SI units), although magnetite has a higher saturation magnetization of 92 A m^2 kg^{-1}, compared to maghemite's 76 A m^2 kg^{-1}. Despite the higher M_s of magnetite, maghemite is also frequently employed in nanotechnology applications, since the spontaneous oxidation of magnetite under standard conditions is very difficult to prevent, and from an engineering perspective it can be useful to pre-oxidize magnetite nanomaterials to maghemite in order to avoid oxidation-induced iron leaching over time, and the inevitable change in magnetic properties that this oxidation process implies.

Superparamagnetism is a nano-specific phenomenon that arises when ferromagnetic (or ferrimagnetic) crystals are reduced in size to the nanoscale. Below a certain size, such nanocrystals can only support a single magnetic domain, and thus some of the above properties of bulk magnetic materials emerging from the collective ensemble of many domains disappear in magnetic nanocrystals (*e.g.*, superparamagnetic nanocrystals do not possess hysteresis in their magnetization curve). Simply put, thermal energy is sufficient to demagnetize small crystals. As stated above, single magnetic domains can be thought of as possessing a single large magnetic moment (the sum of the atomic moments aligned with each other). However after application of an external magnetic field H, for a single domain particle (of volume $\boldsymbol{V}$) to maintain its magnetic polarization against the randomizing thermal background energy, its magnetic anisotropy energy, $\boldsymbol{KV}$, be much greater than thermal energy $\boldsymbol{k_B T}$, or $KV \gg k_B T$. Since KV is a function of volume, below a certain size and above a certain temperature, the magnetic anisotropy energy is too weak to prevent the thermal fluctuation of the particle's magnetic moment, and thus on removal of H, the magnetization of the nanoparticle rapidly flips directions, rendering a net zero magnetization for the particle at zero applied field (*i.e.*, no hysteresis). However, upon application of an external field, the particle's magnetic moment will align in the direction of H and will approach M_s like a bulk ferromagnetic material. Hence this effect was termed superparamagnetism, as the thermal spin randomization is conceptually similar to paramagnetic materials, although the attainable magnetization values in an externally applied field are much higher than for paramagnets. The implication is that superparamagnetic nanocrystals possess no permanent magnetic dipole moment at zero applied field, but when placed in an externally applied field can be temporarily magnetized with strength equivalent to a bulk ferromagnetic material.

It should also be noted that possessing a single magnetic domain is not sufficient to render a particle superparamagnetic; superparamagnetism is an independent function of size. Conveniently, magnetite and maghemite are superparamagnetic at room temperature below crystal sizes of ~30 nm, above which threshold size they regain ferrimagnetic properties, although they may still be single domain. Interfacial effects are also important in nanocrystals, and the measured saturation magnetization of nanocrystals is typically smaller than that of their corresponding bulk materials, due to surface spin canting, undercoordination, or crystal defects.

Although useful in magnetic data recording media, ferromagnetic materials are typically impractical for magnetic separation-based water treatment. Due to their permanent magnetic moments at zero applied field, ferromagnetic particles tend to strongly aggregate in water due to dipolar attraction, reducing the accessible surface area and diffusion coefficient of the particles, and even leading to gravity settling of the aggregates (*i.e.,* the particles removing themselves from the water treatment volume). These problems have been observed for ferromagnetic nanoscale zero-valent iron particles used in water treatment.[37] Thus the primary advantages of using nanoparticles and nanostructured materials for water treatment (viz. high specific surface area, excellent dispersibility throughout the water matrix) are counteracted by magnetic aggregation.

From an engineering perspective, the ideal particles for magnetic separation-based water treatment processes would behave as "on-off" magnetic switches: unmagnetized when dispersed throughout the water matrix for treatment (in order to avoid the aforementioned deleterious magnetic dipolar aggregation), but which can be easily and strongly magnetized after the treatment process in order to be magnetically separated, and then demagnetized again prior being employed in subsequent treatment cycles, etc. This is of course a description of superparamagnetism, where the magnetism of the particles is "switched on" by application of an external magnetic field. Thus the significance of superparamagnetism for magnetic water treatment is primarily to minimize uncontrolled nanoparticle aggregation during the treatment process, yet allow for easy magnetic recovery afterwards. Iron oxide nanoparticles of magnetite or maghemite below 30 nm in diameter are superparamagnetic at room temperature (termed SPIONs, superparamagnetic iron oxide nanocrystals), and are thus heavily employed in water treatment nanotechnologies, although other ferrite materials, or even non-superparamagnetic nanoparticles, can be used if properly stabilized against aggregation.

2.4 Forces in a Magnetic Colloid

As referred to above, typically the ideal magnetic separation-based water treatment nanotechnology can be described as a colloidal dispersion (slurry) of non-interacting nanoparticles or nanomaterials, diffusing freely throughout the volume of water to be treated, which can be rapidly separated from the water once the treatment is complete through application of an externally applied magnetic field. However, achieving such a system is nontrivial, due to the complexity of designing for the number of forces acting on the particles at the different stages of the separation process. Particles may be either too magnetic (leading to extensive interparticle magnetic aggregation) or not magnetic enough (requiring impractically long times for nanoparticle magnetic separation).

In order to achieve directional magnetophoresis, the magnetic force must be greater than the forces opposing motion, namely Brownian motion in the case of nanoparticles. The magnetic force acting on a spherical magnetic particle of volume $\boldsymbol{V}$ (radius $\boldsymbol{r}$) in a magnetic field gradient is

$$\overrightarrow{F_m} = V(\vec{M} \cdot \vec{\nabla})\vec{B} = \frac{4}{3}\pi r^3(\vec{M} \cdot \vec{\nabla})\vec{B} \quad (1)$$

where $\vec{M}$ is the magnetization of the particle per unit volume and $\vec{B}$ is the externally applied magnetic field.

For nanoparticles, gravitational forces are typically insignificant, but may be more important for dense iron-based particles, and should thus be considered for completeness:

$$\overrightarrow{F_g} = m\vec{g} = \frac{4}{3}\pi r^3 \Delta\rho \vec{g} \quad (2)$$

where $\Delta\rho$ is difference of the particle's density from that of the surrounding medium (*e.g.*, water), and $\vec{g}$ is the acceleration due to gravity.

The motion of the nanoparticles is opposed by viscous drag forces, given by Stokes' law as

$$\overrightarrow{F_d} = -3\pi\eta D_H \vec{v} \simeq -6\pi\eta r\vec{v} \quad (3)$$

where η is the dynamic viscosity of the medium ($\eta = 10^{-3}$ Pa s for water at room temperature), D_H is the hydrodynamic diameter of the particle (which can be approximated by $D_H = 2r$), and $\vec{v}$ is the velocity of the particle. The average magnetophoretic velocity of a single particle can thus be estimated by balancing Eqs. 1 and 3:

$$\overrightarrow{F_m} + \overrightarrow{F_d} = 0$$

$$\frac{4}{3}\pi r^3(\vec{M} \cdot \vec{\nabla})\vec{B} - 6\pi\eta r\vec{v} = 0$$

$$\vec{v} = \frac{2r^2(\vec{M} \cdot \vec{\nabla})\vec{B}}{9\eta} \quad (4)$$

More generally however, the motion of the particle in any single direction is opposed by Brownian motion, where a simplified representation of the Brownian force at a particular moment in time can be given by

$$\overrightarrow{F_B} = \vec{\xi}(12\pi\eta r k_B T/dt)^{\frac{1}{2}} \quad (5)$$

where $\vec{\xi}$ is a fluctuating random vector with a Gaussian distribution, k_B is the Boltzmann constant, T is the temperature, and dt is the time increment.[38] An approximation of the time average Brownian force can be simply taken as the thermal energy in opposition to motion of the particle by a significant amount (*e.g.*, distance r) in any specific direction:

$$k_B T = (\overrightarrow{F_m} + \overrightarrow{F_g} + \overrightarrow{F_d}) \cdot \vec{r} \quad (6)$$

When the right-hand side of Eq. 6 is significantly greater than the thermal energy of order $k_B T$, the particle can have directional motion, and if significantly less than $k_B T$, the net directional forces acting on the particle are insufficient to overcome the randomizing Brownian force, and

the particle remains dispersed in suspension. Thus as a rough approximation,[39] the threshold Brownian force for the particle to overcome is

$$F_B \approx \frac{k_B T}{r} \tag{7}$$

This accounts for the size dependence of the Brownian force, where large microparticles are less susceptible to such randomizing molecular motions and can settle under the force of gravity, while for small nanocrystals Brownian forces dominate.[40] Alternatively, comparing Eqs. 1 and 2 with Eq. 5, it can be seen that the directional forces scale with r^3, while the Brownian force only scales as $r^{\frac{1}{2}}$, indicating the diminished significance of Brownian forces for larger particles.

In summary, to achieve directional magnetophoresis, $\overrightarrow{F_m}$ should be $\gg \left(\overrightarrow{F_B} + \overrightarrow{F_g} + \overrightarrow{F_d}\right)$. From Eq. 1 it can be seen that for a constant applied magnetic field gradient there are only two ways to increase $\left|\overrightarrow{F_m}\right|$ through engineering of the nanoparticles: either by selection of a material with higher magnetization, or for a fixed material, by increasing the particle size. However, as stated above, superparamagnetism is a size-dependant nanoscale phenomenon, and upon increasing the size of magnetic nanocrystals above a particular threshold diameter they transition to ferromagnetic behaviour, resulting in deleterious uncontrolled magnetic dipolar aggregation in suspension. Since superparamagnetism is an essential property for many magnetic separation-based water treatment processes, there would appear to be an upper limit on the per-particle $\left|\overrightarrow{F_m}\right|$, since superparamagnetism is limited to nanocrystals $\lesssim$ 30 nm in size (for magnetite/maghemite). However, as discussed in Section 2.5 below, such small nanocrystals are often found to be magnetically inseparable from suspension (*i.e.*, $\left|\overrightarrow{F_m}\right| \ll k_B T/r$), thus requiring a larger $\left|\overrightarrow{F_m}\right|$ to enable magnetophoresis, yet apparently requiring the sacrifice of superparamagnetism in order to achieve it. However, this apparent paradox can be resolved through the use of polycrystalline particles, where every constituent crystal in the polycrystalline particle is below the superparamagnetic threshold in size (*i.e.*, nanocrystals), yet where the $\overrightarrow{F_m}$ of all these crystals sum together to render a larger net $\overrightarrow{F_m}$ for the particle as a whole, enabling magnetophoresis while preserving superparamagnetism. Such polycrystalline or supraparticles can be composed exclusively of magnetic nanocrystals, or multiple SPIONs dispersed in a matrix or composite material (*e.g.*, Dynabeads® as used in biological magnetic separations).

2.5 Interparticle Interactions and Cooperative Magnetophoresis

Magnetic nanocrystals < 20 nm in diameter (SPIONs) should not be magnetically separable at low field gradients (< 100 T m^{-1}) according to the above considerations. For example, for a 10 nm magnetite nanocrystal ($M_s \simeq 4.8 \times 10^5$ A m^{-1}) in a 100 T m^{-1} field gradient at 300 K, $F_m = 2.5 \times 10^{-17}$ N, while $F_B \approx k_B T/r = 8.3 \times 10^{-13}$ N; that is, $F_B \gg F_m$. Indeed, by this logic only magnetite crystals larger than ~135 nm should be magnetically separable. Even without considering Brownian motion, from Eq. 4 the average magnetophoretic velocity of the above 10 nm SPIONs should be only ~0.3 μm s^{-1} in water. However, this is several orders of magnitude

slower than experimentally observed SPION magnetophoretic velocities under similar conditions.[39] This experimental observation that SPIONs can in fact be readily magnetically separable even under low field gradients has thus prompted the expansion of magnetophoretic theory to include interparticle interactions.

To explain the low field gradient magnetic separability of superparamagnetic nanoparticles, it was theorized that when magnetized, nanocrystals would be expected to exhibit very large field gradients near their surface, which could lead to the magnetic aggregation of the particles into larger "effective particles" or aggregate structures with sufficient net magnetic force to overcome Brownian motion.[39] Thus nanoparticles could be expected to accelerate or catalyze their own magnetic separation in a cooperative manner. For superparamagnetic particles, removal of the externally applied magnetic field should dissipate magnetic interactions, resulting in aggregate dissociation. Such transient magnetic aggregation behaviour (chain formation) has been observed experimentally.[41]

The group of Faraudo and Camacho has perhaps done the most work in describing the physical concepts of cooperative magnetophoresis, and the following discussion is derived primarily from references [41–43].

The dipole-dipole interaction energy between two superparamagnetic colloidal particles in an externally applied magnetic field is given by

$$U_{dd} = \frac{\mu_0 {m_d}^2}{4\pi x^3}(1 - 3\cos^2\theta) \tag{8}$$

where μ_0 is the magnetic permeability of free space, x is the distance separating the particles (centre-to-centre), θ is the angle between the direction of the externally applied field and the line joining the centres of the two particles, and m_d is the dipole moment of the particles, given by

$$m_d = \frac{4}{3}\pi r^3 M_s \tag{9}$$

where the assumption is made that under typical fields applied during magnetic separation, the magnetization of the sample reaches saturation. The minimum energy configuration is obtained when $x = d$ (the diameter of the particles) and $\theta = 0$, or

$$U_{dd}^{\max} = -\frac{\mu_0 {m_d}^2}{2\pi d^3} \tag{10}$$

A useful means by which to characterize the relative strength of this magnetic interaction is to take its ratio with the thermal energy, defining a magnetic coupling parameter Γ as

$$\Gamma = \frac{|U_{dd}^{\max}|}{k_B T} = \frac{\mu_0 {m_d}^2}{2\pi d^3 k_B T} = \left(\frac{\lambda_B^m}{d}\right)^3 \tag{11}$$

where λ_B^m is called the magnetic Bjerrum length, the characteristic interparticle distance at which magnetic interactions are significant compared to thermal energy, given by

$$\lambda_B^m = \left(\frac{\mu_0 {m_d}^2}{2\pi k_B T}\right)^{\frac{1}{3}} \tag{12}$$

Physically, interparticle magnetic interactions are significant (*i.e.*, magnetic aggregation and cooperative magnetophoresis are possible) for $\Gamma \gg 1$, while for $\Gamma \ll 1$ thermal energy dominates. For the above example of 10 nm SPIONs, $\Gamma \simeq 3.05$, indicating the possibility of cooperative magnetic separation where the non-interacting model predicted magnetophoresis to be impossible, thus demonstrating the importance of considering interparticle interactions.

With this understanding of the effect of interparticle distance on magnetic interactions, the kinetics of cooperative magnetophoretic separation can be elucidated in terms of particle concentration in suspension (*i.e.*, the higher the particle concentration, the closer their spacing and thus higher their magnetic interactions). The mass concentration of particles in a suspension is given as

$$C = \frac{Nm}{V_t} = \frac{4\pi r^3 \rho N}{3V_t} = \frac{4\pi r^3 \rho}{3x^3} \tag{13}$$

where N is the total number of particles in a suspension of volume V_t, m is the mass of a single particle of density ρ, and $x = \sqrt[3]{V_t/N}$ is the average interparticle distance. A characteristic concentration C^* can be defined when $x = \lambda_B^m$,

$$C^* = \frac{4\pi r^3 \rho}{3{\lambda_B^m}^3} = \frac{\pi\rho}{6\Gamma} \tag{14}$$

Experimentally,[41] the cooperative magnetophoretic separation time t_s of superparamagnetic particles has been found to have an exponential dependence on particle concentration of the form:

$$t_s = t_0 \left(\frac{C^*}{C}\right)^{\alpha} \tag{15}$$

where t_0 (in units of time) and α are experimentally determined parameters dependant on the dimensions of the magnetic separator, field gradient applied, etc., although an *ab initio* argument for $\alpha \simeq \frac{1}{4}$ (which was the experimentally fitted value) is given in reference,[43] which relates to the growth kinetics and magnetophoretic velocity of the particle aggregates/chains.

The obvious assumption in the above discussion is that, apart from their magnetic interactions, the particles are otherwise non-interacting. However, for colloidal nanoparticles, this assumption is generally untrue, and other colloidal interactions can be significant in comparison to the magnetic dipolar energy. In magnetic separation-based water treatment applications, the ideally desirable situation is for the transient magnetic aggregation to behave as a reversible "on-off switch," *i.e.*, for the particles to be relatively non-interacting and highly colloidally stable in the absence of an externally applied magnetic field (in order for the particles to diffuse freely,

expose a high surface area, and exhibit good mass transfer kinetics in the volume of water to be treated), to rapidly form transient aggregates when an external field is applied (for efficient magnetic separation), and then for the aggregates to reversibly dissociate and return the particles to a highly dispersed colloidal state when the external field is removed again. Actually achieving such behaviour in realistic matrices is non-trivial however, since frequently (due to nonmagnetic interactions discussed below) the particles will either be too colloidally stable to form the transient aggregates in the first place (thus remaining magnetically inseparable), or they will form irreversible aggregates which cannot be re-dispersed back to a stable colloid when demagnetized. Avoiding such undesirable outcomes requires understanding and balancing all the colloidal forces present in the system.

Apart from the magnetic interaction energy given above (Eq. 8), other interactions to consider are electrostatics (DLVO theory) and dispersion forces. The van der Waals potential between two spherical particles with radii r_1 and r_2 is given by

$$U_{vdW} = -\frac{A_H}{6}\left[\frac{2r_1r_2}{x^2-(r_1+r_2)^2} + \frac{2r_1r_2}{x^2-(r_1-r_2)^2} + \ln\left(\frac{x^2-(r_1+r_2)^2}{x^2-(r_1-r_2)^2}\right)\right] \quad (16)$$

where A_H is the Hamaker constant between the particles through the surrounding medium ($A_H = 33 \times 10^{-21}$ J for magnetite nanoparticles interacting across water[44]) and x is the distance between the centres of the spheres (where the distance between the surfaces is $D = x - r_1 - r_2$).[45] For equally-sized particles ($r_1 = r_2 = r$), the above equation can be simplified to

$$U_{vdW} = -\frac{A_H}{6}\left[\frac{4x^2r^2 - 8r^4}{x^4 - 4x^2r^2} + \ln\left(\frac{x^2-4r^2}{x^2}\right)\right] \quad (17)$$

Calculation of the electric double layer interaction between two particles is often a complex consideration, typically involving many approximations. For more rigorous equations (beyond Derjaguin's approximation) describing the double layer interaction between nanoparticles at low ionic strengths, refer to [46]. More accessible (and hence more approximate) equations for the interaction potential between two equally sized spheres with equal surface potentials are given below.[46,47] For large interparticle separations ($\kappa D > 4$, where κ is the inverse Debye-Huckel length), assuming the surface potential of one particle does not affect the other, thin double layers and symmetrical electrolytes, the linear superposition approximation can be used:

$$U_{DL} = \frac{64\pi\varepsilon_0\varepsilon_r r^2}{x}\left(\frac{\gamma k_B T}{ze}\right)^2 \exp(-\kappa D) \quad (18)$$

$$\gamma = 4\tanh\left(\frac{\Phi}{4}\right), \text{ for } \kappa x \geq 10 \text{ and } \Phi < 8 \quad (19)$$

$$\Phi = \frac{ze\psi}{k_B T} \quad (20)$$

$$\kappa = \sqrt{\frac{2c_0 z^2 e^2}{\varepsilon_0 \varepsilon_r k_B T}} \tag{21}$$

where ε_0 is the vacuum permittivity, ε_r is the relative permittivity of the solvent, z is the charge number (electrolyte valence), c_0 is the concentration of the symmetrical electrolyte (in units of m^{-3}), e is the elementary charge, and ψ is the surface potential of the particles (which can be estimated from the Grahame equation if only the charge of the colloid is known[42]). For small interparticle separation distances, the Derjaguin approximation can be used:

$$U_{DL} = \frac{\pi \varepsilon_0 \varepsilon_r r \psi^2}{2} \ln[1 + \exp(-\kappa D)] \tag{22}$$

If the particles are surfactant-stabilized (the above assumes simple electrostatic stabilization), additional repulsion forces must be taken into account. However these above equations are sufficient for a basic energy balance on the system during magnetic separation, where the total interaction energy between two nanoparticles in suspension is the sum of Eqs. 8, 17, and 18/22, given by $U = U_{dd} + U_{vdW} + U_{DL}$. This results in a potential energy curve as a function of interparticle separation distance, examples of which are given in Figure 3.

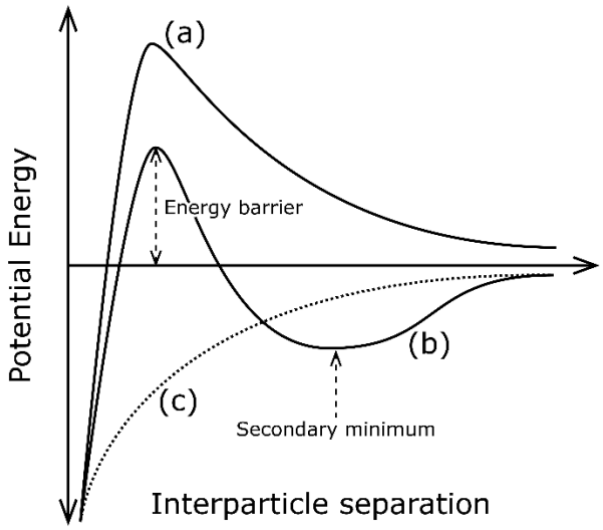

Figure 3. Potential energy profiles of magnetic particles in colloidal dispersion: (a) desirable curve for non-magnetized particles, (b) desirable curve for magnetized particles to enable reversible magnetic aggregation, (c) undesirable curve (dotted line) for magnetized particles, resulting in irreversible magnetic aggregation.

The desirable situation in most magnetic separations (the "on-off switch" as described above) is for the potential energy to be everywhere positive in the absence of an applied magnetic field (Figure 3a, repulsive force to stabilize the colloidal dispersion and prevent aggregation), and exhibit a secondary minimum in the potential energy curve when the particles are magnetized to

allow for transient magnetic aggregation (Figure 3b), but with an energy barrier (provided by electrostatic repulsion) to prevent the particles from approaching each other too closely (resulting in irreversible aggregation at the primary energy minimum). This way, when the magnetic field is removed, the secondary minimum disappears, and the particles repel each other once again, returning to a dispersed colloid. The undesirable situation occurs when the magnetic dipolar interaction is too strong, or electrostatic repulsion insufficient, in which case there is no energy barrier to prevent irreversible aggregation of the magnetized particles at the primary minimum (Figure 3c). As can be seen, this delicate energy balance is a function of particle size, surface charge, applied field gradient, and ionic strength of the water to be treated, and thus many factors must be taken into account to ensure timely and practical reversible magnetic separation is achievable in the system of interest.

2.6 Challenges for Magnetic Water Treatment

Due to the cooperative magnetophoretic mechanism and balance of forces required to prevent irreversible aggregation, designing a reusable magnetic separation-based water treatment system can be challenging from an engineering perspective, and it is usually not obvious to predict whether the magnetic particles of interest will even separate when a magnetic field is applied to the suspension. Several challenges when designing water treatment systems based on magnetic separation nanotechnology are discussed below.

Firstly, as discussed above, the energy balance of the colloidal dispersion of nanoparticles should be considered under both magnetized and demagnetized conditions (assuming demagnetization is possible, given superparamagnetic particles). If the repulsive interparticle interactions are too strong, the particles may not be able to transiently aggregate even when magnetized, inhibiting cooperative magnetophoresis and resulting in magnetic inseparability of the particles from suspension. Conversely, if repulsive interactions are low, irreversible aggregation of the particles could result during magnetic separation, rendering them essentially single use. Although only electrostatic stabilization was considered above, steric stabilization of the colloidal particles with polymers can either help or hinder magnetic separability according to the same principles (*i.e.*, if particles cannot approach each other closely enough, cooperative magnetophoresis will be impossible). When not magnetized, high colloidal stability of the nanoparticle dispersion is typically desired, in order to expose a high surface area throughout the volume of water to be treated. Ensuring colloidal stability in realistic matrices (*i.e.*, water with ionic strength, dissolved contaminants, humic acids, etc.) is challenging for even nonmagnetic particles, as adsorption of contaminants or flocculation with dissolved substances can change the surface energy balance of the particles, or result in premature flocculation and sedimentation. Such destabilizing of otherwise too-stable nanoparticle dispersions can be desirable in some cases (enabling magnetic separation of otherwise inseparable particles through the formation of larger aggregates/supraparticles), but uncontrolled aggregation is difficult to predict through modeling.

Another engineering challenge is the different length scales at work in typical magnetic separations, from within angstroms from the surface of single nanoparticles to the scale of meters

in a magnetic separator. Although this brief review has focused primarily on the nanoscale, predicting and designing a system for a particular required magnetic separation duration or magnetophoretic velocity will also incorporate macroscopic considerations, such as the geometry of the magnetic separator and magnetic fields. For example, macroscopic time scales for separating magnetic nanoparticles are influenced by the cooperative magnetic separation mechanisms discussed above, while these mechanisms are simultaneously influenced by field gradients which are a function of separator design; the micro- and macroscopic are convoluted. Furthermore, many of the equations provided herein assume static fluid, although for magnetic separations involving flowing water (*e.g.*, a flow-through magnetic separator), additional fluid dynamics must be brought to bear on the system.

It should also be emphasized that the cooperative magnetophoresis mechanism discussed herein, while enabling the separation of nanoparticles that would be individually nonmagnetically separable, still has a strong built-in size dependence, and does not guarantee the separation of magnetic nanoparticles. For example, it is still controversial whether SPIONs are magnetically separable under low field conditions.[48] Indeed, the main industrial application of SPIONs is as ferrofluids, which are designed to be magnetically inseparable. Thus although use of nanoparticles (SPIONs) may be especially desirable in water treatment applications due to their extraordinary specific surface area, care should be taken to ensure that they will still be magnetically separable from the target matrix.

Finally, an additional concern of the cooperative magnetic separation paradigm is the potential for trace residual nanoparticles remaining in suspension after the magnetic separation process. That is, if nanoparticles require cooperative assembly into transient magnetic aggregates to enable magnetic separability, there is the possibility that particles which are not incorporated into the transient aggregates in time would be "stranded" in suspension, unable to magnetically separate on their own. Given the concerns about environmental contamination by nanoparticles or nanoparticle toxicity, the potential for adding low concentrations of nanoparticles to treated water in the process of magnetic separation is clearly of concern. Thus for practical applications of magnetic separation nanotechnology, at least until this potential problem of nanoparticles left behind is investigated further, magnetic separators should probably be coupled with a filtration process, to separate any residual trace nanoparticles which were not recovered in the "first pass" magnetic separation step.

2.7 Application to Photocatalysis

Photocatalysis over nanoscale titanium dioxide is a highly promising technique for the deactivation or mineralization of a broad spectrum of waterborne contaminants, due to the low cost, abundance and minimal toxicity of TiO_2, as well as the central concept that the TiO_2 can theoretically be reused indefinitely for cost-effective purification of large volumes of water. In photocatalytic water treatment, the most efficient reactors involve dispersion of the nanocatalyst into the contaminated water as a slurry.[22,24,25] Nanoparticle recovery after the treatment process is essential not only for reuse of the catalyst, but also to prevent nanoparticle contamination of

the treated effluent. Unfortunately, nanoparticle separation challenges remain a critical hurdle to practical application of this promising treatment technology.[26–28]

Magnetic separation is especially useful in nanotechnology for collection of nanoparticles which are challenging to manipulate by other means.[30,49–52] To render non-magnetic nanomaterials magnetically separable, typically composite nanoparticles are synthesized by immobilizing the functional nanomaterial on a superparamagnetic support (*e.g.*, in a core-shell structure).[53–58] We have previously employed this strategy to synthesize magnetically recyclable TiO_2 photocatalysts.[54] To adapt the magnetic separation paradigm to practical TiO_2 recycling, we started with a larger polycrystalline magnetite core to increase the total magnetic moment of each particle for faster separation, yet where the individual magnetite nanocrystals in the core are each below the ferromagnetic threshold size and thus collectively preserve the crucial property of superparamagnetism. Thus, application of magnetic recycling has been successfully demonstrated for photocatalyst recycling, and implementation of magnetic recovery concepts are presented in Chapter 5.

Chapter 3
Solar Photocatalytic Degradation of Naphthenic Acids in Oil Sands Process-Affected Water†

3.1 Summary

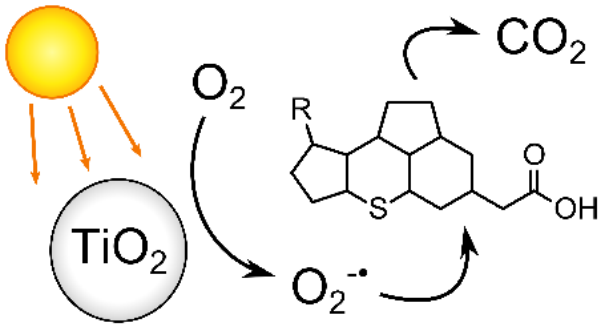

Bitumen mining in the Canadian oil sands creates large volumes of oil sands process-affected water (OSPW), the toxicity of which is due in part to naphthenic acids (NAs) and other acid extractable organics (AEO). The objective of this work was to evaluate the potential of solar photocatalysis over TiO_2 to remove AEO from OSPW. One day of photocatalytic treatment under natural sunlight (25 MJ/m^2 over ~14 h daylight) eradicated AEO from raw OSPW, and acute toxicity of the OSPW toward *Vibrio fischeri* was eliminated. Nearly complete mineralization of organic carbon was achieved within 1-7 day equivalents of sunlight exposure, and degradation was shown to proceed through a superoxide-mediated oxidation pathway. High resolution mass spectrometry (HRMS) analysis of oxidized intermediate compounds indicated preferential degradation of the heavier and more cyclic NAs (higher number of double bond equivalents), which are the most environmentally persistent fractions. The photocatalyst was shown to be recyclable for multiple uses, and thus solar photocatalysis may be a promising "green" advanced oxidation process (AOP) for OSPW treatment.

3.2 Introduction

Bitumen mining in the Athabasca oil sands is one of the largest industrial projects in the world, and development in the region continues to expand. An alkaline hot water method is used to extract surface-mined bitumen, generating large volumes of oil sands process-affected water (OSPW) in the process. OSPW has been found to be acutely and chronically toxic to many forms of life,[59–61] and is therefore stored on site in tailings ponds due to the industry's "zero discharge" policy, as there is currently no established method to treat the water for environmental discharge.

---

† This chapter is adapted from a previously published article: Leshuk, T.; Wong, T.; Linley, S.; Peru, K. M.; Headley, J. V.; Gu, F. Solar Photocatalytic Degradation of Naphthenic Acids in Oil Sands Process-Affected Water. *Chemosphere* **2016**, *144*, 1854–1861.

To date, an estimated 1 billion m^3 of OSPW has been accumulated in over 170 km^2 of tailings ponds in Alberta.[62,63]

OSPW is a complex saline solution containing high concentrations of suspended clays, dissolved organic compounds (including naphthenic acids, polycyclic aromatic hydrocarbons (PAHs), and BTEX compounds), trace heavy metals, and residual bitumen and solvents. A primary source of OSPW toxicity has been attributed to the acid extractable organics (AEO), including naphthenic acids (NAs), which are structurally diverse alkyl-branched acyclic and cycloaliphatic carboxylic acids with the conventional formula $C_nH_{2n+z}O_2$ (where z is a negative even integer related to the number of rings and double bonds).[12,13] Recently, high resolution mass spectrometry (HRMS) has also identified aromatic and diamondoid acids in OSPW AEO, as well as species containing multiple carboxylates or heteroatoms.[64–66] NAs and OSPW toxicity are also associated with the base-neutral extractable organic fractions, although the focus of this work is on the AEO. While low molecular weight NAs are somewhat biodegradable, the heavier branched fractions are recalcitrant and highly environmentally persistent.[8,9,67] Thus, a water treatment solution is required for reclamation of the tailings ponds.

Among the methods investigated for OSPW treatment, advanced oxidation processes (AOPs) have been shown to be particularly effective for degrading NAs and reducing OSPW toxicity.[14–18] Photocatalysis over TiO_2 is an extremely powerful AOP that has been proven to eliminate a broad spectrum of organic pollutants in wastewaters, including NAs.[68–70] In aqueous suspension, photocatalysts absorb light to generate highly reactive free radicals, such as hydroxyl and superoxide radicals, which are capable of mineralizing even recalcitrant organic contaminants.[22,23] TiO_2 is a low-cost, earth abundant, and chemically stable photocatalytic material which can be recovered and reused over multiple treatment cycles.

Although powerful, the high capital and operating costs of AOPs could limit large-scale industrial application. Sunlight is a free and renewable energy source with the potential to greatly reduce the operating costs associated with water treatment, and it is well established that TiO_2 can absorb solar UV radiation to power the photocatalytic process.[27,71] Without the need to add chemical oxidants to the water, and considering the recyclability of the catalyst material, solar photocatalysis may be more practical than conventional methods for OSPW treatment.

The objective of this work was to evaluate the performance of solar photocatalysis to remove AEO from real OSPW. This research builds on the previous investigations into photocatalysis by Headley and co-workers.[69,70] Headley et al. previously demonstrated ~75% destruction of OSPW NAs through solar photocatalysis,[69] and Mishra et al. showed that UV_{254} photocatalytic treatment could eliminate acute NA toxicity according to the Microtox assay.[70] Despite these promising results, there has since been no research into how the process performs in OSPW, as previous researchers used either commercial NAs or model waters.[19,69,70] This is significant since the high ionic strength and suspended solids in the OSPW may have deleterious effects on the process efficacy or degradation kinetics. We thus sought to examine the feasibility of photocatalytic

treatment of real OSPW using natural sunlight. For this study we chose to use a TiO_2 nanoparticle slurry, a system which is often employed as a benchmark standard in the literature, to establish a treatability baseline for photocatalysis in OSPW. We also explored the photocatalytic reaction pathway and oxidized intermediate compounds using high resolution MS, and assessed the acute toxicity of the treated water toward *Vibrio fischeri*.

3.3 Experimental

3.3.1 Materials

OSPW collected on March 17, 2014 was provided by Shell Canada, and stored in sealed polyethylene containers in the dark. The OSPW was homogenized by stirring before each use, herein referred to as raw OSPW. For experiments where it was desirable to remove the suspended solids, the OSPW was centrifuged at 14,000 xg prior to use, and then referred to as centrifuged OSPW. A commercial mixture of naphthenic acids (technical grade), dichloromethane (DCM, ≥99.9%, HPLC grade), ammonium oxalate monohydrate (>99%, ACS grade), 1,4-benzoquinone (98%), sodium persulfate (≥99%), and *tert*-butyl alcohol (≥99.7%, ACS grade) were purchased from Sigma-Aldrich and used as received. Sulfuric acid (95-98%, ACS grade, Fisher), formic acid (Caledon Laboratories Ltd., Georgetown, ON), acetonitrile (HPLC grade, Caledon Laboratories Ltd., Georgetown, ON) and titanium dioxide nanoparticles (Aeroxide P25, ~10-50 nm particle diameter, 55 m^2 g^{-1} surface area, Acros) were used as received. P25 TiO_2 nanoparticles have been extensively studied and characterized in the literature, and are often used as a benchmark photocatalyst.

3.3.2 Photocatalysis Experiments

Outdoor solar photocatalytic experiments were performed during July – September 2014 at the University of Waterloo (Waterloo, ON, Canada). All experiments were performed in duplicate or triplicate. TiO_2 powder was first stirred into 200 mL of OSPW in a borosilicate glass beaker (82 mm O.D.) and dispersed by bath sonication. Beakers were sealed with polyethylene film (Glad, measured to be UV transparent by spectrophotometry) to prevent evaporation during the experiments. The mixture was then placed on a rooftop outdoors (43°28'17.9"N 80°32'32.2"W) and exposed to sunlight while stirring at 500 rpm. Controls included OSPW exposed to sunlight in the absence of TiO_2, and the TiO_2 OSPW mixture stored in the dark. Following solar treatment, the OSPW mixture was centrifuged to remove the TiO_2 nanoparticles, retaining the supernatant for analysis (stored at 4 °C in the dark). For one experiment, the TiO_2 collected by centrifugation was subsequently washed thrice with deionized water by centrifugation, dried overnight at 70 °C, and then redispersed into a fresh sample of OSPW for solar treatment, in order to test the photocatalyst's recyclability.

In one experiment, to investigate the radical species involved in the photocatalytic reaction, 0.1 g/L of a radical scavenger (ammonium oxalate, 1,4- benzoquinone, sodium persulfate or *tert*-butyl alcohol)[72,73] was added to the suspension (0.5 g/L TiO_2 in centrifuged OSPW) immediately before sunlight exposure. Inhibition of photocatalytic activity was calculated from the residual

AEO concentration following treatment in the presence and absence of the radical scavenger (C_s and C_n, respectively), according to the equation

$$\%\ \text{inhibition} = \frac{C_s - C_n}{C_0 - C_n}$$

where C_0 was the initial concentration of AEO in the OSPW.

The dates and weather conditions for the solar photocatalytic experiments described herein are presented in Table 1. Weather data was obtained from the University of Waterloo Weather Station archives.[74] Cumulative insolation was calculated by integrating the incoming shortwave radiation (measured by the weather station using a Kipp & Zonen CM11 pyranometer) over the duration of each experiment.

Table 1. Weather conditions for the outdoor photocatalytic experiments performed in this chapter.

Experiment	Date & Time Started	Date & Time Ended	Cumulative Insolation (MJ/m^2)	Ambient Air Temperature During Daylight Hours	
				Average Daily High (°C)	Average Daily Low (°C)
Figure 4a	16/07/2014 21:16	17/07/2014 20:55	24.7	22.2	9.6
Figure 4b (centrifuged OSPW)	21/07/2014 21:02	22/07/2014 20:55	25.3	29.0	15.8
Figure 4b (raw OSPW)	24/07/2014 21:01	25/07/2014 21:47	23.4	23.9	9.9
Figure 11, 6 and 7 (midpoint)[a]	13/09/2014 19:30	16/09/2014 13:30	31.4	15.9	6.2
Figure 11 (endpoint)[b]	17/09/2014 19:45	29/09/2014 12:00	181.4	20.9	8.9
Figure 17	18/08/2014 17:33	19/08/2014 17:28	20.5	25.0	9.2
Figure 5	05/08/2014 16:00	08/08/2014 16:03	63.8	24.1	14.0
Figure 8	30/07/2014 16:58	16/08/2014 14:25	89.4	22.0	11.5
Cycle 1	30/07/2014 16:58	31/07/2014 16:58	23.2	23.7	11.3
Cycle 2	05/08/2014 16:00	06/08/2014 15:57	21.2	24.7	12.6
Cycle 3	07/08/2014 15:57	08/08/2014 16:03	21.9	24.4	9.9
Cycle 4	13/08/2014 16:30	14/08/2014 16:28	14.4	16.7	10.9
Cycle 5	15/08/2014 16:12	16/08/2014 14:25	8.7	20.5	12.9
Figure 9	17/08/2014 17:00	18/08/2014 17:33	21.5	23.8	10.2

[a]Experiment was paused (beakers moved indoors) from 15/09/2014 12:17 PM to 16/09/2014 7:15 AM due to predicted rain.

[b]Experiment was paused (beakers moved indoors) from 20/09/2014 8:00 PM to 22/09/2014 1:00 PM due to predicted rain.

To assess the temperature dependence of the photocatalytic degradation kinetics, an Arrhenius plot was prepared using the data from all experiments performed with 0.5 g/L TiO_2 in centrifuged OSPW which had a measured AEO concentration greater than zero. An apparent rate constant was calculated for each data point from a pseudo-first order kinetics model, which was then correlated with the average ambient temperature measured during the period of treatment.

3.3.3 Analysis

The concentration of AEO was measured by Fourier transform infrared spectroscopy (FTIR, Bruker Tensor 27) according to the standard method[75,76] with minor modifications (*viz.*, the acidified samples were extracted thrice with DCM in a 1:12.5 solvent to sample volumetric ratio, with 65% total recovery), using the commercial NA mixture to prepare the calibration curve. The method detection limit (MDL) was 0.6 mg/L. AEO is a composite measure of classical NAs, oxy-NAs ($C_nH_{2n+z}O_x$, where x > 2), and other organic acids.[64]

Samples were filtered prior to the following analyses (Whatman 934-AH glass fiber filter), with the exception of analyses where suspended solids were of interest (*i.e.*, UV/vis, turbidity, TSS, TDS).

Electrospray ionization high resolution mass spectrometry (ESI-HRMS) was used to analyze the composition and speciation of the OSPW AEO. For ESI-HRMS, solid phase extraction (SPE), as previously described by Headley et al.[77] was used as a concentration and cleanup technique (method recovery was 79 ± 7%). In brief, 10 mL of each sample was acidified using concentrated formic acid to a pH of ~2 . SPE cartridges (200mg, ENV+, Biotage®, Charlotte, NC), were preconditioned with 7 mL each of acetonitrile and Milli-Q water. Eluents were discarded and the organic fraction eluted at a flow rate of ~1 mL/min using 7 mL of acetonitrile. Extracts were collected in 10 mL glass test tubes and evaporated using N_2 to just dryness. The dried residue was then reconstituted in 1 mL of 50:50 Milli-Q water:acetonitrile with 0.1% ammonium hydroxide and transferred to 2 mL amber GC vials.

The ESI-HRMS chemical analysis was conducted using an LTQ Orbitrap Elite (Thermo Fisher Scientific, San Jose, CA) operating in full scan and negative-ion mode. Mass resolution was set to 240,000 with an *m/z* scan range of 100-600. ESI source had the following conditions: sheath gas flow rate 25 (arbitrary units), spray voltage 2.90 kV, auxiliary gas flow rate 5 (arbitrary units), S lens RF level 67%, heater temperature 50 °C, and capillary temperature 275 °C. Infusion solvent used was 50:50 acetonitrile:water containing 0.1% ammonium hydroxide at a flow rate of 200 µL/min. The mass accuracy was <2 ppm error for all mass assignments, and the root mean square (RMS) error for all assignments associated with the entire mass spectra was in the range of 0.12 – 0.45 ppm. The instrumental detection limit was 1 mg/L and the method detection limit was 0.10 mg/L for AEO. Software used for molecular analysis was Xcalibur v 2.1 (Thermo Fisher Scientific, San Jose, CA) and Composer v 1.0.6 (Sierra Analytics, Inc., Modesto, CA).

The total AEO concentration measured by ESI-HRMS is referred to below as AEO_{MS} (where not specified, AEO was measured by the FTIR method). For ESI-HRMS quantification, external standard calibration was performed using a pre-defined 5-point regression of OSPW-derived organic acids at known concentrations and used to determine resulting AEO concentrations in samples. The values of total AEO_{MS} measured in the initial and treated OSPW samples should be considered semi-quantitative due to: a) a lack of certified naphthenic acid standards or alternatives; b) limited method validation and uncertainty estimates. The method and analytical parameters used in the present method can be found in SOPs (available from the Environment Canada website). It should be understood that the present semi-quantitative method is a step in progression to a final quantitation goal.

UV/visible optical absorption was measured with a spectrophotometer (BioTek Epoch). Turbidity (APHA 2130B), total suspended solids (TSS, APHA 2540D), total dissolved solids (TDS, APHA 2540C), mineral oil and grease (APHA 5520B), total organic carbon (TOC, APHA 5310B, combustion temperature 800 °C), chemical oxygen demand (COD, APHA 5220D), biochemical oxygen demand (BOD, APHA 5210B), anion concentration by ion chromatography (bromide, chloride, fluoride, nitrate, nitrite and sulfate, EPA 300.0), speciated alkalinity (as $CaCO_3$, EPA 310.2), dissolved metals by inductively coupled plasma mass spectrometry (ICPMS, EPA 200.8), free chlorine, total residual chlorine (SM 4500-CL G, EPA 330.5) and total trihalomethanes (SW846 8260) were measured according to standard methods by ALS Environmental (Waterloo, ON, Canada), a laboratory accredited by the Canadian Association for Laboratory Accreditation (CALA) according to international standards (ISO 17025).

The acute toxicity of the OSPW towards *Vibrio fischeri* was measured according to the Microtox assay, performed according to Environment Canada protocol EPS 1/RM/24 by AquaTox Testing & Consulting Inc. (Guelph, ON, Canada), a CALA certified laboratory. The Microtox assay measures changes in light emission of the luminescent bacteria following 15 min sample incubation, where the IC_{20} (inhibitory concentration 20%) refers to the concentration of test sample at which the intensity of bacteria light emission is reduced by 20%.

3.4 Results and Discussion

3.4.1 Degradation of AEO by Solar Photocatalysis

AEO and NA concentration, along with other water quality characteristics of the OSPW used in these experiments, are presented in Table 2 and Table 3. The measured values were found to be within the range of values typically reported for OSPW,[78] and the majority of the dissolved organic carbon (TOC) was accounted for by the AEO (assuming ~75% of the AEO mass is carbon). Centrifuged OSPW (i.e., with suspended solids removed) was used for most experiments, since suspended solids content in OSPW varies between different process streams and tailings ponds, and so to avoid these complications and ensure our findings are generally applicable, we focused our study on the water matrix and dissolved compounds.

Table 2. Water quality characteristics of OSPW.

Parameter	**Raw OSPW**
pH	8.38
Mineral Oil & Grease (mg/L)	<1.0
Turbidity (NTU)	>200
TSS (mg/L)	49.5
TDS (mg/L)	1450
Conductivity (mS/cm)	1.695
Anions[a]	
Bromide (mg/L)	<0.50
Chloride (mg/L)	158
Fluoride (mg/L)	3.87
Nitrate (mg/L)	<0.50
Nitrite (mg/L)	<0.50
Sulphate (mg/L)	204
Alkalinity (mg/L as $CaCO_3$)	444
Dissolved Metals	
Aluminum (Al) (mg/L)	<0.10
Antimony (Sb) (mg/L)	<0.0050
Arsenic (As) (mg/L)	<0.010
Barium (Ba) (mg/L)	0.197
Beryllium (Be) (mg/L)	<0.0050
Bismuth (Bi) (mg/L)	<0.010
Boron (B) (mg/L)	2.29
Cadmium (Cd) (mg/L)	<0.00090
Calcium (Ca) (mg/L)	20.8
Chromium (Cr) (mg/L)	<0.0050
Cobalt (Co) (mg/L)	<0.0050
Copper (Cu) (mg/L)	<0.010
Iron (Fe) (mg/L)	<0.50
Lead (Pb) (mg/L)	<0.0050
Lithium (Li) (mg/L)	<1.0
Magnesium (Mg) (mg/L)	10.6

Manganese (Mn) (mg/L)	<0.010
Molybdenum (Mo) (mg/L)	0.0675
Nickel (Ni) (mg/L)	<0.010
Phosphorus (P) (mg/L)	<0.50
Potassium (K) (mg/L)	18
Selenium (Se) (mg/L)	<0.0040
Silicon (Si) (mg/L)	<10
Silver (Ag) (mg/L)	<0.0010
Sodium (Na) (mg/L)	315
Strontium (Sr) (mg/L)	0.499
Thallium (Tl) (mg/L)	<0.0030
Tin (Sn) (mg/L)	<0.010
Titanium (Ti) (mg/L)	<0.020
Tungsten (W) (mg/L)	<0.10
Uranium (U) (mg/L)	<0.010
Vanadium (V) (mg/L)	<0.0050
Zinc (Zn) (mg/L)	<0.030
Zirconium (Zr) (mg/L)	<0.040

[a]Determined for centrifuged and filtered OSPW

The initial experiment exposed OSPW containing different concentrations of photocatalyst (0.01 – 0.5 g/L) to natural sunlight to evaluate the feasibility of the method and optimize treatment conditions (Figure 4a). One day of sunlight exposure (typically ~25 MJ/m^2 over ~14 h daylight, Table 1) was found to virtually eliminate AEO at a TiO_2 loading of 0.5 g/L, and substantial removal was observed at significantly lower TiO_2 concentrations, validating the potential of solar photocatalysis. These results compare favourably to a previous study by Headley et al. which showed 75% removal of AEO spiked into deionized water (64 mg/L) after 8 h of photocatalytic treatment.[69] TiO_2 concentrations above 0.5 g/L offered no further improvements in AEO degradation rate, presumably due to excess TiO_2 occluding light penetration into solution, and thus 0.5 g/L TiO_2 was used in subsequent experiments.

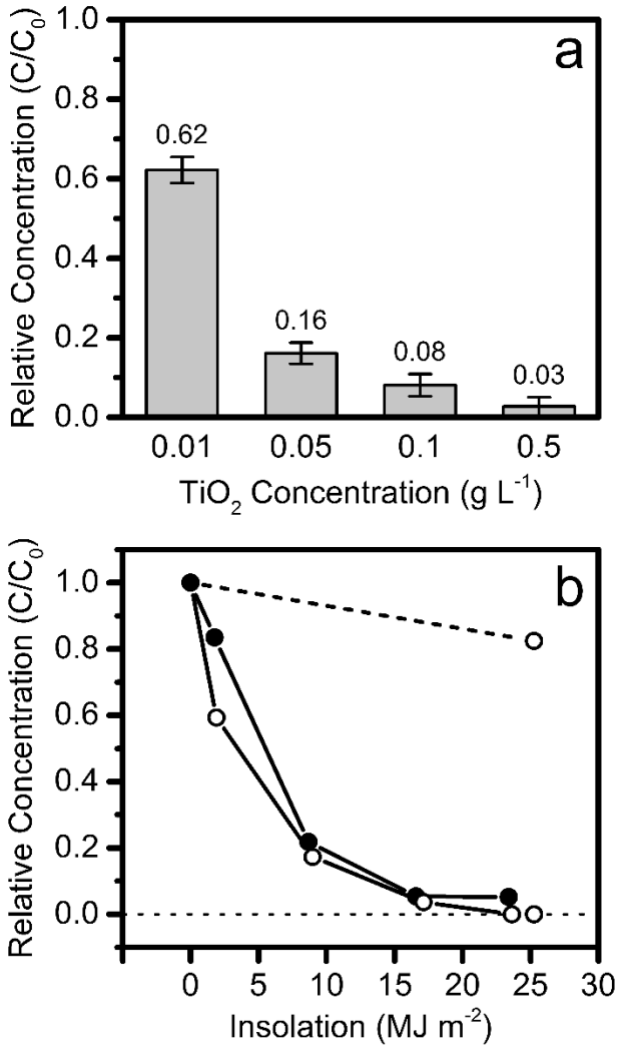

Figure 4. (a) Remaining AEO in centrifuged OSPW after 1 day of solar photocatalytic treatment at various concentrations of TiO_2. (b) Solar photocatalytic degradation of AEO in centrifuged (○) and raw (●) OSPW over the course of 1 day in the presence of 0.5 g/L TiO_2; the dashed trend indicates OSPW exposed to sunlight in the absence of TiO_2.

The rate of the photocatalytic AEO removal was investigated (Figure 4b). The results demonstrated that the process obeyed apparent first-order kinetics (pseudo-first order rate constant $1.86 \pm 0.13 \times 10^{-7}$ m^2/J), with 80% of the AEO eliminated within the first 6 hours of sunlight exposure (~9 MJ/m^2 insolation, from dawn until noon), and complete removal achieved after 14 hours (i.e., at 25 MJ/m^2 insolation by the end of the day). Even at a comparatively low TiO_2 loading of 0.01 g/L, substantial AEO removal (74 ± 14%) could be achieved within three days of sunlight exposure (64 MJ/m^2 insolation over 41.5 hours, Figure 5). Put into context of other AOPs, potassium permanganate and sodium persulfate (at 5 and 10 g/L respectively) each required between 20-40 days to remove 80% of OSPW AEO (from an initial concentration of

~56 mg/L).[14] Without sunlight exposure, 4% of the AEO was removed after 24 h of stirring with TiO_2 in the dark, representing only slight adsorption to the catalyst, and confirming that the extensive AEO removal observed under sunlight is the result of a photochemical process. Minimal AEO removal (~10-15%) was observed under sunlight alone in the absence of the photocatalyst (Figure 4b, Figure 5). This minor degradation is attributed to the natural photolysis of NAs, presumably due to absorbance of the carbonyl group or aromatic species (Figure 6).[79]

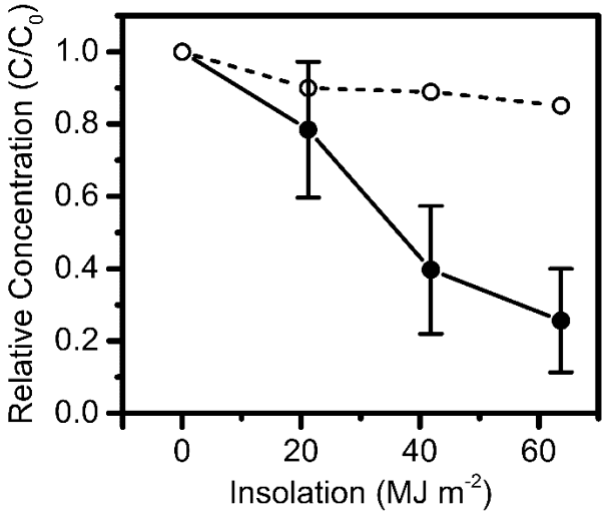

Figure 5. Solar photocatalytic degradation of AEO in centrifuged OSPW in the presence of 0.01 g/L TiO_2; the dashed trend indicates OSPW exposed to sunlight in the absence of TiO_2.

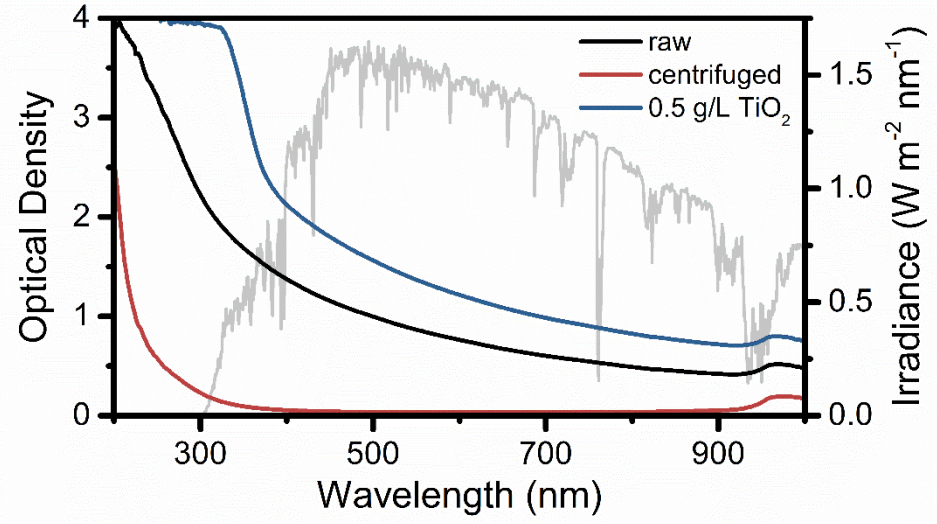

Figure 6. UV/visible optical density of raw and centrifuged OSPW, and 0.5 g/L TiO_2 suspension in centrifuged OSPW, with the solar spectrum for comparison (ASTM G173-03 global tilt). Note

that for the raw OSPW and TiO_2 suspension, optical density includes contributions from particle light scattering.

The temperature dependence of the degradation kinetics was assessed through an Arrhenius treatment (Figure 7), yielding an apparent activation energy of 31.9 kJ/mol for the reaction, which is within the range previously reported for photocatalytic reactions.[80,81] However, since our experiments were performed at ambient outdoor conditions subject to natural environmental variation, the effect of temperature on the photocatalytic treatment will be examined more closely in future work under controlled conditions.

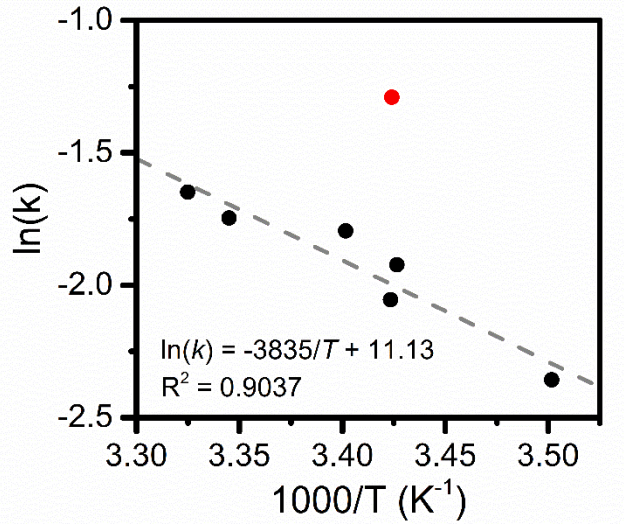

Figure 7. Arrhenius plot of solar photocatalytic degradation of AEO in centrifuged OSPW in the presence of 0.5 g/L TiO_2, where *k* is the apparent rate constant (with units of m^2/MJ). The linear regression fit is given as a dashed line, where the data point highlighted in red is taken as an outlier.

The photocatalysts were also found to be largely reusable with minimal loss in photocatalytic activity (Figure 8). Some loss in performance after five treatment cycles (~20% lower apparent rate constant) is possibly due to aggregation of the particles (arising from compaction during collection by centrifugation), or fouling of the TiO_2 surface over time, and could likely be mitigated with better dispersion or particle washing techniques. However, such process optimization was beyond the scope of this work.

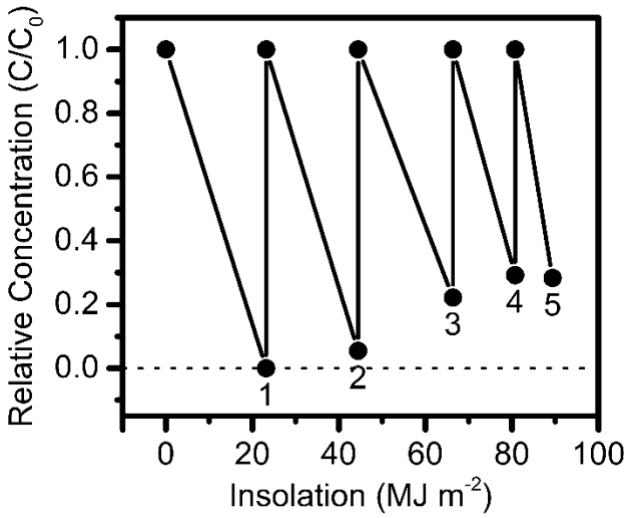

Figure 8. Recyclability of a single batch of TiO_2 nanoparticles to degrade AEO in centrifuged OSPW at 0.5 g/L TiO_2 under sunlight.

While clarified water offers idealized conditions for photochemical experiments, light penetration into turbid wastewaters is a practical concern for realistic usage scenarios. To understand the effect of suspended solids on the photocatalytic treatment, the treatment was also performed in raw OSPW containing 50 mg/L suspended solids (turbidity >200 NTU, Table 2), which has a much greater light attenuation compared to centrifuged OSPW (Figure 6). Remarkably, the degradation rate was not significantly different in raw versus centrifuged OSPW (Figure 4b, $p = 0.07$), which is surprising since the turbidity of OSPW has previously been assumed to be an insurmountable barrier for application of light-dependent treatment processes.[13,79] However, considering that UV light attenuation by 0.5 g/L TiO_2 is actually greater than that due to natural suspended solids in the OSPW (Figure 6), we hypothesized that the majority of the observed photocatalytic activity was originating near the surface of the water where light absorption by the catalyst was greatest. Indeed, not stirring the OSPW during photocatalytic treatment resulted in significantly less degradation of AEO (Figure 9), as the TiO_2 nanoparticles settle out of suspension under the influence of gravity (Figure 10). Thus solar photocatalysis is feasible even in raw OSPW provided the system is sufficiently well-mixed to facilitate mass transfer to the interface and illumination of the catalyst.

It must also be acknowledged that the impact of natural suspended solids in the raw OSPW could affect the photocatalytic treatment through more complex mechanisms beyond simply light screening. Suspended OSPW clays could serve as a source of adsorbed AEO, which could be released throughout the treatment, and similarly as a sink for sorption of partially oxidized intermediates. Furthermore, heterocoagulation with clays could lower available surface area of TiO_2 nanoparticles for treatment. However, given the similar treatment kinetics observed

between the centrifuged and raw OSPW, these potential mechanisms are not thought to be practically significant.

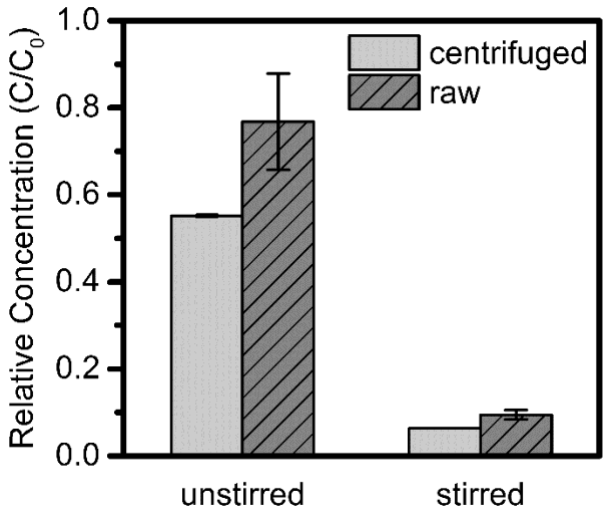

Figure 9. The influence of stirring on the remaining AEO in OSPW after solar photocatalytic treatment for 1 day at 0.5 g/L TiO_2.

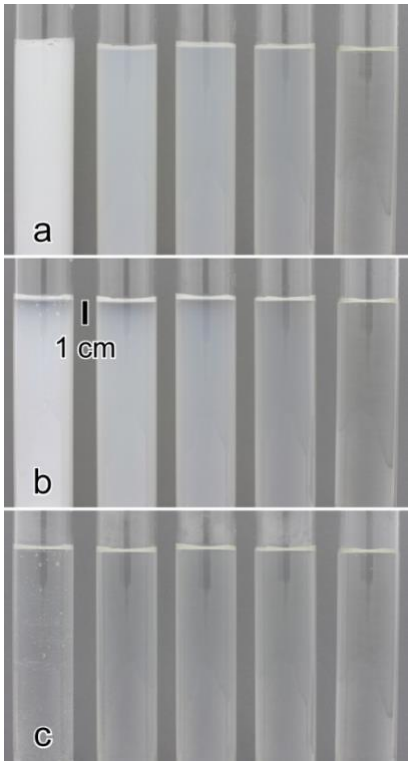

Figure 10. Gravity settling of TiO_2 suspensions in vials of centrifuged OSPW after 0 h (a), 1 h (b) and 24 h (c). From left-to-right, the vials contain 0.5, 0.1, 0.05, 0.01 and 0 g/L TiO_2, respectively.

3.4.2 Mineralization, Toxicity, and Biodegradability Assessment

A more detailed study was conducted of the organic constituents in the photocatalytically treated water (Table 3, Figure 11). Both FTIR and HRMS, two independent measurement techniques, revealed the same trend in AEO degradation. While HRMS confirmed photodegradation of the majority of the AEO within ~1 day-equivalent of sunlight exposure (90% AEO_{MS} removal after 30 MJ/m^2 insolation), only 45% of the TOC was removed, indicating that photocatalytic mineralization had not yet proceeded to completion, but suggesting rather the transformation of the AEO into oxidized intermediates. This residual organic carbon was found to be significantly more biodegradable than the initial AEO however, where the ratio of BOD to TOC or COD is taken as a rough metric of biodegradability (i.e., the BOD/TOC ratio was found to increase throughout the course of treatment, Figure 11). Furthermore, after photocatalytic treatment the initial acute toxicity of the OSPW towards the microorganism *Vibrio fischeri* was eliminated, which is notable since degradation intermediates and byproducts are sometimes implicated to have greater toxicity than the parent compounds. With sufficient treatment time (~1 week-equivalent of sunlight exposure, Table 3, Treated OSPW Endpoint), AEO was undetectable by FTIR or HRMS, and TOC had dropped to near the detection limit (of 1.0 mg/L). This may indicate that mineralization eventually proceeds to completion, implying that all AEO and

intermediate species are susceptible to photocatalytic degradation. This is significant since other AOPs, such as ozonation, cannot fully oxidize AEO to completion, leaving degradation byproducts and a high residual TOC concentration in the treated water.[16,82,83]

Table 3. Changes in OSPW water quality characteristics due to solar photocatalytic treatment.

Parameter	**Initial OSPW[a]**	**Treated OSPW[b] (Midpoint)**	**Treated OSPW[b] (Endpoint)**	**Solar Control[c] (Endpoint)**
Insolation (MJ/m^2)	0	31.4	181.4	181.4
AEO (mg/L)[d]	39.8 ± 1.1	0.7 ± 0.3	<0.6	28.9 ± 1.0
AEO_{MS} (mg/L)	43.4	4.2	0.2	
TOC (mg/L)	45.1	24.7	3.5	
COD (mg/L)	135	54	<10	
BOD (mg/L)	<2.0	12.7	4.4	
Microtox 15 min IC_{20} (% v/v)	77.2 ± 3.4	>90	>90	75.7 ± 5.0

[a]Centrifuged OSPW [b]Treated with 0.5 g/L TiO_2 under the insolation indicated [c]Insolated in the absence of TiO_2; AEO_{MS}, TOC, COD and BOD were not measured for this sample [d]Determined by FTIR

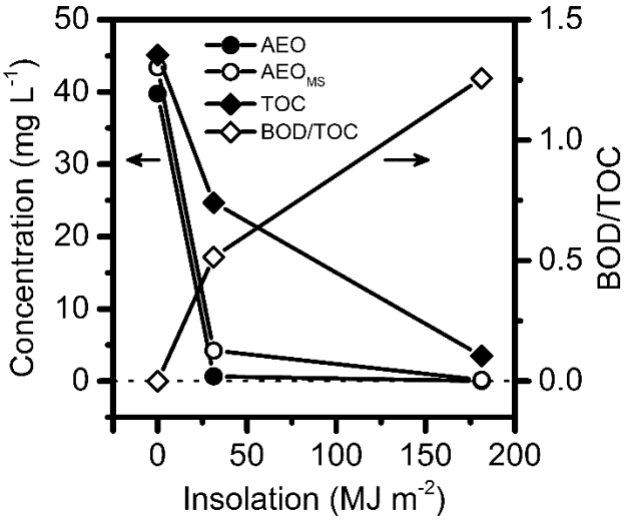

Figure 11. Solar photocatalytic removal of AEO (measured by FTIR), AEO_{MS} and TOC, and increase in organic carbon biodegradability (BOD/TOC ratio), over the course of ~1 week-equivalent insolation of centrifuged OSPW containing 0.5 g/L TiO_2. Lines connecting data points are simply a visual guide.

3.4.3 Analysis of Degradation Intermediates

In order to investigate the photocatalytic degradation process in OSPW, and gain a better understanding as to the composition of the organic intermediates formed, high resolution MS analysis of the treated water was performed (Figure 12). The initial OSPW AEO was found to be primarily composed of O_2, O_3 and O_4 species, along with their singly sulfur-substituted counterparts (O_xS classes, Figure 13). Following photocatalysis, a dramatic shift towards higher oxygen content in the residual AEO was observed (Figure 13). Similar trends have been observed previously in the photooxidation of petroleum samples,[84–88] albeit by a different mechanism in the absence of a photocatalyst, and given that OSPW AEO composes predominantly saturated compounds known to be resistant to natural photolysis.[13,79] The total AEO concentration after treatment was only 4.2 mg/L (Table 3, Figure 14), and thus the majority of the initial AEO was presumably oxidized to intermediate compounds, still measurable as TOC and COD. These findings indicate that the photocatalytic degradation of AEO proceeds via progressive addition of oxygen to the AEO en route to complete mineralization. This is significant since some oxidized NAs have been previously reported to have lower toxicity and higher biodegradability than their parent NAs,[16,89] which correlates well with the BOD and Microtox results (Table 3). Interestingly, following treatment, O_xS classes were found to comprise a relatively smaller fraction of the AEO than initially (0.07 vs. 0.32 O_xS:O_x, respectively), potentially indicating preferential photocatalytic degradation of the sulfur heteroatomic species (Figure 13). Preferential photochemical reactivity of sulfur heterotomic petroleum compounds has also been previously observed, and has been attributed to the availability of the sulfur non-bonding electrons.[85–87,90]

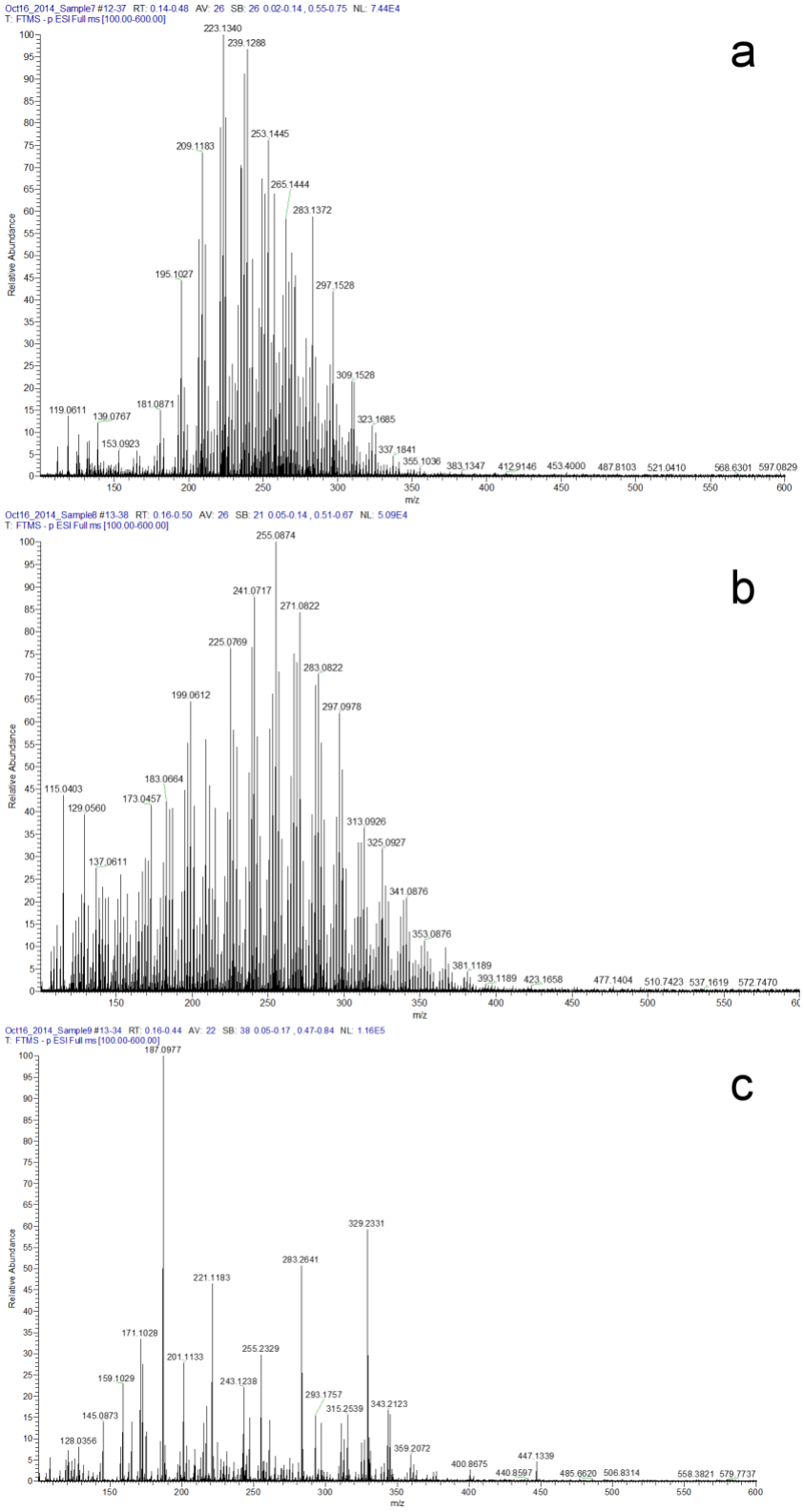

Figure 12. Mass spectra of the initial OSPW (a), OSPW after photocatalytic treatment with 31 MJ/m^2 insolation (b) and 181 MJ/m^2 insolation (c) (c.f. Table 3). Note that the AEO

concentrations measured from (c) were at the detection limit of the instrument, and thus the mass spectrum (c) likely represents artefacts from the sampling or extraction process.

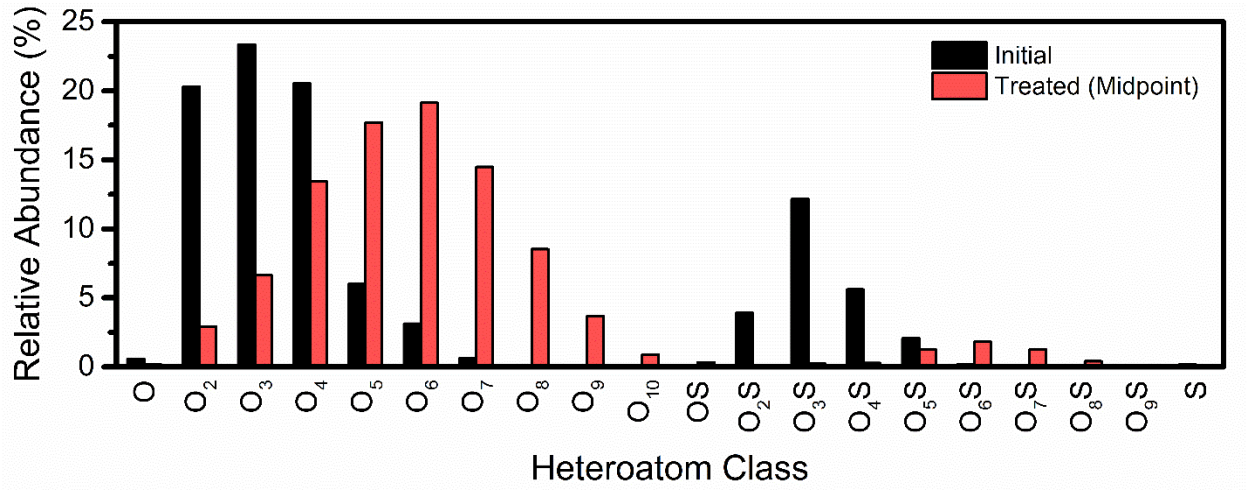

Figure 13. Distribution of O_x and O_xS classes in OSPW AEO (normalized based on the relative abundance of each species within the individual samples) before and after photocatalytic treatment (31 MJ/m^2 insolation, c.f. Table 3). Other heteroatomic classes were at negligible concentration and thus excluded from this figure. Note that the total AEO concentration in the treated sample is only ~10% that of the initial OSPW (c.f. Table 3).

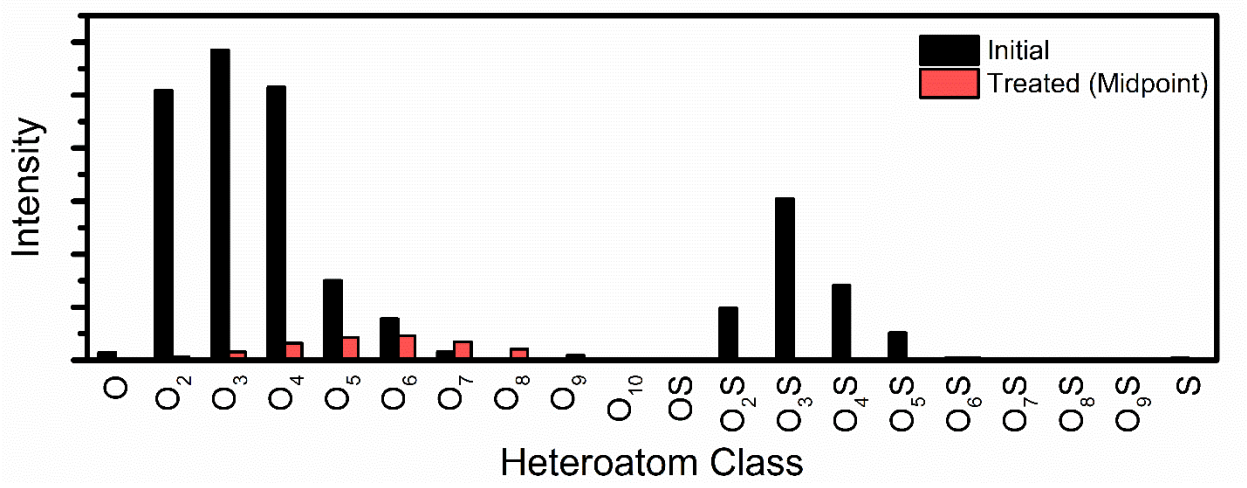

Figure 14. Distribution of O_x and O_xS classes in OSPW AEO (based on intensity values) before and after photocatalytic treatment (31 MJ/m^2 insolation, c.f. Table 3). Other heteroatomic classes were at negligible concentration and thus excluded from this figure.

In addition to monitoring the change in oxygen content of the AEO, the O_2 and O_4 NA classes were selected as representative classes for investigating changes in the molecular weight and structural complexity of the AEO following photocatalytic treatment (Figure 15). A shift towards lower carbon numbers after treatment was observed for both the O_2 and O_4 classes, suggesting preferential photocatalytic oxidation of higher molecular weight species. Furthermore, the initial cluster in the range of 6-8 double bond equivalents (DBE) for the O_2 distribution (Figure 15a) was almost completely photodegraded after treatment (Figure 15c), indicating higher reactivity of photocatalysis towards NAs with more complex molecular structures (i.e., more cyclic or unsaturated compounds). Photocatalysis and other radical-based AOPs have been previously reported to preferentially target branch points in NAs and other aliphatic contaminants.[15,89,91,92] Similar trends of reduced carbon numbers and DBEs following treatment were observed for the O_5 – O_7 classes (Figure 16); if it is assumed that some of the initial O_2 & O_4 AEO are oxidized to O_5 – O_7 species during treatment, the effect is similarly pronounced. These findings are very promising since AEO species with higher DBE and carbon numbers are the most environmentally persistent and resistant to biodegradation,[8,9,67] and thus higher priority targets for alternative water treatment methods.

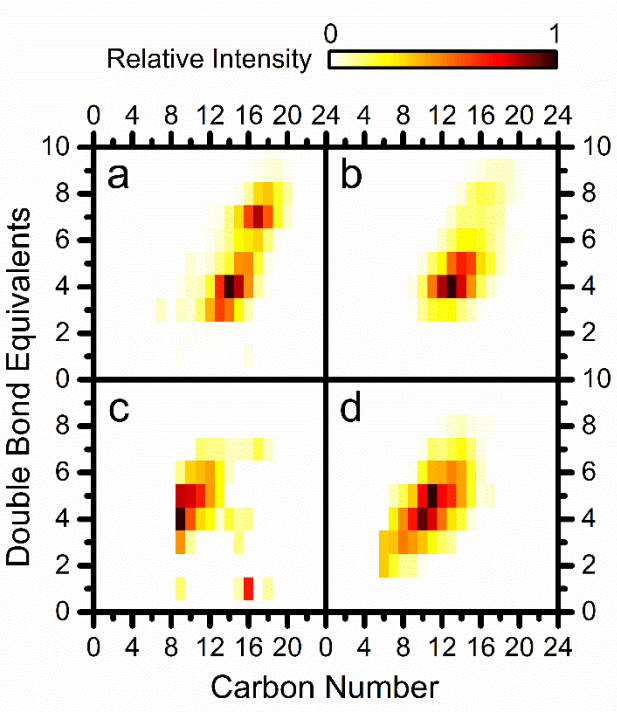

Figure 15. Relative distribution of O_2 (a & c) and O_4 (b & d) AEO classes before (a & b) and after (c & d) photocatalytic treatment (31 MJ/m^2 of insolation, c.f. Table 3). The data is normalized based on the relative abundance of each species within the individual samples; note that the total AEO concentration in the treated sample is only ~10% that of the initial OSPW (c.f. Table 3).

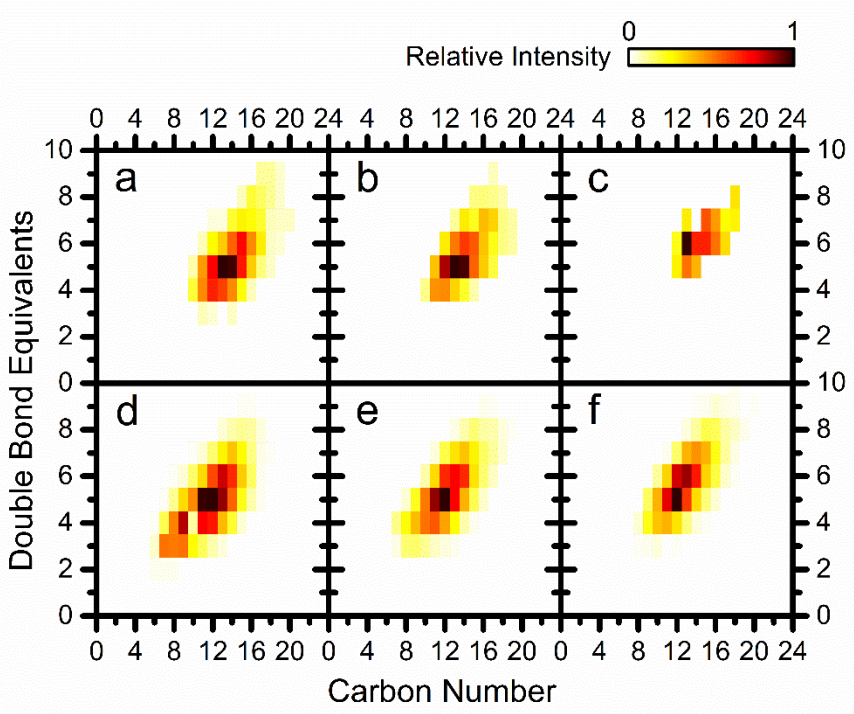

Figure 16. Relative distribution of O_5 (a & d), O_6 (b & e) and O_7 (c & f) AEO classes before (a–c) and after (d–f) photocatalytic treatment (31 MJ/m^2 of insolation, c.f. Table 3). The data is normalized based on the relative abundance of each species within the individual samples; note that the total AEO concentration in the treated sample is only ~10% that of the initial OSPW (c.f. Table 3).

3.4.4 Superoxide-Mediated Reaction Pathway

To gain further insight into the photocatalytic reaction mechanism and radical species involved in the NA degradation process, we spiked various radical scavengers into the OSPW prior to treatment in order to selectively quench specific free radical species formed during photocatalysis. Addition of benzoquinone, a scavenger for superoxide anion radicals, resulted in a dramatic inhibition of AEO degradation (Figure 17), implicating superoxide as the critical radical species mediating photocatalysis in OSPW. This is an unanticipated finding, as conventionally hydroxyl radicals or valence band holes are identified as the primary oxidants driving photocatalysis, and superoxide is often considered merely as a byproduct formed from the reduction half-reaction at the conduction band.[27,93] In OSPW however, superoxide appears to be the primary radical species driving the reaction.

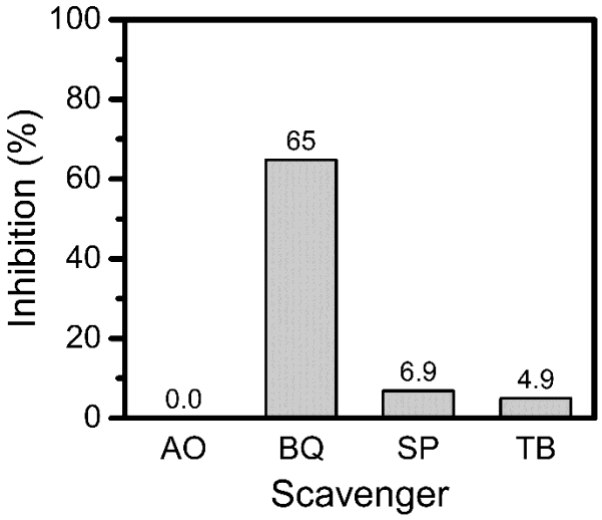

Figure 17. Inhibition of TiO_2 solar photocatalytic activity in the presence of different radical scavengers: ammonium oxalate (AO, scavenger of photogenerated holes), 1,4-benzoquinone (BQ, scavenger of superoxide radicals), sodium persulfate (SP, scavenger of photogenerated electrons), and *tert*-butyl alcohol (TB, scavenger of hydroxyl radicals).

Halide and bicarbonate anions are known to be strong scavengers of hydroxyl radicals and valence band holes, which react to form less powerful halide and carbonate radicals.[22,94] Given the high concentration of these anions in the OSPW (Table 2), it is presumed that hydroxyl radicals and valence band holes are already strongly suppressed during the photocatalytic reaction, and thus providing additional scavengers for these species had little effect (Figure 17). Superoxide anion is known to be significantly less susceptible to anion quenching, with a half-life on the order of hundreds of seconds.[95,96]

While superoxide can simply add to organic contaminants to form ketones or hydroxyl groups,[97] we hypothesize that the primary reason the photocatalytic degradation of NAs is so heavily superoxide dependent is that superoxide may be essential for ring-opening, which is a necessary intermediate step when mineralization is the known endpoint. Although less reactive than hydroxyl radicals, halide radicals are known to be selective oxidants capable of one-electron oxidation and hydrogen abstraction,[94] and the carbon-centered radicals formed in these processes could subsequently react with superoxide to initiate ring-opening.[98] For example, one potential mechanism of superoxide-mediated C-C bond cleavage is the elimination of a β-hydrogen via a hydroperoxide intermediate (Scheme 1), as reported for lipid peroxides.[99,100] Superoxide is also well known to react across double-bonds through a dioxetane, as in the photocatalytic ring-opening of aromatics (Scheme 2).[101–103,81] Further reaction according to the photo-Kolbe process could then degrade the linearized NAs.[104,105]

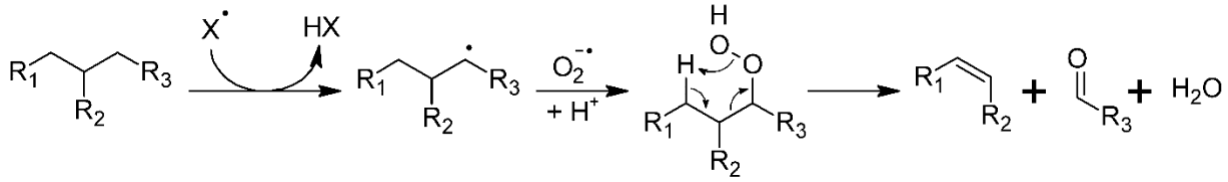

Scheme 1. Suggested mechanism of superoxide bond cleavage via a hydroperoxide intermediate, where X• represents an oxidizing free radical.

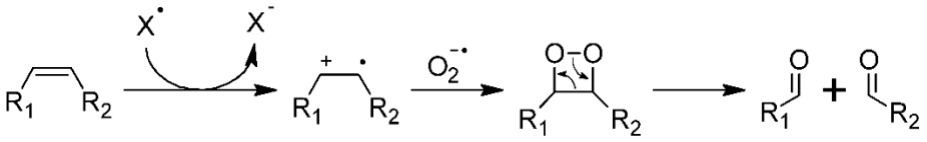

Scheme 2. Suggested mechanism of superoxide bond cleavage via a dioxetane intermediate, where X• represents an oxidizing free radical.

Considering that halide radicals may be involved in the photocatalytic degradation process, we were concerned as to potential formation of toxic chlorinated byproducts, as has been observed previously for photocatalysis in saline waters.[106–108] We thus had the treated OSPW tested for residual chlorine or trihalomethanes, but found no measurable concentrations of either. Combined with the absence Microtox toxicity post-treatment, the treated OSPW appears to be free of at least these particular byproducts.

3.5 Environmental Significance

We have demonstrated that solar photocatalysis is feasible in raw OSPW, with the potential to eliminate toxicity and completely mineralize recalcitrant compounds through a superoxide-mediated oxidative pathway. Efficient degradation kinetics were achieved despite the water's high ionic strength and suspended solids content. This study thus represents the successful solar photocatalytic remediation of a highly complex target pollutant in a challenging industrial wastewater.

Given the large increase in biodegradability of the oxidized intermediate species and elimination of toxicity achieved after only one day of treatment, complete mineralization by photocatalysis is likely not required, but rather photocatalysis may serve to complement existing treatment methods, such as biodegradation. Ensuring sufficient mixing to keep the catalyst and contaminants suspended near the illuminated interface will be a key concern in the continued development of this technology. Practical methods to recover and recycle the photocatalyst nanoparticles must also be assessed, although a number of potential solutions have already been described.[54,109]

Many well-established water treatment methods, while proven effective for OSPW treatment in the lab, are defeated by the scale of the problem for practical implementation. While natural photolysis of OSPW organics in the tailings ponds is presumably negligible,[79] considering that photocatalysts are in principle indefinitely recyclable, and given the vast surface area of the ponds exposed to sunlight, we believe that solar photocatalysis is a compelling "green" AOP with the potential to address challenging water treatment problems in the oil industry.

Chapter 4
Photocatalytic degradation kinetics of naphthenic acids in oil sands process-affected water: multifactorial determination of significant factors‡

4.1 Summary

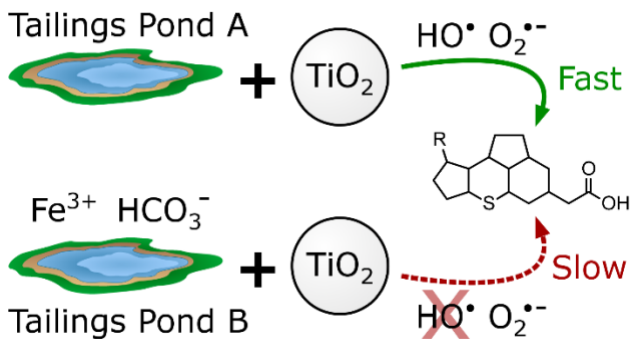

Oil sands process-affected water (OSPW) is generated as a byproduct of bitumen extraction in Canada's oil sands. Due to the water's toxicity, associated with dissolved acid extractable organics (AEO), especially naphthenic acids (NAs), along with base-neutral organics, OSPW may require treatment to enable safe discharge to the environment. Heterogeneous photocatalysis is a promising advanced oxidation process (AOP) for OSPW remediation, however, predicting treatment efficacy can be challenging due to the unique water chemistry of OSPW from different tailings ponds. The objective of this work was to study various factors affecting the kinetics of photocatalytic AEO degradation in OSPW. The rate of photocatalytic treatment varied significantly in two different OSPW sources, which could not be accounted for by differences in AEO composition, as studied by high resolution mass spectrometry (HRMS). The effects of inorganic water constituents were investigated using factorial and response surface experiments, which revealed that hydroxyl ($HO^{\bullet}$) radical scavenging by iron (Fe^{3+}) and bicarbonate (HCO_3^-) inhibited the NA degradation rate. The effects of NA concentration and temperature on the treatment kinetics were also evaluated in terms of Langmuir-Hinshelwood and Arrhenius models; pH and temperature were identified as weak factors, while dissolved oxygen (DO) was critical to the photo-oxidation reaction. Accounting for all of these variables, a general empirical kinetic expression is proposed, enabling prediction of photocatalytic treatment performance in diverse sources of OSPW.

---

‡ This chapter is adapted from a previously published article: Leshuk, T.; de Oliveira Livera, D.; Peru, K. M.; Headley, J. V.; Vijayaraghavan, S.; Wong, T.; Gu, F. Photocatalytic Degradation Kinetics of Naphthenic Acids in Oil Sands Process-Affected Water: Multifactorial Determination of Significant Factors. *Chemosphere* **2016**, *165*, 10–17.

4.2 Introduction

Surface mining of bitumen in Canada's Athabasca region produces large quantities of oil sands process-affected water (OSPW) as a byproduct of bitumen extraction, which is stored on site in tailings ponds for reuse. Despite water recycling efforts, fresh water consumption by the oil sands industry was ~170 million m^3 in 2014,[110] and over 1 billion m^3 of tailings have been accumulated in at least 170 km^2 of ponds in Alberta.[62,63] OSPW is a saline mixture of suspended clays and bitumen-derived dissolved organics, known to be acutely and chronically toxic to aquatic and mammalian species;[59–61,111,112] thus there is currently no deliberate release of OSPW to the environment. The toxicity of OSPW is attributed in part to the acid extractable organics (AEO), especially naphthenic acids (NAs),[113] a complex mixture of acyclic and cycloaliphatic carboxylic acids with the conventional formula $C_nH_{2n+z}O_2$ (where *z* is a negative even integer related to the number of rings and double bonds).[12,13] OSPW AEO also contains a broad range of organics not conforming to this classical NA structure, including aromatic and heteroatom-containing acids, as well as low polarity species.[114–116,64] As NAs are resistant to biodegradation,[8,9] and their toxicity persists after decades of environmental exposure,[10] reclamation of the oil sands tailings ponds and safe discharge OSPW will require new water treatment strategies.[1]

The exceptionally large volume of water, and the recalcitrance of the AEO contaminants, may render OSPW treatment using conventional processes impractical or cost-prohibitive. Advanced oxidation processes (AOPs) have been shown to be particularly effective at detoxifying low concentrations of persistent organic pollutants, including NAs.[15,19,117,118] Heterogeneous photocatalysis is an especially powerful AOP, and solar photocatalysis over TiO_2 has been demonstrated to eliminate AEO from OSPW through oxidative mineralization.[69,70,119] Using sunlight as an abundant free energy source, and given the ability of the photocatalyst to be recycled without the need for continuous chemical amendment of the water, photocatalysis may not suffer from the same limitations of cost and scale as other AOPs, and may instead share some advantages of passive treatment processes.

Given the potential of photocatalysis for OSPW treatment, this study aimed to address some outstanding questions related to the kinetics and efficiency of the process. One challenge in translating technology from the laboratory into real use scenarios is that different wastewater streams, or tailings ponds in the case of OSPW, may have unique compositions, which may unpredictably affect treatment efficacy. Thus an objective of this work was to investigate factors affecting the kinetics of photocatalytic AEO degradation in OSPW, studied in two different OSPW samples. Another goal of this work was to provide a general kinetic expression for photocatalytic AEO degradation in different OSPW sources, to facilitate modelling of large-scale treatment systems, which is a critical step towards potential implementation.

4.3 Experimental

4.3.1 Materials

OSPW samples were provided by each of two producers operating in the Athabasca oil sands (Industry A and B), and stored at 4 °C in the dark. Prior to use, the OSPW was homogenized by stirring, and then centrifuged at 14,000 xg to remove suspended solids.

A commercial mixture of naphthenic acids (technical grade, carbon numbers 6 – 20, z-classes 0 to -4, as characterized by Damasceno et al.[120]), dichloromethane (DCM, ≥99.9%, HPLC grade), iron(III) nitrate nonahydrate (≥98%, ACS grade), sodium fluoride (≥99%, ACS grade), sodium phosphate dibasic (≥99%), nitrotetrazolium blue chloride (~98%) and terephthalic acid (98%) were purchased from Sigma-Aldrich and used as received. Sulfuric acid (95-98%, ACS grade, Fisher), sodium sulfate (≥99%, ACS grade, EMD), sodium chloride (≥99%, ACS grade, EMD), sodium bicarbonate (≥99%, ACS grade, Anachemia) and titanium dioxide nanoparticles (Aeroxide P25, ~10-50 nm particle diameter, 55 m^2 g^{-1} surface area, Acros) were used as received. P25 TiO_2 nanoparticles have been extensively studied and characterized in the literature, and are often used as a benchmark photocatalyst.

Simulated OSPW was prepared using the commercial NA mixture, and unless otherwise stated, typically contained 85 mg/L NAs (from a 55.2 g/L stock solution in 1 M NaOH), 800 mg/L HCO_3^- (from $NaHCO_3$), 200 mg/L Cl^- (from NaCl), and 200 mg/L SO_4^{2-} (from Na_2SO_4), with a final pH of 8.7 (adjusted with HNO_3).

4.3.2 Photocatalytic Experiments

Photocatalytic experiments were performed under in a custom photoreactor enclosure, consisting of an array of UVA fluorescent bulbs (Philips F20T12/BL, peak emission ~350 nm) suspended above the samples (Figure 18). The UV intensity was measured to be ~40 W/m^2 with a UVA/B light meter (Sper Scientific, NIST certified calibration), which is similar to the UV content of the solar spectrum (ASTM G173-03 global tilt). Natural sunlight, however, due to its periodicity and variation in intensity, is significantly different from the constant UV intensity provided in this photoreactor. TiO_2 powder (0.1 g) was first stirred into 200 mL of OSPW in a borosilicate glass beaker (63 mm diameter) and dispersed by bath sonication. Beakers were sealed with polyethylene film (Glad, measured to be UV transparent by spectrophotometry) to prevent evaporation during the experiments, and the sides were wrapped with Al foil. The mixture was then placed in the photoreactor and exposed to UV light while stirring at 500 rpm. Following the UV treatment, the OSPW mixture was centrifuged to remove the TiO_2 nanoparticles, retaining the supernatant for analysis (stored at 4 °C in the dark).

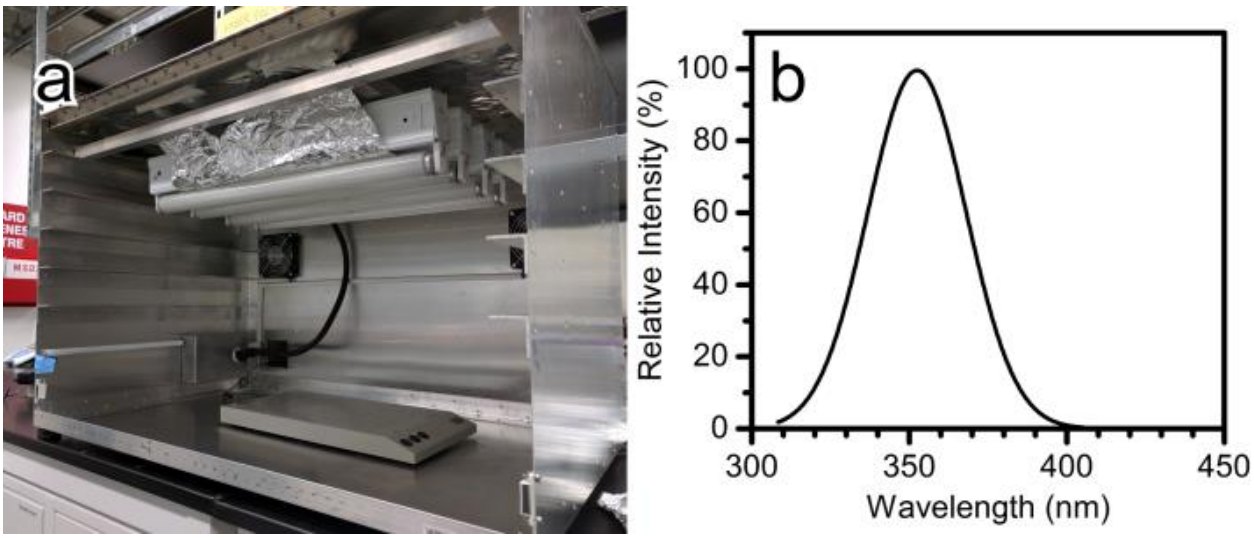

Figure 18. (a) UV photoreactor used for the photocatalytic tests, and (b) the relative spectral distribution of its emission.

In one experiment, to compare photocatalysis of AEO in the absence of matrix ions, AEO was extracted from each of the Industry A and B OSPW (using the same protocol as described for FTIR analysis below), reconstituted into 1 M NaOH, and then dissolved into deionized water at a concentration of ~70 mg/L. The pH of each solution was adjusted to ~8.7, and the AEO extracts in water were then photocatalytically treated as above for 2.5 h.

To investigate the effect of dissolved ions on the photocatalytic treatment, factorial screening and response surface designed experiments were conducted using simulated OSPW with ion concentrations as indicated in the text (the concentrations of Cl^- and SO_4^{2-} were kept at 200 mg/L for all samples in the response surface study), and a UV exposure of 2 h.

To test the effect of dissolved ions in real OSPW, in one experiment OSPW from Industry A was amended with $Fe(NO_3)_3 \cdot 9H_2O$ and $NaHCO_3$ to have the same concentrations of Fe and HCO_3^- as Industry B OSPW (c.f. Table 4), prior to photocatalytic treatment (2 h UV exposure).

Table 4. Water quality characteristics of OSPW from Industry A and Industry B.

Parameter	**Industry A**	**Industry B**
AEO (mg/L)	39.8	49
TOC (mg/L)	45.1	56.8
COD (mg/L)	135	193
BOD (mg/L)	<2.0	<2.0

pH	8.38	8.67
Conductivity (mS/cm)	1.695	3.062
Anions		
Bromide (mg/L)	<0.50	0.14
Chloride (mg/L)	158	101
Fluoride (mg/L)	3.87	0.37
Nitrate (mg/L)	<0.50	0.67
Nitrite (mg/L)	<0.50	<0.10
Sulphate (mg/L)	204	15.1
Alkalinity (mg/L as $CaCO_3$)	444	796
Dissolved Metals		
Aluminum (Al) (mg/L)	<0.10	<0.10
Antimony (Sb) (mg/L)	<0.0050	<0.0050
Arsenic (As) (mg/L)	<0.010	<0.010
Barium (Ba) (mg/L)	0.197	0.288
Beryllium (Be) (mg/L)	<0.0050	<0.0050
Bismuth (Bi) (mg/L)	<0.010	<0.010
Boron (B) (mg/L)	2.29	2.67
Cadmium (Cd) (mg/L)	<0.00090	<0.00090
Calcium (Ca) (mg/L)	20.8	13.8
Chromium (Cr) (mg/L)	<0.0050	<0.0050
Cobalt (Co) (mg/L)	<0.0050	<0.0050
Copper (Cu) (mg/L)	<0.010	<0.010
Iron (Fe) (mg/L)	<0.50	13.1
Lead (Pb) (mg/L)	<0.0050	<0.0050
Lithium (Li) (mg/L)	<1.0	<1.0
Magnesium (Mg) (mg/L)	10.6	6.3
Manganese (Mn) (mg/L)	<0.010	0.045
Molybdenum (Mo) (mg/L)	0.0675	0.0369
Nickel (Ni) (mg/L)	<0.010	<0.010
Phosphorus (P) (mg/L)	<0.50	7.01
Potassium (K) (mg/L)	18	11

Selenium (Se) (mg/L)	<0.0040	<0.0040
Silicon (Si) (mg/L)	<10	<10
Silver (Ag) (mg/L)	<0.0010	<0.0010
Sodium (Na) (mg/L)	315	698
Strontium (Sr) (mg/L)	0.499	0.373
Thallium (Tl) (mg/L)	<0.0030	<0.0030
Tin (Sn) (mg/L)	<0.010	<0.010
Titanium (Ti) (mg/L)	<0.020	<0.020
Tungsten (W) (mg/L)	<0.10	<0.10
Uranium (U) (mg/L)	<0.010	<0.010
Vanadium (V) (mg/L)	<0.0050	<0.0050
Zinc (Zn) (mg/L)	<0.030	0.943
Zirconium (Zr) (mg/L)	<0.040	<0.040

The effect of temperature on the photocatalytic kinetics was studied in OSPW from Industry A. Samples were equilibrated at temperature for 1 h in the dark before UV exposure.

The effect of dissolved oxygen on the photocatalytic kinetics was assessed using simulated OSPW (50 mg/L NAs) in a septum-sealed flask, sparged with either air or pure N_2 for 2 h in the dark before UV exposure, as well as continuously during the photocatalytic treatment.

4.3.3 Radical Probe Assays

Nitrotetrazolium blue chloride (NBT) at a concentration of 4×10^{-5} M was used to quantitatively detect superoxide radical ($O_2^{\bullet -}$) generated by the TiO_2 photocatalytic system. Superoxide concentrations were indirectly determined by monitoring the NBT maximum absorbance at 259 nm with a spectrophotometer (BioTek Epoch) at set time intervals.[121–123] The role of hydroxyl radicals ($OH^{\bullet}$) was investigated using a terephthalic acid (TA) fluorescence probe method,[124,125] with TA present at a concentration of 1×10^{-3} M in dilute NaOH (1×10^{-2} M). Fluorescence spectra were recorded on a Photon Technology International QM-4SE fluorimeter. The above procedure for photocatalytic experiments was adapted for these probe molecules, with NBT or TA replacing the NAs.

4.3.4 Analysis

The concentration of AEO (NAs in the case of simulated OSPW) was measured by Fourier transform infrared spectroscopy (FTIR) according to the standard method[75,76] with minor modifications (*viz.*, the acidified samples were extracted thrice with DCM in a 1:12.5 solvent to sample volumetric ratio, with 80 ± 4% total recovery), using the commercial NA mixture to

prepare the calibration curve. AEO is a composite measure of classical NAs, oxy-NAs ($C_nH_{2n+z}O_x$, where x > 2), and other organic acids.[64]

Samples were filtered prior to the following analyses (Whatman 934-AH glass fiber filter). UV/visible optical absorption was measured with a spectrophotometer (BioTek Epoch). Total organic carbon (TOC, APHA 5310B, combustion temperature 800 °C), chemical oxygen demand (COD, APHA 5220D), biochemical oxygen demand (BOD, APHA 5210B), anion concentration by ion chromatography (bromide, chloride, fluoride, nitrate, nitrite and sulfate, EPA 300.0), speciated alkalinity (as $CaCO_3$, EPA 310.2), and dissolved metals by inductively coupled plasma mass spectrometry (ICPMS, EPA 200.8) were measured according to standard methods by ALS Environmental (Waterloo, ON, Canada), a laboratory accredited by the Canadian Association for Laboratory Accreditation (CALA) according to international standards (ISO 17025).

4.3.4.1 High Resolution Mass Spectrometry

Electrospray ionization high resolution mass spectrometry (ESI-HRMS) was used to analyze the composition and speciation of the OSPW AEO. For ESI-HRMS, solid phase extraction (SPE), as previously described by Headley et al.[77] was used as a concentration and cleanup technique (method recovery was 79 ± 7%). In brief, 10 mL of each sample was acidified using concentrated formic acid to a pH of ~2 . SPE cartridges (200mg, ENV+, Biotage®, Charlotte, NC), were preconditioned with 7 mL each of acetonitrile and Milli-Q water. Eluents were discarded and the organic fraction eluted at a flow rate of ~1 mL/min using 7 mL of acetonitrile. Extracts were collected in 10 mL glass test tubes and evaporated using N_2 to just dryness. The dried residue was then reconstituted in 1 mL of 50:50 Milli-Q water:acetonitrile with 0.1% ammonium hydroxide and transferred to 2 mL amber GC vials.

The ESI-HRMS chemical analysis was conducted using an LTQ Orbitrap Elite (Thermo Fisher Scientific, San Jose, CA) operating in full scan and negative-ion mode. Mass resolution was set to 240,000 with an *m/z* scan range of 100-600. ESI source had the following conditions: sheath gas flow rate 25 (arbitrary units), spray voltage 2.90 kV, auxiliary gas flow rate 5 (arbitrary units), S lens RF level 67%, heater temperature 50 °C, and capillary temperature 275 °C. Infusion solvent used was 50:50 acetonitrile:water containing 0.1% ammonium hydroxide at a flow rate of 200 µL/min. The mass accuracy was <2 ppm error for all mass assignments, and the root mean square (RMS) error for all assignments associated with the entire mass spectra was in the range of 0.12 – 0.45 ppm. The instrumental detection limit was 1 mg/L and the method detection limit was 0.10 mg/L for AEO. Software used for molecular analysis was Xcalibur v 2.1 (Thermo Fisher Scientific, San Jose, CA) and Composer v 1.0.6 (Sierra Analytics, Inc., Modesto, CA).

4.3.4.2 Fractal Image Analysis

Photomicrographs of TiO_2 aggregates were obtained using an optical microscope (Zeiss Axioskop with AxioCam ERc 5s camera). Images were converted to binary using the GNU Image Manipulation Program, and then the aggregate size and shape descriptors were measured

in ImageJ (only aggregates with a projected area ≥4 μm^2 were counted, due to optical resolution limitations).

The specific surface area of aqueous TiO_2 nanoparticle aggregates was estimated from the microscopy measurements according to fractal scaling properties,[126–129] combining data from multiple micrographs of the same sample. The two-dimensional fractal dimension of aggregates (D_2) were determined through regression of the projected area (A) and Feret diameter (or maximum length, L), of the aggregates as

$$A \propto L^{D_2} \tag{23}$$

The three-dimensional fractal dimension (D_3) was then estimated according to the model provided by Lee and Kramer:[127]

$$D_3 = 1.391 + 0.01e^{2.164D_2} \tag{24}$$

The number of primary particles in an aggregate (N) can be estimated as

$$N = k_f \left(\frac{L}{d_0}\right)^{D_3} \tag{25}$$

where d_0 is the diameter of the primary particles (taken as 28 nm for P25 TiO_2 nanoparticles), and k_f is a proportionality prefactor, estimated according to Ehrl et al. as:[128]

$$k_f = 4.46{D_3}^{-2.08} \tag{26}$$

The mass of the aggregates could then be calculated given the density of TiO_2. The surface area of the aggregates (A_S) was estimated as $A_S = 4A$, which holds for randomly oriented convex particles, and is only a first-order approximation in the case of fractal aggregates.[130] The specific surface area (A_{sp}) was then calculated as simply A_S divided by aggregate mass.

4.3.4.3 Statistics

Multiple linear regression was used to fit the models for the factorial screening and response surface experiments according to standard methods.[131,132] Error bars given in figures represent sample standard deviation (where replicates are indicated), or the standard error of the AEO/NA concentration measurement (arising primarily from the uncertainty in the method extraction efficiency) for single data points. For computed quantities, error bars represent the standard error of the corresponding regression coefficients.

4.4 Results and Discussion

4.4.1 Photocatalytic kinetics can vary significantly with OSPW source

The rate of photocatalytic AEO removal was investigated in two samples of OSPW from different industrial suppliers (Figure 19). Apparent first-order kinetics were observed for each sample, with pseudo-first order rate constants of 11.0 ± 0.5 × 10^{-5} s^{-1} and 1.33 ± 0.06 × 10^{-5} s^{-1} measured for OSPW from Industry A and B, respectively. Given the similar AEO concentration,

pH and conductivity of the OSPW samples (Table 4), it was unexpected that the degradation rate in Industry B OSPW would be fully 8.3 times slower than Industry A OSPW. We hypothesized that this difference in photocatalytic reactivity between the two samples could be due to (1) different AEO compositions, given the structure-reactivity dependence of NAs demonstrated in other AOPs;[15,91] (2) different water content of inorganic species; or (3) a combination of organic and inorganic factors.

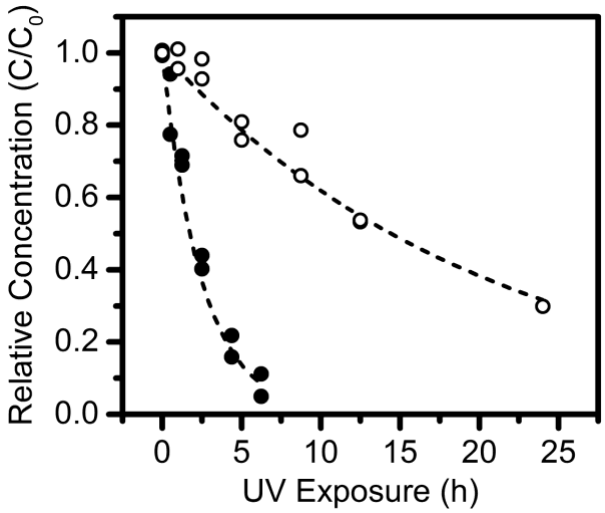

Figure 19. Photocatalytic degradation of AEO in OSPW from Industry A (●) and Industry B (○), where *C* and C_0 are the concentration and initial concentration of AEO, respectively.

4.4.2 AEO speciation does not explain variation in photocatalytic rate between OSPW sources

To investigate the first hypothesis above, *i.e.*, whether the presence of any significant differences in molecular structure could account for the different photocatalytic reactivity, the AEO composition of the OSPW samples was analysed by high resolution mass spectrometry (HRMS). The AEO class distributions of the two samples were found to be largely similar, primarily composed of O_2, O_3 and O_4 compounds, along with their singly sulfur-containing counterparts (O_xS classes, Figure 20). These sulfur classes, thought to be more photocatalytically reactive,[119] comprised a slightly larger fraction of the Industry A AEO (0.32 O_xS:O_x vs. 0.23 in Industry B). The O_2 class was taken as representative to investigate further structural differences, wherein both samples were found to have similar distributions of carbon numbers and double bond equivalents (DBE), including two foci of intensity centred on the same species (Figure 21). While the Industry B O_2 compounds had a slightly higher carbon number and DBE averages (15.4 and 5.4, respectively) than the Industry A source (15.2 and 5.2), the overall differences between the two AEO samples appeared to be relatively minor.

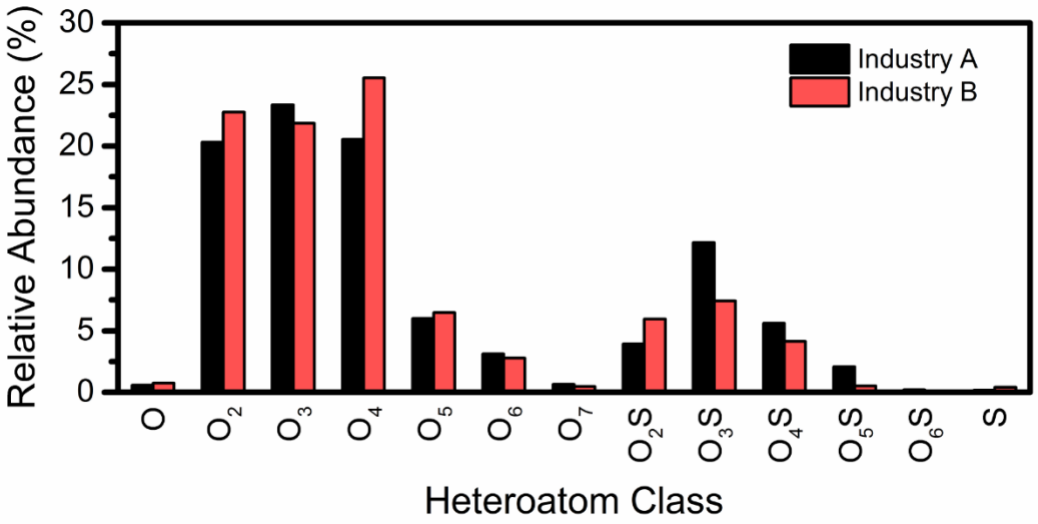

Figure 20. Distribution of O_x and O_xS classes in AEO from Industry A and B OSPW (normalized based on the relative abundance of each species within the individual samples). Other heteroatomic classes were at negligible concentration and thus excluded from this figure.

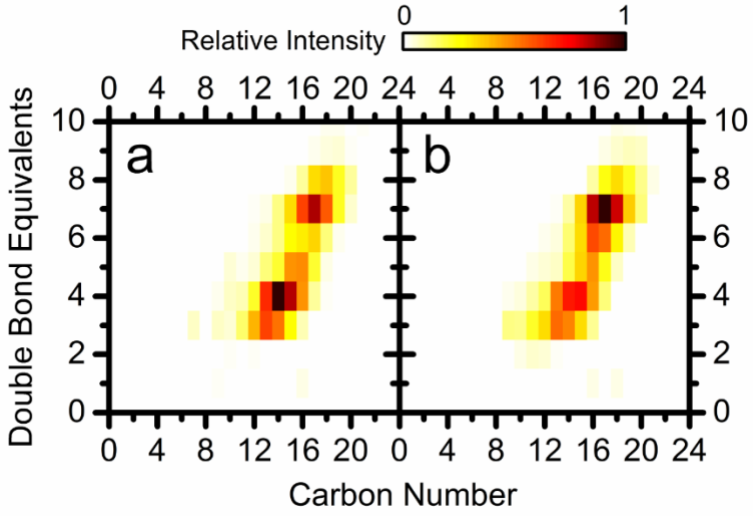

Figure 21. Relative distribution of O_2 class AEO from (a) Industry A and (b) Industry B OSPW. The data is normalized based on the relative abundance of each species within the individual samples.

As a preliminary test of whether differences in molecular composition could explain the lower reactivity of the Industry B AEO towards photocatalytic degradation, AEO was extracted from each OSPW sample and spiked into deionized water. Photocatalytic treatment of these spiked solutions (0.36 MJ/m^2 UV exposure) revealed that the two AEO samples were equivalently

susceptible to degradation when isolated from their original matrices (Figure 22). While this experiment was only a gross assessment of photocatalytic non-specificity toward different AEO mixtures, the result suggested the possibility of an inhibitory matrix effect, without precluding a more complex interaction between AEO and dissolved inorganics in OSPW. Furthermore, the most striking visual difference between the two OSPW samples was the strong yellow color of the Industry B OSPW, which was revealed in the course of this experiment to be associated with the OSPW matrix rather than the AEO (Figure 23). This observation suggested a significant difference in inorganic water constituents between the two OSPW samples, which may have affected the photocatalytic rate.

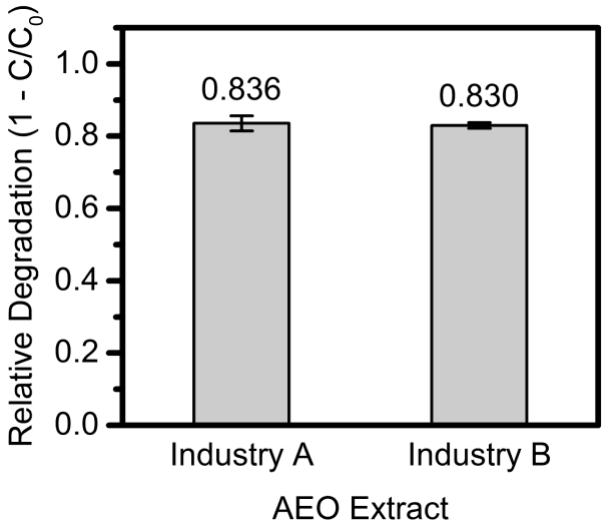

Figure 22. Photocatalytic degradation of OSPW AEO extracts spiked into deionized water (*n* = 2).

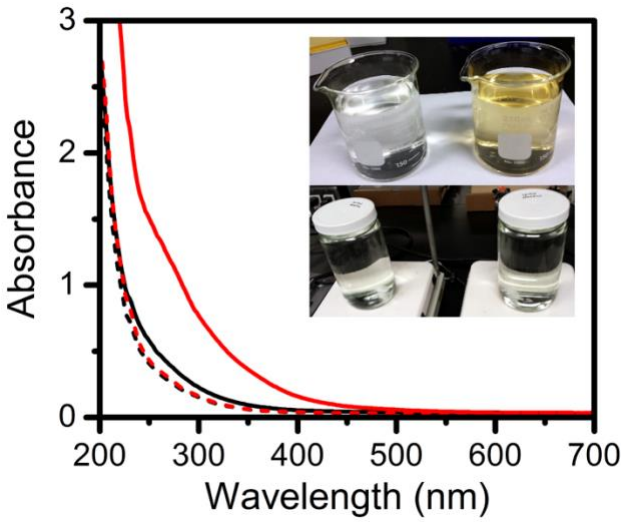

Figure 23. UV/visible absorption of Industry A (black) and Industry B (red) OSPW (solid lines) and OSPW AEO extracts spiked into deionized water (dashed lines). Inset: Industry A (left) and Industry B (right) OSPW (upper) and OSPW AEO extracts spiked into deionized water (lower).

4.4.3 Iron and bicarbonate inhibit photocatalytic NA degradation

The effect of inorganic matrix constituents on photocatalytic NA degradation was investigated under controlled conditions, focusing on six factors (listed in Table 5), which were found at significantly different concentrations in the Industry A and B OSPW samples (Table 4). Many of these species have been previously reported to modulate photocatalytic activity.[133,134] Considering the alkaline pH, the dissolved iron measured in the Industry B OSPW was likely ligated with organic acids,[135,136] which could also account for the water's color (Figure 23), given the strong optical absorption of iron complexes.[27]

A factorial experiment in simulated OSPW was designed to screen the ions for their effect on the photocatalytic treatment. It was assumed that higher order interactions between the ions would be negligible, so the scope of the test was limited to main effects and second-order interactions. Therefore a 2^{6-2} fractional factorial design was employed to minimize the number of experiments required, while still providing resolution IV data. The ranges of each ion were chosen to bracket the concentrations measured in the two OSPW samples (as well as for OSPW in literature, Table 5), and relative NA degradation (measured after a fixed UV exposure) was taken as the response variable (i.e., $y = 1 - C/C_0$). The design matrix and results are given in Table 6. It is important to note that this statistical analysis is agnostic as to the solubility state of the ions during the treatment, and is performed on the basis of the total ions initially spiked into the samples, such that any complexation or precipitation phenomena are accounted for in the interaction terms of the model.

Table 5. Range, levels and coding of the experimental variables in the factorial screening experiment. Levels refer to total rather than dissolved concentrations of each species.

Designation	Factor	Range and Level		
		-1	0	1
A	Iron (mg/L)	0	25	50
B	Fluoride (mg/L)	0	10	20
C	Phosphate (mg/L)	0	25	50
D	Sulfate (mg/L)	0	150	300
E	Chloride (mg/L)	10	255	500
F	Bicarbonate (mg/L)	100	550	1000

Table 6. Design matrix, experimental results, fitted values and residuals for the 2_{IV}^{6-2} factorial screening experiment with 4 center point replicates. Factor and level coding corresponds to Table 5.

Run	Factor Levels						Relative Degradation ($1 - C/C_0$), y_i	Fitted Values, $\hat{y}_i$	Residuals, e_i	Standardized Residuals, d_i	Internally Studentized Residuals, r_i
	A	B	C	D	E = ABC	F = BCD					
1	-1	-1	-1	-1	-1	-1	0.5256	0.5517	-0.0262	-0.2631	-0.2896
2	-1	-1	-1	1	-1	1	0.4223	0.3904	0.0319	0.3209	0.3533
3	-1	-1	1	-1	1	1	0.5821	0.3904	0.1917	1.9271	2.1217
4	-1	-1	1	1	1	-1	0.5242	0.5517	-0.0275	-0.2769	-0.3048
5	-1	1	-1	-1	1	1	0.3451	0.3904	-0.0453	-0.4555	-0.5015
6	-1	1	-1	1	1	-1	0.5083	0.5517	-0.0435	-0.4371	-0.4812
7	-1	1	1	-1	-1	-1	0.5988	0.5517	0.0470	0.4728	0.5205
8	-1	1	1	1	-1	1	0.4748	0.3904	0.0844	0.8485	0.9342
9	1	-1	-1	-1	1	-1	0.3846	0.2694	0.1152	1.1578	1.2747
10	1	-1	-1	1	1	1	0.1593	0.1081	0.0512	0.5146	0.5666
11	1	-1	1	-1	-1	1	0.0170	0.1081	-0.0911	-0.9162	-1.0087
12	1	-1	1	1	-1	-1	0.2511	0.2694	-0.0183	-0.1841	-0.2027
13	1	1	-1	-1	-1	1	0.1451	0.1081	0.0370	0.3719	0.4094
14	1	1	-1	1	-1	-1	0.4518	0.2694	0.1824	1.8335	2.0186
15	1	1	1	-1	1	-1	0.2529	0.2694	-0.0165	-0.1662	-0.1830
16	1	1	1	1	1	1	0.0609	0.1081	-0.0472	-0.4745	-0.5224
17	0	0	0	0	0	0	0.2993	0.3299	-0.0306	-0.3081	-0.3161
18	0	0	0	0	0	0	0.2105	0.3299	-0.1194	-1.2000	-1.2312
19	0	0	0	0	0	0	0.2151	0.3299	-0.1148	-1.1539	-1.1839
20	0	0	0	0	0	0	0.1696	0.3299	-0.1603	-1.6116	-1.6535

A simple probability plot was sufficient to identify iron, bicarbonate, and the iron-phosphate and iron bicarbonate interactions as the significant effects (Figure 24). Four centre point replicates in the experiment were used to obtain an error estimate, which was then used for analysis of variance (ANOVA). ANOVA confirmed the results of the normal probability plot, although only the main iron and bicarbonate effects were found to be significant with $p < 0.05$ (Table 7). Regression yielded the reduced empirical model

$$\hat{y} = 0.3299 - 0.1412A - 0.0807F \tag{27}$$

which, in terms of the natural variables, is given as

$$\hat{y} = 0.5697 - (5.647 \times 10^{-3})C_{\mathrm{Fe^{3+}}} - (1.792 \times 10^{-4})C_{\mathrm{HCO_3^-}} \tag{28}$$

where $C_{\mathrm{Fe^{3+}}}$ is the concentration of iron (mg/L), and $C_{HCO_3^-}$ is the concentration of bicarbonate (mg/L). ANOVA and regression diagnostics for this model are presented in Table 8 and Figure 25, respectively.

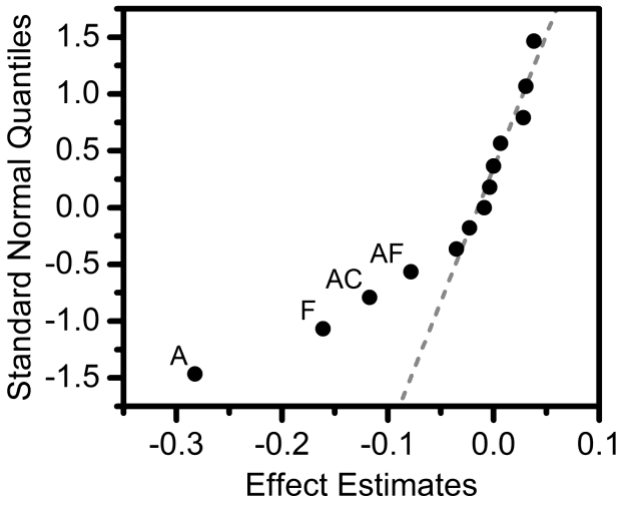

Figure 24. Half-normal probability plot of main effects and interactions for the factorial screening experiment.

Table 7. Analysis of variance for the factorial screening experiment, full model. Factor coding corresponds to Table 5.

Source of Variation	**Effect Estimate**	**Sum of Squares**	**Degrees of Freedom**	**Mean Squares**	***F₀***	***P*-Value**
Regression		0.5227	13	0.0402	3.5233	0.0656
A	-0.2823	0.3189	1	0.3189	27.9422	**0.0019**

B	-0.0036	0.0001	1	0.0001	0.0045	0.9489
C	-0.0225	0.0020	1	0.0020	0.1780	0.6878
D	0.0002	0.0000	1	0.0000	0.0000	0.9971
E = ABC	-0.0086	0.0003	1	0.0003	0.0262	0.8768
F = BCD	-0.1613	0.1041	1	0.1041	9.1224	**0.0234**
AB = CE	0.0282	0.0032	1	0.0032	0.2796	0.6159
AC = BE	-0.1172	0.0549	1	0.0549	4.8135	0.0707
AD = EF	0.0307	0.0038	1	0.0038	0.3301	0.5865
AE = BC = DF	0.0068	0.0002	1	0.0002	0.0163	0.9027
AF = DE	-0.0782	0.0245	1	0.0245	2.1440	0.1935
BD = CF	0.0383	0.0059	1	0.0059	0.5136	0.5005
BF = CD	-0.0351	0.0049	1	0.0049	0.4325	0.5352
Curvature		0.0565	1	0.0565	19.0714	**0.0222**
Residual		0.0685	6	0.0114		
Pure Error		0.0089	3	0.0030		
Total		0.5911	19	0.0311		

Table 8. Analysis of variance for the factorial screening experiment, reduced model. Factor coding corresponds to Table 5.

Source of Variation	**Sum of Squares**	**Degrees of Freedom**	**Mean Squares**	F_0	***P*-Value**
Regression	0.4230	2	0.2115	21.3764	2.2896E-05
A	0.3189	1	0.3189	32.2305	2.7275E-05
F	0.1041	1	0.1041	10.5224	0.00478
Curvature	0.0565	1	0.0565	19.0714	0.02220
Residual	0.1682	17	0.0099		
Lack-of-fit	0.1593	14	0.0114	3.8432	0.14715
Pure error	0.0089	3	0.0030		
Total	0.5911	19	0.0311		

Coefficients of multiple determination: $R^2 = 0.715$, $R^2_{\text{adj}} = 0.682$

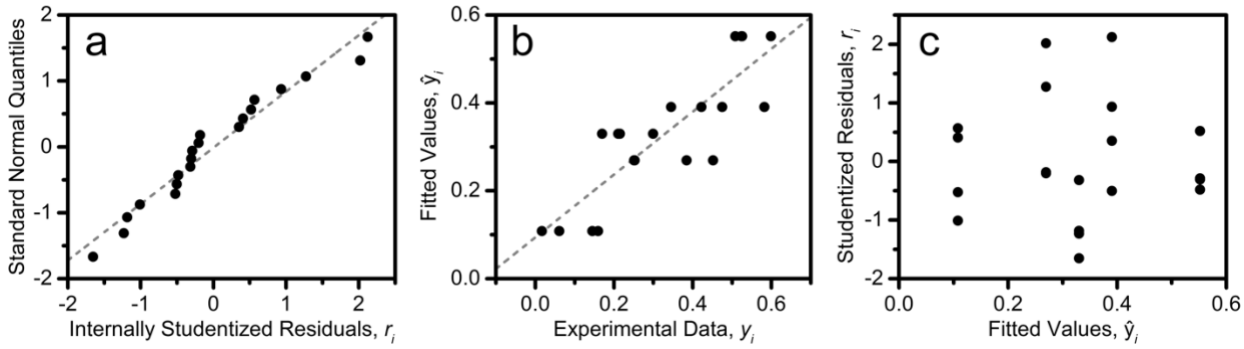

Figure 25. (a) Half-normal probability plot of residuals, (b) predicted vs. actual degradation values and (c) residual plot for the factorial screening experiment, reduced model.

To confirm the findings of this factorial screening study in real OSPW, Industry A OSPW was amended with both Fe^{3+} and HCO_3^- so as to have the same concentrations of each ion as was measured in the Industry B OSPW (Table 4), and then photocatalytically tested. The NA degradation in the Industry A OSPW was significantly diminished at the higher ion concentrations, and became indistinguishable from the photocatalytic activity measured in Industry B OSPW (Figure 26), validating the inhibitory role of these two species in the treatment.

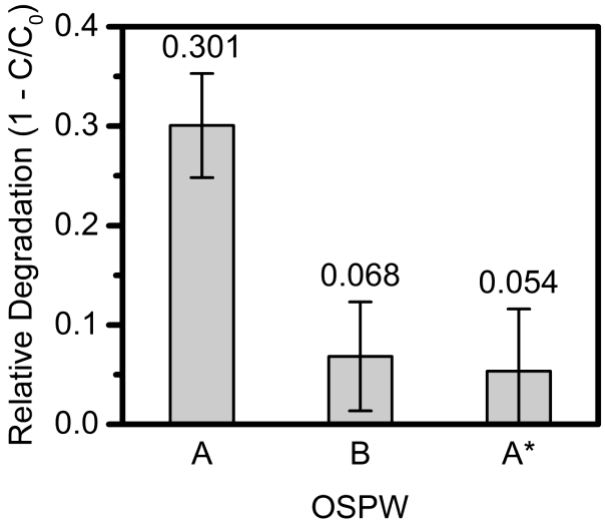

Figure 26. Photocatalytic degradation of AEO in OSPW from Industry A, Industry B, and Industry A amended with iron and bicarbonate (A*).

Notably however, ANOVA indicated the presence of significant curvature within the experimental domain ($p < 0.05$, Table 8), which was not adequately captured by the above model (Equations (27) and (28)). Therefore, while the fractional factorial design was an efficient method to identify the critical matrix factors, a secondary factorial experiment was undertaken to probe their effects with higher resolution.

4.4.4 Response surface modelling of the iron and bicarbonate effects

Response surface methodology was used to develop an empirical model for the effects of Fe^{3+} and HCO_3^+ on NA photocatalysis, following a central composite design (Table 9, Table 10), again taking relative degradation as the response.

Table 9. Range, levels and coding of the experimental variables in the response surface study. Levels refer to total rather than dissolved concentrations of each species.

Designation	**Factor**	**Range and Level**		
		-1	0	1
x_1	Iron (mg/L)	0	25	50
x_2	Bicarbonate (mg/L)	100	800	1500

Table 10. Central composite design, experimental results, fitted values and residuals for the response surface study with 3 center point replicates, and 3 additional replicates (runs 12 – 14). Factor and level coding corresponds to Table 9.

Run	Factor Levels					Relative Degradation (1 - C/C$_0$), y_i	Fitted Values, $\hat{y}_i$	Residuals, e_i	Standardized Residuals, d_i	Internally Studentized Residuals, r_i
	x_1	x_2	x_1^2	x_2^2	x_1x_2					
1	-1	-1	1	1	1	0.5116	0.4974	0.0142	0.3478	0.6370
2	1	-1	1	1	-1	0.3349	0.3333	0.0016	0.0387	0.0512
3	-1	1	1	1	-1	0.2995	0.3317	-0.0321	-0.7866	-1.5375
4	1	1	1	1	1	0.0176	0.0111	0.0065	0.1592	0.3409
5	-1	0	1	0	0	0.3631	0.3367	0.0264	0.6467	0.7894
6	1	0	1	0	0	0.0351	0.0944	-0.0593	-1.4528	-1.9263
7	0	-1	0	1	0	0.2916	0.3193	-0.0277	-0.6776	-0.8190
8	0	1	0	1	0	0.1009	0.0753	0.0256	0.6274	0.8593
9	0	0	0	0	0	0.1008	0.1195	-0.0187	-0.4579	-0.5267
10	0	0	0	0	0	0.1463	0.1195	0.0268	0.6572	0.7561
11	0	0	0	0	0	0.1528	0.1195	0.0333	0.8146	0.9370
12	1	-1	1	1	-1	0.3845	0.3333	0.0512	1.2549	1.6606
13	-1	0	1	0	0	0.3283	0.3367	-0.0085	-0.2079	-0.2538
14	0	-1	0	1	0	0.2799	0.3193	-0.0394	-0.9638	-1.1649

The least squares regression fit of the response surface is given in Figure 27, described by the relationship

$$\hat{y} = 0.1195 - 0.1212x_1 - 0.1220x_2 + 0.0961{x_1}^2 + 0.0778{x_2}^2 - 0.0391x_1x_2 \quad (29)$$

or specified in the natural variables as

$$\begin{aligned}\hat{y} = 0.5332 &- (1.075 \times 10^{-2})C_{Fe^{3+}} - (3.725 \times 10^{-4})C_{HCO_3^-} \\ &+ (1.538 \times 10^{-4})C^2_{Fe^{3+}} + (1.588 \times 10^{-7})C^2_{HCO_3^-} \\ &- (2.234 \times 10^{-6})C_{Fe^{3+}}C_{HCO_3^-}\end{aligned} \quad (30)$$

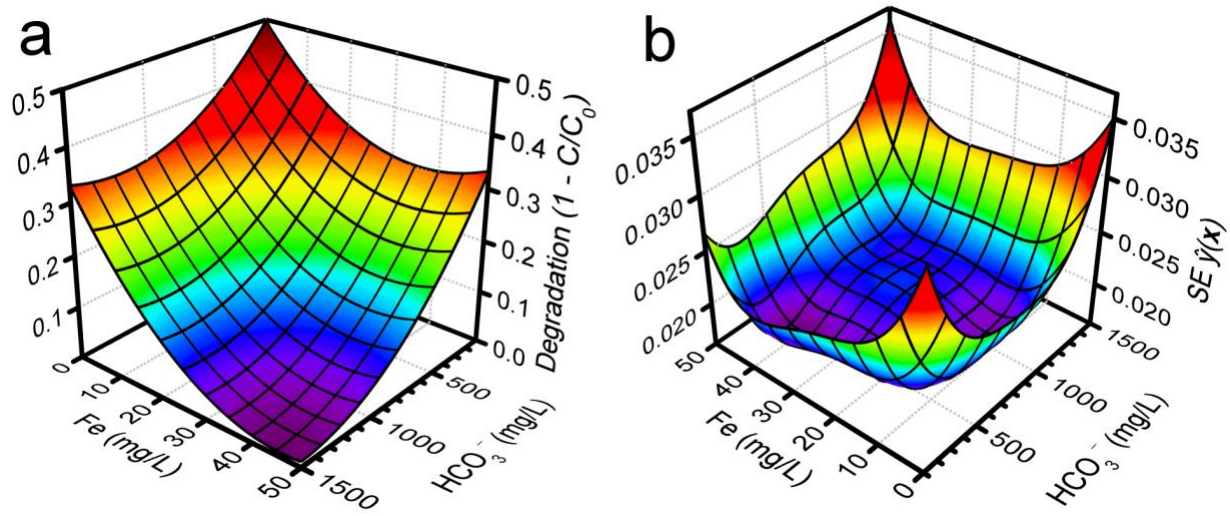

Figure 27. (a) Response surface fit ($\hat{y}$) of the relative photocatalytic degradation of NAs in simulated OSPW in the presence of iron and bicarbonate, and (b) the corresponding standard error of the estimated response.

Canonical analysis of the model revealed a stationary point (minimum) located outside the experimental domain at $x_s = (1.194, 1.384)$. ANOVA and regression diagnostics for the response surface are presented in Table 11 and Figure 28, respectively. The model is approximately comparable to the initial model from the ion screening study (Equations (27) and (28)), and the R^2 values are significantly improved.

Table 11. Analysis of variance for the response surface study (Type III partial sum of squares). Factor coding corresponds to Table 9.

Source of Variation	**Sum of Squares**	**Degrees of Freedom**	**Mean Squares**	***F₀***	***P*-Value**
Regression	0.2676	5	0.0535	32.0952	4.329E-05

x_1	0.1100	1	0.1100	65.9500	3.919E-05
x_2	0.1087	1	0.1087	65.2112	4.082E-05
x_1^2	0.0307	1	0.0307	18.4364	0.0026
x_2^2	0.0192	1	0.0192	11.5008	0.0095
x_1x_2	0.0071	1	0.0071	4.2800	0.0724
Residual	0.0133	8	0.0017		
Lack-of-fit	0.0117	6	0.0020	2.4375	0.3192
Pure error	0.0016	2	0.0008		
Total	0.2809	13	0.0216		

Coefficients of multiple determination: $R^2 = 0.953$, $R^2_{\text{adj}} = 0.923$

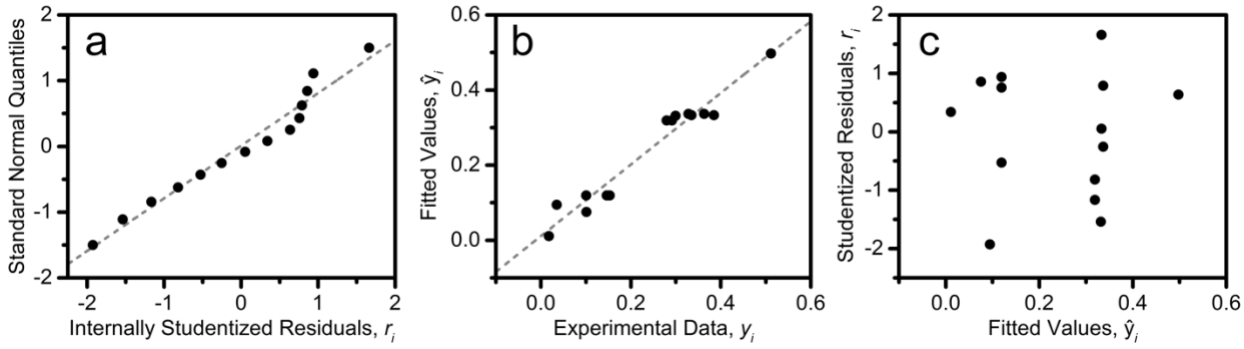

Figure 28. (a) Half-normal probability plot of residuals, (b) predicted vs. actual degradation values and (c) residual plot for the response surface regression.

The results of this study highlight the significant influence of Fe^{3+} and HCO_3^- on the photocatalytic reaction (Figure 27). Independently, each ion has a limited impact on degradation efficacy, however in combination their inhibitory effect is strong, essentially completely deactivating the catalyst at high concentrations. It is unclear from this experiment however whether their effect is synergistic (p = 0.07 for the interaction term, Table 11).

4.4.5 Iron inhibits photocatalytic $HO^{\bullet}$ generation

The detrimental effect of iron was a surprising finding, given previous reports of iron enhancement of TiO_2 photocatalytic activity.[137–143] A number of chemical and physico-chemical mechanisms could be hypothesized to explain this differing result. Therefore, the involvement of Fe^{3+} and HCO_3^- in the photocatalytic chemistry was investigated using radical probe techniques (Figure 29).

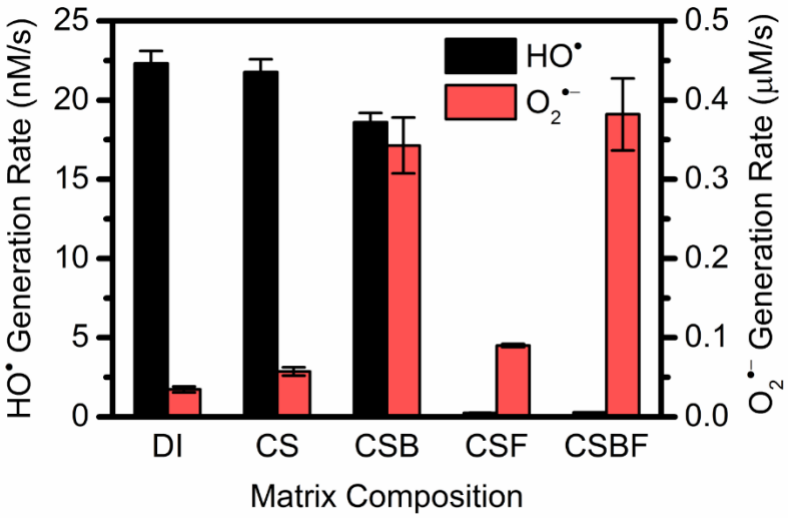

Figure 29. Photocatalytic free radical generation in deionized water (DI), or saline solutions containing 200 mg/L Cl^- (C), 200 mg/L SO_4^- (S), 800 mg/L HCO_3^- (B), or 25 mg/L Fe^{3+} (F).

While HCO_3^- was observed to diminish photocatalytic $HO^\bullet$ radical production, through its role as a moderate $HO^\bullet$ scavenger ($k = 8.5 \times 10^6\ M^{-1}\ s^{-1}$), [17,144] the presence of Fe drastically inhibited the $HO^\bullet$ generation rate. Ferrous iron is a potent $HO^\bullet$ scavenger ($k = 2.6 - 5.8 \times 10^8\ M^{-1}\ s^{-1}$),[27] and it is hypothesized that Fe^{2+} is readily available throughout the photocatalytic process from reduction of Fe^{3+} by TiO_2 conduction band electrons,[138] or by $O_2^{\bullet-}$ through the Haber-Weiss mechanism:

$$Fe^{3+} + O_2^{\bullet-} \rightleftharpoons Fe^{2+} + O_2 \qquad (31)$$

Insignificant photocatalytic H_2O_2 production in the alkaline saline solution presumably negated any $HO^\bullet$ contributions by means of Fe^{2+} as a Fenton catalyst.

While the presence of iron appeared to slightly enhance photocatalytic $O_2^{\bullet-}$ production, HCO_3^- significantly increased the observed $O_2^{\bullet-}$ generation rate, as has been reported previously.[145] Although the origin of this HCO_3^- effect is unclear, we hypothesize that excess $O_2^{\bullet-}$ may arise through HCO_3^- scavenging of TiO_2 valence band holes, reducing recombination of photogenerated electrons, and thereby accelerating the reduction of dissolved oxygen; or alternatively through the decay process of photocatalytically generated $CO_3^{\bullet-}$ radicals.[146,147]

These radical probe results may be explained by the model for photocatalytic NA degradation proposed previously,[119] namely a two-step reaction initiated through single-electron oxidation or hydrogen abstraction from the NA (by $HO^\bullet$ or derived $Cl^\bullet$, $SO_4^{\bullet-}$ and $CO_3^{\bullet-}$), followed by $O_2^{\bullet-}$ reaction at the resultant carbon-centered radical. Thus interference of Fe^{3+} in the first step of this oxidation process through $HO^\bullet$ quenching likely serves to limit the overall photocatalytic NA degradation rate.

Physico-chemically, iron is a potent coagulant, and iron-induced TiO_2 nanoparticle aggregation could essentially eliminate reactive surface area from the system. Another possibility, assuming NA degradation occurs at the TiO_2 surface, is that Fe^{3+} may compete with the surface reaction through NA complexation in solution, or through occupying active surface sites, thereby blocking NA adsorption. Dissolved Fe^{3+} also strongly absorbs UV, and could attenuate the light impinging the photocatalyst. As for bicarbonate, it may serve to destabilize TiO_2 nanoparticles through double layer compression at high ionic strength, according to DLVO theory. Some combination of all these mechanisms could be at work to produce the performance deterioration observed in the presence of Fe^{3+} and HCO_3^-.

4.4.6 Effect of NA concentration

While the experiments described above appear to have identified the primary cause of the different photocatalytic rate observed in the two industrial OSPW samples (Figure 19), we sought a more comprehensive description of photocatalytic kinetics in OSPW, towards development of a predictive model for the performance of photocatalysis in new OSPW streams. The concentration of OSPW AEO can significantly vary by tailings pond, typically in the range of 20 – 120 mg/L.[12,78,148] Thus the effect of initial NA concentration on the photocatalytic degradation rate was investigated (Figure 30).

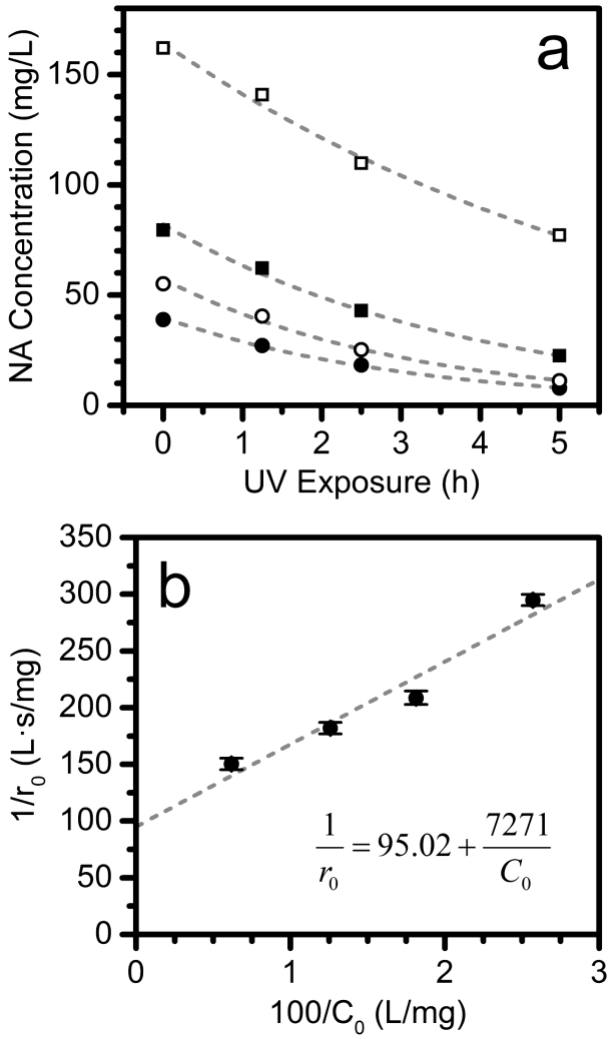

Figure 30. (a) Photocatalytic degradation of different concentrations of NAs in simulated OSPW (mg/L): 40 (●), 55 (○), 80 (■), and 160 (□). (b) Dependence of the initial photocatalytic degradation rate, r_0, on the initial concentration of naphthenic acids, C_0.

Heterogeneous photocatalytic kinetics are conventionally described by the Langmuir-Hinshelwood (L-H) model

$$r = -\frac{\mathrm{d}C}{\mathrm{d}t} = k_r\theta = \frac{k_r K C}{1 + K C_0} \tag{32}$$

where r is the reaction rate, C is the concentration of organic species, k_r is the reaction rate constant, θ is the fraction of occupied catalyst surface sites, and K is the Langmuir adsorption constant. The C_0 term in the denominator accounts for the competitive adsorption of degradation intermediates, under the assumption that these competing species, with concentration C_i, have similar adsorption constants, K_i, as the parent compounds,[149] *i.e.*,

$$KC + \sum_i K_i C_i = KC_0 \tag{33}$$

The model assumes dynamic equilibrium, and no competition for catalyst surface sites (*e.g.*, by degradation intermediates). At low organics concentration, integration of Equation (32) yields the typical pseudo-first order form:

$$\ln\left(\frac{C_0}{C}\right) = k_r K t = k_{\text{app}} t \tag{34}$$

where k_{app} is the apparent first-order rate constant, and t is the reaction time. The linearized form of Equation (32) enables determination of k_r and K:

$$\frac{1}{r_0} = \frac{1}{k_r K C_0} + \frac{1}{k_r} \tag{35}$$

where r_0 is the initial rate.

Regression of $1/r_0$ against $1/C_0$ yielded $k_r = 1.05 \pm 0.24 \times 10^{-2}$ mg L^{-1} s^{-1} and $K = 1.31 \pm 0.37 \times 10^{-2}$ L mg^{-1} (Figure 30b). For the typical AEO concentrations found in OSPW, these values represent the transitional regime between adsorption-limited and reaction-limited kinetics (*i.e.*, $KC \approx 1$). The measured value of K is comparable to values previously reported for adsorption of organic acids on TiO_2.[150–152] Notably, K here only represents the adsorption constant under illuminated conditions, and would also be expected to change with molecular composition of the AEO. Furthermore, both k_r and K are only apparent constants, as the actual form of the reaction is presumably more complex (*e.g.*, involving dissolved oxygen, free radicals, intermediate compounds, etc.).[27] Nevertheless, the L-H description is useful from an engineering perspective.

4.4.7 Temperature minimally affects treatment rate

Given the northern climate of the oil sands and seasonal variability of OSPW temperature,[148] it is important to understand the effect of temperature on proposed treatment processes. Therefore, the rate of photocatalytic AEO degradation was investigated at 4, 20 and 40 °C.

While the pseudo-first order rate constant k_{app} was lowest at 4 °C, at 40 °C it was measured to be equivalent to that at 20 °C (Table 12). However, in the course of the experiment, it was observed that the TiO_2 dispersion appeared unstable at 40 °C, and after the test the particles settled more quickly than at 4 °C. Microscopic observation revealed the presence of TiO_2 nanoparticle aggregates ~5-10 µm in diameter in all the dispersions, although those formed at 40 °C appeared slightly larger and denser than those at lower temperatures (Figure 31). Image analysis revealed the aggregate size distribution of the 40 °C sample to indeed be larger than the 4 °C sample (Figure 32, $p < 0.01$ for the log-transformed data). This observation complicated analysis of rate temperature dependence according to standard Arrhenius theory, as the concentration of one "reactant" (*i.e.*, active surface sites on the catalyst) was not constant with temperature, but rather changed with nanoparticle aggregation state.

Table 12. Temperature dependent photocatalytic properties.

Parameter	Description	Temperature (°C)		
		4	20	40
$k_{app} \times 10^5$ (s^{-1})	Apparent first order rate constant	2.544 ± 0.052	3.433 ± 0.270	3.308 ± 0.270
$\hat{k}_{app} \times 10^5$ (s^{-1})	Apparent first order rate constant, normalized with respect to surface area	3.569 ± 0.074	4.743 ± 0.373	6.344 ± 0.518
n	Number of aggregates measured	321	304	372
L (μm)	Mean Feret diameter	6.23 ± 2.67	7.39 ± 3.97	7.10 ± 3.09
D_2	2D fractal dimension	1.803 ± 0.035	1.807 ± 0.027	1.881 ± 0.027
D_3	Mass (3D) fractal dimension	1.886 ± 0.037	1.890 ± 0.029	1.976 ± 0.034
A_{sp} (m^2/g)	Estimated specific surface area	39.2 ± 8.7	39.8 ± 8.4	28.7 ± 5.8

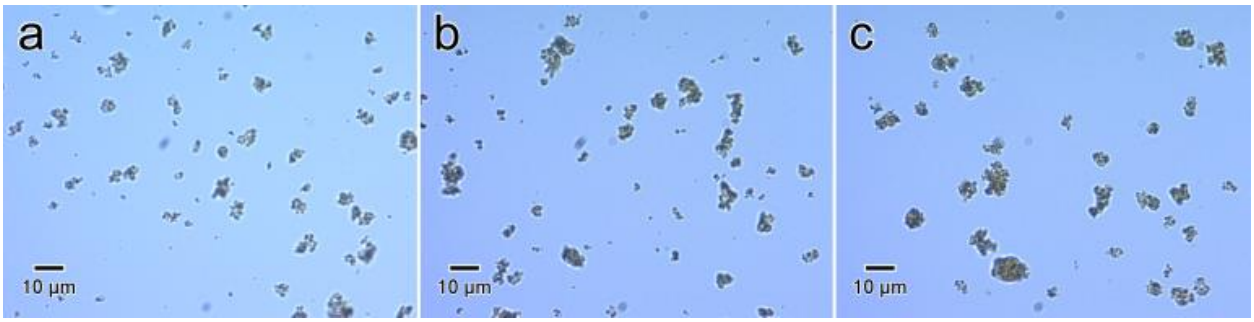

Figure 31. Microscope images of TiO_2 nanoparticle aggregates formed at (a) 4 °C, (b) 20 °C and (c) 40 °C, in OSPW.

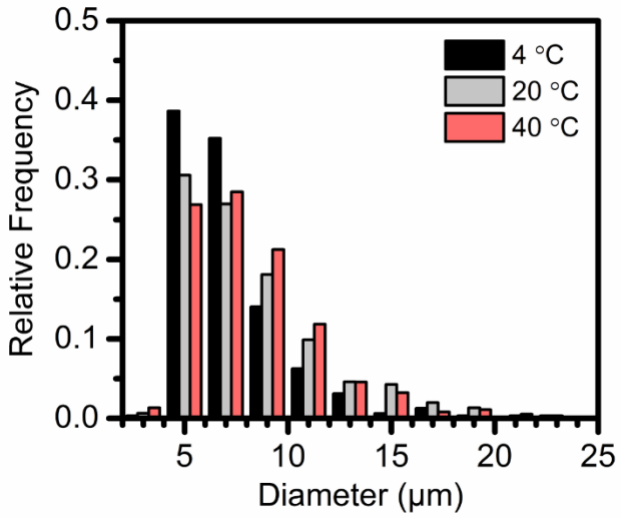

Figure 32. Size distribution (Feret diameter) of TiO_2 nanoparticle aggregates formed at different temperatures, as observed by optical microscopy.

To account for this differential thermal aggregation, the measured rate constants were normalized with respect to accessible catalyst surface area. Image analysis of the micrographs yielded the fractal dimensions of the TiO_2 aggregates formed at different temperatures (Figure 33), which were used to obtain an estimate of the specific surface area of the aggregates (A_{sp}, Table 12).[126–129] Surface area analysis by gas adsorption was not attempted over concerns that drying would affect the aggregate structure, and light scattering could not be used to measure the mass fractal dimension (D_3), as the aggregate size and refractive index were too large for Rayleigh-Gans-Debye (RGD) theory to apply.[153,154] The lower A_{sp} of the TiO_2 aggregates formed at 40 °C is congruous with their larger size (L) and more compact structure (D_3), compared to the lower temperature samples. It is hypothesized that higher thermal energy lowers solution viscosity and increases particle collision frequency, allowing the aggregated nanoparticles to access more thermodynamically favourable compact structures with higher fractal dimensions.[155] The measured rate constants (k_{app}) were then normalized relative to 55 m^2 g^{-1}, which corresponds to the specific surface area of the photocatalyst in its non-aggregated state ($\hat{k}_{app}$, Table 12).[156–158]

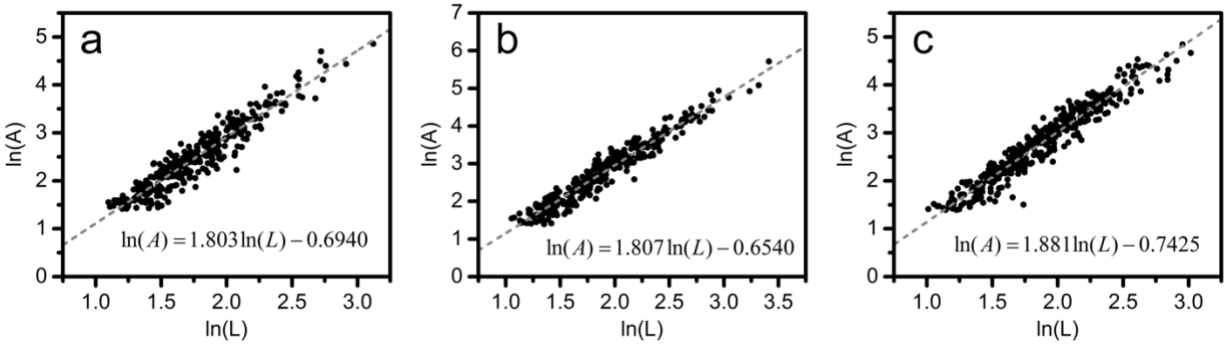

Figure 33. Estimate of the two-dimensional fractal dimension (D_2) of TiO_2 nanoparticle aggregates formed at (a) 4 °C, (b) 20 °C and (c) 40 °C, from the linear regression of their projected area (A) and Feret diameter (L), as measured by optical microscopy.

The Arrhenius plot of the adjusted pseudo-first order rate constants (adjusted to account for TiO_2 nanoparticle aggregation as discussed above) indicated an activation energy (E_a) of 11.53 ± 0.26 kJ mol^{-1} for the photocatalytic reaction (Figure 34a), within the range typically reported for the degradation of organics over TiO_2.[149,159,160] Relatively low apparent activation energies are expected for photocatalysis, where the driving energy is optical absorption.[161] Treatment of the same data according to the Eyring equation

$$\ln\left(\frac{k}{T}\right) = -\frac{\Delta H^{\ddagger}}{RT} + \ln\left(\frac{k_B}{h}\right) + \frac{\Delta S^{\ddagger}}{R} \tag{36}$$

where $\Delta H^{\ddagger}$ and $\Delta S^{\ddagger}$ are the enthalpy and entropy of activation, and R, k_B, and h are the gas, Boltzmann and Planck constants, respectively, yielded $\Delta H^{\ddagger}$ = 9.07 ± 0.30 kJ mol^{-1} and $\Delta S^{\ddagger}$ = -297 ± 1 J K^{-1} mol^{-1} (Figure 34b). The large negative value of $\Delta S^{\ddagger}$ indicates an associative mechanism in the transition state, which could correspond to a surface reaction of adsorbed NAs, consistent with the L-H model above.

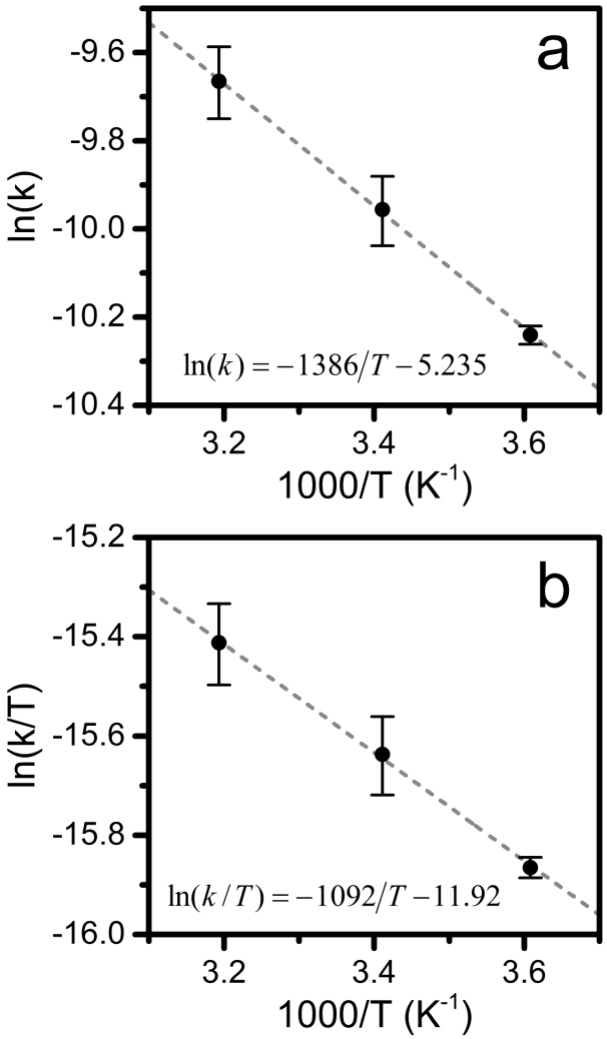

Figure 34. (a) Arrhenius plot and (b) Eyring plot of photocatalytic degradation of AEO in OSPW, where *k* is the apparent rate constant (with units of s^{-1}), normalized with respect to surface area.

In terms of impact on treatment efficacy, the real effect of temperature on the degradation rate was relatively small (k_{app} at 4 °C was only ~25% lower than at 40 °C), due to the mitigating effect of increased catalyst aggregation with temperature. The effect of temperature on nanoparticle aggregation merits further investigation, as aggregation state is known to have a large impact on photocatalytic kinetics in slurry systems.[162]

4.4.8 pH has negligible effect on treatment rate

Photocatalytic reactions are often observed to be pH dependent, where the catalyst's surface charge is determined by solution pH in relation to its point of zero charge (PZC), with implications for adsorption of ionic species. Solution pH also affects the flatband potential of

semiconducting oxides according the Nernstian relation,[163] where higher pH should increase the overpotential of conduction band electrons driving reduction of dissolved O_2 to superoxide.[164] Therefore photocatalytic performance was tested within the typical range of pH encountered in OSPW (pH 7 – 9, Figure 35).

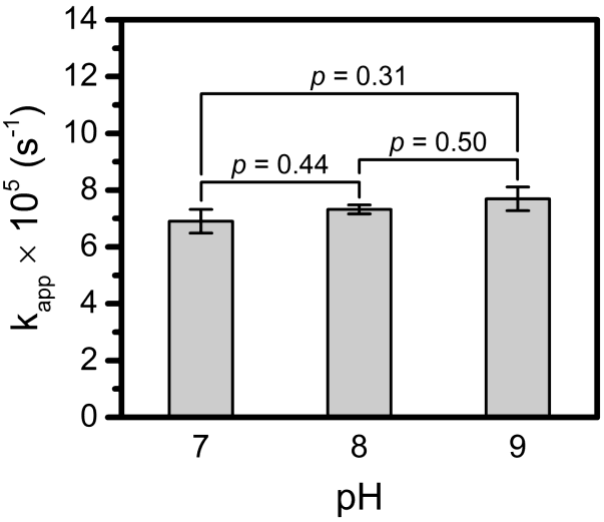

Figure 35. Effect of pH on the pseudo-first order rate constant (k_{app}) of the photocatalytic degradation of NAs in simulated OSPW.

Within the typical range found in OSPW, pH had no significant effect on the reaction rate. Given that the PZC of TiO_2 is ~5.5,[23,27] the catalyst surface was consistently negatively charged between pH 7-9, and thus no significant change in the adsorption of naphthenate anions would be expected, from an electrostatic perspective. Note that the pH of OSPW does not change throughout the photocatalytic treatment, presumably due to the strong buffering capacity of dissolved bicarbonate.

4.4.9 Dissolved oxygen is necessary for NA degradation

Dissolved oxygen (DO) plays an important role in photocatalytic water treatment as the primary acceptor for excited conduction band electrons from the photocatalyst. Electron transfer to DO has even been implicated as the rate limiting step for photocatalysis as a whole, where electron accumulation on the catalyst accelerates recombination with photogenerated holes, degrading quantum efficiency.[165,166] Reduction of DO also generates superoxide, which has been identified as a critical radical species involved in photocatalytic NA degradation in OSPW.[119]

The dependence of the photocatalytic treatment on DO was assessed in suspensions sparged continuously with either air or pure N_2 (Figure 36). The results highlight the significant influence of DO, where k_{app} varied between $1.22 \pm 0.08 \times 10^{-4}$ s^{-1} and $9.78 \pm 4.41 \times 10^{-6}$ s^{-1} for the air and

N_2 sparged tests, respectively (although it could not be ascertained with confidence whether the N_2 purged condition followed first-order kinetics). Furthermore, the 78% inhibition of NA degradation under N_2 purge is comparable to the 65% inhibition observed previously in the presence of 1,4-benzoquinone, a $O_2^{\bullet-}$ scavenger (Chapter 3),[119] where either eliminating DO or quenching any DO-derived $O_2^{\bullet-}$ would be expected to have the same effect on the photocatalytic reaction. This experiment is therefore consistent with the purported role of $O_2^{\bullet-}$ in the treatment process. From an application perspective, DO limitations are unlikely to be encountered in practice, despite hypoxic/anoxic conditions biologically induced in deeper tailings pond strata, as photocatalytic OSPW treatment would presumably only be implemented in illuminated surface waters, corresponding to DO enriched conditions.

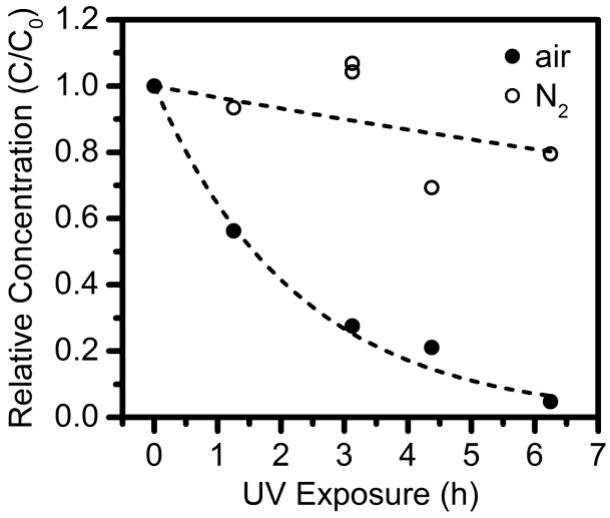

Figure 36. Photocatalytic degradation of NAs in simulated OSPW sparged with air or nitrogen.

4.4.10 Empirical kinetics model

To develop a more comprehensive description of the photocatalytic kinetics in OSPW, it was hypothesized that the NA degradation rate could be modeled by the expression

$$r = k^* e^{-\frac{E_a}{RT}} \ln\left(\frac{1}{1-\hat{y}}\right)\frac{KC}{1+KC_0} \qquad (37)$$

where k^* is a constant subsuming multiple preexponential factors, $\hat{y}$ is calculated according to Eq. (30) (taken within a natural logarithm term as the kinetics of the response surface study assumed to be pseudo-first order), and other variables are given as previously.[149,159] Regression fitting (on the data from Figure 30) yielded k^* = 2.57 ± 0.09 mg L^{-1} s^{-1}. The apparent first-order rate constant can thus be estimated as

$$k_{\text{app}} = k^* e^{-\frac{E_a}{RT}} \ln\left(\frac{1}{1-\hat{y}}\right)\frac{K}{1+KC_0} \quad (38)$$

An assumption of this treatment is that *K* does not significantly vary with temperature, $C_{Fe^{3+}}$ or $C_{HCO_3^-}$, or rather, that any variation in *K* is accounted for by the other terms in the model. The model also makes no attempt to account for aggregation state of the catalyst, as aggregation phenomena are highly complex, and influenced by other factors than temperature alone (*e.g.*, mixing conditions, dissolved and suspended solids content). In practice, the treatment rate will also depend on solar UV intensity, which varies with time (unlike the constant intensity UV source used in this study).

Substituting values from Table 4, Eq. (38) predicted the photocatalytic rate constant in the Industry A OSPW to be 1.27 x 10^{-4} s^{-1}, which compares favorably to the measured value of 1.10 x 10^{-4} s^{-1}. However, for a measured rate of 1.33 x 10^{-5} s^{-1} in the Industry B OSPW, the model predicted k_{app} to be 5.94 x 10^{-5} s^{-1}. Given that E_a was experimentally determined in the Industry A OSPW, it is possible that the model was not specified correctly for the Industry B sample. Thus if E_a is instead taken as 15.3 kJ mol^{-1}, the equation can accurately calculate the Industry B OSPW rate constant at 300 K. A higher apparent activation energy in the Industry B OSPW could potentially arise from its higher ionic strength affecting AEO interaction with the catalyst, or possibly from more recalcitrant or complex AEO molecular structures. The structure-activity relationship of photocatalytic NA degradation is the subject of ongoing investigations in our laboratory.

4.4.11 Estimation of external quantum efficiency (EQE)

The external quantum efficiency (EQE), or apparent photonic efficiency, of a photocatalytic reaction can be estimated as

$$EQE = \frac{r}{\Phi} \quad (39)$$

where *r* is the rate (mol L^{-1} s^{-1}), and Φ is the incident photon flux (mol L^{-1} s^{-1}).[134] According to Eq. (37), taking $C = C_0$ = 50 mg L^{-1}, $C_{Fe^{3+}}$ = 0 mg L^{-1}, $C_{HCO_3^-}$ = 800 mg L^{-1}, T = 300 K, and assuming an average NA molecular weight of ~225 g mol^{-1},[120] r = 1.82 x 10^{-8} mol L^{-1} s^{-1}. Given the light intensity of 40 W m^{-2} (with spectral distribution as given, Figure 18b), beaker diameter of 63 mm, and reaction volume 0.2 L, Φ = 1.84 x 10^{-6} mol L^{-1} s^{-1}.

The external quantum efficiency (EQE), or apparent photonic efficiency, of the treatment was estimated as ~0.99%. Note that this value merely represents an approximate lower bound on the efficiency, as photochemically rigorous calculations use absorbed photon flux, and account for the degradation mechanism.[167] While ~1% EQE is typical of photocatalysis,[168,169] efficiencies as high as 50% have been reported,[170] indicating an opportunity for significant enhancement in OSPW treatment kinetics with optimized catalysts and reactor geometries.

4.5 Environmental significance

This study addresses a number of key process variables affecting the behaviour and kinetics of photocatalytic treatment in various OSPW streams. It is anticipated that the models proposed herein will be useful for estimation of UV dose requirements, contact time, and other operating parameters necessary for the design of scaled treatment systems.

The utility of statistical design of experiments (DoE) is also highlighted for efficient troubleshooting of unknown obstacles when adapting a treatment process to new environmental sources, where complex water composition may obscure assessment of the underlying factors. The strong deleterious effect of iron on photocatalytic NA degradation is a new finding that may have significant implications for OSPW treatment, where $HO^{\bullet}$ radical quenching may limit degradation rates in brackish waters. Where possible, integrating photocatalysis following ion exchange or desalination steps in a treatment train has the potential to significantly improve photocatalytic kinetics.

Solar photocatalysis is very promising for OSPW treatment and environmental remediation applications. Nevertheless, the technology's full potential has not yet been realised in an optimized system, and there is still great opportunity for significant advances in process efficiency, accessible through materials engineering, catalyst optimization, and deployment strategy.

Chapter 5
Magnetic flocculation for nanoparticle separation and catalyst recycling[§]

5.1 Summary

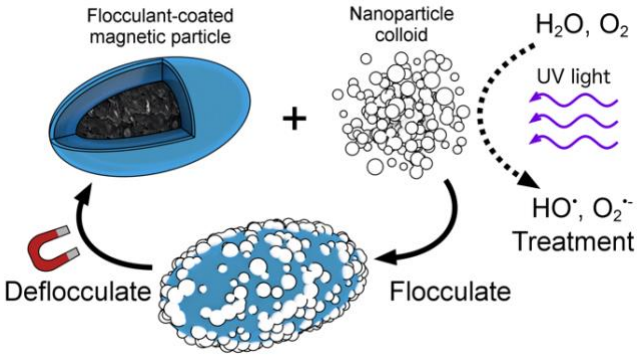

Nanoparticles are heavily researched for environmental applications, such as photocatalytic water treatment, however practical separation of nanoparticles from colloidal dispersions remains a critical challenge. Here, we demonstrate a new approach to nanoparticle recovery, combining the advantages of flocculation with magnetic separation to enable simple collection of non-magnetic nanoparticles. Flocculant polymers were coated onto magnetic nanoparticles (Fe_3O_4@SiO_2) to prepare reusable magnetic flocculants (MFs). When added to colloidal nanoparticle dispersions, MFs aggregate with the suspended nanoparticles to form magnetically responsive flocs, which upon separation can be reversibly deflocculated for nanoparticle release, and reuse in a closed loop process. High separation efficiency was attained in a variety of nanoparticle suspensions, including Au, Ag, Pd, Pt, and TiO_2, stabilized by different coatings and surface charge. The MFs were shown to be recyclable for photocatalytic treatment of naphthenic acids in oil sands process-affected water (OSPW) and selenium in flue gas desulfurization wastewater (FGDW). Magnetic flocculation thus represents a general platform and alternative paradigm for nanoparticle separation, with potential applications in water treatment and remediation of nanoparticle pollution. Furthermore, given that flocculant chemicals can be recovered and reused in this process, magnetic flocculation may also serve as an environmentally sustainable solution to conventional flocculation challenges.

5.2 Introduction

[§] This chapter is adapted from a previously published article: Leshuk, T.; Holmes, A. B.; Ranatunga, D.; Chen, P. Z.; Jiang, Y.; Gu, F. Magnetic Flocculation for Nanoparticle Separation and Catalyst Recycling. *Environ. Sci.: Nano* **2018**, *5* (2), 509–519.

The advent of nanotechnology has led to diverse practical applications of colloidal nanoparticle dispersions in numerous fields of research and engineering, from biotechnology to environmental remediation.[171–175,119] However, nanoparticle dispersions are often difficult to work with, primarily due to the challenge of separating nanoparticles from suspension upon completion of their function.[176,177] Colloidal nanoparticles can remain stably suspended against gravitational settling for decades, and frequently can only be disrupted by intensive and expensive membrane filtration processes.[178,179] For example, in photocatalytic water treatment, the most efficient reactors involve dispersion of the nanocatalyst into the contaminated water as a slurry.[22,24,25] Nanoparticle recovery after the treatment process is essential not only for reuse of the catalyst, but also to prevent nanoparticle contamination of the treated effluent. Unfortunately, nanoparticle separation challenges remain a critical hurdle to practical application of this promising treatment technology.[26–28]

Magnetic separation is a powerful method for particle recovery, and has been researched for biomolecule enrichment,[180,181] biosensing,[182–184] and catalyst recycling.[31,32,185] Magnetic separation is especially useful in nanotechnology for collection of nanoparticles which are challenging to manipulate by other means.[30,49–52] Superparamagnetism is a useful property in magnetic nanoparticle separation, a phenomenon whereby a nanostructured magnetic material is essentially magnetized only in the presence of an applied magnetic field.[34] Superparamagnetic nanoparticles can thus form stable colloids, which can be reversibly magnetized and separated on demand.

Extrinsic magnetic separation, *i.e.*, the addition of magnetic particles to bind or capture a non-magnetic material, has been previously studied for small molecule adsorption or cell harvesting,[49,186–188] however nanoparticles are more challenging to separate, *e.g.*, due to the lack of specific affinity interactions available to biomolecules. To render non-magnetic nanomaterials magnetically separable, typically composite nanoparticles are synthesized by immobilizing the functional nanomaterial on a superparamagnetic support (*e.g.*, in a core-shell structure).[53–58] However, this immobilization strategy imposes various synthesis and process constraints, and can inhibit nanocatalyst efficiency by reducing accessible surface area, while introducing mass transfer and illumination limitations. Furthermore, shearing of the immobilized nanomaterial from the magnetic core has been previously reported, leading to poor recyclability,[56,189,190] and raising concerns of nanoparticle water pollution. Herein, we propose an alternative paradigm for magnetic nanoparticle separation, surmounting these complications by drawing inspiration from some of the earliest particle separation technologies developed, coagulation and flocculation.

Coagulation and flocculation (CF) processes are well established separation techniques for precipitating a broad range of suspended solids, and have been extensively used in the water treatment industry for over a century.[191–193] These methods involve chemical dosing of the water with metallic salts or polymers to aggregate suspended fine particles, forming larger agglomerates which can be removed by settling or filtration. Although effective at separating a diverse spectrum of colloidal materials,[194–196] CF have not been successfully implemented for

nanoparticle recovery and recycling due to the irreversible nature of the aggregation process. Furthermore, recent reports have raised various health and ecotoxicity concerns associated with CF chemical additives.[197–201] In response, biodegradable flocculants have been investigated as a renewable alternative,[202,203] and reusing flocculant polymers has been recently proposed,[204] thereby avoiding chemical discharge altogether.

It was hypothesized that the advantages of both CF and magnetic separation processes could be combined to form magnetic flocculants, through binding flocculant polymers to magnetic nanoparticles, enabling a new approach to nanoparticle separation challenges. By leveraging the broad spectrum separation capabilities characteristic of CF processes, while achieving reversible aggregation through magnetic separation, magnetic flocculation could thus provide a general platform for recovery and recycling of a wide variety of functional nanoparticles. A first demonstration of this concept is reported herein. The magnetic flocculants are only added to a nanoparticle suspension when required at the point of separation, avoiding the problems associated with immobilizing nanoparticles on a magnetic support. The target nanoparticles in suspension are separated through flocculation, while the magnetic properties of the flocculant enable a reversible aggregation process. A key novelty of this system is that both the nanoparticles and flocculant material are reusable, which avoids chemical amendment of the water, and thus magnetic flocculants may represent not only a new approach to nanoparticle separations, but also an environmentally sustainable alternative to conventional CF processes, by providing a means for recovery of polymer additives.

5.3 Experimental

5.3.1 Materials

$FeCl_3 \cdot 6H_2O$ (Sigma-Aldrich, ≥99%), NaH_2PO_4 (Amresco, reagent grade), NH_4OH (Sigma-Aldrich, ACS reagent, 28.0-30.0 % NH_3 basis), ethanol (EtOH, ≥99%, ACS reagent), tetraethyl orthosilicate (TEOS, Sigma-Aldrich, 98%), poly(diallyldimethylammonium chloride) (PDADMAC, Sigma-Aldrich, 100-200 kDA), NaOH (Sigma-Aldrich, ACS reagent), NaCl (EMD, ACS reagent), poly(sodium 4-styrenesulfonate) (PSS, Sigma-Aldrich, 70 kDa), $NaBH_4$ (Sigma-Aldrich, 99.99%), trisodium citrate dihydrate (Sigma-Aldrich, ≥99%), $HAuCl_4 \cdot xH_2O$ (Sigma-Aldrich, 99.999%), hexadecyltrimethylammonium bromide (CTAB, Sigma-Aldrich, ≥99%), $AgNO_3$ (Sigma-Aldrich, ≥99%), K_2PdCl_4 (Sigma-Aldrich, 98%), ethylene glycol (EG, Sigma-Aldrich, anhydrous, 99.8%), poly(vinylpyrrolidone) (PVP, Sigma-Aldrich, 40 kDa), $H_2PtCl_6 \cdot 6H_2O$ (Sigma-Aldrich, ACS reagent, ≥37.50% Pt basis), $NaNO_3$ (Sigma-Aldrich, ACS reagent), dichloromethane (DCM, ≥99.9%, HPLC grade), and TiO_2 nanoparticles (Evonik Aeroxide P25, ~21 nm particle diameter, 55 $m^2\ g^{-1}$ surface area, Acros) were used as received. P25 TiO_2 nanoparticles have been extensively studied and characterized in the literature, and are often used as a benchmark photocatalyst. Poly(acrylic acid) (PAA, Sigma-Aldrich, 250 kDa), at 10 wt.% in water, was neutralized with NaOH to pH 7 before use. Chitosan (CS, Sigma-Aldrich,

50 kDa, deacetylated chain, poly(D-glucosamine)) was dissolved at 1 g/L in a 1 wt.% acetic acid (Fisher Scientific, ACS reagent) aqueous saline solution (0.5 mol/L NaCl) at 70 °C before use. Oil sands process-affected water (OSPW) was provided by Shell Canada, and stored at 4 °C in the dark. The concentrations of the organic and inorganic constituents of the OSPW are given in Table 13. Flue gas desulphurization wastewater (FGDW) was provided by by a coal-fired power plant in the southeastern United States, and stored at 4 °C in the dark. Prior to use, the OSPW and FGDW were homogenized by stirring, and filtered through glass microfiber filters (Whatman 934-AH) to remove suspended solids.

Table 13. Water quality characteristics of OSPW. All parameters apart from NAs and AEO were measured according to standard methods by ALS Environmental (Waterloo, ON, Canada), a laboratory accredited by the Canadian Association for Laboratory Accreditation (CALA) according to international standards (ISO 17025).

Parameter	**Value**
NAs (mg/L)	79.5 ± 2.3
AEO (mg/L)[a]	40.9 ± 2.4
TOC (mg/L)	54
COD (mg/L)	153
BOD (mg/L)	3.0
pH	8.30
Conductivity (mS/cm)	1.630
Anions	
Bromide (mg/L)	<0.50
Chloride (mg/L)	172
Fluoride (mg/L)	3.00
Nitrate (mg/L)	<0.10
Nitrite (mg/L)	<0.050
Sulphate (mg/L)	207
Alkalinity (mg/L as $CaCO_3$)	400
Dissolved Metals	
Aluminum (Al) (mg/L)	<0.050
Antimony (Sb) (mg/L)	0.0011
Arsenic (As) (mg/L)	0.0027
Barium (Ba) (mg/L)	0.0976

Beryllium (Be) (mg/L)	<0.0010
Bismuth (Bi) (mg/L)	<0.00050
Boron (B) (mg/L)	2.00
Cadmium (Cd) (mg/L)	<0.00010
Calcium (Ca) (mg/L)	15.7
Chromium (Cr) (mg/L)	<0.0050
Cobalt (Co) (mg/L)	0.0022
Copper (Cu) (mg/L)	0.0021
Iron (Fe) (mg/L)	<0.10
Lead (Pb) (mg/L)	<0.00050
Lithium (Li) (mg/L)	0.140
Magnesium (Mg) (mg/L)	14.4
Manganese (Mn) (mg/L)	0.0205
Molybdenum (Mo) (mg/L)	0.0613
Nickel (Ni) (mg/L)	0.0075
Phosphorus (P) (mg/L)	<0.50
Potassium (K) (mg/L)	15.6
Rubidium (Rb) (mg/L)	0.0144
Selenium (Se) (mg/L)	0.00056
Silicon (Si) (mg/L)	2.81
Silver (Ag) (mg/L)	<0.00050
Sodium (Na) (mg/L)	300
Strontium (Sr) (mg/L)	0.468
Sulfur (S) (mg/L)	71.0
Tellurium (Te) (mg/L)	<0.0020
Thallium (Tl) (mg/L)	<0.00010
Thorium (Th) (mg/L)	<0.0010
Tin (Sn) (mg/L)	<0.0010
Titanium (Ti) (mg/L)	<0.0030
Tungsten (W) (mg/L)	0.0047
Uranium (U) (mg/L)	0.00376
Vanadium (V) (mg/L)	<0.0050
Zinc (Zn) (mg/L)	<0.010

Zirconium (Zr) (mg/L)	<0.0030

[a]AEO = acid extractable organics, measured by FTIR and quantified using a calibration curve prepared from a commercial naphthenic acid mixture, described previously.[205]

5.3.2 Magnetic Flocculant Synthesis

α-Fe_2O_3 ellipsoids were prepared by aging an aqueous solution of 20 mmol/L $FeCl_3$ and 0.2 mmol/L NaH_2PO_4 at 105 °C for 50 h,[206] washing the product thrice with deionized (DI) water, once with 1 mol/L NH_3, and thrice again with water by centrifugation. The α-Fe_2O_3 ellipsoids were then coated with silica using a modified Stöber process.[207,208] The α-Fe_2O_3 powder was dispersed into a solution of EtOH and DI water by probe sonication. NH_4OH was then added to the dispersion, followed by the dropwise addition of 1 mol/L TEOS in EtOH solution over 1 h, under vigorous mechanical stirring, such that the final concentrations of reagents were 25 mmol/L TEOS, 0.3 mol/L NH_3, 12 mol/L H_2O, and 1.5 g/L α-Fe_2O_3. This mixture was then stirred at room temperature for 18 h, after which the product (α-Fe_2O_3@SiO_2) was washed thrice with EtOH by centrifugation. The α-Fe_2O_3@SiO_2 powder was then reduced in a tube furnace at 350 °C under 100 cm^3/min of 50% H_2 in Ar for 6 h, washing the product (Fe_3O_4@SiO_2) thoroughly with DI water by magnetic decantation. The Fe_3O_4@SiO_2 particles were then coated with flocculant polymers using a layer-by-layer (LbL) technique.[209,210] The Fe_3O_4@SiO_2 powder was dispersed into a pH 12 NaOH aqueous solution by probe sonication, to which a 1 g/L PDADMAC aqueous saline solution (0.5 mol/L NaCl) was added under vigorous mechanical stirring, such that the final concentrations of reagents were 0.5 g/L PDADMAC, 0.25 mol/L NaCl, and 5 g/L Fe_3O_4@SiO_2. The mixture was gently stirred for 20 min, after which the particles were washed thrice with DI water by magnetic decantation, and resuspended into DI water by probe sonication (1st layer PDADMAC). A 1 g/L PSS aqueous saline solution (0.5 mol/L NaCl) was then added under vigorous mechanical stirring, such that the final concentrations of reagents were 0.5 g/L PSS, 0.25 mol/L NaCl, and 5 g/L Fe_3O_4@SiO_2. The mixture was gently stirred for 20 min, after which the particles were washed thrice with DI water by magnetic decantation, and resuspended into DI water by probe sonication (2nd layer PSS). A 1 g/L PDADMAC aqueous saline solution (0.5 mol/L NaCl) was then added under vigorous mechanical stirring, such that the final concentrations of reagents were 0.5 g/L PDADMAC, 0.25 mol/L NaCl, and 5 g/L Fe_3O_4@SiO_2. The mixture was gently stirred for 20 min, after which the particles were washed thrice with DI water by magnetic decantation, and resuspended into DI water by probe sonication (3rd layer PDADMAC). These three-layer coated particles (PDADMAC, PSS, PDADMAC), referred to as Fe_3O_4@SiO_2@PDADMAC, were used as a base to prepare the other magnetic flocculant formulations. A fourth layer was coated to prepare each of Fe_3O_4@SiO_2@PSS and Fe_3O_4@SiO_2@PAA formulations: either a 1 g/L PAA or PSS aqueous saline solution (0.5 mol/L NaCl) was added under vigorous mechanical stirring, such that the final concentrations of reagents were 0.5 g/L PAA or PSS, 0.25 mol/L NaCl, and 5 g/L Fe_3O_4@SiO_2. The mixture was gently stirred for 20 min, after which the particles were washed

thrice with DI water by magnetic decantation, and resuspended into DI water by probe sonication (4th layer PAA or PSS). A fifth layer was coated on Fe_3O_4@SiO_2@PSS particles to prepare the Fe_3O_4@SiO_2@CS: a 1 g/L CS aqueous saline solution (0.5 mol/L NaCl in 1 wt. % acetic acid) was added under vigorous mechanical stirring, such that the final concentrations of reagents were 0.5 g/L CS, 0.25 mol/L NaCl, 0.5 wt. % acetic acid, and 5 g/L Fe_3O_4@SiO_2. The mixture was gently stirred for 20 min, after which the particles were washed thrice with DI water by magnetic decantation, and resuspended into DI water by probe sonication (5th layer CS). In all cases, the polymer designated in the sample name refers to the terminal or outermost polymer layer.

5.3.3 Metallic Nanoparticle Synthesis

Citrate-stabilized Au nanoparticles were prepared reductively at room temperature.[211–213] 60 μL of freshly prepared, ice-cold 0.1 mol/L $NaBH_4$ were added to an aqueous solution of 2.5 x 10^{-4} mol/L $HAuCl_4 \cdot xH_2O$ and 10^{-4} mol/L trisodium citrate dihydrate under vigorous stirring, and left overnight. Then, the solution was filtered using a 0.2 μm syringe filter and stored in the dark at 4 °C until use. CTAB stabilized Ag nanoparticles were prepared by dropwise addition of an aqueous solution of 8 mmol/L $NaBH_4$ and 0.5 mmol/L CTAB to an equal volume of a 2 mmol/L $AgNO_3$, 0.4 mol/L NH_3, and 0.5 mmol/L CTAB aqueous solution under vigorous stirring in an ice bath, followed by stirring for 4 h, and then heating the solution at 90 °C for 1 h.[214,215] PVP stabilized Pd nanoparticles were prepared by simultaneously injecting 3 mL of a 0.157 mol/L K_2PdCl_4 solution in EG and 3 mL of a 26.67 g/L solution of PVP in EG each at 45 mL/h into 5 mL of EG at 110 °C under vigorous stirring, reacting at 110 °C for 3 h, and washing the product once with acetone and thrice with EtOH, by centrifugation, before resuspending into DI water.[216] PVP stabilized Pt nanoparticles were prepared by adding 1 mL of a $H_2PtCl_6 \cdot 6H_2O$ solution in EG to 7 mL of a solution of $NaNO_3$ and PVP in EG at 160 °C under vigorous stirring, such that the final concentrations of reagents were 10 mmol/L H_2PtCl_6, 33 mmol/L $NaNO_3$, and 3.33 g/L PVP.[217] The solution was stirred at 160 °C for 15 min, followed by washing the product once with acetone and thrice with EtOH by centrifugation before resuspending the into DI water.

5.3.4 Flocculation Experiments

The flocculation experiments were performed in triplicate in glass vials. TiO_2 nanoparticle powder was dispersed into DI water by probe sonication at a typical concentration of 100 mg/L. A sonicated suspension of magnetic flocculant (10 g/L) was rapidly added to the TiO_2 suspension, which was then rapidly mixed for 60 s by vortex mixing, followed by 20 min of slow mixing at 25 rpm on a rotary mixer. The mixture was then settled over an Nd rare earth block magnet (5.08 x 5.08 x 2.54 cm l x w x h) for 30 min, and the supernatant sampled to determine remaining TiO_2 concentration in suspension. Following separation of the supernatant by magnetic decantation, the settled flocs were dispersed into an equal volume of aqueous HCl solution (typically pH 2.5), and sonicated for 20 min to induce deflocculation. The magnetic flocculant particles were then magnetically settled for 30 min as above, and the supernatant TiO_2 suspension separated by magnetic decantation for reuse in another flocculation cycle, following neutralization to pH 7 with NaOH. A control TiO_2 suspension, without addition of magnetic

flocculant, was run alongside each experiment according to the same conditions, and relative TiO_2 concentrations in the flocculated samples were calculated in comparison to this control.

In one experiment, to study the effect of pH, the flocculation tests were performed in 10 mmol/L phosphate or carbonate buffer instead of DI water. In another experiment, to study recyclability of the system, the flocculation tests were performed in PTFE beakers instead of vials, and the same set of TiO_2 nanoparticles and magnetic flocculant nanoparticles were reused continuously throughout the experiment.

TiO_2 nanoparticle concentrations were determined by UV/Vis spectroscopy at 250 nm, comparing to calibration curves prepared from TiO_2 suspensions of known concentration (Figure 37 and Table 14). In the case that the measured absorbance at 250 nm was >1.5, the absorbance at 350 or 400 nm was used instead. In one experiment, to measure the nanoparticle residual after flocculation, TiO_2 concentrations were instead determined ICPMS of total Ti (EPA method 200.8, limit of detection 3 µg/L Ti) by ALS Environmental (Waterloo, ON, Canada), comparing to a calibration curve prepared from TiO_2 suspensions of known concentration (Figure 38). This method was also used to measure TiO_2 concentrations in the recyclability study (Figure 59a).

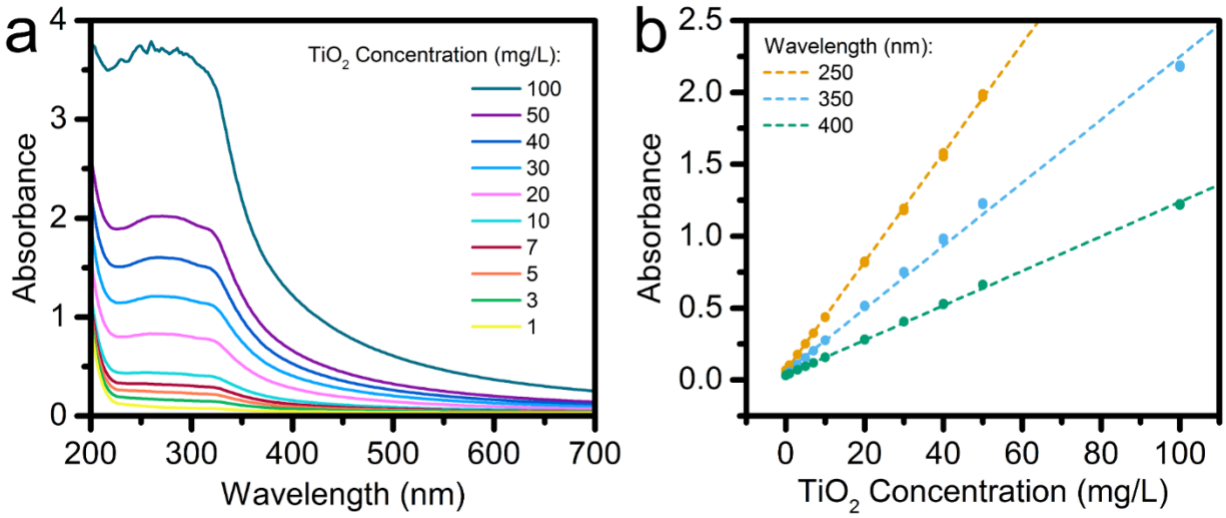

Figure 37. (a) UV/Vis spectra of TiO_2 nanoparticle aqueous suspensions and (b) calibration curves prepared from the spectra in (a).

Table 14. Regression parameters of the UV/Vis calibration curves used to determine TiO_2 concentration.

	250 nm	**350 nm**	**400 nm**
Slope x 10^3 (L/mg)	37.94 ± 0.10	21.95 ± 0.21	12.02 ± 0.06

Intercept x 10^3	62.44 ± 2.08	54.63 ± 7.18	36.79 ± 2.02
Limit of Detection (mg/L)	0.16	0.98	0.50
Limit of Quantification (mg/L)	0.55	3.27	1.68

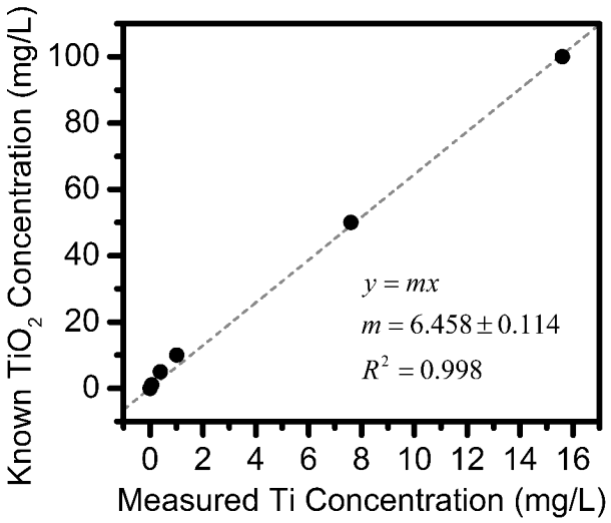

Figure 38. Calibration curve relating TiO_2 nanoparticle concentration to total Ti measured by ICPMS.

5.3.5 Photocatalytic Treatment Experiments

The OSPW photocatalytic treatment experiment was performed in a custom photoreactor enclosure described previously,[205] consisting of an array of UVA fluorescent bulbs (Philips F20T12/BL, peak emission ~350 nm, Figure 18) suspended above the samples. The UV intensity was measured to be ~45 W/m^2 with a UVA/B light meter (Sper Scientific, NIST certified calibration), which is similar to the UV content of the solar spectrum (ASTM G173-03 global tilt). TiO_2 nanoparticles were stirred into 80 mL of OSPW (0.1 g/L) in a borosilicate glass beaker (46 mm diameter) and dispersed by sonication. The beaker was sealed with polyethylene film (Glad, measured to be UV transparent by spectrophotometry) to prevent evaporation during the experiment, and its sides were wrapped with Al foil. The mixture was stirred in the dark for 1 h to attain adsorption-desorption equilibrium of organics with the TiO_2 surface, and then placed in the photoreactor and exposed to UV light while stirring, with 1 mL aliquots sampled periodically for measurement of NA concentration, which were subsequently returned to the beaker.

The FGDW photocatalytic treatment experiment was performed in a custom photoreactor enclosure consisting of an array of UVC fluorescent bulbs (Sani-Ray RRDHO36-4, peak emission ~254 nm) suspended above the samples. The UV intensity was measured to be ~16 W/m^2 with a UVC light meter (Sper Scientific, NIST certified calibration) at the surface of the

water within the reaction chamber through the quartz window. TiO_2 nanoparticles were stirred into 350 mL of FGDW (0.2 g/L) in a polytetrafluoroethylene (PTFE) beaker (76 mm diameter) along with 300 ppm formic acid to act as an electron hole scavenger for the reduction reaction. The beaker was sealed in an air tight stainless steel vessel with a quartz window to prevent exposure to oxygen during the experiment, while N_2 gas was purged throughout the reaction to remove any H_2Se gas generation which was flowed through two subsequent liquid scrubbers of $CuSO_4$ and NaOH, respectively.[218,219] The mixture was stirred in the dark for 1 h to attain adsorption-desorption equilibrium of inorganics with the TiO_2 surface, and then placed in the photoreactor and exposed to UV light while stirring, with 5 mL aliquots sampled periodically for measurement of Se concentration, which were centrifuged so the TiO_2 could be returned to the beaker at the end of the experiment.

For both the OSPW and FGDW experiments, following the UV treatment, the TiO_2 suspension was separated by magnetic flocculation and deflocculated as described above, using Fe_3O_4@SiO_2@PDADMAC particles (at 0.316 g/L) as the MF, and stirring at 120 rpm and 15 rpm with a mechanical stirrer for the flash and slow mix periods respectively. The recovered TiO_2 was then dispersed into a fresh sample of either OSPW or FGDW for a subsequent cycle of photocatalytic treatment.

Naphthenic acid fraction extractable organics (NAs) concentrations were determined by UV/Vis spectroscopy at 220 nm,[220] comparing to a calibration curve prepared from NAs extracted from the same OSPW sample. Briefly, OSPW was adjusted to pH 10.5 with NH_4OH, extracted thrice with DCM (in total 1:2 solvent to sample volumetric ratio), acidified to pH 7 with H_2SO_4, extracted thrice with DCM, and finally acidified to pH 2 with H_2SO_4, and extracted thrice with DCM. The acidic, neutral, and basic DCM extracts were then combined, and dried under N_2. While naphthenic acids are defined by the classic formula $C_nH_{2n+z}O_2$ (where *z* is a negative even integer related to the number of rings and double bonds), OSPW naphthenic acid fraction extractable organics (referred to as NAs herein) also contain a broad range of organics not conforming to this classic structure, including aromatic and heteroatom-containing acids, as well as basic and low polarity species.[114–116,64]

Selenium concentrations were determined using a hydride generation set-up (CETAC, HGX-200 Advanced Membrane Cold-Vapor and Hydride Generation System) prior to quantification using inductively coupled plasma optical emission spectroscopy (ICP-OES, Teledyne Leeman Prodigy). The samples were acid digested in 6M hydrochloric acid (HCl) and 0.2M nitric acid (HNO_3) by adding 3.9 mL of HCl and 0.1 mL HNO_3 to a 4 mL aqueous sample. Samples were then boiled for 30 minutes prior to hydride generation and analysed using ICP-OES to pre-reduce all selenate to selenite. The LOD of the above Se detection technique is 2 μg/L. The starting concentration of the FGDW, 300 ± 15 μg/L, was reduced past the detection limit for the first 4 cycles.

5.3.6 Materials Characterization

Particle size and structure was analyzed by TEM (Philips CM-10, 60 keV). The hydrodynamic diameter of the particles in water was measured by DLS (Brookhaven 90Plus Particle Size Analyzer, lognormal volume-weighted median diameter). Crystal phase was assessed by powder XRD (Bruker D8-Advance, Våntec-1 detector, 1.5405 Å Cu-Kα radiation). The magnetic properties of the powders were measured at 300 K with SQUID VSM (Quantum Design MPMS). The surface area of the particles (pre-dried at 200 °C in N_2) was calculated from the Brunauer–Emmett–Teller (BET) equation using data from N_2 adsorption isotherms obtained at 77 K (Micrometrics Gemini VII 2390 Surface Area Analyser). Zeta potential measurements were taken with a Malvern Zetasizer Nano ZS. FTIR spectra were obtained for powder samples in KBr pellets (Bruker Tensor 27). XPS was performed at room temperature (VG Scientific ESCALab 250, Al Kα radiation), and the binding energy scale was corrected by referencing the C 1s peak to 285 eV. TGA was performed at 10 °C/min in air (TA Instruments Q500). Photomicrographs of flocs were obtained using an optical microscope (Zeiss Axioskop with AxioCam ERc 5s camera).

5.4 Results and Discussion

To create recyclable flocculants for nanoparticle separation, the critical challenges involve deflocculation of separated flocs, and collection of the flocculant from the released nanoparticles for reuse. As flocculation processes are based on electrostatic surface interactions of polymer flocculants with suspended solids, deflocculation is possible provided either the flocculant or target solid is amphoteric, or that their isoelectric points differ, such that a pH shift can reverse charge polarity and thus induce a repulsive force to dissolve the flocs. It was hypothesized that flocculant recollection could be most conveniently accomplished by designing the flocculant to be magnetic.

Scheme 3 illustrates this concept of an entirely recyclable CF system using magnetic flocculants (MFs), in the example of photocatalytic water treatment using colloidal TiO_2. Following photocatalysis, TiO_2 nanoparticles are flocculated by addition of MF particles, settling the flocs either magnetically or gravitationally, to enable discharge of the treated water free of nanoparticles. In a smaller volume or sludge, the flocs can then be deflocculated by pH shift: given that TiO_2 is amphoteric with an isoelectric point of ~5.5 (negatively charged at neutral pH, Figure 39), and using MFs with a permanent positive charge, pH adjustment to below 5.5 induces electrostatic repulsion between the TiO_2 and MF, dissolving the flocs to form a dispersion of free TiO_2 and MF particles. Since TiO_2 is non-magnetic, the MFs can then be easily separated from this mixture by magnetic separation, and both the TiO_2 and MFs can be recycled in the process (following pH reneutralization).

Scheme 3. Process for recycling TiO_2 nanoparticles with reusable magnetic flocculants for photocatalytic water treatment: (a) photocatalytic treatment of contaminated water with a TiO_2

nanoparticle slurry, (b) flocculation with magnetic flocculants following treatment, (c) magnetic separation of flocs and discharge of treated water, (d) deflocculation to release the nanoparticles, and (e) magnetic separation of flocculants, for recycling of both the TiO_2 and flocculants.

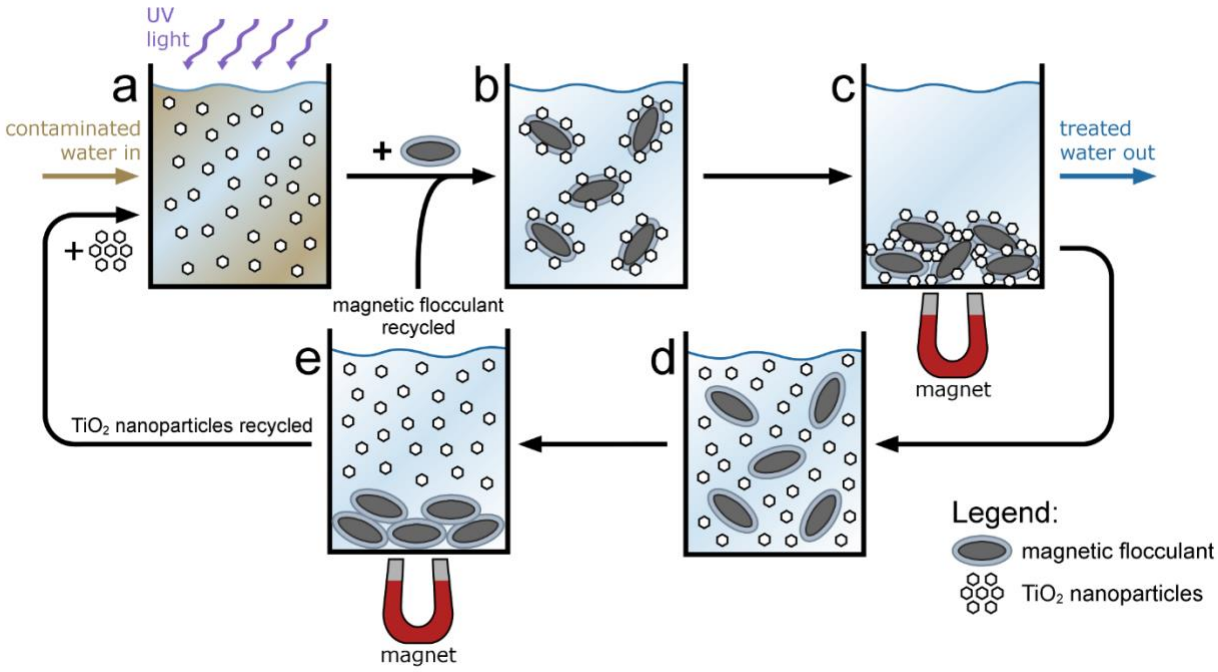

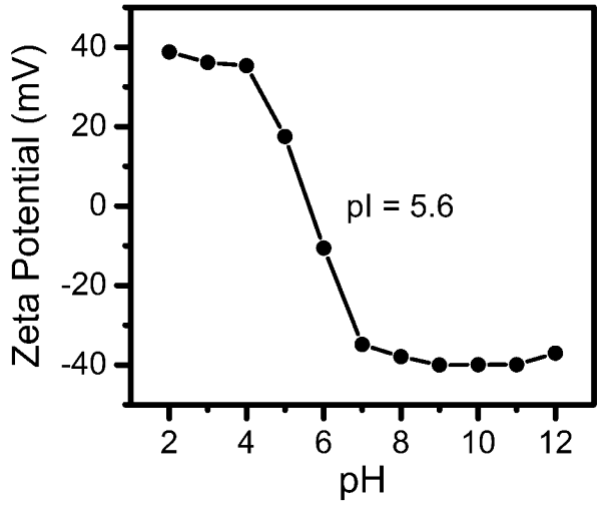

Figure 39. Zeta potential of aqueous TiO_2 nanoparticle suspensions as a function of pH, where pI is the isoelectric point.

5.4.1 Magnetic flocculant synthesis and characterization

The MF particles were synthesized according to the process indicated in Figure 40a. Hematite ellipsoids were synthesized according to an aqueous precipitation process, and encapsulated with a silica shell to serve as a protective barrier against oxidation and dissolution of the magnetic core during repeated flocculation cycles. The particles were then subjected to mild reduction in H_2 to convert the hematite cores to magnetite, rendering them magnetically responsive. This synthesis strategy was designed to produce polycrystalline Fe_3O_4 cores (to achieve high per-core magnetic moment while retaining superparamagnetism) starting from a clean, polymer-free iron oxide surface. These Fe_3O_4@SiO_2 ellipsoids were then coated with various flocculant polymers according to a layer-by-layer (LbL) process, a well-established technique to immobilize polyelectrolytes through strong multivalent ionic bonds.[209,210]

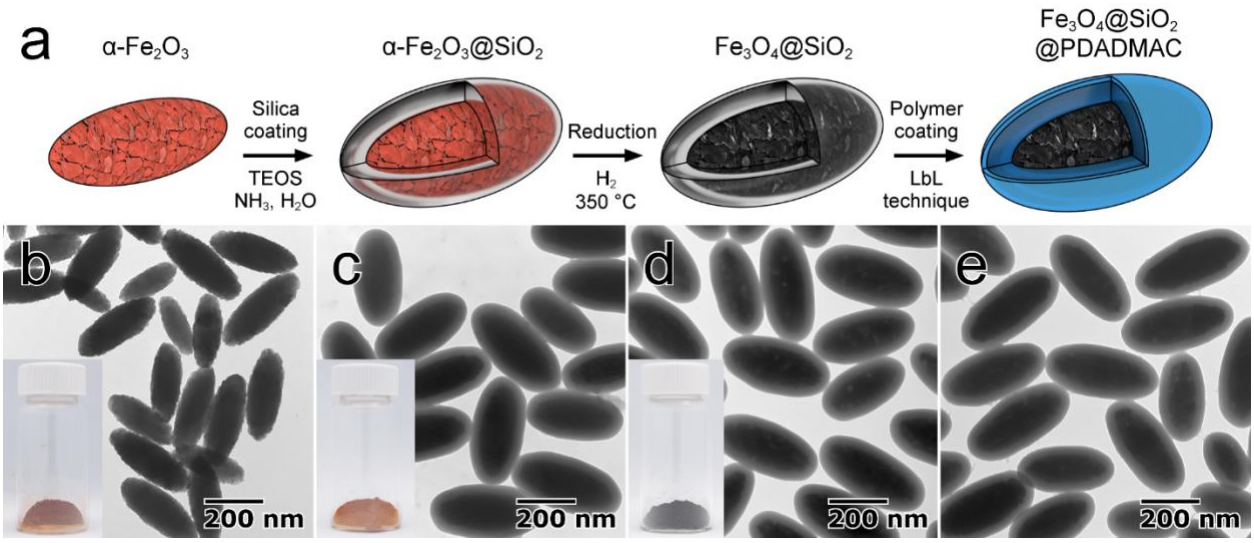

Figure 40. Synthesis process of MF particles (a) and TEM images taken at each stage: (b) α-Fe_2O_3 ellipsoids, (c) α-Fe_2O_3@SiO_2, (d) Fe_3O_4@SiO_2 and (e) Fe_3O_4@SiO_2@PDADMAC. Insets show photos of the sample appearance.

The particle structure was confirmed at each stage of the synthesis process by transmission electron microscopy (TEM) and dynamic light scattering (DLS) (Figure 40, Table 15). The close agreement of TEM and DLS measured diameters indicated the particles remained non-aggregated and monodispersed throughout the synthesis process. In the precipitation of the α-Fe_2O_3 ellipsoids, phosphate concentration controls both particle size and axial ratio (yielding an ellipsoidal structure),[206] therefore a particle size of ~115 nm diameter and ~290 nm length was selected to minimize final particle size and thus maximize specific surface area for flocculation, while simultaneously providing sufficient core volume to enable rapid magnetic separability.[48,221] The silica shell was measured to be ~33 nm thick, and provided a suitably charged surface for stable polymer binding.[222]

X-ray diffraction (XRD) confirmed complete conversion of α-Fe_2O_3 to polycrystalline Fe_3O_4 in the reduction step (Figure 41), with an average Fe_3O_4 crystal size of 14.9 nm calculated by the Scherrer formula from the (311) reflection. While this crystal size is well below the single domain threshold for magnetite (typically reported as ~30 nm),[223] below which particles are superparamagnetic at room temperature, magnetic measurements on the MFs revealed some hysteresis, and a remanence of 7.7 emu g^{-1} (Figure 42). Nevertheless, in practice the MFs in suspension behaved as though they were superparamagnetic, exhibiting a high saturation magnetization of 33.9 emu g^{-1} without magnetic aggregation in the absence of an applied field, presumably due to a balance of other colloidal forces.[52,42]

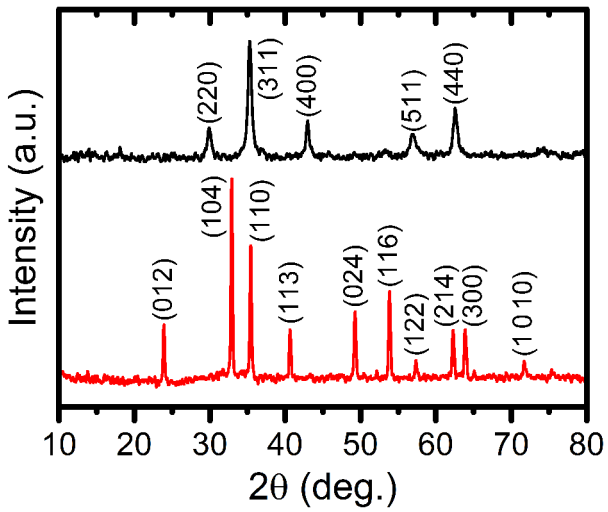

Figure 41. Powder XRD patterns of the α-Fe_2O_3@SiO_2 particles (lower), α-Fe_2O_3 indexed to JCPDS no. 33-0664, and the Fe_3O_4@SiO_2 particles (upper), Fe_3O_4 indexed to JCPDS no. 19-0629.

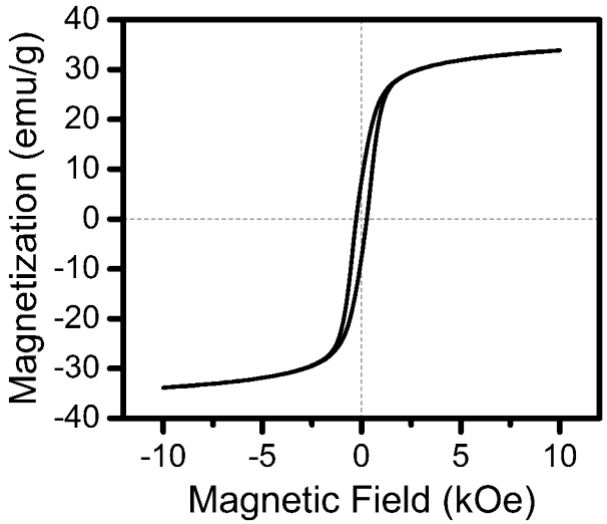

Figure 42. Magnetic hysteresis curve of the Fe_3O_4@SiO_2@PDADMAC particles at 300 K.

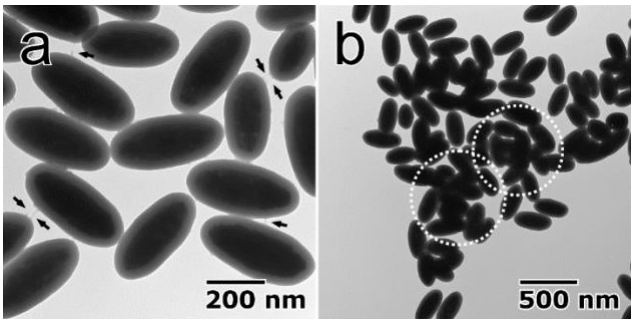

Figure 43. TEM images of (a) Fe_3O_4@SiO_2@PDADMAC particles, exhibiting strands as potential evidence of the polymeric coating, and (b) Fe_3O_4@SiO_2@CS particles exhibiting ~1 µm aggregates.

Several MF formulations were prepared by depositing different polymers as the outermost LbL layer, including poly(diallyldimethylammonium chloride) (PDADMAC) and chitosan (CS) as positively charged polyelectrolytes (PEs), and poly(sodium 4-styrenesulfonate) (PSS) and poly(acrylic acid) (PAA) as negatively charged PEs. These polymers have all been used as flocculants in conventional CF processes.[224] While the polymeric coatings were not clearly visible by TEM (Figure 40e, Figure 43a), an increase in the hydrodynamic diameter of the particles following PE coating possibly indicated swelling of the polymer shell in water (Table 15). The significantly larger hydrodynamic size of the CS-coated particles was the result of interparticle bridging in the LbL process (Figure 43b). Although the molecular weights of the polymers used to coat the particles were lower than those of flocculants typically used in water treatment, since multiple polymer chains were bound to each $Fe_3O_4@SiO_2$ core, it was hypothesized that the coated particles as a whole would behave as flocculants with a higher effective molecular weight, given their relatively large hydrodynamic volumes (Table 15). Indeed, the hydrodynamic volume of polymer flocculants in a random coil configuration is on the order of 100 nm.[224]

Table 15. Particle size and charge, measured by TEM, DLS and zeta potential.

	α-Fe_2O_3	**α-Fe_2O_3@SiO_2**	**Fe_3O_4@SiO_2**	**Fe_3O_4@SiO_2 @PDADMAC**	**Fe_3O_4@SiO_2 @PSS**	**Fe_3O_4@SiO_2 @PAA**	**Fe_3O_4@SiO_2 @CS**
Long axis mean (nm)	287 ± 49.1	351 ± 55.2	353 ± 57.3	359 ± 44.9			
Short axis mean (nm)	113 ± 16.9	176 ± 16.3	182 ± 18.6	178 ± 14.4			
Diameter of equivolume sphere (nm)[a]	154	221	227	225			
Hydrodynamic diameter (nm)	175	265.1	258.6	272	278.1	462	1180.3
Geometric standard deviation, σ_g	1.427	1.163	1.224	1.303	1.155	1.599	1.717
Zeta potential (mV)			-51.3	29.0 ± 3.48	-56.2 ± 5.53	-52.1 ± 3.97	-35.9 ± 4.87

[a]Calculated from ellipsoid volume according to the mean axis lengths measured by TEM.

Alternating polarity of the particles' surface charge was observed by zeta potential throughout the LbL coating process (Figure 44), characteristic of successful binding of each polymer layer,[210] although the charge density of CS was apparently insufficient to fully compensate the negative charge from the underlying PSS layer in the Fe_3O_4@SiO_2@CS sample. While Fourier transform infrared spectroscopy (FTIR) could not detect any specific functional groups associated with the PEs (Figure 45), X-ray photoelectron spectroscopy (XPS) of the Fe_3O_4@SiO_2@PDADMAC sample revealed the presence of nitrogen and sulfur (attributed to PDADMAC and PSS) and a significant increase in surface carbon content following the polymer coating (Figure 46). N and S were present at the particle surface in approximately equal concentration (3.93 and 3.49 atomic %, respectively), and no Na or Cl peaks were detected, indicating the PDADMAC and PSS layers were acting as counterions for each other as expected. Thermal gravimetric analysis (TGA) of the Fe_3O_4@SiO_2@PDADMAC particles revealed a mass loss of 1.52 wt.% at 600 °C attributed to burn off of the polymeric coating (Figure 47).

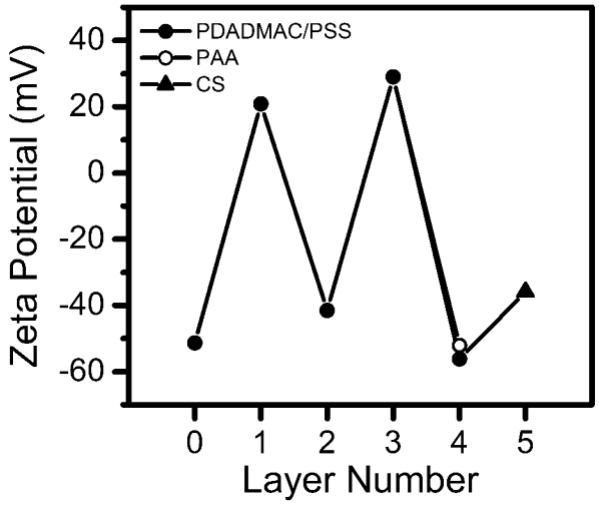

Figure 44. Zeta potential of aqueous suspensions of MF particles throughout the LbL coating process, where the positive potentials represent PDADMAC coatings.

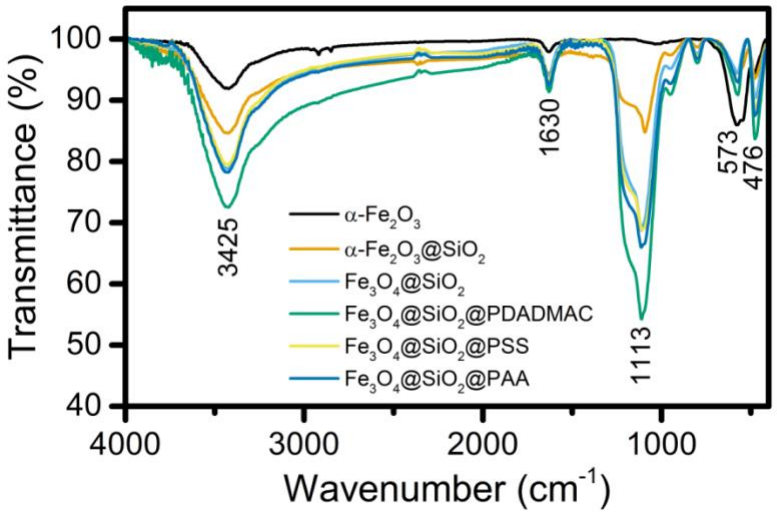

Figure 45. FTIR spectra of the particle formulations, where the 1113 cm^{-1} peak is characteristic of silica, and the 3425 cm^{-1} peak is attributed to hydroxyl groups.

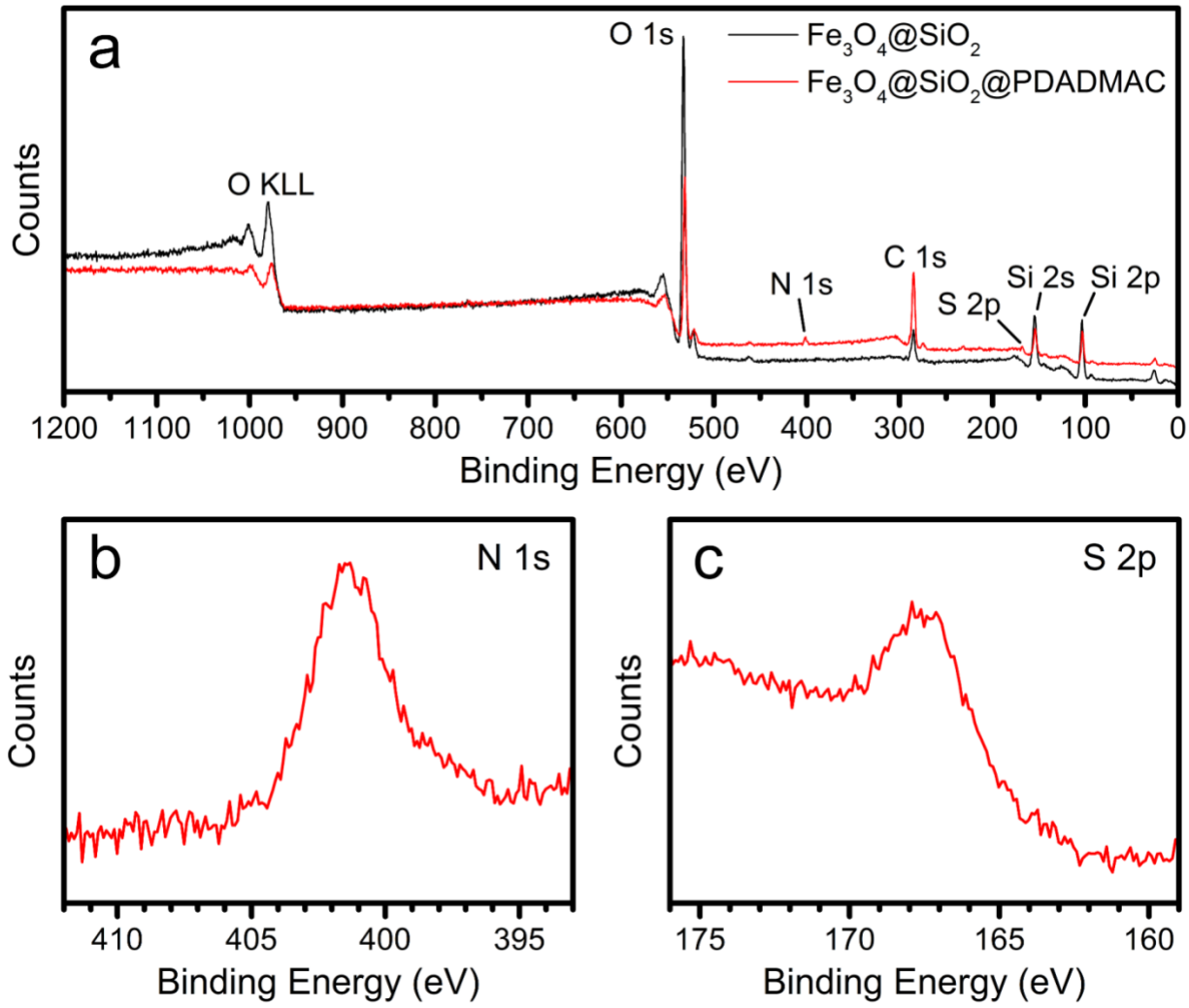

Figure 46. XPS (a) survey spectra of the Fe_3O_4@SiO_2 and Fe_3O_4@SiO_2@PDADMAC particles, as well as (b) N 1s and (c) S 2p narrow scan spectra of the Fe_3O_4@SiO_2@PDADMAC particles.

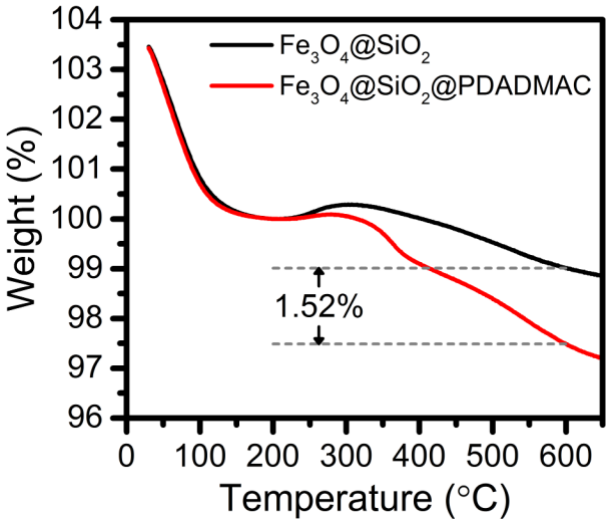

Figure 47. TGA curves of the Fe_3O_4@SiO_2 and Fe_3O_4@SiO_2@PDADMAC particles, with the weight of each sample normalized at 200 °C (weight loss below this temperature taken as water evaporation).

A BET surface area of 12.3 m^2 g^{-1} was calculated for the Fe_3O_4@SiO_2@PDADMAC particles by N_2 adsorption, which matched closely to the theoretical specific surface area of 9.8 m^2 g^{-1} as calculated geometrically from the TEM ellipsoidal dimensions, indicating the MF particles were relatively smooth and non-porous. Qualitatively, all of the MF samples readily formed aqueous colloidal dispersions, and were strongly magnetically responsive for easy recollection. Therefore the conclusion of the above materials characterization confirmed synthesis of MF particles with the intended structure.

5.4.2 Separation of TiO_2 nanoparticles by magnetic flocculants with different polymer coatings

The synthesized MF particles were subsequently assessed for flocculation performance toward TiO_2 nanoparticle recovery, where TiO_2 is a prominent photocatalyst researched for water decontamination, serving here as an example heterogeneous catalyst separation challenge. Since the flocculation performance of different polymers varies with respect to the suspended solid material, water matrix composition, and especially pH, several MF formulations (coated with the different polymers as described above) were tested for their ability to flocculate with TiO_2 nanoparticles (Aeroxide P25, Figure 48) and remove them from aqueous suspension across a range of pH values, the results of which are shown in Figure 49a.

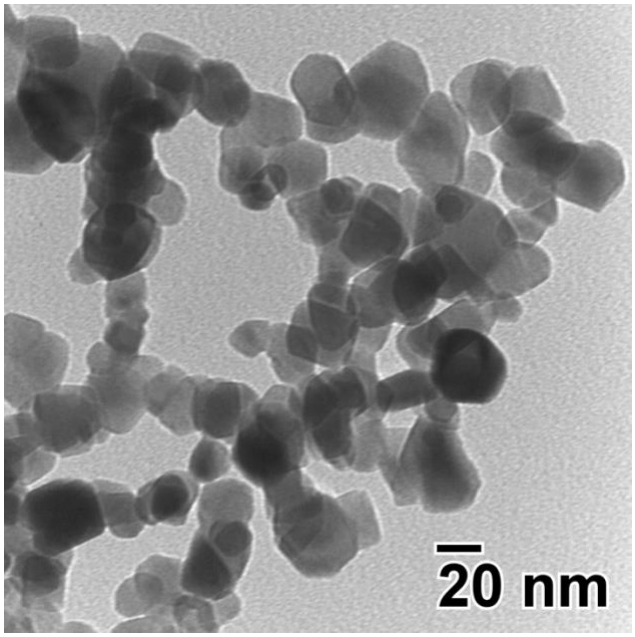

Figure 48. TEM image of the TiO_2 nanoparticles used in this work (Evonik Aeroxide P25). The mean primary particle diameter was measured to be 24.0 ± 7.1 nm (n = 121), and is reported by the manufacturer to be ~21 nm.

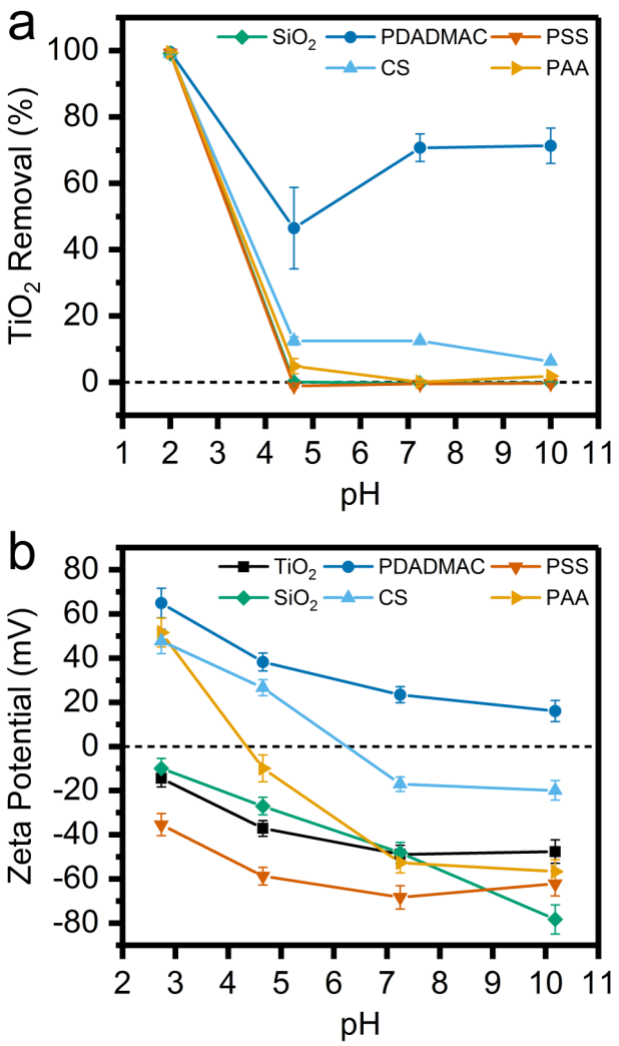

Figure 49. (a) Flocculation efficacy of MFs (0.1 g L^{-1}), coated with the different polymers indicated (SiO_2 refers to the uncoated Fe_3O_4@SiO_2 particles), toward separation of TiO_2 nanoparticles (0.1 g L^{-1} in 10 mmol L^{-1} aqueous buffers), and (b) zeta potentials of the particles in the same conditions.

A large difference was observed between the MF formulations, with the Fe_3O_4@SiO_2@PDADMAC particles removing a significant fraction of the TiO_2 nanoparticles at all pH values, while the CS coated particles exhibited only ~12% removal, and the uncoated and PAA and PSS coated particles minimally interacted with the TiO_2 above pH 4. The TiO_2 suspension was observed to be colloidally unstable at pH 2, and therefore all MF particles non-specifically facilitated TiO_2 settling. These results confirmed that, at least for the PDADMAC coated MFs, the bound polymers were still sufficiently accessible to interact with suspended nanoparticles to enable magnetic separation. Furthermore, the superior performance of the

cationic polymer coated MFs over the negatively charged samples suggested an electrostatic interaction with the TiO_2, the same mechanism by which PEs interact with suspended solids in conventional CF.[192,224] Therefore, the zeta potential of the particles was studied as a function of pH (Figure 49b).

In buffer, the TiO_2 nanoparticles possessed a negative zeta potential across the pH range, while the Fe_3O_4@SiO_2@PDADMAC particles, the most effective MFs, were the only formulation with a constant positive charge, supporting electrostatic attraction as the mechanism of interaction. The Fe_3O_4@SiO_2 particles and PAA and PSS coated MFs exhibited negative zeta potential above pH 4, thus presumably electrostatically repelling the suspended TiO_2. Colloidal instability of the TiO_2 nanoparticles near their isoelectric point (shifted to lower pH in phosphate buffer) accounted for their easy separability by all MF samples at pH 2. Thus as in conventional CF, the relative charge of the flocculant with respect to the suspended solid was a critical factor to enable separation.

5.4.3 Magnetic flocculation of metallic nanoparticle suspensions

To further investigate the zeta potential dependence and specificity of the flocculation process, the MF particles were tested for their ability to remove other types of colloidal nanoparticles from suspension: citrate stabilized Au, hexadecyltrimethylammonium bromide (CTAB) stabilized Ag, poly(vinylpyrrolidone) (PVP) stabilized Pd, and PVP stabilized Pt (Figure 50a). These nanomaterials also represent practically important targets for magnetic separation, with applications in plasmonic photocatalysis,[225,226] water treatment,[227,228] and environmental analysis.[229] Furthermore, controlling environmental release of Ag nanoparticles is a significant concern for wastewater treatment plants.[230–232] PDADMAC and PSS coated MFs, as positively and negatively charged particles, were compared against each type of nanoparticle. The Fe_3O_4@SiO_2@PDADMAC particles demonstrated excellent separation of the negatively charged Au, Pd, and Pt nanoparticles (Figure 50b), while similarly as with TiO_2, the Fe_3O_4@SiO_2@PSS MFs exhibited minimal interaction with these suspensions. Notably however, the PSS coated MFs were efficient at separating cationic Ag nanoparticles, while the PDADMAC MFs failed in this system (Figure 51), thus providing further evidence of the electrostatic interaction mechanism. Furthermore, since aqueous nanoparticle colloidal dispersions frequently possess a surface charge for electrostatic stabilization, these results demonstrate that magnetic flocculation could serve as a general method for nanoparticle separation.

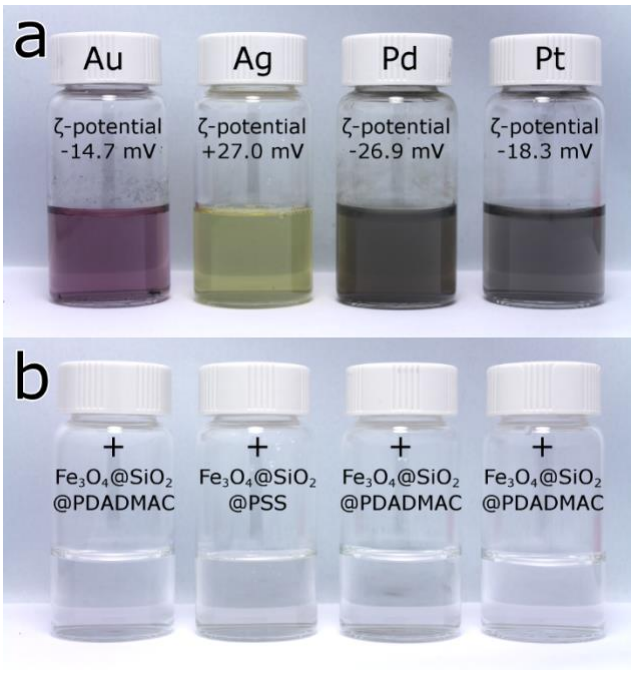

Figure 50. Photos of Au, Ag, Pd, and Pt nanoparticle aqueous suspensions, with zeta potentials indicated, (a) before and (b) after separation by magnetic flocculation with the MF particles indicated (added at 0.316 g L^{-1}).

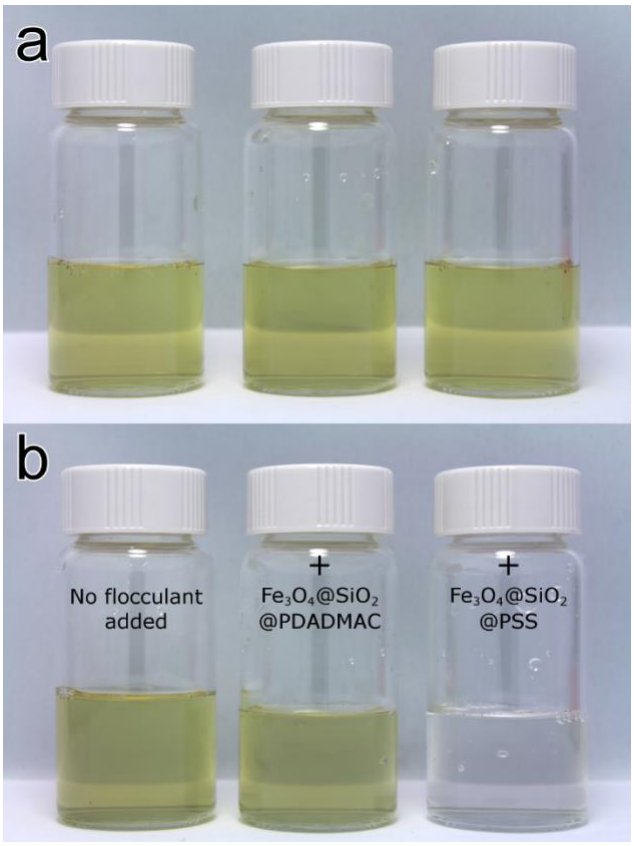

Figure 51. Photos of CTAB stabilized Ag nanoparticle aqueous suspensions (a) before and (b) after separation by magnetic flocculation with the MF particles indicated (added at 0.316 g L^{-1}).

5.4.4 Concentration dependence of nanoparticle separation performance

The success of conventional CF processes for water clarification typically exhibits a strong concentration dependence, where selecting the correct flocculant dose for optimal separation of a given suspended solids concentration represents a significant challenge faced by water treatment operators. Therefore a factorial study was used to investigate the separation efficacy of magnetic flocculation at different concentrations of both TiO_2 and PDADMAC coated MF particles (Figure 52), where the TiO_2 concentration range studied (≤1 g L^{-1}) is typical of photocatalytic applications.

Increasing the concentration of MF particles added to the suspensions (C_{MF}) increased the TiO_2 removal percentage, to ~100% at C_{MF} >300 mg L^{-1}, thereby indicating that the incomplete separation achieved by the Fe_3O_4@SiO_2@PDADMAC particles in the initial study (Figure 49a) was simply the result of an unoptimized MF:TiO_2 ratio. At low MF concentrations, a valley was observed in the response, with high TiO_2 separation achieved at both low and high TiO_2

concentrations (C_{TiO2}), but poor recovery attained at intermediate C_{TiO2}. To interpret this result, it was hypothesized that at low C_{TiO2}, the ratio of MF particles was sufficient to bind and remove the majority of the TiO_2, while increasing C_{TiO2} overwhelmed the MF surface area available for nanoparticle attachment, and at high C_{TiO2} of ~1 g L^{-1} the TiO_2 nanoparticles were suspended as micron scale aggregates rather than individually dispersed nanoparticles,[27] and thus susceptible sweep flocculation at even low C_{MF}. Finally, the ~100% removal achieved at even a high MF:TiO_2 ratio is an important result, as this contrasts with the behaviour of conventional flocculant polymers, where polymer overdosing can electrosterically re-stabilize suspended particles and reduce separation efficiency; thus determining optimal polymer concentration is a critical implementation challenge for conventional flocculants.[191,192,224] The MF particles do not appear to exhibit this overdosing issue, since no matter the configuration by which they bind the suspended nanoparticles, magnetic separation is enabled.

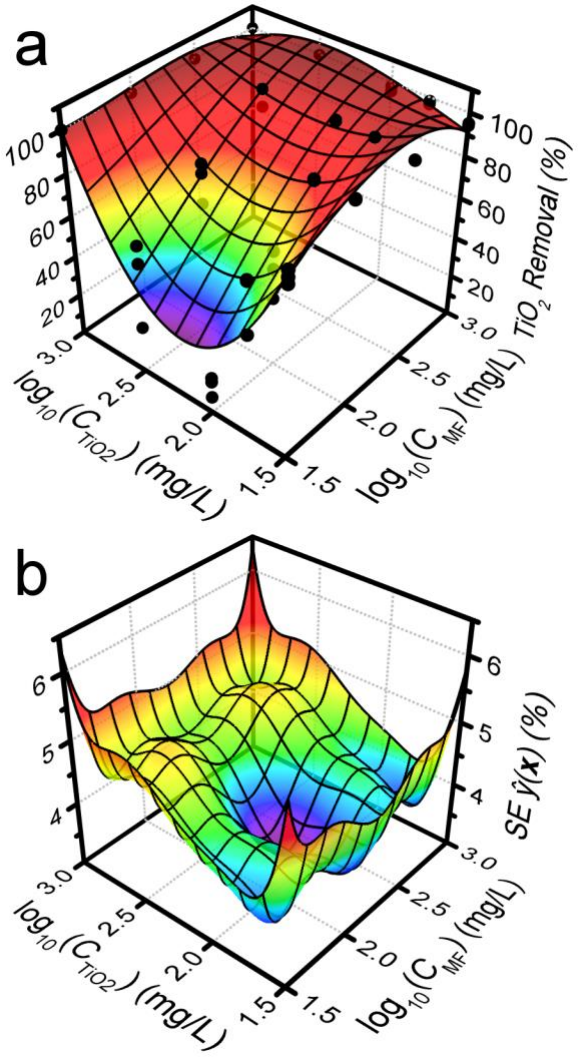

Figure 52. (a) Third order response surface fit ($\hat{y}$) of TiO_2 nanoparticle recovery by magnetic flocculation, as a function of the concentration of TiO_2 (C_{TiO2}) and Fe_3O_4@SiO_2@PDADMAC particles (C_{MF}), and (b) the corresponding standard error of the estimated response.

Following magnetic flocculation, inductively coupled plasma mass spectrometry (ICPMS) was used to measure trace residual TiO_2 nanoparticles remaining in suspension at concentrations below the detection limits of UV/Vis spectroscopy (Figure 53). Fe_3O_4@SiO_2@PDADMAC particles, added at 316 mg L^{-1} to 100 mg L^{-1} TiO_2, reduced the TiO_2 nanoparticle concentration to 0.52 mg L^{-1}. Subsequent passes of MF particles were therefore investigated for removal of this nanoparticle residual, and it was found that a second round of flocculation was sufficient to reduce TiO_2 concentration to below the ICPMS detection limit (3 µg L^{-1} Ti). While further study is required to probe even lower detection limits, magnetic flocculation apparently provides

logarithmic reduction in suspended particle concentration, and the process is effective at separating ultra-low nanoparticle concentrations.

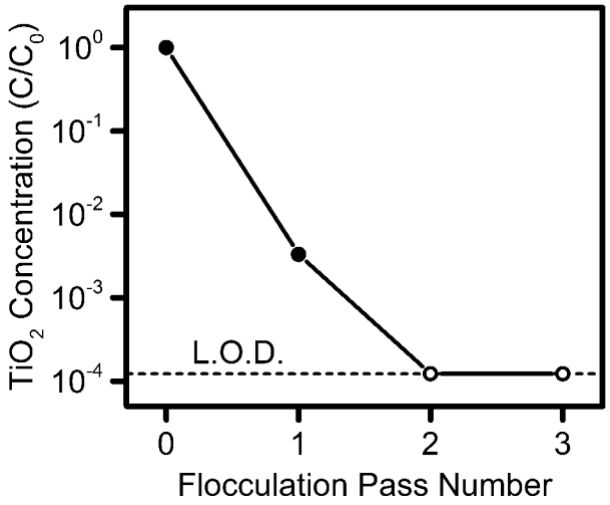

Figure 53. Relative TiO_2 concentration remaining in suspension after sequential magnetic flocculation passes of Fe_3O_4@SiO_2@PDADMAC particles (added at 316 mg L^{-1}). LOD refers to the ICPMS limit of detection.

The flocculation efficacy of the Fe_3O_4@SiO_2@PDADMAC particles was compared to freely dissolved polymeric PDADMAC (Figure 54). At low concentrations (<0.5 mg L^{-1}), the free polymer was more efficient than the MFs at nanoparticle separation, presumably since in the MF formulation a large fraction of the PDADMAC quaternary ammonium groups were already consumed through binding to the MF surface, which may have also constricted PDADMAC conformational configurations and rendered it less available for nanoparticle interaction. Provided at sufficient concentration however, the MFs matched the performance of free PDADMAC to achieve high TiO_2 removal rates, while the free polymer exhibited a prominent overdosing and re-stabilization effect at higher concentrations.

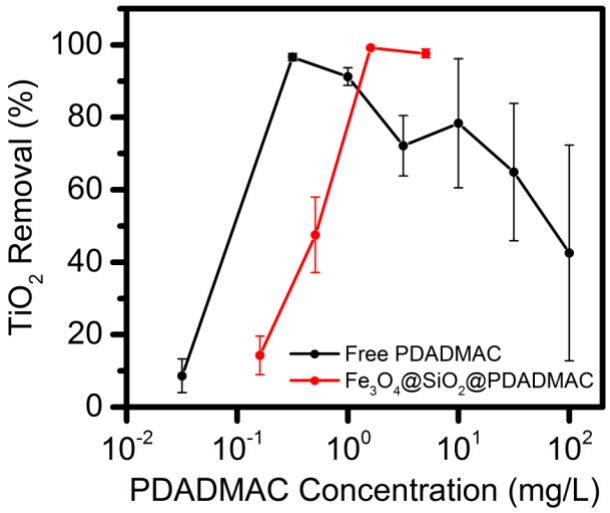

Figure 54. Flocculation efficacy of free polymeric PDADMAC compared to PDADMAC bound on Fe_3O_4@SiO_2@PDADMAC MFs, toward separation of TiO_2 nanoparticles (0.1 g L^{-1}). The concentration of PDADMAC in the MF sample was calculated from the mass fraction of the terminal PDADMAC layer, taken as one third of the total polymer coating mass measured by TGA, *i.e.*, 0.51 wt.%.

5.4.5 Microscopic observation of floc structure

Although the magnetic separation process of nanoparticle suspensions qualitatively appeared to follow a flocculation mechanism, the mixtures were analyzed microscopically to study the interparticle interactions and aggregate structures (Figure 55). Large aggregates >10 µm in size were observed at $C_{MF} \geq 100$ mg L^{-1}, which increased in both size and density with increasing MF concentration, confirming the magnetic separation proceeded by flocculation. A benefit of forming such large flocs is that they can be rapidly magnetically collected (within seconds), another advantage of magnetic flocculation over the relatively slow gravitational settling provided with conventional CF. Only small aggregates <3 µm in size were observed at $C_{MF} = 32$ mg L^{-1} (Figure 55a&b), suggesting nanoparticle adsorption to the MF surface may also be a process occurring at low MF:TiO_2 mass ratios.

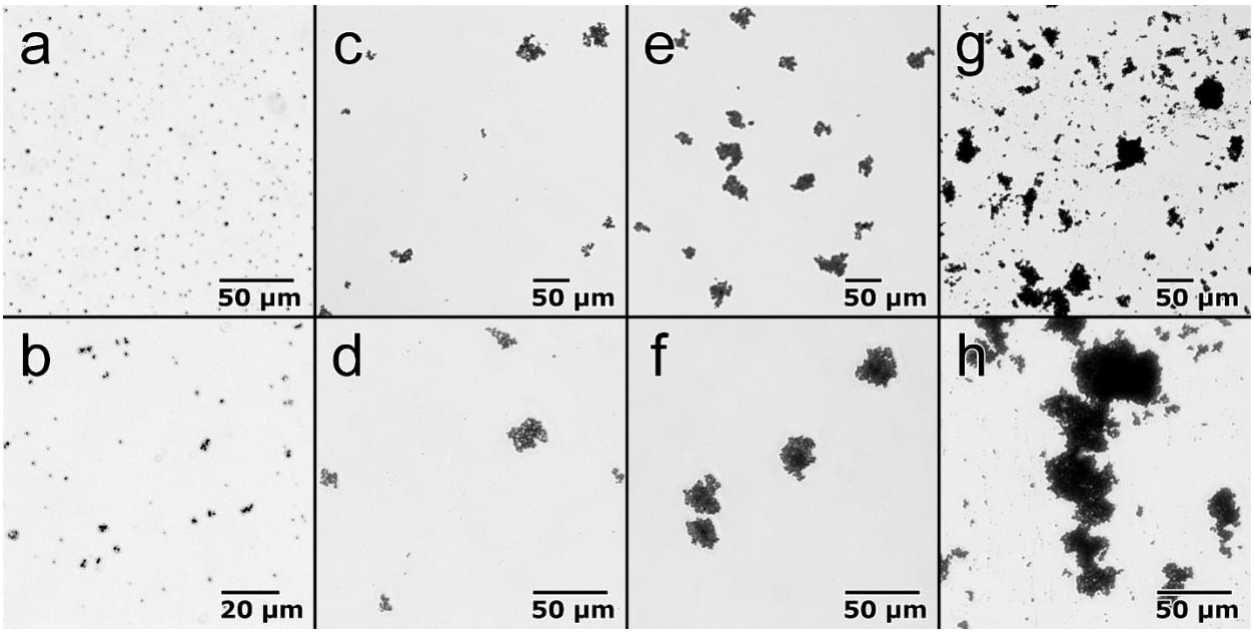

Figure 55. Optical micrographs of flocs formed in TiO_2 nanoparticle suspensions (0.1 g L^{-1}) following addition of Fe_3O_4@SiO_2@PDADMAC particles at different concentrations: (a) & (b) 31.6 mg L^{-1}, (c) & (d) 100 mg L^{-1}, (e) & (f) 316 mg L^{-1}, and (g) & (h) 1 g L^{-1}.

Floc structure was also observed by TEM. At low C_{MF}, significant quantities of free unbound TiO_2 was observed (Figure 56a&b), correlating with the low TiO_2 recovery measured in this condition (Figure 49). In contrast, at $C_{MF} \geq 316$ mg L^{-1}, associated with ~100% recovery, TiO_2 nanoparticles were completely encompassed by a network of MF particles (Figure 56e-h). From these observations, it is hypothesized that magnetic flocculation efficiency is associated with particle surface area ratios, where the threshold C_{MF} for complete nanoparticle separation occurs when the surface area of the MFs and suspended nanoparticles are approximately equal (*e.g.*, at C_{TiO2} = 100 mg L^{-1}, this threshold $C_{MF} \approx 316$ mg L^{-1}, corresponding to surface areas of 5.5 and 3.9 m^2 L^{-1} for the TiO_2 and MF particles, respectively). This theory may provide a useful basis for adapting magnetic flocculation to other nanoparticle systems.

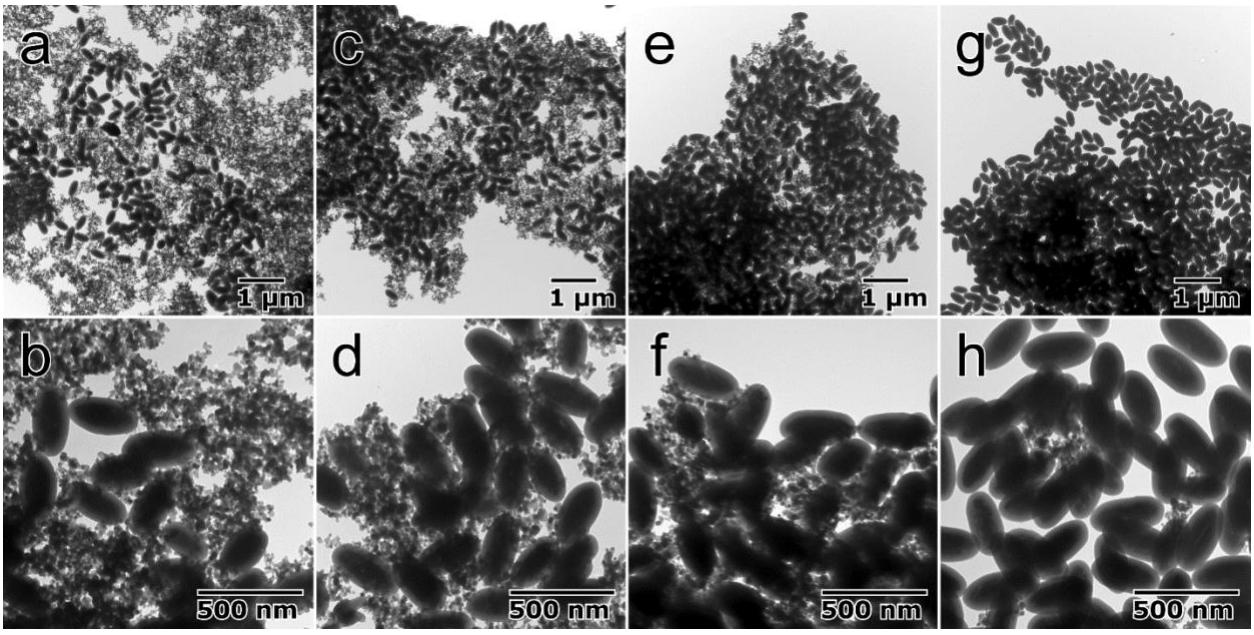

Figure 56. TEM images of flocs formed in TiO_2 nanoparticle suspensions (0.1 g L^{-1}) following addition of Fe_3O_4@SiO_2@PDADMAC particles at different concentrations: (a) & (b) 31.6 mg L^{-1}, (c) & (d) 100 mg L^{-1}, (e) & (f) 316 mg L^{-1}, and (g) & (h) 1 g L^{-1}.

5.4.6 Deflocculation and flocculant recycling

Since the above experiments indicated an electrostatic mechanism of flocculation, pH shift was investigated as a deflocculation mechanism to release nanoparticles from separated flocs. While the TiO_2 and the Fe_3O_4@SiO_2@PDADMAC particles possessed opposite surface charge at neutral pH, resulting in flocculation, below its isoelectric point TiO_2 takes on a positive charge (Figure 39), which was expected to induce electrostatic repulsion towards the MF particles leading to floc disintegration. Importantly, LbL PE coatings are known to be extremely stable over a wide pH range.[233] Flocs formed from addition of PDADMAC coated MFs (at 316 mg L^{-1}) to a TiO_2 suspension (100 mg L^{-1}) were collected and redispersed into acidic solutions, resulting in ~100% TiO_2 release at pH ~2.5 (Figure 57). This deflocculation did not show a strong pH dependence in the range studied, although TiO_2 release was strongly inhibited at pH 1, presumably due to protonation of the PSS in the LbL layer at its pKa. This experiment thus confirmed that the magnetic flocculation process was easily reversible.

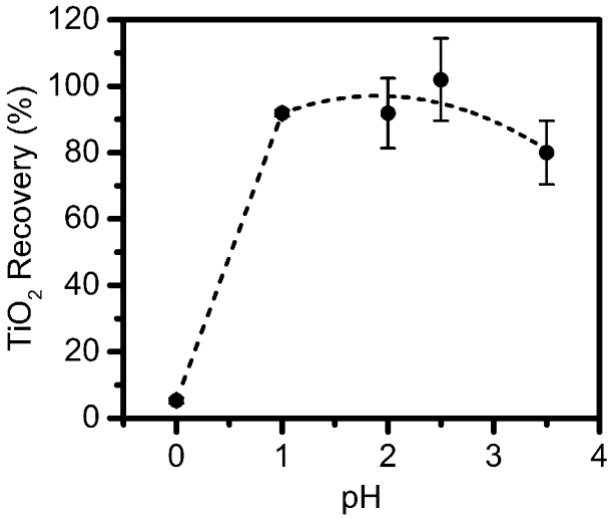

Figure 57. TiO_2 nanoparticle recovery following deflocculation of Fe_3O_4@SiO_2@PDADMAC/TiO_2 flocs as a function of pH.

Therefore, to assess the reusability of the MF particles for nanoparticle recycling, three cycles of flocculation and deflocculation were performed using the same set of Fe_3O_4@SiO_2@PDADMAC and TiO_2 nanoparticles (Figure 58). Flocculation performance remained the same over the course of the experiment ($p > 0.1$), confirming that the properties of the MF particles remain intact over multiple flocculation cycles, and thus demonstrating the concept of magnetically recyclable flocculants.

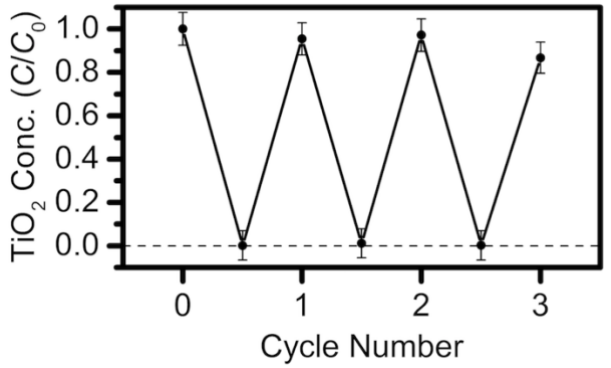

Figure 58. Separation of TiO_2 nanoparticles from aqueous suspension (0.1 g L^{-1}) by magnetic flocculation and deflocculation recovery with Fe_3O_4@SiO_2@PDADMAC particles, where the same TiO_2 and MF particles were recycled and used throughout each test.

To demonstrate the full closed loop magnetic flocculation process of Scheme 3, TiO_2 nanoparticles were used as photocatalysts for the oxidative and reductive treatment of both organic and inorganic water contaminants, wherein the TiO_2 was recycled by magnetic flocculation and reused over multiple treatment cycles (Figure 59). Inorganic selenium oxyanions, of recent interest due to the reduction in effluent limit guidelines by the US EPA[234] and a primary source of toxicity in flue gas desulphurization wastewater (FGDW),[235,236] were removed through photocatalytic reduction (Figure 5a).[218,219] Naphthenic acid fraction extractable organics (NAs), a complex mixture of bitumen-derived water soluble acyclic and cycloaliphatic compounds and a primary source of toxicity in oil sands process-affected water (OSPW),[6,113,237] were degraded through photocatalytic oxidation (Figure 59b).[70,119,205] The photocatalytic properties of TiO_2 nanoparticles remained largely intact following magnetic flocculation, where apparent losses in performance may have been due to fouling or aggregation of the TiO_2 over multiple cycles without rinsing. Extrapolating these results, the particles could be recycled 13 times in FGDW and 5 times in OSPW before losing 50% of initial photocatalytic activity. Both treatments were performed in real wastewater samples, demonstrating practical performance and tolerance of the MFs to dissolved species.

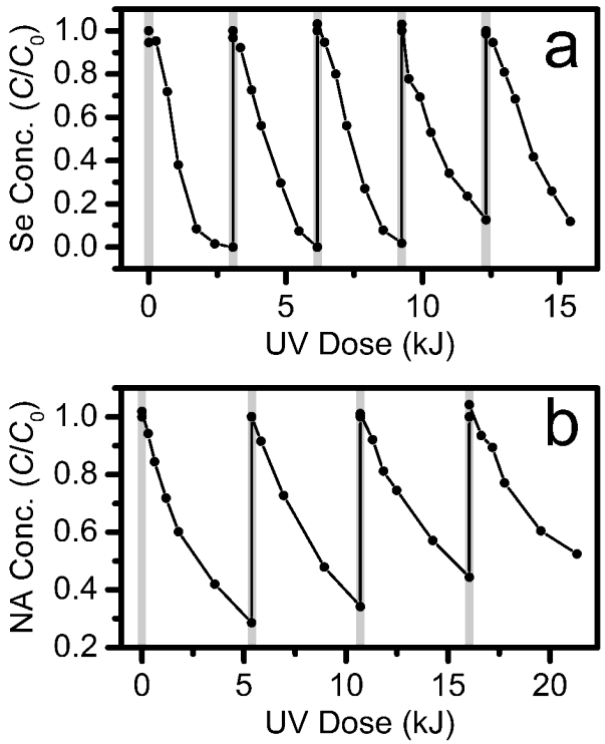

Figure 59. Photocatalytic treatment of (a) Se in FGDW and (b) NAs in OSPW using TiO_2 nanoparticles (0.1 g L^{-1}) recycled by magnetic flocculation, where the grey bands indicate points at which the TiO_2 was magnetically separated, deflocculated into a fresh sample of FGDW or

OSPW, and equilibrated in the dark. In each experiment Fe_3O_4@SiO_2@PDADMAC particles were used as the flocculant, and the same TiO_2 and MF particles were recycled and used throughout each test.

As far as limitations of the magnetic flocculation for nanoparticle recovery in water treatment applications, the presence of natural suspended solids (TSS) in water could represent a competing interference. However, this is not anticipated as a practical concern for recycling of photocatalytic nanoparticles, as advanced oxidation processes (AOPs) like photocatalysis are typically applied as tertiary treatments for water that has already been pre-treated to remove TSS. Similarly, dissolved ions or organic matter (NOM) could interfere to reduce flocculation efficiency, however the above experiment in real FGDW and OSPW demonstrates performance at even relatively high ion and NOM concentrations. Another practical limitation of the magnetic flocculation process is the increase in salinity (total dissolved solids, TSS), induced by the pH swings required for deflocculation and water reneutralization, which is undesirable from a water quality perspective. A further treatment stage downstream of the magnetic flocculation process may therefore be required for desalination.

5.5 Conclusions

Magnetic flocculation is presented as an alternative paradigm for nanoparticle recycling by magnetic separation, without disadvantages associated with immobilizing nanoparticles in core-shell magnetic nanocomposites. The MF particles were effective at flocculating a variety of different nanoparticles through an electrostatic association mechanism, without the overdosing issues associated with conventional flocculants, and logarithmic reduction in suspended particle concentration was possible over multiple flocculation passes. With the recent research focus on applications of plasmonic nanoparticles in catalysis and sensing, the effective separation of several metallic nanoparticles herein is significant, and further studies on metallic nanoparticle recycling are warranted. The MFs were also capable of collecting ultra-low concentrations of nanoparticles, and were reusable over multiple flocculation cycles. Furthermore, given that flocculant chemicals can be recovered and reused in this process, magnetic flocculation represents an environmentally sustainable solution to conventional flocculation challenges, and may have applications not only for nanocatalyst recycling, but also in remediation of nanoparticle pollution, algae dewatering, and wastewater treatment.

Chapter 6
Floating photocatalysts for passive solar degradation of naphthenic acids in oil sands process-affected water[**]

6.1 Summary

Oil sands process-affected water (OSPW), generated from bitumen extraction in the Canadian oil sands, may require treatment to enable safe discharge to receiving watersheds, as dissolved naphthenic acids (NAs) and other acid extractable organics (AEO), identified as the primary toxic components of OSPW, are environmentally persistent and poorly biodegradable. However, conventional advanced oxidation processes (AOPs) are impractically expensive to treat the volumes of OSPW stockpiled in the Athabasca region. Here we prepared floating photocatalysts (FPCs) by immobilizing TiO_2 on glass microbubbles, such that the composite particles float at the air-water interface for passive solar photocatalysis. The FPCs were demonstrated to outperform P25 TiO_2 nanoparticles in degrading AEO in raw OSPW under natural sunlight and gentle mixing conditions. The FPCs were also found to be recyclable for multiple uses through simple flotation and skimming. This paper thus demonstrates the concept of a fully passive AOP that may be scalable to oil sands water treatment challenges, achieving efficient NA reduction solely through the energy provided by sunlight and natural mixing processes (wind and waves).

6.2 Introduction

Bitumen extraction in Canada's oil sands uses large volumes of water, which is contaminated in the process by compounds leached from the oil sands ore, and referred to as oil sands process-affected water (OSPW). Release of OSPW to the environment is hindered by the toxicity of the water, due primarily to dissolved naphthenic acids (NAs) and other acid extractable organics (AEO),[113,238] and thus an estimated 1 billion m^3 of OSPW to date has been retained in tailings ponds on site. NAs are not fully biodegradable,[8,239] and their toxicity persists over decades,[10] therefore a water treatment solution may be required to enable OSPW discharge.

[**] This chapter is adapted from a previously published article: Leshuk, T.; Krishnakumar, H.; de Oliveira Livera, D.; Gu, F. Floating Photocatalysts for Passive Solar Degradation of Naphthenic Acids in Oil Sands Process-Affected Water. *Water* **2018**, *10* (2), 202.

Recently the oil sands industry has sought passive, or low energy, water treatment technologies capable of addressing large volumes of OSPW.[11] Considering the large sunlight-exposed surface area of oil sands tailings ponds, solar photocatalysis is a promising advanced oxidation process (AOP) with demonstrated capability to fully degrade OSPW AEO through hydroxyl and superoxide radical-mediated oxidative mineralization.[69,119,205] In contrast to other advanced oxidation processes (AOPs) that have been tested for OSPW treatment,[16,108] solar photocatalysis enables complete degradation of even recalcitrant NAs, without the need for chemical amendment of the water or electrical power consumption. Nevertheless, there remain a number of key technical challenges towards application of photocatalysis for OSPW treatment. Previous research has studied photocatalytic nanoparticles dispersed into OSPW as a slurry, and while slurries enable high treatment rates through efficient mass transfer, they require continuous mixing to remain suspended, as without mixing the photocatalyst near the water surface, the turbidity of OSPW is likely to occlude sunlight from reaching the catalyst. Indeed our previous measurements indicated the UV light penetrates <1 cm into OSPW.[119] Since the photocatalytic reaction thus only occurs at the water surface, the bulk majority of slurried catalyst dispersed in the dark zone below the surface is not effectively utilized, resulting in unnecessary material oversupply. Furthermore, slurries present challenges for cost effective nanocatalyst recovery and reuse at a large scale.

It was hypothesized that immobilizing a photocatalyst onto a buoyant support could address the above challenges, while adapting this promising treatment technology into a passive platform enabling large-scale deployment. On floating cores, the photocatalyst is naturally concentrated without any mixing at the water surface, where sunlight intensity is greatest, and the catalyst can be easily collected by simple skimming. Thus in this work we sought to demonstrate treatment of AEO in raw OSPW by use of floating photocatalysts under natural sunlight. While buoyant photocatalysts have been synthesized previously,[240–242] this report represents the first demonstration of such materials as a passive treatment for OSPW remediation.

6.3 Experimental

6.3.1 Materials

OSPW collected on March 17, 2014 was provided by Shell Canada, and stored in sealed polyethylene containers in the dark at 4 °C. The OSPW was homogenized by stirring before each use, herein referred to as raw OSPW. The OSPW was characterized previously to have a conductivity of 1.695 mS/cm, 1450 mg/L total dissolved solids (TDS), 49.5 mg/L total suspended solids (TSS), and a turbidity >200 NTU.[119] The AEO concentration was measured by the FTIR method below to be 26.3 mg/L.

A commercial mixture of naphthenic acids (technical grade, carbon numbers 6 – 20, z-classes 0 to -4, as characterized by Damasceno et al.[120]), dichloromethane (DCM, ≥99.9%, HPLC grade) NaOH (≥98%, ACS grade) and nitric acid (70%, ACS grade) were purchased from Sigma-Aldrich and used as received. Sulfuric acid (95-98%, ACS grade, Fisher) and titanium dioxide nanoparticles (Aeroxide P25, ~10-50 nm particle diameter, 55 $m^2 g^{-1}$ surface area, Acros) were used as received. Glass microbubbles (3M iM30k, soda-lime-borosilicate glass, ~10-30 µm diameter, 0.6 g/cm^3 density) were washed by 1 mol/L HNO_3 and 0.1 mol/L NaOH before use (at 125 g/L microbubbles), rinsing thrice with deionized (DI) water after each wash, then drying at 120 °C in air.

6.3.2 Floating Photocatalyst Synthesis and Characterization

TiO_2 nanoparticle powder was dispersed at 60 g/L into DI water by probe sonication, after which 0.1 mol/L HNO_3 was added to a concentration of 1 mmol/L, thereby adjusting the suspension to a nominal pH of ~3. This TiO_2 suspension was then added to microbubble powder (17.75 mL per g microbubbles), and the mixture was stirred at 500 rpm for 2 h, before transferring to a separatory funnel. The floating layer was collected after 1 h, vacuum filtered to form a cake, dried and crushed to a powder, which was then calcined for 4 h at 500 °C in air (5 °C/min ramp rate) to form the floating photocatalysts (FPCs).

Particle morphology was analysed by SEM (Zeiss Merlin FESEM), and elemental composition was measured by EDX (EDAX). Crystal phase was assessed by powder XRD (Bruker D8-Advance, Våntec-1 detector, 1.5405 Å Cu-Kα radiation).

6.3.3 Photocatalysis Experiments

Outdoor solar photocatalytic experiments were performed between August 22-28, 2015 at the University of Waterloo (Waterloo, ON, Canada). 1 g of FPC powder (or 0.5 g of P25 TiO_2) was stirred into 500 mL of raw OSPW in a borosilicate glass beaker (90 mm O.D.). Beakers were sealed from above with polyethylene film (Glad, measured to be UV transparent by spectrophotometry) to prevent evaporation during the experiments, and wrapped around the sides with Al foil. The beakers were then placed on a rooftop outdoors (43°28'17.9"N 80°32'32.2"W) and exposed to sunlight while stirring at 130 rpm, where a control included OSPW exposed to sunlight in the absence of TiO_2. The stirring Reynolds number was calculated according to the formula $\mathrm{Re} = fr^2\upsilon^{-1}$, where f is the rotational frequency (130 rpm), r is the radius of the stir bar (1.905 cm) and υ is the kinematic viscosity of water.[243] Following solar treatment, the photocatalyst was separated from the OSPW by flotation or centrifugation, retaining the water for analysis (stored at 4 °C in the dark).

Weather data was obtained from the University of Waterloo Weather Station archives.[74] Cumulative insolation was calculated by integrating the incoming shortwave radiation (measured by the weather station using a Kipp & Zonen CM11 pyranometer, spectral range 285 to 2800

nm) over the duration of the experiment (Figure 60). Cumulative UV exposure was estimated on the basis of the ASTM G173-03 global tilt solar spectrum as 4.72% of the cumulative insolation.

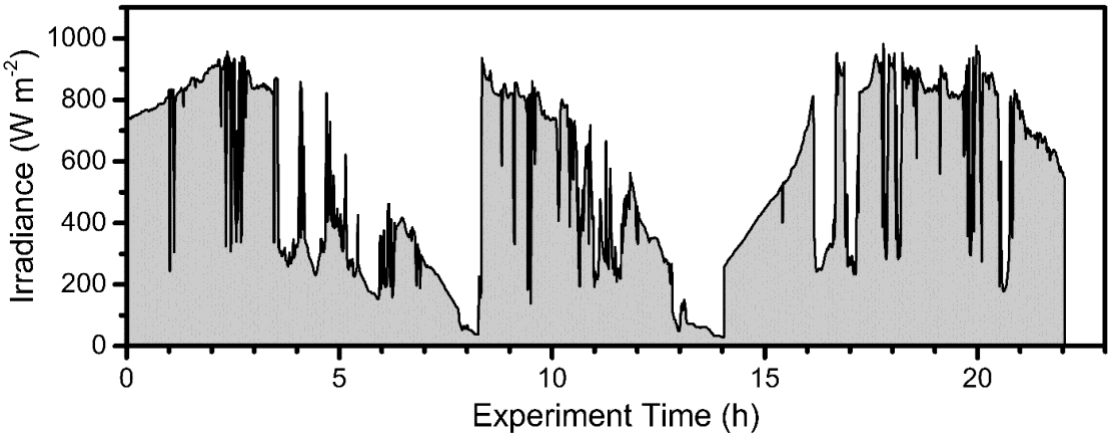

Figure 60. Solar irradiance measured throughout the duration of the photocatalytic experiment of Figure 2.

Photocatalyst recyclability experiments were performed under in a custom photoreactor enclosure, consisting of an array of UVA fluorescent bulbs (Philips F20T12/BL, peak emission ~350 nm, Figure 18) suspended above the samples.[205] The UV intensity was measured to be ~40 W/m^2 with a UVA/B light meter (Sper Scientific, NIST certified calibration), which is similar to the UV content of the solar spectrum (ASTM G173-03 global tilt). Following UV exposure, the photocatalyst was separated from the OSPW by flotation, and then directly redispersed into a fresh sample of OSPW for another round of photocatalytic testing.

6.3.4 Analysis

The concentration of AEO was measured by Fourier transform infrared spectroscopy (FTIR) according to the standard method[75,76] with minor modifications (*viz.*, the acidified samples were extracted thrice with DCM in a 1:12.5 solvent to sample volumetric ratio, with 80 ± 4% total recovery), using the commercial NA mixture to prepare the calibration curve. AEO is a composite measure of classical NAs, oxy-NAs ($C_nH_{2n+z}O_x$, where x > 2), and other organic acids.[64] Samples were filtered prior to the analysis (Whatman 934-AH glass fiber filter). Pseudo-first order rate constants were calculated on the basis of cumulative incoming solar shortwave insolation (285-2800 nm).

6.4 Results and Discussion

Photocatalysts were immobilized on the outer surface of buoyant microspheres, such that the composite particles would passively float at the air-water interface and degrade aqueous organic contaminants under sunlight illumination (Figure 61a). A heterocoagulation and sintering process was used to adhere photocatalytic TiO_2 nanoparticles to a high strength glass microbubble (GMB) core, wherein the TiO_2 and GMBs were mixed together at a pH between their respective isoelectric points to induce electrostatic attraction, followed by high temperature calcination to fix the nanoparticles in place. Thermal sintering has been previously demonstrated to promote strong adhesion of immobilized TiO_2 to glass supports,[244–246] although reducing specific surface area of the TiO_2 in the process.[247] Floating photocatalysts synthesized previously have used plastic supports susceptible to photocatalytic degradation,[248–253] or fragile materials such as perlite,[254–256] which sink upon breaking. The floating photocatalyst (FPC) composites prepared herein are entirely inorganic and resistant to photodissolution, and thus more suitable towards long term emplacement in a passive treatment system. The synthesized particles were observed to readily float at the water surface as intended (Figure 61b).

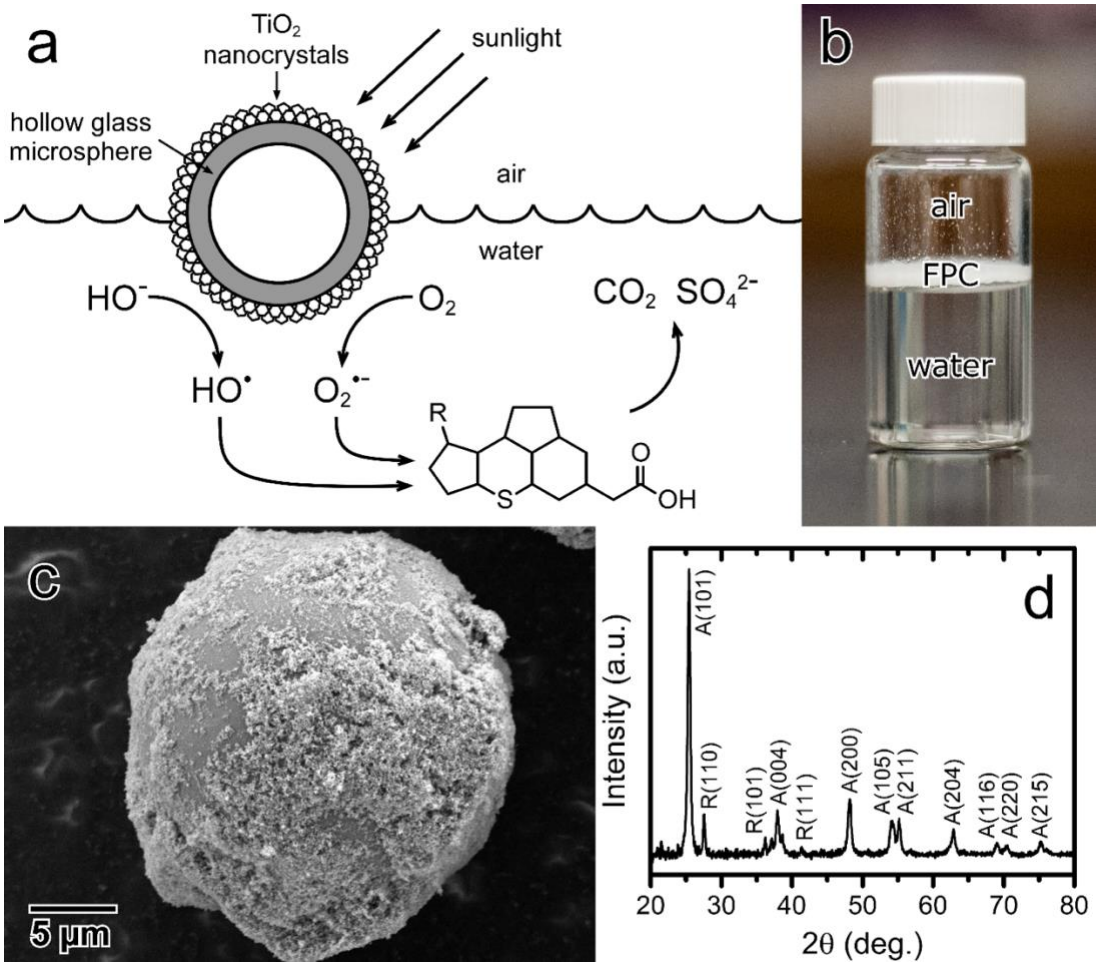

Figure 61. (a) Schematic of the floating photocatalyst (FPC) structure and mechanism of solar water treatment for napthenic acid mineralization (not to scale), (b) photograph of the FPCs added to water, (c) SEM image of a single FPC particle, and (d) XRD pattern of the FPC powder.

SEM was used to confirm the presence of immobilized TiO_2 on the surface of the GMBs, observed as a rough particulate coating (Figure 61c), with a particle diameter of ~25 nm, similar to the diameter of the TiO_2 nanocrystals used (Figure 62). SEM images of the uncoated GMBs are presented in Figure 63. EDX analysis further confirmed the presence of Ti, and the TiO_2 content of the composite particles was estimated to be 36.6 ± 4.1 wt. % (Figure 64). TiO_2 nanocrystals are known to partially sinter at the temperatures applied during the synthesis,[247] which is proposed to be the mechanism of TiO_2 adhesion.[257,258] XRD revealed the presence of anatase and rutile phases in the FPCs, characteristic of the mixed-phase TiO_2 nanocrystals used,[259] confirming that the calcination step did not significantly affect the crystal phase of the

particles. In fact, mild calcination at the temperatures applied herein has been reported to enhance the photocatalytic activity of TiO_2 nanoparticles.[247]

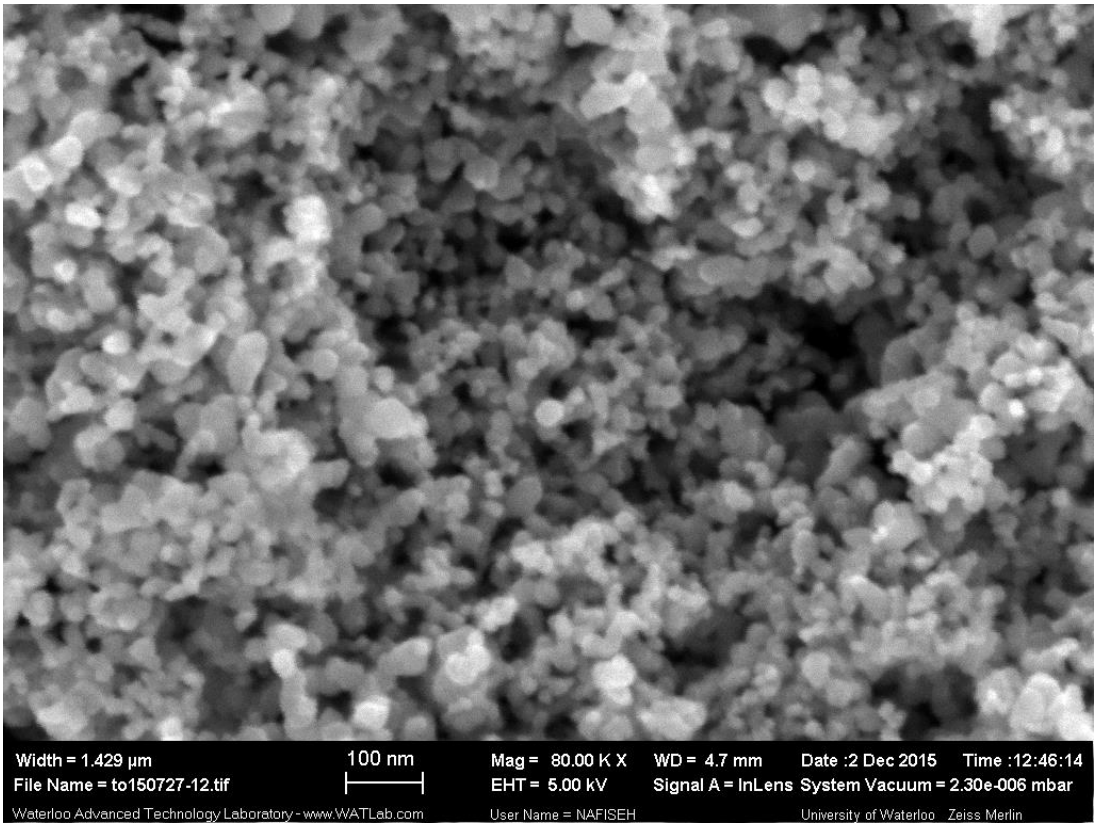

Figure 62. SEM image of TiO_2 nanostructures on the surface of a FPC particle.

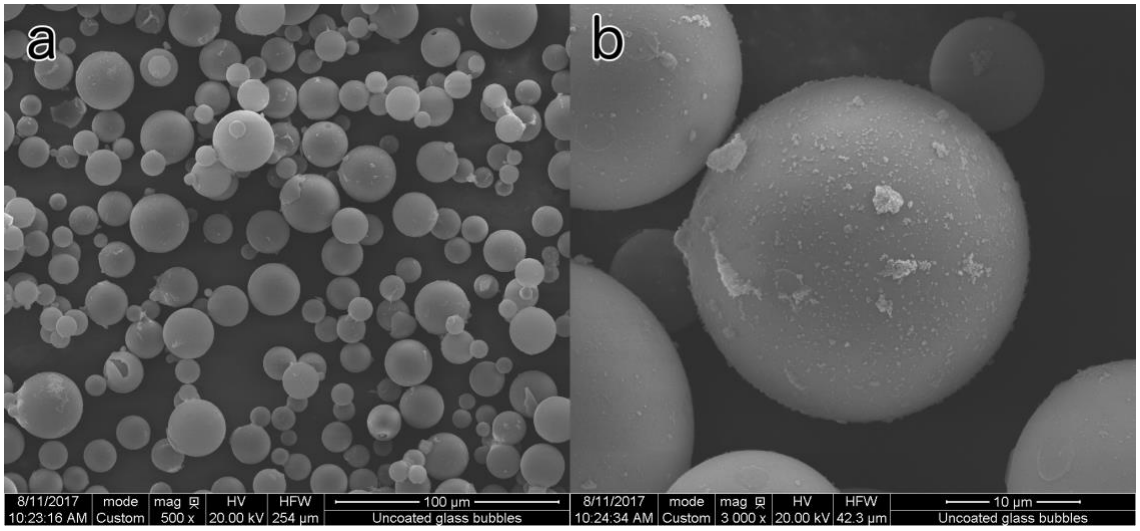

Figure 63. SEM images of uncoated glass microbubbles (GMBs) at (a) 500x and (b) 3000x magnification. GMBs were sputtered with Au prior to imaging.

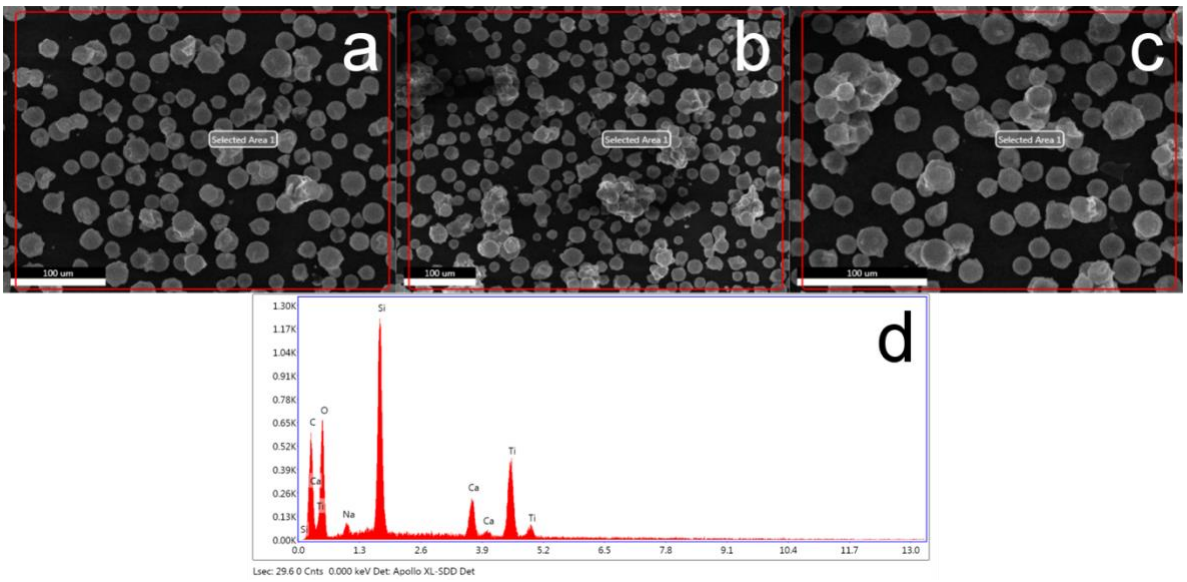

Figure 64. (a)-(c) SEM regions used for EDX elemental analysis and (d) typical EDX spectrum, as obtained from region (b).

The photocatalytic activity of the FPC particles was assessed under natural sunlight for the degradation of AEO in raw OSPW under gentle mixing conditions (Figure 65). The FPC particles degraded >80% of the AEO within 22 h of sunlight exposure (~33.4 kJ L^{-1} cumulative

solar UV), from a starting concentration of ~30 mg L^{-1} down to 4 mg L^{-1}. The oxidized intermediate compounds produced during photocatalytic AEO degradation have been thoroughly characterized in our previous work, where photocatalysis was demonstrated to result in nearly complete mineralization of organic carbon.[119,205] The kinetics were apparently first order, as observed previously,[119] and the pseudo-first order rate constant for the FPCs was 3.46 ± 0.20 x 10^{-8} m^2 J^{-1}. The FPCs compared favourably to P25 TiO_2 as a benchmark photocatalyst, which had a pseudo-first order rate constant of 4.15 ± 0.34 x 10^{-8} m^2 J^{-1}, where the measured rate constants were indistinguishable from each other ($p > 0.1$). However, normalized on a TiO_2 mass basis, the FPCs outperformed the P25 TiO_2, with a rate constant of 9.45 x 10^{-8} m^2 J^{-1} g^{-1} compared to 8.30 x 10^{-8} m^2 J^{-1} g^{-1}, respectively. Conventionally, nanoparticle slurries would be expected to outperform immobilized photocatalysts, such as the FPCs, due to enhanced contaminant mass transfer and higher accessible catalyst surface area.[24,27] However, in the low mixing regimes studied herein, the advantages provided by the FPCs of concentrating the photocatalyst at the water surface where sunlight intensity is highest apparently outweighed the typical disadvantages of immobilized systems. Thus the FPCs exceeded the activity of a known excellent photocatalyst formulation while enabling a convenient means of recycling through their buoyant properties.

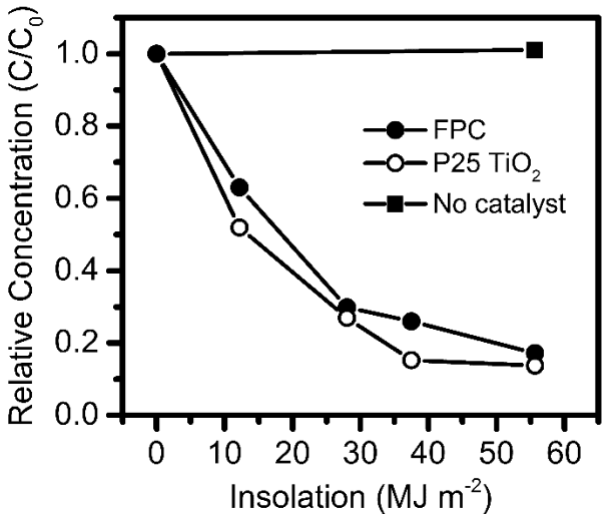

Figure 65. Photocatalytic degradation of AEO in raw OSPW under natural sunlight, where *C* and C_0 are the concentration and initial concentration of AEO, respectively.

The Reynolds number of mixing during the test was calculated to be 786, characteristic of a gentle laminar flow regime. The OSPW cap layer in oil sands tailings ponds is known to be well

mixed by wind and waves,[260–262] and NAs are furthermore constantly replenished to the interface by methanogenic bubbling in a similar process to dissolved gas flotation (estimated flux of 12 g CH_4 m^{-2} day^{-1}).[263] Thus as the above photocatalytic results were observed under gentle mixing conditions, it is anticipated that the natural mixing processes provided in the tailings ponds could be sufficient for OSPW treatment, although this question will be the topic of future studies. These results suggest the possibility for photocatalysis to serve as a truly passive AOP process with no electrical power input, where energy is provided solely by sunlight and wind.

Finally, the recyclability of the FPC particles for treating multiple batches of raw OSPW was tested under controlled illumination conditions (Figure 66), simply separating the catalyst by flotation. The catalyst was found to be reusable with equivalent activity for at least 3 cycles. Some deterioration in treatment performance was observed after the third cycle, possibly due to experimental difficulties in transferring 100% of the FPC material between cycles with small sample volumes, or alternatively due to progressive surface fouling of the catalyst. Effects of long term FPC exposure to raw OSPW is the topic of ongoing investigations in our laboratory. Signficantly, the durability of the FPCs to freeze-thaw cycling must also be evaluated to determine whether solar OSPW treatment would need to be paused over the winter months (*i.e.*, collection & redeployment of the FPCs seasonally).

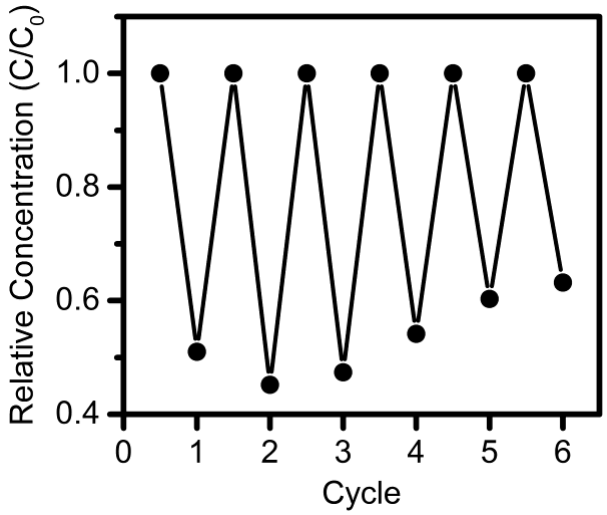

Figure 66. Recyclability of a single batch of FPC particles to degrade AEO in raw OSPW, where C and C_0 are the concentration and initial concentration of AEO, respectively.

6.5 Conclusions

A floating photocatalyst composite was demonstrated to match the photocatalytic activity of P25 TiO_2 in raw OSPW under natural sunlight. This is a significant finding, since photocatalytic activity was not sacrificed through this immobilization strategy, while the following advantages were gained:

- Due to their buoyancy, FPCs naturally concentrate at the air-water interface where sunlight intensity and dissolved oxygen concentrations are highest (i.e., the optimal treatment zone);
- Substantially less photocatalyst material is needed to achieve the same treatment rate as slurry deployment, since TiO_2 comprises only a minority of the buoyant composite mass, while in photocatalytic slurries, the vast majority of particles suspended below the illuminated air-water interface do not participate in the treatment process;
- NAs are naturally enriched at the air-water interface due to their surfactant properties, and are replenished to the surface from deeper OSPW in tailings ponds by methane bubbling, and through natural mixing provided by wind and waves;
- FPCs can be easily contained and collected by skimming from the surface, compared with the significant technical challenges of collecting colloidal nanoparticles from a slurry.

The use of sunlight and low energy mixing suggests the possibility that photocatalysis could serve as a truly passive water treatment process amenable to large scale deployment in the oil sands.

Chapter 7
Petroleomic analysis of the treatment of naphthenic organics in oil sands process-affected water with buoyant photocatalysts††

7.1 Summary

The persistence of toxicity associated with the soluble naphthenic organic compounds (NOCs) of oil sands process-affected water (OSPW) implies that a treatment solution may be necessary to enable safe return of this water to the environment. Due to recent advances in high-resolution mass spectrometry (HRMS), the majority of the toxicity of OSPW is currently understood to derive from a subset of toxic classes, comprising only a minority of the total NOCs. Herein, oxidative treatment of OSPW with buoyant photocatalysts was evaluated under a petroleomics paradigm: chemical changes across acid-, base- and neutral-extractable organic fractions were tracked throughout the treatment with both positive and negative ion mode electrospray ionization (ESI) Orbitrap MS. Transformation of OS^+ and NO^+ classes of concern in the earliest stages of the treatment, along with preferential degradation of high carbon-numbered O_2^- acids, suggest that photocatalysis may detoxify OSPW with higher efficiency than previously thought. Application of petroleomic level analysis offers unprecedented insights into the treatment of petroleum impacted water, allowing reaction trends to be followed across multiple fractions and thousands of compounds simultaneously.

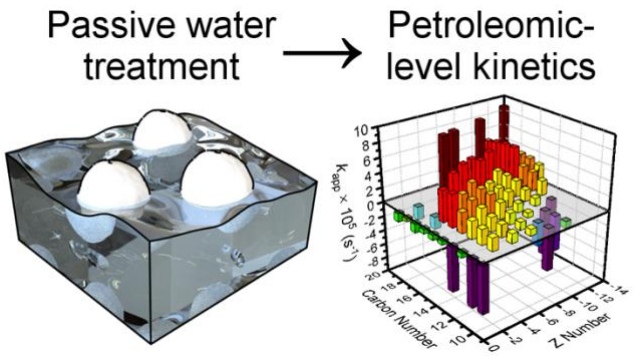

7.2 Introduction

†† This chapter is adapted from a paper that has been submitted for publication: Leshuk, T.; Peru, K. M.; de Oliveira Livera, D.; Tripp, A.; Bardo, P.; Headley, J. V.; Gu, F. Petroleomic analysis of the treatment of naphthenic organics in oil sands process-affected water with buoyant photocatalysts. *Water Res.* Submitted Feb. 4, 2018 (Manuscript No.: WR43113).

The Clark process used for extraction of bitumen in Canada's oil sands generates large volumes of water as a by-product, referred to as oil sands process-affected water (OSPW), which is stored on site in tailings ponds for water recycling. The oil sands mining companies are obligated to eventually return this water to the environment,[1–3] but currently are operating on a zero-discharge policy, due in part to the water's toxicity, which is primarily attributed to dissolved bitumen-derived organics.[4–7] Fractions of these organics are highly persistent,[8,9] and remain potently toxic even after decades of aging.[10] Thus treatment of OSPW may be required to enable safe discharge, and the industry is currently exploring passive remediation solutions.[11]

In the past, the organic constituents of OSPW were thought to simply comprise naphthenic acids (NAs), of the classical formula $C_cH_{2c+Z}O_2$, where Z indicates hydrogen deficiency from rings or double bonds.[12] However, with the advance of analytical capabilities such as high-resolution mass spectrometry (HRMS), far more complexity has been revealed:[64,114,116] OSPW is now understood to contain not only these conventional NAs, but also oxidized and heteroatomic classes,[264] and non-acid neutral and basic species,[265] referred to collectively herein as naphthenic organic compounds (NOCs, of general formula $C_cH_{2c+Z}N_nO_oS_s$). While classic NAs are known toxicants,[5] recent effects-directed analyses have also shown these base-neutral organics contribute significantly to the toxicity of OSPW,[113,266] and may also be implicated in its endocrine disruptive effects.[267,268] With the petroleomic level insights afforded by such rich HRMS datasets,[269,270] it has even been proposed recently that the whole effluent toxicity (WET) of OSPW may be predictable simply through mass spectral analysis.[271]

While many of these analytical advances have been driven by the goals of environmental forensics,[115,272–274] it is important for water treatment technologies to keep pace with the scientific progress and be evaluated with the same analytical rigor, to provide validated remediation tools for emergent environmental priorities. In terms of technologies studied for OSPW treatment, solar photocatalysis (PC) has been shown to be particularly effective at eliminating NAs,[69,119,205,275,276] and may be the only advanced oxidative process (AOP) with the potential for deployment in passive treatment systems, given the vast sunlight-exposed surface area of tailings ponds. However, the capacity of PC to treat base-neutral fraction NOCs has not been previously studied.

The objective of this work was to evaluate the performance of buoyant photocatalysts (BPCs) to degrade NOCs in OSPW, while tracking chemical changes across acid-, base- and neutral-extractable organic fractions with HRMS. Through combining pH fractionation with both positive and negative ion mode MS, we aimed to gain an unprecedented petroleomic perspective of the PC treatment of OSPW, by following molecular transformations across thousands of species simultaneously. To our knowledge, this is the first time PC has been studied through the lens of petroleomics, not only capturing a more holistic picture of the chemical changes occurring during NOC oxidation, but also exposing new insights into treatment of emerging

classes of concern (COCs). As not all OSPW organics are equally toxic,[5,113] tracking transformation of specific COCs in a complex mixture, rather than simply measuring reduction of bulk organic metrics, may represent a new standard for evaluating treatment solutions for petroleum impacted waters.

7.3 Experimental

7.3.1 Materials

OSPW was provided by an industrial producer operating in the Athabasca oil sands, and stored in sealed polyethylene containers in the dark at 4 °C. The OSPW was homogenized by stirring before each use, and then centrifuged (14,000 xg) or filtered (Whatman 934-AH glass fiber filter) to remove suspended solids.

A commercial mixture of naphthenic acids (technical grade, carbon numbers 6 – 20, *Z* numbers 0 to -4, as characterized by Damasceno et al.[1]), dichloromethane (DCM, ≥99.9%, HPLC grade), NH_4OH (28-30%, ACS grade), HNO_3 (70%, ACS grade), HCl (37%, ACS grade) tetraethylorthosilicate (TEOS, 98%) and Pluronic F127 were purchased from Sigma-Aldrich and used as received. Sulfuric acid (95-98%, ACS grade, Fisher), ethanol (EtOH, ACS grade) and TiO_2 nanoparticles (Aeroxide P25, ~10-50 nm particle diameter, 55 $m^2\ g^{-1}$ surface area, Acros) were used as received. Hollow glass microspheres (HGMs, 3M iM30k, soda-lime-borosilicate glass, ~10-30 µm diameter, 0.6 g/cm^3 density) were washed by 1 mol/L HNO_3 or H_2SO_4 before use (at 125 g/L microspheres), 3-5 times with deionized (DI) water by flotation, then dried at 120 °C in air.

7.3.2 Buoyant photocatalyst (BPC) synthesis

A silica sol-gel solution was prepared as previously.[277] Briefly, an acidic ethanolic TEOS solution of molar ratio TEOS:EtOH:H_2O:HCl = 1:4:10:0.01 was hydrolysed at 60 °C for 1 h, and then cooled to room temperature before use. TiO_2 nanoparticles and Pluronic F127 were then dispersed into DI H_2O by probe sonication, after which silica sol-gel solution and 1 mol/L HNO_3 were added to achieve a molar ratio of Ti:Si:F127 = 1:1:0.01, 0.1 mol/L HNO_3, and 25 g/L TiO_2. This TiO_2 suspension was then added to HGM powder at a 2:1 volume:mass ratio, and dried at room temperature for ≥24 h. The dried cake was then crushed to a powder, calcined for 6 h at 400 °C in air to remove the polymeric templates, and then washed with DI H_2O by flotation and dried. Particle morphology was analyzed by SEM (Zeiss Merlin FESEM).

7.3.3 Photocatalytic experiments

Photocatalytic experiments were performed in a custom photoreactor enclosure, consisting of an array of UVA fluorescent bulbs (Philips F20T12/BL, peak emission ~350 nm, Figure 18) suspended above the samples.[205] The UV intensity was measured to be ~36 W/m^2 with a UVA/B

light meter (Sper Scientific, NIST certified calibration), which is similar to the UV content of the solar spectrum (ASTM G173-03 global tilt).

BPCs were added at 300 g/m^2 (≈13.8 g/m^2 TiO_2) to 1 L of OSPW in a borosilicate glass beaker (11 cm I.D., sides wrapped with Al foil), which was sealed with UV-transparent polyethylene film. Beakers were equilibrated in the dark for 1 h, then placed in the photoreactor and exposed to UV light while stirring at 300 rpm (PTFE coated stir bar, 3.81 × 0.95 cm l × d), with periodically sampling (1 mL for UV_{220}) and addition of DI H_2O (Millipore, ≥15 MΩ·cm) to correct for evaporation losses. Following the UV treatment, the OSPW mixture was vacuum filtered (Whatman 934-AH glass fiber filter) to remove BPC particles, and the filtrate retained for analysis (stored at 4 °C in the dark).

Preliminary experiments on the effect of depth, mixing intensity, catalyst concentration and recyclability (Figure 69-Figure 72) were conducted in 500 mL PTFE beakers (7.2 cm I.D.) at a UV intensity of ~26 W/m^2, with typical BPC coverage of 125 g/m^2 (≈5.8 g/m^2 TiO_2), 300 mL OSPW, and 130 rpm stirring, with kinetics measured by UV_{220}. For the recyclability study, between UV exposures BPCs were separated by flotation, rinsed thrice with DI H_2O, then added to fresh OSPW for another treatment cycle.

7.3.4 Liquid-liquid extraction (pH fractionation)

For organics extraction, 200 mL OSPW was adjusted with H_2SO_4 to either pH 2.0 for acid-extractable organics (AEO), pH 7.0 ± 0.1 for neutral-extractable organics (NEO), or with NH_4OH to pH 10.5 for base-extractable organics (BEO), then extracted with 100 mL DCM (40, 40, and 20 mL sequentially), after which the extract was dried under N_2.

For total extractable organics, 400 mL OSPW was first adjusted to pH 10.5 with NH_4OH and extracted with 100 mL DCM, then to pH 7.0 ± 0.1 with H_2SO_4 and again extracted with 100 mL DCM, then to pH 2.0 with H_2SO_4 and again extracted with 100 mL DCM, after which the extracts were combined and dried under N_2. This extract was used to prepare a standard curve for UV_{220} (Figure 67), and from the absorbance of OSPW, extraction efficiency was determined to be 49.1%.

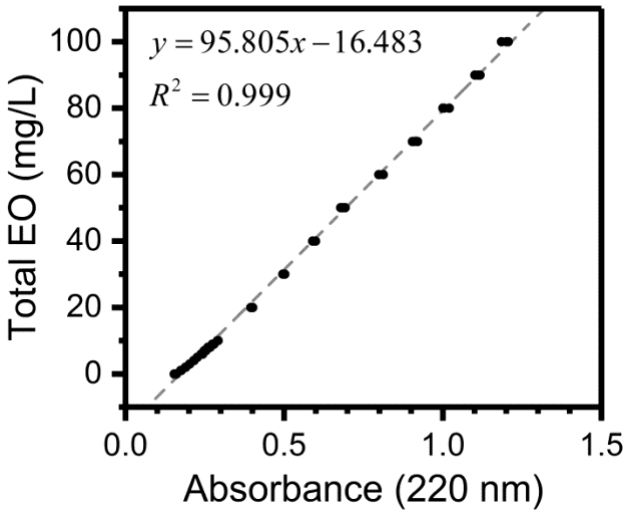

Figure 67. Calibration curve for determination of total extractable organics (EO) concentration from OSPW absorbance at 220 nm (UV_{220}).

7.3.5 Analysis

AEO_{FTIR} was measured by Fourier transform infrared spectroscopy (FTIR) according to the standard method[75,76] with minor modifications (*viz.*, the acidified samples were extracted thrice with DCM in a 1:12.5 solvent:sample volumetric ratio, with 80 ± 4% total recovery), using the commercial NA mixture to prepare the calibration curve. UV absorbance at 220 nm (UV_{220}) was measured with a spectrophotometer (BioTek Epoch).[220] Chemical oxygen demand (COD) was measured with a test kit (Hach, APHA 5220D). Total organic carbon (TOC, APHA 5310B), biochemical oxygen demand (BOD, APHA 5210B), anion concentration by ion chromatography (EPA 300.1), alkalinity (as $CaCO_3$, EPA 310.2), and dissolved metals by inductively coupled plasma mass spectrometry (ICPMS, APHA 3030B/6020A) were measured according to standard methods by ALS Environmental (Waterloo, ON, Canada), a laboratory accredited by the Canadian Association for Laboratory Accreditation (CALA) according to international standards (ISO 17025).

7.3.5.1 HRMS Analysis

Dried extracts from the pH fractionation liquid-liquid extractions as described above (AEO, NEO and BEO) were each individually re-dissolved in DCM. Each DCM solution was split into two equal portions (with the exception of the NEO extract) and again brought to dryness under a gentle stream of N_2. The split dried extracts were then re-dissolved in a solvent system based on the corresponding HRMS analysis listed below. For the AEO extract: one dried extract was re-dissolved in 50:50 acetonitrile (ACN):water with 0.1% NH_4OH, and run in negative ion mode

with 50:50 ACN:H_2O with 0.1% NH_4OH as the LC eluent; the second extract was re-dissolved in 50:50 ACN:H_2O with no pH modifier, and run in positive ion mode with 0.1% formic acid (HCOOH) as the LC eluent. For the BEO extract: one dried extract was re-dissolved in 50:50 ACN:H_2O with 0.1% HCOOH, and run in positive ion mode with 50:50 ACN:H_2O with 0.1% HCOOH as the mobile phase; the second extract was re-dissolved in 50:50 ACN:H_2O with no pH modifier, and run in negative ion mode with 0.1% NH_4OH as the mobile phase. For the NEO extract: the dried extract was re-dissolved in in 50:50 ACN:H_2O with no pH modifier, and run in positive ion with 50:50 ACN:H_2O with 0.1% ACN:H_2O as the mobile phase, and again in negative ion mode with 50:50 ACN:H_2O with 0.1% NH_4OH as the mobile phase.

Mass spectrometry analysis was preformed using an LTQ Orbitrap Elite (Thermo Fisher Scientific, San Jose, CA) operating in full scan in negative and positive ion mode. Mass resolution was set to 240,000 with an m/z scan range of 100-600. For negative ion mode the ESI source was operated as follows: sheath gas flow rate 10 (arbitrary units), spray voltage 2.90 kV, auxiliary gas flow rate 5 (arbitrary units), S lens RF level 67 %, heater temperature 50 ^oC, and capillary temperature 275 ^oC. For positive ion mode the ESI source was operated as follows: sheath gas flow rate 10 (arbitrary units), spray voltage 3.00 kV, auxiliary gas flow rate 5 (arbitrary units), S lens RF level 63 %, heater temperature 50 ^oC, and capillary temperature 275 ^oC. As per Composer data analysis, the mass accuracy was < 2 ppm error for all mass assignments.

For negative ion analysis, the mobile phase solvent used was 50:50 ACN:H_2O containing 0.1 % NH_4OH, while positive ion analysis used 50:50 ACN:H_2O containing 0.1 % HCOOH. Given that the same mobile phase was used for all samples in each ionization mode, class ionization efficiency was assumed to be independent of extraction pH when comparing between the different pH fractions. A flow rate of 200 uL min^{-1} was used for both, delivered by an Accela 1250 solvent pump (Thermo Fisher Scientific, San Jose, CA). A volume of 5 µL was injected into the mobile phase stream using a Thermo PAL-HTC Accela autosampler (Thermo Fisher Scientific, San Jose, CA). Quantitation was performed using linear regression obtained from a 5 point external calibration.[5]

The software used for instrument control/data acquisition and molecular analysis was Xcalibur version 2.1 (Thermo Fisher Scientific, San Jose, CA) and Composer version 1.5.2 (Sierra Analytics, Inc., Modesto, CA) respectively. Pseudo-first order rate constants were fit to the $O_2^{\pm}$ class data based on initial trends of when congeners were first detected in the reaction (since some congeners displayed complex trends of intensity increasing initially, but decreasing later in the treatment). For comparisons between the different pH fractions, it was assumed that the ionization efficiency of a given class was independent of extraction pH, given that pH of the mobile phase was the same

7.4 Results and Discussion

7.4.1 Buoyant photocatalyst (BPC) design

Previous OSPW treatment studies have evaluated nanoparticle photocatalysts dispersed as slurries in the OSPW,[69,70,119] which, while useful as performance benchmarks, are impractical for passive deployment due to the requirement for vigorous mixing to keep the particles suspended, challenges of catalyst recovery, and concern of environmental release of nanoparticles. Since solar PC is driven by sunlight absorption at the water surface, we hypothesized that by immobilization on buoyant supports, photocatalysts could remain suspended in the illuminated zone without the requirement for vigorous mixing. Such a design should also result in more efficient materials utilization, since any photocatalyst particles dispersed in the dark zone below the water surface are unreactive, resulting in catalyst oversupply in slurry deployments where the catalyst is dispersed throughout the water column. BPCs have been successfully demonstrated for treatment of simulated oil spills and dissolved organics.[278–280] Therefore we sought to demonstrate BPCs for OSPW treatment.

BPC composite particles were synthesized by coating TiO_2 nanoparticles on hollow glass microspheres, using mesoporous silica as a binder (Figure 68). Purely inorganic materials were selected for the composites to resist photocatalytic attack,[249,252,281] and a porous silica binder was used to enhance nanoparticle adhesion to the microsphere support,[282] while still allowing access of solution to the catalyst via mesopores.[277] The synthesized BPC material was hydrophilic, and floated at the surface of water as a frothy film (Figure 68d&e).

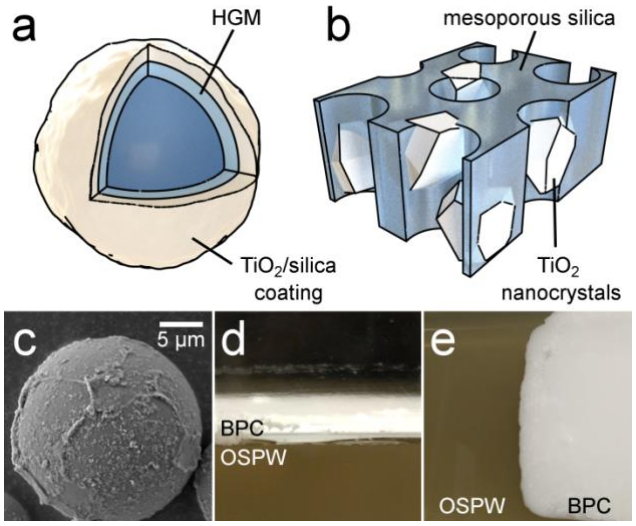

Figure 68. Schematic drawings of (a) BPC composite structure and (b) TiO_2 nanoparticles immobilized in mesoporous silica, (c) SEM image of a BPC composite particle, and photographs of a BPC film floating on OSPW, from (d) side and (e) top views.

The PC performance of the BPCs were evaluated in OSPW. Treatment rate diminished as a function of water column depth (Figure 69), consistent with a surface driven reaction. Notably, the apparent rate of the BPCs (~4.3×10^{-6} s^{-1}) was similar to that of a TiO_2 nanoparticle slurry (P25) at low concentrations (<5 g/m^2 TiO_2, Figure 70) and gentle mixing conditions (Re < 1000, Figure 71), although the TiO_2 slurry was more efficient under vigorous mixing and at higher concentrations. The BPCs were also found to maintain their performance over 10 batch treatment cycles (Figure 72). Thus when operating under non-turbulent flow regimes anticipated for passive deployment, BPCs match the performance of TiO_2 slurries, while enabling easier retention and recycling than free nanoparticle dispersions.

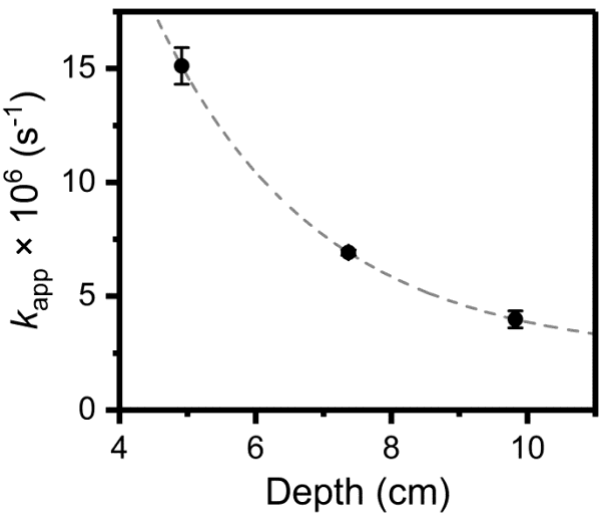

Figure 69. Variation of BPC apparent pseudo-first order rate constant (k_{app}) with OSPW depth. Depth was changed by varying the volume of OSPW. BPC concentration was 125 g/m^2 (≈5.8 g/m^2 as TiO_2), and beakers were stirred at 130 rpm.

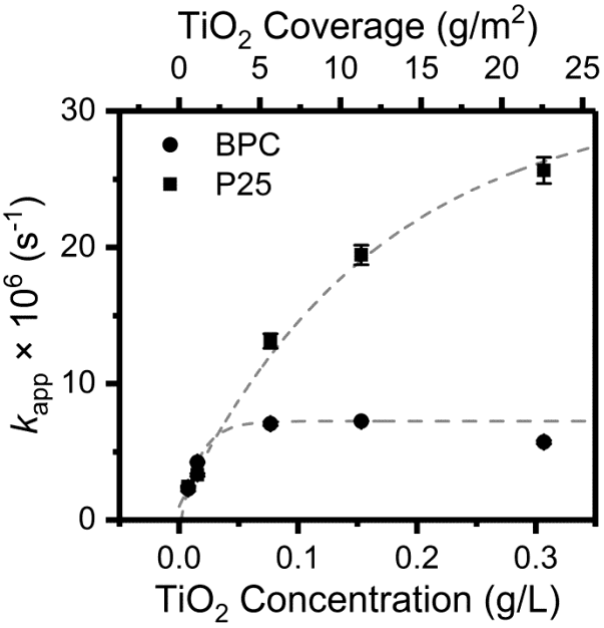

Figure 70. Variation of apparent pseudo-first order rate constant (k_{app}) of BPC and P25 as a function of equivalent TiO_2 concentration. OSPW volume was 300 mL (7.4 cm depth), and beakers were stirred at 130 rpm.

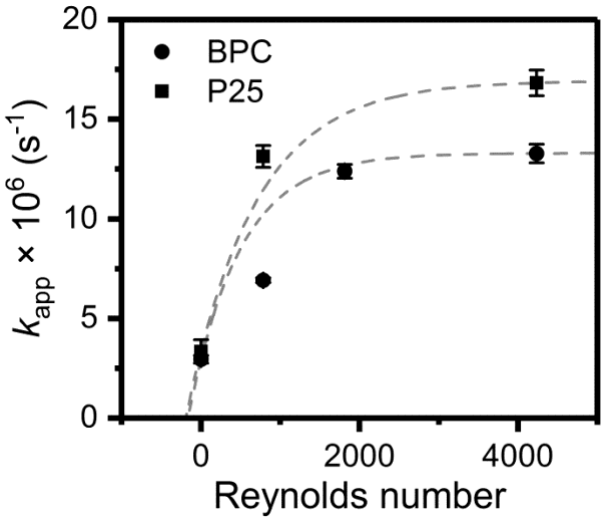

Figure 71. Variation of apparent pseudo-first order rate constant (k_{app}) of BPC and P25 as a function of the stirring Reynolds number. OSPW volume was 300 mL (7.4 cm depth), and BPC concentration was 125 g/m^2 (≈5.8 g/m^2 as TiO_2).

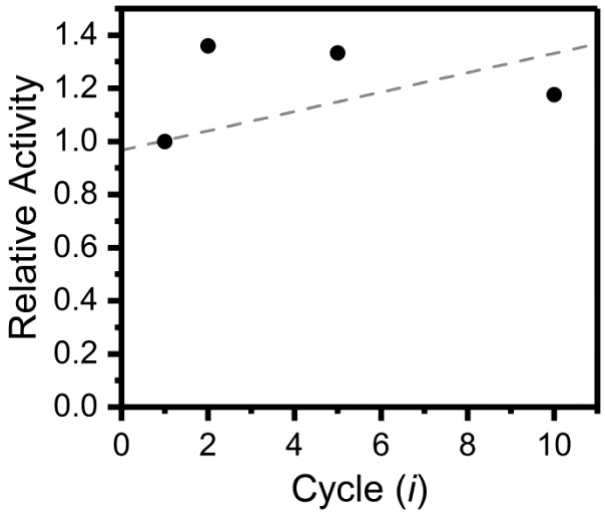

Figure 72. Relative activity of BPCs over multiple treatment cycles, $(1\text{-}C/C_0)_i/(1\text{-}C/C_0)_1$, *i.e.*, the fraction of NAs degraded on cylcle *i* relative to the first cycle.

7.4.2 Overall treatment kinetics

Following these preliminary experiments, the transformation of NOCs during the photocatalytic process was thoroughly investigated. The initial organics concentrations in the OSPW were measured by several methods (Table 16; inorganic parameters given in Table 17). The difference of AEO concentrations measured by FTIR and MS is likely due to the use of a commercial NA mixture (with low average molecular weight) as the calibration standard for the FTIR method.[283] In terms of fractionation, the most organics (by ESI(-) MS) were extracted at neutral pH with 113.5 mg/L NEO, ~42% more than the acidic extract, and ~19-fold more than the basic extract, where previous studies have similarly measured reduced extraction of negative ion species at high pH.[83,284] This comparison assumes class response factors are independent of extraction pH for a given ionization mode. The high NEO:AEO ratio may be evidence of polar non-acids partitioning to the neutral fraction.

Table 16. Measures of dissolved organics in raw OSPW.

Parameter	Concentration (mg/L)
AEO_{FTIR}	40.9 ± 2.4
AEO_{MS}[a]	79.9
NEO_{MS}[a]	113.5
BEO_{MS}[a]	6.0
Total EO (UV_{220})	78.9 ± 1.9
TOC	54
COD	153
BOD	3.0

[a] Concentrations calculated only from negative ion MS data, assuming an extraction efficiency of 49.1%.

Table 17. Water quality characteristics of OSPW

Parameter	Value
pH	8.30
Turbidity (NTU)	5.79
TSS (mg/L)	5.8
TDS (mg/L)	1080

Conductivity (mS/cm)	1.630
Anions	
Bromide (mg/L)	<0.50
Chloride (mg/L)	172
Fluoride (mg/L)	3.00
Nitrate (mg/L)	<0.10
Nitrite (mg/L)	<0.050
Sulphate (mg/L)	207
Alkalinity (mg/L as $CaCO_3$)	400
Dissolved Metals	
Aluminum (Al) (mg/L)	<0.050
Antimony (Sb) (mg/L)	0.0011
Arsenic (As) (mg/L)	0.0027
Barium (Ba) (mg/L)	0.0976
Beryllium (Be) (mg/L)	<0.0010
Bismuth (Bi) (mg/L)	<0.00050
Boron (B) (mg/L)	2.00
Cadmium (Cd) (mg/L)	<0.00010
Calcium (Ca) (mg/L)	15.7
Cesium (Cs) (mg/L)	<0.00010
Chromium (Cr) (mg/L)	<0.0050
Cobalt (Co) (mg/L)	0.0022
Copper (Cu) (mg/L)	0.0021
Iron (Fe) (mg/L)	<0.10
Lead (Pb) (mg/L)	<0.00050
Lithium (Li) (mg/L)	0.140
Magnesium (Mg) (mg/L)	14.4
Manganese (Mn) (mg/L)	0.0205
Molybdenum (Mo) (mg/L)	0.0613
Nickel (Ni) (mg/L)	0.0075
Phosphorus (P) (mg/L)	<0.50

Potassium (K) (mg/L)	15.6
Rubidium (Rb) (mg/L)	0.0144
Selenium (Se) (mg/L)	0.00056
Silicon (Si) (mg/L)	2.81
Silver (Ag) (mg/L)	<0.00050
Sodium (Na) (mg/L)	300
Strontium (Sr) (mg/L)	0.468
Sulfur (S) (mg/L)	71.0
Tellurium (Te) (mg/L)	<0.0020
Thallium (Tl) (mg/L)	<0.00010
Thorium (Th) (mg/L)	<0.0010
Tin (Sn) (mg/L)	<0.0010
Titanium (Ti) (mg/L)	<0.0030
Tungsten (W) (mg/L)	0.0047
Uranium (U) (mg/L)	0.00376
Vanadium (V) (mg/L)	<0.0050
Zinc (Zn) (mg/L)	<0.010
Zirconium (Zr) (mg/L)	<0.0030

During the photocatalytic reaction, FTIR was found to be a good surrogate measure for MS kinetics, with the apparent pseudo-first order rate constant (k_{app}) of AEO_{FTIR} removal, $9.2 \pm 0.4 \times 10^{-6}$ s^{-1}, matching closely to that of AEO_{MS} removal, $11.4 \pm 0.4 \times 10^{-6}$ s^{-1} (Figure 73a).[283,285] The NEO and BEO were eliminated significantly more quickly than the AEO, with $k_{app} = 25.1 \pm 0.7 \times 10^{-6}$ s^{-1} and $14.9 \pm 1.3 \times 10^{-6}$ s^{-1} respectively, which is reasonable on the basis that ring-opening photocatalytic reactions form carboxylic acid groups,[102,286–288] which would lead to accumulation of originally base-neutral species in the AEO fraction over the course of the treatment (Figure 73b). Continuation of photocatalytic exposure resulted in final organics mineralization (reduced COD and TOC, Figure 73a), in contrast to weaker oxidation processes such as ozonation, which have been shown to leave a toxic organic residual in OSPW even after high O_3 doses.[16,83,289] Faster transformation of extractable organics compared to UV_{220}, COD, and TOC, confirms that photocatalytic oxidation rapidly increases the polarity of the organics to the point where they are no longer extractable by DCM at any pH, after which they are steadily mineralized. The apparent increase in TOC at Time 2 is likely an analytical artefact arising from interference of background salinity in the sample.

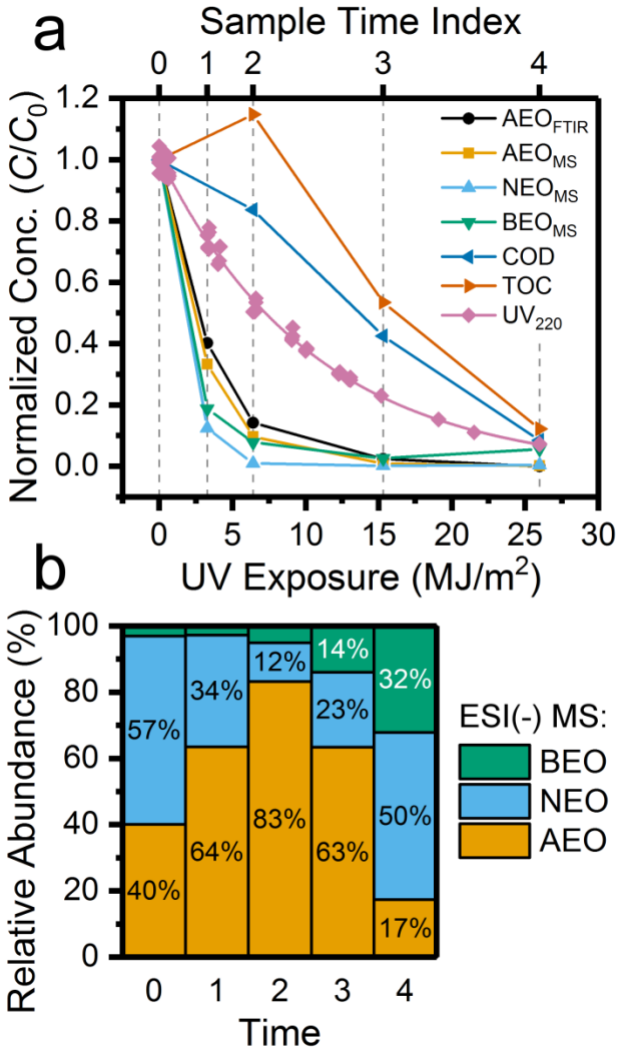

Figure 73. (a) Photocatalytic treatment kinetics by various organics measures. (b) Ratios of AEO, NEO, and BEO negative ion concentrations throughout the photocatalytic reaction, with time indices corresponding to those labeled in (a).

7.4.3 Heteroatomic class transformations

Recently, heteroatomic and positive ion classes have been implicated in the toxicity of OSPW,[113,266,290] therefore it is important to understand their transformations during PC. It is important to note that the scope of the current study is limited to the extractable organics, where

it is understood that a variety of polar organics remain non-extractable with DCM at any pH. However, as the aquatic toxicity of OSPW has been repeatedly found to be correlated only with the extractable organics, the non-extractables are not a priority from a water treatment perspective.

In terms of initial speciation of negative ions, the neutral and basic fractions were dominated by O_2^- (classic NAs), while the AEO additionally contained minority O_3^-, O_4^- and O_3S^- classes (Figure 74), where a high O_2^- ratio (relative to O_o^- classes with o >2) may indicate a relatively fresh OSPW sample, as o increases with environmental aging.[8] As observed previously,[114] a greater diversity of heteroatomic classes were detected in positive ion mode (Figure 75), with the BEO primarily characterized by OS^+ (28%), O_8^+ (23%) and NO_8^+ (26%) classes, the AEO by SO_3^+ (59%), and the NEO by OS^+ (29%) and O_3S^+ (32%), along with minor NO^+ (3.8%), O_2^+ (7.7%), O_3^+ (4.2%), O_8^+ (5.8%) and O_2S^+ (3.6%).

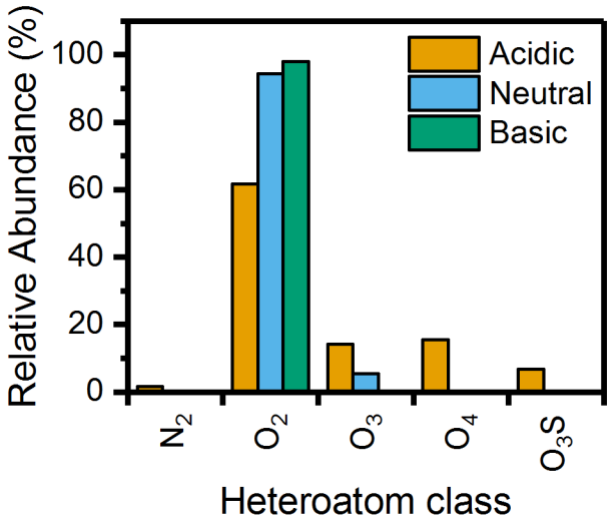

Figure 74. Initial relative abundance of species by heteroatom class within each extract from raw OSPW by negative ion mode MS. Relative abundances within each extract should not be compared as concentrations between extracts.

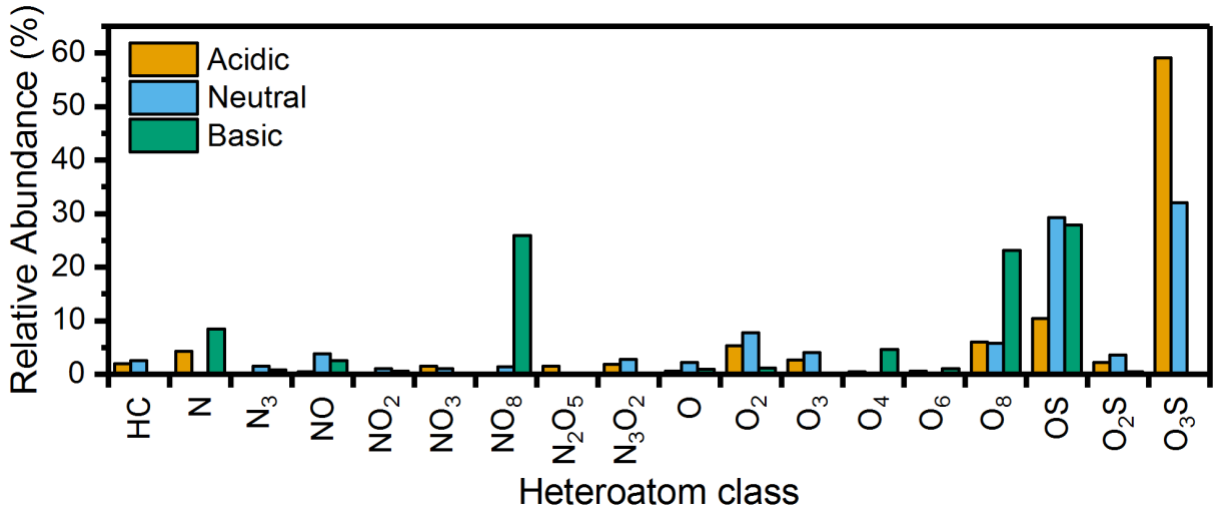

Figure 75. Initial relative abundance of species by heteroatom class within each extract from raw OSPW by positive ion mode MS. Note that $[H]^+$ and $[Na]^+$ ions were counted together. Relative abundances within each extract should not be compared as concentrations between extracts.

In terms of environmental implications, O_2^- has been repeatedly confirmed as one of the most acutely toxic negative ion classes,[5,113,238] with a narcotic mechanism arising from the NAs' surfactant properties, while higher oxygen numbered species are less acutely toxic.[65] O_3S^- may comprise sulfonic acids, and thus impart similar surfactant modes of toxicity.[291] O_o positive ions likely contain hydroxyl or ketone groups, and may be implicated in the endocrine disrupting effects of OSPW.[268] The O_8^+ and NO_8^+ signals may be evidence of "ARN"-like tetra-carboxylates,[292–294] which would mark their first detection in OSPW. The O_3S^+ class is thought to comprise thiophenic hydroxylated aldehydes,[295,296] and has previously been found in non-toxic NOC fractions.[113,266] The O_2^-, O^+ and OS^+ classes have among the highest measured membrane partitioning ratios, with potential to bioaccumulate.[297,298] While typically measured at lower intensity than the O_2^- NAs, OS^+ and NO^+ species are also thought to be potent toxicants,[271] with potential to inhibit membrane transport proteins and damage DNA through oxidative stress.[266,290,296]

During the photocatalytic treatment, both positive and negative ions of the heteroatomic O_oS_s family were initially preferentially degraded, such that the class distributions shifted to almost exclusively O_o at intermediate time points (Figure 76). These changes in relative composition of heteroatomic classes, especially in the positive ion data (where the O_o fraction increases to ~90% from ~20% in the raw OSPW), are much larger than observed previously following OSPW treatment with O_3, UV/H_2O_2 and Fe(VI) (relative changes of only ~20%),[299] potentially indicating a more selective oxidation mechanism for PC, in accordance with previous

observations.[119] In the final stages of the photocatalytic reaction, the ratio of $O_oS_s^-$ and $N_nO_o^+/N_nO_oS_s^+$ increased again in the AEO/NEO and NEO/BEO extracts, respectively, concurrently with decreasing AEO fraction (Figure 73b). Under the assumption that ionization efficiency of a given class is similar across all samples investigated, it is hypothesized that while raw O_oS_s species are initially the most reactive NOCs, oxidized intermediates produced during the photocatalytic process are more reactive still, possibly due to preferential adsorption of acidic and catecholic moieties to TiO_2,[300,301] such that in the final stages of the treatment acidic O_o compounds are preferentially degraded over base-neutral heteroatomics.

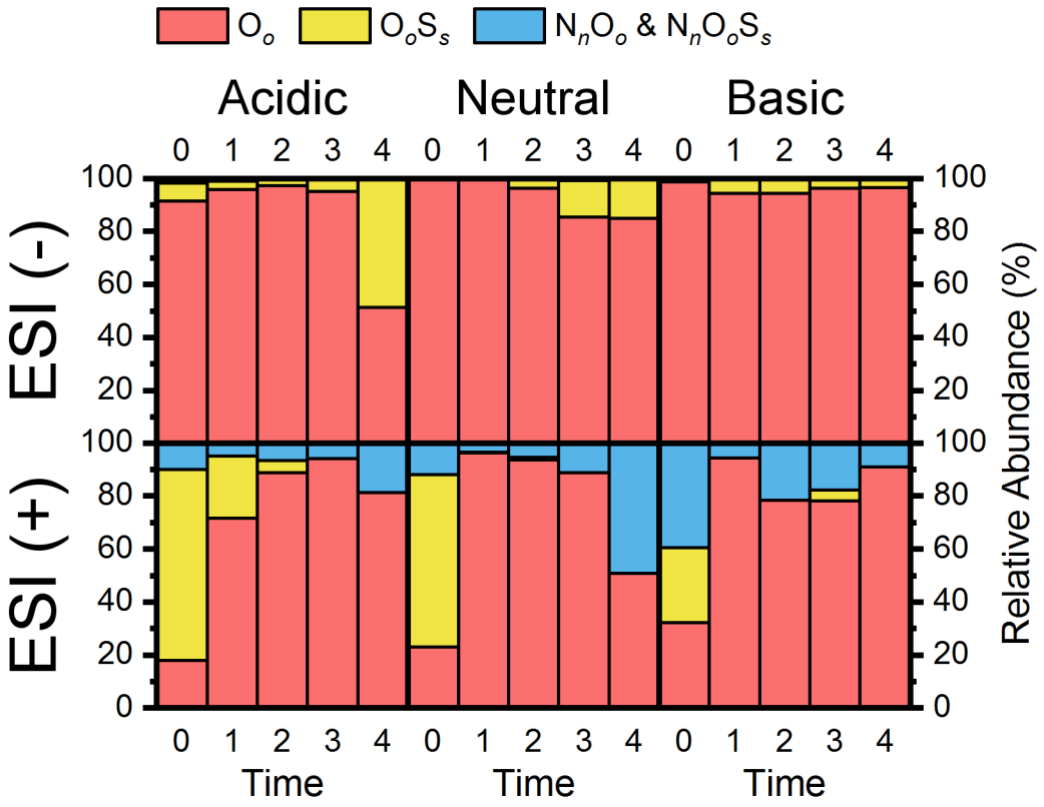

Figure 76. Relative distribution of heteroatomic families within each time point, where time indices correspond to those labelled in Figure 73a.

7.4.4 Class oxidation trends

Oxygen number $o > 2$ has been generally shown to be inversely correlated with acute toxicity for OSPW NOCs, as the polarity of added oxygen functionalities counteracts the molecules'

surfactant properties.[238,302] While the intensity of the negative ions was significantly diminished by the first sampling time point (Figure 77), clear trends of increasing *o* with time were observed in all extracts for both O_o^- and O_oS^- classes (Figure 78). In the AEO, average *o* increased from 2.5 in the raw OSPW to 4.3 by the third time point of photocatalytic exposure, which is once again a stronger shift than was reported for OSPW AEO oxidation using other AOPs,[299] while a similarly large increase in *o* has been observed previously for photocatalytic OSPW AEO oxidation.[119] Apparent deviation from this trend in some extracts at the final two time points may simply be due to poor extraction efficiency in DCM.

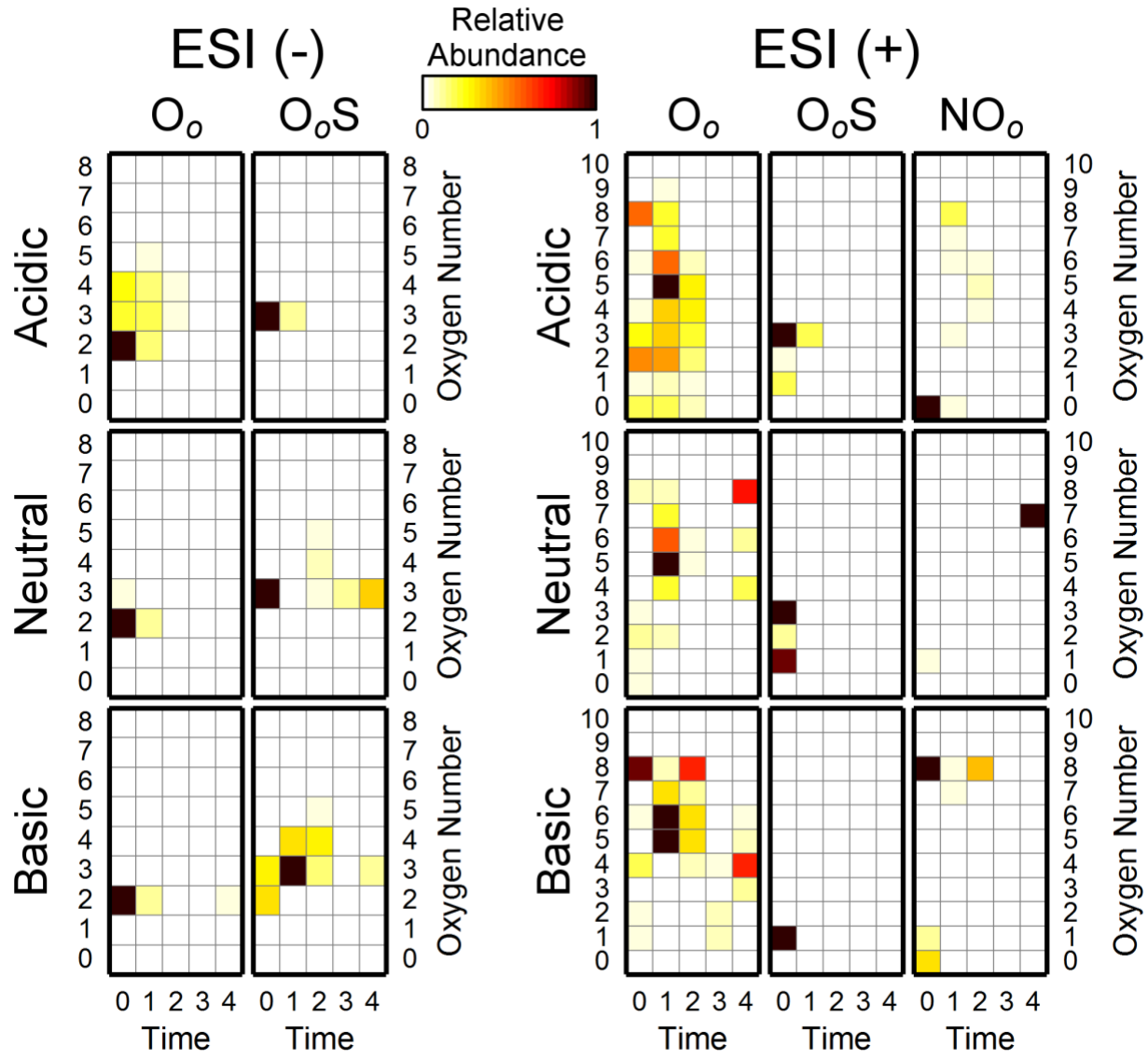

Figure 77. Trends in oxygen number (*o*) with time for different heteroatomic classes. Relative abundance of species by oxygen number is presented normalized to the maximum intensity measured within each class, where time indices correspond to those labelled in Figure 73a.

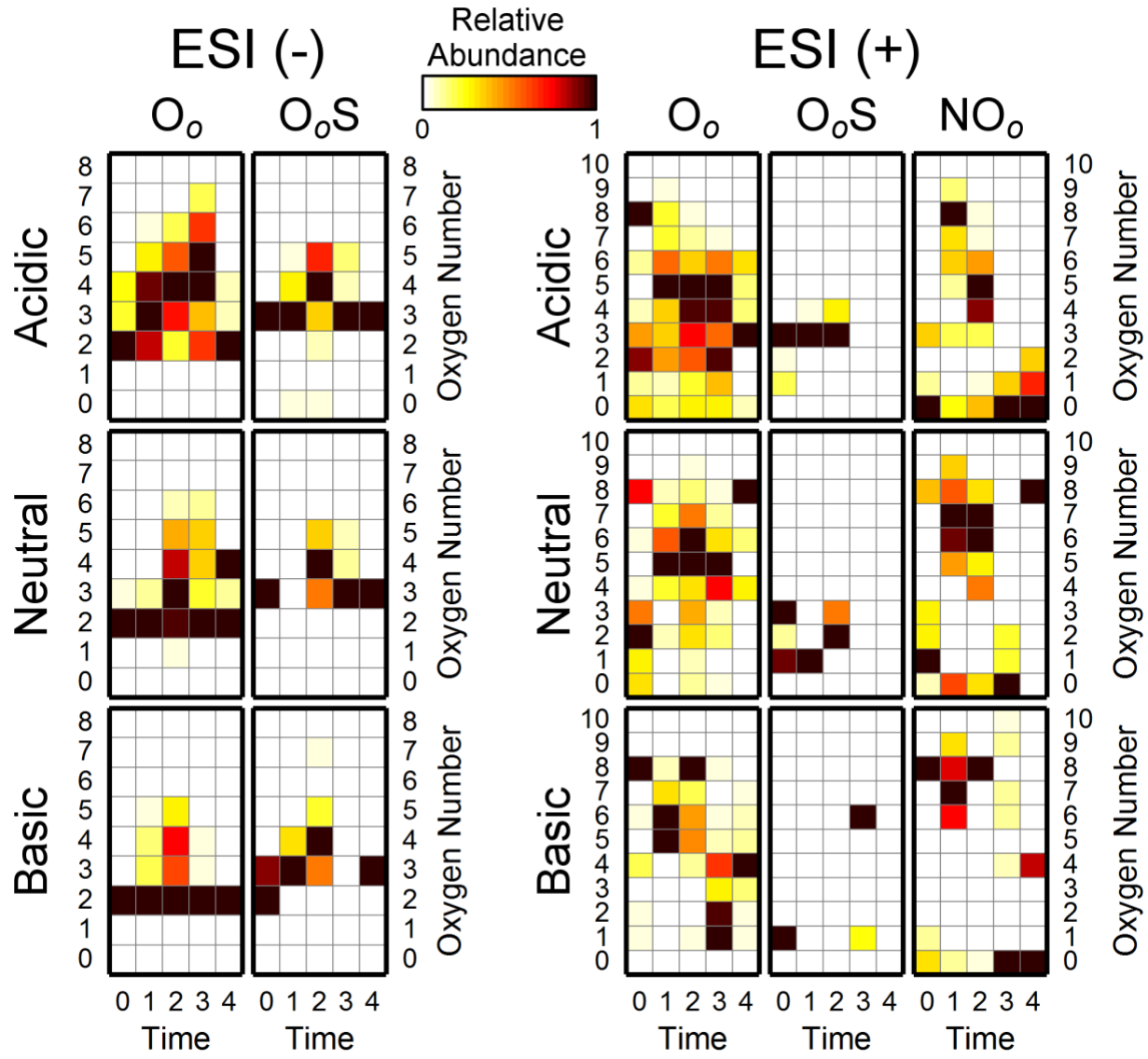

Figure 78. Trends in oxygen number (*o*) with time for different heteroatomic classes. Relative abundance of species by oxygen number is presented normalized to the maximum intensity measured within each time point for each class, where time indices correspond to those labelled in Figure 73a.

In positive ion mode, any trends in *o* with time were less clear: the broad distributions in O_o^+ in the acidic and neutral extracts may be attributed to the appearance of hydroxylated oxidation intermediates.[296] Indeed, the increased O_o^+ intensity at Time 1 is correlated with the reduction in

O_o^- and O_oS^- abundance. Some single-class conclusions may also be drawn from the ESI(+) data: the OS^+ COC was eliminated by the first time point in the BEO and NEO. Similarly, the NO^+ species in the neutral extract were eliminated by the first time point, along with the O_2^+ and O_3^+ classes.

The rapid transformation of the presumed most toxic COCs (O_2^-, OS^+ and NO^+)[113,296] in the earliest stages of the treatment (when AEO_{FTIR} is still measured as 40%) is promising for the practicality of photocatalytic OSPW treatment, as only a relatively short exposure may be needed to meet WET targets, rather than full organics mineralization. This is supported by our previous finding that OSPW toxicity towards *Vibrio fischeri* could be eliminated by solar PC prior to full organics mineralization,[119] although more rigorous toxicity testing of PC treated OSPW is warranted.

Previous studies have shown that oxidized NOCs are more readily biodegradable,[89,303,304] thus given the oxidation patterns observed herein, supplementation of PC with biodegradation may be another promising strategy to increase overall OSPW treatment efficiency, *e.g.*, by combination of solar PC with passive treatment wetlands.[275,305,306]

7.4.5 Carbon and Z number kinetics

In addition to following chemical transformations between classes, through HRMS it was also possible to investigate the molecular weight (carbon number *c*) and hydrogen deficiency (*Z* number) distribution within any single class throughout the photocatalytic treatment. We thus fit a pseudo-first order rate constant to each $O_2^{\pm}$ species as a function *c* and *Z* (Figure 79). It should be emphasized that the O_2^+ species are likely hydroxylated NOCs rather than NAs, but they are still presented together with the O_2^- NAs to understand the relative reactivity of positive and negative ions within the same treatment. Furthermore, since very little O_2^+ compounds were detected in the initial BEO (Figure 75), the data for Figure 79f is sparse.

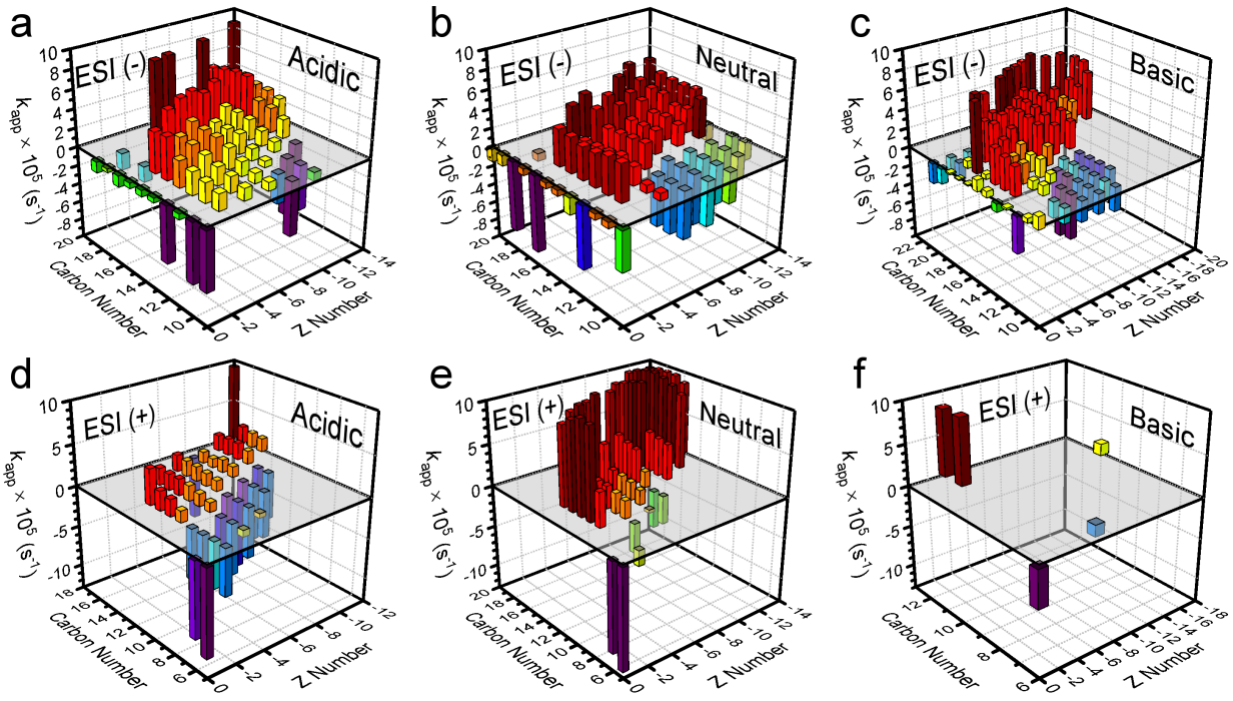

Figure 79. Estimates of pseudo-first order rate constants (k_{app}) of photocatalytic degradation of (a)-(c) O_2^- and (d)-(f) O_2^+ species in the (a)&(d) AEO, (b)&(e) NEO and (c)&(f) BEO fractions. Rates of appearance of new species are plotted as negative values of k_{app}.

The initial raw OSPW profiles of $O_2^{\pm}$ in each of the extracts are presented in Figure 80. For the O_2^-, the NEO and BEO were distributed to higher *c* and |*Z*| relative to the AEO, which is as expected, since only the most hydrophobic NAs (highest ratio of aliphatic carbon to the carboxylate anion) should be extractable at higher pH values. In ESI(+), the O_2^+ distribution in NEO was also observed to be shifted to slightly higher *c* and *Z* numbers versus the AEO.

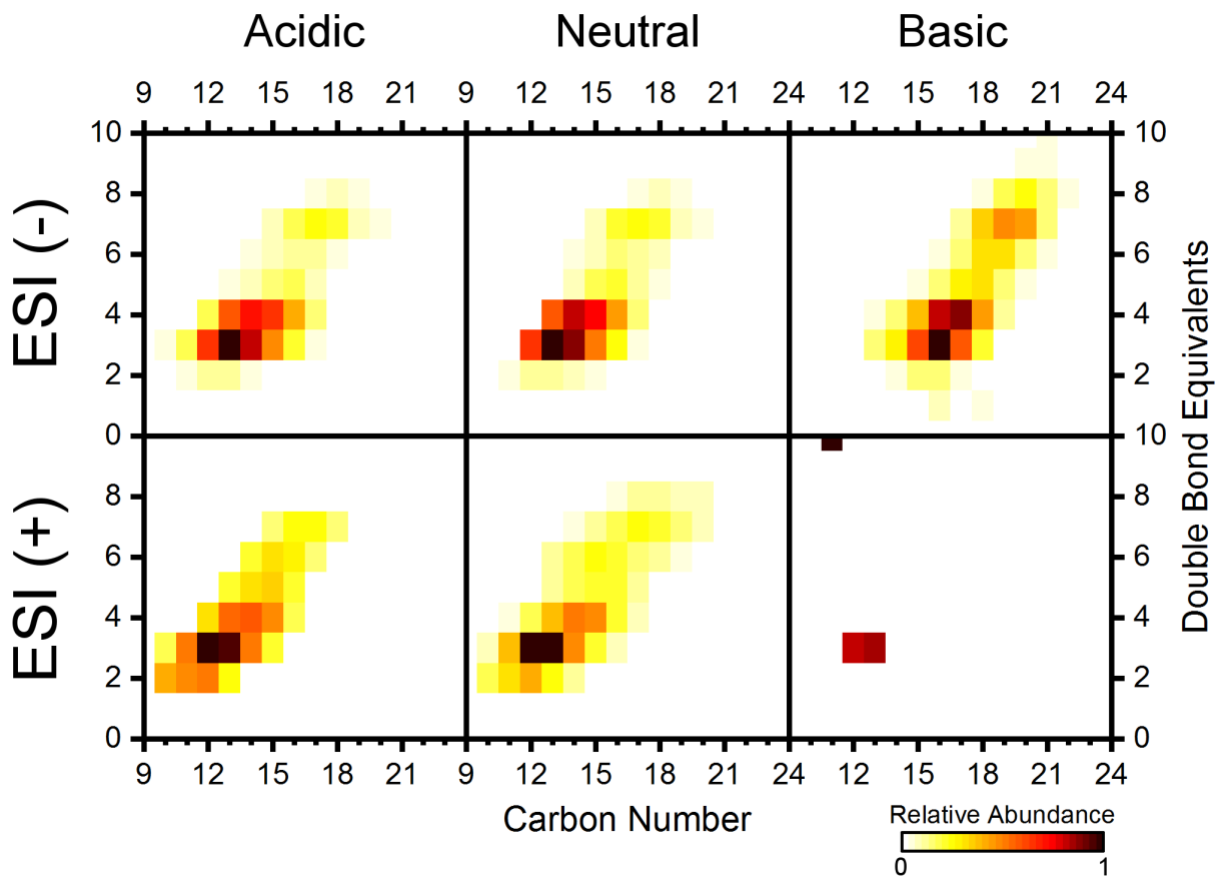

Figure 80. Initial relative distribution of $O_2^{\pm}$ species within each extract from raw OSPW.

The photocatalytic kinetics show a clear trend, across all fractions, of reactivity increasing with carbon number (Figure 79), up to $k_{app} \approx 10 \times 10^{-5}$ s^{-1} for congeners of highest *c*, while new species of lower *c* and |*Z*| numbers, which did not appear in the initial profiles (Figure 80), were produced over the course of the treatment. This trend is interpreted as arising from photocatalytic C-C bond scission, *e.g.*, through ring opening or decarboxylative chain shortening, generating smaller, more linear NOCs as reaction by-products. Indeed, it is likely that the true rate constants are approximately equal across the O_2^- class and largely independent of *c* and *Z*, as would be expected for a non-specific $HO^{\bullet}$ directed AOP, where the apparent dependence is simply the result of intermediate *c* and *Z* numbered organics being simultaneously created from the degradation of higher *c* and *Z* numbered species. Similarly, if acid-extractable O_2^+ compounds are indeed hydroxylated aldehydes or ketones, the relatively lower rate constants in Figure 79d could be interpreted as evidence of their formation during PC, as would be expected from multiple pathways of $O_2^{\bullet-}$ driven C-C cleavage.[81,286,307]

The environmental significance of these results is that both the most toxic and environmentally persistent NAs are preferentially eliminated during PC treatment. Hughes *et al.* reported that NAs with $c \geq 17$ were the most acutely toxic constituents of OSPW to rainbow trout (*Oncorhynchus mykiss*),[5] while Yue *et al.* found that NAs with $14 \leq c \leq 18$ and $-6 \leq Z \leq -4$ were those most correlated with acute toxicity towards *Vibrio fischeri*,[238] similar to the trend of increasing NA toxicity with c measured by Jones *et al.*[308] Similarly, NOCs with high c and $|Z|$ numbers are known to be the most recalcitrant fractions in OSPW, while smaller and less cyclic NAs are more readily biodegradable.[8,239,309] However, further research is merited to evaluate the toxicity of the lower c and $|Z|$ numbered intermediates formed in the PC treatment process.

7.5 Conclusions

With recent insights into the structure-activity relationships driving various modes of observed OSPW toxicity, it has become clear that only specific classes of organics, comprising only a minority of the total NOCs, compose the majority of the toxicity associated with OSPW.[5,113] Through implementing a fractionated HRMS investigation, these COCs could be individually tracked in the context of PC oxidation trends occurring in the NOCs as a whole. Revelation that the OS^+ and NO^+ classes were eliminated in the earliest stages of the PC reaction, and that the highest molecular weight O_2^- NAs were preferentially degraded, may indicate that only relatively low solar doses would be required to detoxify OSPW, which could result in more efficient treatments as compared to the solar exposures required for complete NOCs oxidation or DOC mineralization. This study also demonstrates application of a buoyant photocatalyst formulation as a passive treatment concept for oil sands remediation challenges, and further studies to develop this paradigm of a passive AOP are ongoing in our lab.

Chapter 8
Conclusions and Future Work

8.1 Summary

This thesis presents new findings in the fields of chemical engineering, nanotechnology, materials science, and water treatment. Solar photocatalysis over TiO_2 was found to degrade OSPW AEO through superoxide-dependent oxidative mineralization. The kinetics of OSPW treatment were found to be impacted by dissolved inorganic species, strongly dependent on dissolved oxygen, and weakly affected by temperature and pH, and an empirical model was proposed to predict OSPW treatment kinetics in different tailings ponds. Magnetic flocculation was developed as a new paradigm for magnetic nanoparticle capture, and demonstrated to efficiently separate and recycle colloidally dispersed TiO_2 in a closed-loop photocatalytic process. Floating photocatalysts were also synthesized to adapt the photocatalytic process towards a passive deployment paradigm, by immobilizing TiO_2 nanoparticles onto buoyant glass microspheres. Floating photocatalysts were demonstrated to preferentially treat OSPW base- and neutral-extractable organics and priority toxic naphthenic organic classes of concern. In terms of future work, recommendations are given towards materials research for potentially higher treatment efficiency, as well as development of the treatment method towards practical deployment.

8.2 Conclusions

Photocatalytic degradation of AEO in raw OSPW was demonstrated within 1 day of natural sunlight exposure in the presence of a slurry of TiO_2 nanoparticles, demonstrating that neither the water's natural suspended and dissolved solid content, nor the solar spectrum's minor UV power content, were insurmountable barriers towards achieving practical treatment rates through heterogeneous photocatalytic oxidation. With sufficient sunlight exposure (approx. 1 week-equivalent, 181.4 MJ/m^2 insolation), essentially complete photocatalytic mineralization of all organics in the water was achieved. However, with only partial oxidation (approx. 1 day-equivalent of sunlight exposure, 31.4 MJ/m^2 insolation), the acute toxicity of the OSPW towards *Vibrio fischeri* was eliminated, and an increased BOD/TOC ratio indicated that the residual dissolved organics may have been rendered more readily biodegradable. HRMS analysis confirmed the oxidation mechanism, and evidenced a significant increase in oxygen content of the intermediate organic species. Radical scavenging studies indicated a significant role of superoxide radicals in the oxidation process. Overall, photocatalytic efficacy in OSPW treatment was demonstrated, motivating further investigation into treatment kinetics and catalyst recycling systems.

The rate of AEO degradation was measured to vary significantly between two sources of OSPW from different suppliers. Following analysis of the organic constituents of the AEO by HRMS, and the inorganic content of the water matrix, a factorial screening experiment of several inorganic species in simulated OSPW revealed the deleterious roles of both iron and bicarbonate on the photocatalytic treatment rate. Response surface modelling of the Fe and HCO_3 effects failed to confirm a synergistic interaction of the two factors. The role of Fe in significantly inhibiting the photocatalytic generation of $HO^{\bullet}$ in OSPW may explain its effect on the AEO degradation rate. Langmuir-Hinshelwood treatment revealed that at a TiO_2 concentration of 0.5 g/L, the kinetics of NA degradation were both adsorption- and reaction-limited. Variation of the treatment temperature between 4 – 40 °C revealed a relatively low activation energy of 11.53 ± 0.26 kJ/mol for the photocatalytic reaction, consistent with optically driven photocatalytic processes. While OSPW pH was found to have a negligible impact on the treatment rate within the range of pH 7-9, dissolved oxygen was found to be significantly involved in the photocatalytic process, consistent with a superoxide-mediated reaction mechanism. The apparent external quantum efficiency (EQE) of photocatalytic AEO degradation was estimated to be ~1%, consistent with other photocatalytic treatment processes. An empirical kinetics model of photocatalytic OSPW treatment was developed, which may aid in predicting efficacy of the PC treatment in different OSPW sources.

Given the challenges associated with separation of colloidal nanoparticulate TiO_2 from slurry photocatalytically-treated water, the concepts of polymeric flocculation and magnetic separation were combined to synthesize magnetic flocculant particles (MFs): polyelectrolyte coated Fe_3O_4@SiO_2 core-shell ellipsoids. Successful synthesis of the designed MF particle structure was confirmed through a variety of materials characterization techniques, including TEM, DLS, XRD, XPS and zeta-potential measurements. Similar to conventional water treatment flocculation, magnetic flocculation was demonstrated to proceed through an electrostatic association mechanism. By varying the charge of the polyelectrolyte MF coating, targeted flocculation of oppositely-charged nanoparticles could be achieved, and the separation process was demonstrated to be generalizable to a variety of different nanoparticle and catalyst materials with different charge and surface coatings, including TiO_2, Au, Ag, Pd and Pt nanoparticles. The optimum MF dose to separate TiO_2 nanoparticles was found to coincide with approximately equal surface area concentrations of TiO_2 and MFs in suspension. Logarithmic reduction in residual nanoparticle concentration was demonstrated through multiple MF cycles. Deflocculation of TiO_2-MF flocs was possible through zeta-potential polarity inversion via pH shift, enabling reuse of both the TiO_2 and MF particles in a closed-loop process. This new separation system was demonstrated in both the photocatalytic treatment of OSPW and FGDW, illustrating the potential of a low-energy, membrane-free nanoparticle separation technique, as well as a novel implementation of magnetic particle recycling compared conventional magnetic particle separation strategies.

To enable a passive deployment implementation for solar photocatalytic OSPW treatment, as well as providing a convenient catalyst capture and recovery system, TiO_2 nanoparticles were immobilized on the surface of hollow glass microspheres (HGMs) as buoyant supports by calcination sintering. Successful TiO_2 immobilization was confirmed through SEM, EDX and XRD analysis. Under gentle mixing conditions, these synthesized floating photocatalysts (FPCs) were measured to match the AEO degradation rate of a slurry dispersion of a benchmark TiO_2 nanoparticle formulation (P25) in raw OSPW under natural sunlight, and on a TiO_2 mass-normalized basis, the FPCs were more efficient than the nanoparticulate TiO_2. The FPCs were also found to be reusable over at least 3 photocatalytic OSPW treatment cycled through natural flotation separation. Given the competitive performance of the FPCs, the concept of catalyst immobilization to a buoyant support was concluded to be a promising strategy to apply photocatalysis towards passive OSPW treatment.

The photocatalytic treatment kinetics of naphthenic organic compounds (NOCs) in OSPW was studied by HRMS in both positive and negative ion mode across multiple extracts (acidic, neutral, and basic), providing a petroleomic picture of the transformations occurring to numerous NOC classes throughout the photocatalytic treatment process. FPCs were synthesized by immobilizing TiO_2 nanoparticles onto HGMs through use of mesoporous silica as an inorganic binder, and these particles were confirmed to be recyclable for multiple OSPW treatments, and match the performance of slurried TiO_2 nanoparticles under gentle mixing conditions. Base and neutral extractable organics were photocatalytically degraded more quickly than the conventional AEO, and heteroatomic NOCs were also preferentially treated. Transformation of OS^+ and NO^+ classes of concern in the earliest stages of the treatment, along with preferential degradation of high carbon-numbered O_2^- acids (key NOC classes identified as potently toxic in prior research), suggest that photocatalysis may detoxify OSPW with higher efficiency than previously thought. As not all OSPW organics are equally toxic, tracking transformation of specific COCs in a complex mixture, rather than simply measuring reduction of bulk organic metrics, may represent a new standard for evaluating treatment solutions for petroleum impacted waters.

Overall, this thesis advances the understanding of the photocatalytic treatment of OSPW, as well as separation processes for nanoparticle photocatalysts. Combining a sunlight-driven, chemical-oxidant-free catalytic oxidation process with a low-energy, membrane-free catalyst separation and recovery technique may represent a promising strategy to adapt advanced oxidation process (AOP) technology for the passive treatment of OSPW, or other remote mining-impacted waters.

8.3 Recommendations for future work

The following research directions are recommended based on the conclusions drawn above, to further advance this water treatment technology towards practical application:

1. Explore the combination of photocatalytic OSPW treatment with biodegradation or phytoremediation treatments in a multi-stage process. As has been demonstrated with various other AOPs, oxidation of biologically recalcitrant organics can increase their bioavailability and render them biodegradable. Considering the elevated BOD/TOC ratio observed in partially-oxidized OSPW in Chapter 3, there is some evidence that such an effect may also be possible in this system. Furthermore, given that OSPW naturally harbours bacteria tolerant to NOCs, and that fractions of NOCs are readily biodegradable, passive bioremediation is a possibility. Finally, considering that the oil sands industry is currently heavily researching treatment wetlands as another passive treatment solution,[310] and that initial reports indicate that fractions of NOCs remain non-biodegradable post-wetlands treatment,[9,275] mild photocatalytic pre-treatment of the OSPW fed to wetlands systems may be a natural coupling of two passive technologies, with the potential to greatly reduce the solar exposure times required in the PC step (*i.e.*, targeting mild oxidation rather than full mineralization), while compensating for a natural limitation of the wetlands process.
2. Research alternate photocatalytic materials beyond TiO_2. While TiO_2 possesses many intrinsic benefits as a low-cost, (photo)chemically stable material, given the relatively low quantum efficiency measured for OSPW treatment in Section 4.4.11, improving the efficiency of the catalyst itself is a logical progression. Perhaps an obvious strategy to photocatalytic materials improvement for solar applications is to tailor the electronic band structure of the semiconductor photocatalyst to productively absorb and utilize visible light, comprising a much larger fraction of solar power output compared to the UV emission alone, which TiO_2 is limited to. One promising direction may be to explore "black" defective (vacancy-doped) TiO_2 as a catalyst, which has shown large increases in efficiency relative to intrinsic TiO_2.[311–313] An alternate strategy may be to explore co-catalyst materials such as single-atom catalysts or metal clusters,[170,314–316] with the aim of tuning the free-radical production of the photocatalyst, to generate tailored blends of free radicals. Given the involvement of superoxide in the oxidation mechanism observed herein, it may be promising to attempt to design a material capable of enhanced superoxide production.
3. Synthesize photocatalyst-adsorbent composites. The Langmuir-Hinshelwood analysis in Chapter 4 revealed that adsorption to the TiO_2 surface may be rate limiting, thus combination of the photocatalyst with an adsorbent material (such as activated carbon, AC) may overcome this limitation. Indeed, NOCs are known to readily sorb to AC.[317,318] A more elaborate implementation of this combined adsorption-degradation strategy would be to design materials with tailored adsorption capacity, similar to molecularly imprinted polymers.[319,320] As discussed in Chapter 7, given that only a few classes of NOCs are thought to be responsible for the bulk of the toxicity of OSPW, designing a composite catalyst material with needle-in-a-haystack targeted adsorption capabilities for these particular toxic classes

could greatly enhance overall treatment efficiency, by focusing the photocatalytic reactivity towards the priority toxicants.

4. Evaluate the long-term durability of the floating photocatalysts (FPCs) developed herein. While recyclability up to 10 treatments was demonstrated in Chapter 7, in field deployment FPCs would be expected to endure days to years of continuous exposure to OSPW and the elements. Rigorous chemical and mechanical wear studies would be valuable to determine the useful lifetime of the material and failure mechanisms, where this knowledge could then be used to further improve the composite formulation. Significantly, durability of the FPCs to freeze-thaw cycling must also be evaluated, to inform whether the material would need to be collected and redeployed at the beginning and end of the winter, or could be left in-place over a number of years.
5. Study the impact of photocatalytic OSPW treatment towards toxicity endpoints. It has been proposed that when an OSPW release regulations are implemented, they will be specified in terms of whole effluent toxicity (WET) targets, rather than specific chemical metrics, given the complexity of the NOC composition in OSPW. While the potential for total mineralization of OSPW organics has been shown to be possible through photocatalytic treatment, only a much shorter treatment may be needed to meet WET targets, which could greatly enhance treatment throughputs. On the other hand, while this thesis has evaluated chemical transformations of NOCs during photocatalytic oxidation, it is important to confirm that none of these photocatalytically generated intermediates (oxidized organics) are more toxic than the precursor compounds. Studying the progression of OSPW toxicity during treatment in combination with detailed HRMS analysis could further elucidate important NOC structure-activity relationships throughout the treatment process, which would be valuable towards setting photocatalytic treatment thresholds, as well as further optimizing the process.
6. Model the performance of the photocatalytic treatment at large scale. While this thesis has demonstrated the concept of a passive deployment system for solar photocatalysis, it remains uncertain how the rate of OSPW treatment will scale with water volume, depth, and mixing conditions. Computational fluid dynamics (CFD) has been used in many other chemical engineering problems to predict the performance of a design at scales beyond those feasible to test,[321,322] provided sufficient relations and boundary conditions can be determined at the lab scale. The kinetics information in Chapter 4 can provide a foundation to input to a CFD model to predict the rate of photocatalytic OSPW treatment at industrially relevant scales.
7. Evaluate the performance of photocatalysis to treat OSPW at the field scale. There must be several steps of scale up to develop this technology to treat any practical volumes of OSPW in the oil sands. A likely first step would be to evaluate treatment kinetics in deeper water columns at the mesocosm scale. Scalable synthesis processes to produce kg to tonnes of FPCs may be needed to conduct these experiments. Conducting these larger-scale tests while

also evaluating combination with treatment wetlands and measuring toxicity endpoints, as recommended above, may be an efficient approach to explore these various directions in tandem.

Bibliography

(1) Martin, J. W. The Challenge: Safe Release and Reintegration of Oil Sands Process-Affected Water. *Environ. Toxicol. Chem.* **2015**, *34* (12), 2682–2682.

(2) *Lower Athabasca Region - Tailings Management Framework for the Mineable Athabasca Oil Sands*; Government of Alberta, 2015.

(3) *Directive 085: Fluid Tailings Management for Oil Sands Mining Projects*; Alberta Energy Regulator, 2017.

(4) Verbeek, A. G.; Mackay, W. C.; MacKinnon, M. D. Acute Toxicity of Oil Sands Wastewater: A Toxic Balance. In *Proceedings of the Twentieth Annual Aquatic Toxicity Workshop*; 1994; Vol. 26, p 9.

(5) Hughes, S. A.; Mahaffey, A.; Shore, B.; Baker, J.; Kilgour, B.; Brown, C.; Peru, K. M.; Headley, J. V.; Bailey, H. C. Using Ultrahigh-Resolution Mass Spectrometry and Toxicity Identification Techniques to Characterize the Toxicity of Oil Sands Process-Affected Water: The Case for Classical Naphthenic Acids. *Environ. Toxicol. Chem.* **2017**, *36* (11), 3148–3157.

(6) Brown, L. D.; Ulrich, A. C. Oil Sands Naphthenic Acids: A Review of Properties, Measurement, and Treatment. *Chemosphere* **2015**, *127*, 276–290.

(7) McQueen, A. D.; Kinley, C. M.; Hendrikse, M.; Gaspari, D. P.; Calomeni, A. J.; Iwinski, K. J.; Castle, J. W.; Haakensen, M. C.; Peru, K. M.; Headley, J. V.; et al. A Risk-Based Approach for Identifying Constituents of Concern in Oil Sands Process-Affected Water from the Athabasca Oil Sands Region. *Chemosphere* **2017**, *173*, 340–350.

(8) Han, X.; MacKinnon, M. D.; Martin, J. W. Estimating the in Situ Biodegradation of Naphthenic Acids in Oil Sands Process Waters by HPLC/HRMS. *Chemosphere* **2009**, *76* (1), 63–70.

(9) Quagraine, E. K.; Peterson, H. G.; Headley, J. V. In Situ Bioremediation of Naphthenic Acids Contaminated Tailing Pond Waters in the Athabasca Oil Sands Region—Demonstrated Field Studies and Plausible Options: A Review. *J. Environ. Sci. Health, Part A* **2005**, *40* (3), 685–722.

(10) Marentette, J. R.; Frank, R. A.; Bartlett, A. J.; Gillis, P. L.; Hewitt, L. M.; Peru, K. M.; Headley, J. V.; Brunswick, P.; Shang, D.; Parrott, J. L. Toxicity of Naphthenic Acid Fraction Components Extracted from Fresh and Aged Oil Sands Process-Affected Waters, and Commercial Naphthenic Acid Mixtures, to Fathead Minnow (Pimephales Promelas) Embryos. *Aquat. Toxicol.* **2015**, *164*, 108–117.

(11) COSIA Challenge #0014: Passive Organics Treatment Technology http://www.cosia.ca/initiatives/water/water-challenge-statements (accessed Oct 29, 2016).

(12) Clemente, J. S.; Fedorak, P. M. A Review of the Occurrence, Analyses, Toxicity, and Biodegradation of Naphthenic Acids. *Chemosphere* **2005**, *60* (5), 585–600.

(13) Kannel, P. R.; Gan, T. Y. Naphthenic Acids Degradation and Toxicity Mitigation in Tailings Wastewater Systems and Aquatic Environments: A Review. *J. Environ. Sci. Health, Part A* **2012**, *47* (1), 1–21.

(14) Sohrabi, V.; Ross, M. S.; Martin, J. W.; Barker, J. F. Potential for in Situ Chemical Oxidation of Acid Extractable Organics in Oil Sands Process Affected Groundwater. *Chemosphere* **2013**, *93* (11), 2698–2703.

(15) Afzal, A.; Drzewicz, P.; Pérez-Estrada, L. A.; Chen, Y.; Martin, J. W.; Gamal El-Din, M. Effect of Molecular Structure on the Relative Reactivity of Naphthenic Acids in the UV/H2O2 Advanced Oxidation Process. *Environ. Sci. Technol.* **2012**, *46* (19), 10727–10734.

(16) Scott, A. C.; Zubot, W.; MacKinnon, M. D.; Smith, D. W.; Fedorak, P. M. Ozonation of Oil Sands Process Water Removes Naphthenic Acids and Toxicity. *Chemosphere* **2008**, *71* (1), 156–160.

(17) Afzal, A.; Drzewicz, P.; Martin, J. W.; Gamal El-Din, M. Decomposition of Cyclohexanoic Acid by the UV/H2O2 Process under Various Conditions. *Sci. Total Environ.* **2012**, *426*, 387–392.
(18) Drzewicz, P.; Afzal, A.; El-Din, M. G.; Martin, J. W. Degradation of a Model Naphthenic Acid, Cyclohexanoic Acid, by Vacuum UV (172 Nm) and UV (254 Nm)/H2O2. *J. Phys. Chem. A* **2010**, *114* (45), 12067–12074.
(19) Liang, X.; Zhu, X.; Butler, E. C. Comparison of Four Advanced Oxidation Processes for the Removal of Naphthenic Acids from Model Oil Sands Process Water. *J. Hazard. Mater.* **2011**, *190* (1–3), 168–176.
(20) Chan, P. Y.; Gamal El-Din, M.; Bolton, J. R. A Solar-Driven UV/Chlorine Advanced Oxidation Process. *Water Res.* **2012**, *46* (17), 5672–5682.
(21) Wang, C.; Klamerth, N.; Huang, R.; Elnakar, H.; Gamal El-Din, M. Oxidation of Oil Sands Process-Affected Water by Potassium Ferrate(VI). *Environ. Sci. Technol.* **2016**.
(22) Chong, M. N.; Jin, B.; Chow, C. W. K.; Saint, C. Recent Developments in Photocatalytic Water Treatment Technology: A Review. *Water Res.* **2010**, *44* (10), 2997–3027.
(23) Henderson, M. A. A Surface Science Perspective on TiO2 Photocatalysis. *Surf. Sci. Rep.* **2011**, *66* (6–7), 185–297.
(24) Spasiano, D.; Marotta, R.; Malato, S.; Fernandez-Ibañez, P.; Di Somma, I. Solar Photocatalysis: Materials, Reactors, Some Commercial, and Pre-Industrialized Applications. A Comprehensive Approach. *Appl. Catal., B* **2015**, *170–171*, 90–123.
(25) Liu, T.; Liu, Y.; Zhang, Z.; Li, F.; Li, X. Comparison of Aqueous Photoreactions with TiO2 in Its Hydrosol Solution and Powdery Suspension for Light Utilization. *Ind. Eng. Chem. Res.* **2011**, *50* (13), 7841–7848.
(26) Cates, E. L. Photocatalytic Water Treatment: So Where Are We Going with This? *Environ. Sci. Technol.* **2017**, *51* (2), 757–758.
(27) Malato, S.; Fernandez-Ibanez, P.; Maldonado, M.; Blanco, J.; Gernjak, W. Decontamination and Disinfection of Water by Solar Photocatalysis: Recent Overview and Trends. *Catal. Today* **2009**, *147* (1), 1–59.
(28) Dong, H.; Zeng, G.; Tang, L.; Fan, C.; Zhang, C.; He, X.; He, Y. An Overview on Limitations of TiO2-Based Particles for Photocatalytic Degradation of Organic Pollutants and the Corresponding Countermeasures. *Water Res.* **2015**, *79*, 128–146.
(29) Ambashta, R.; Sillanpaa, M. Water Purification Using Magnetic Assistance: A Review. *J. Hazard. Mater.* **2010**, *180* (1–3), 38–49.
(30) Yavuz, C.; Prakash, A.; Mayo, J.; Colvin, V. Magnetic Separations: From Steel Plants to Biotechnology. *Chem. Eng. Sci.* **2009**, *64* (10), 2510–2521.
(31) Shylesh, S.; Schunemann, V.; Thiel, W. Magnetically Separable Nanocatalysts: Bridges between Homogeneous and Heterogeneous Catalysis. *Angew. Chem. Int. Ed.* **2010**, *49* (20), 3428–3459.
(32) Polshettiwar, V.; Luque, R.; Fihri, A.; Zhu, H.; Bouhrara, M.; Bassett, J.-M. Magnetically Recoverable Nanocatalysts. *Chem. Rev.* **2011**, *111* (5), 3036–3075.
(33) Teja, A. S.; Koh, P.-Y. Synthesis, Properties, and Applications of Magnetic Iron Oxide Nanoparticles. *Prog. Cryst. Growth Charact. Mater.* **2009**, *55* (1–2), 22–45.
(34) Tartaj, P. Superparamagnetic Composites: Magnetism with No Memory. *Eur. J. Inorg. Chem.* **2009**, *2009* (3), 333–343.
(35) Cullity, B. D.; Graham, C. D. *Introduction to Magnetic Materials*; IEEE/Wiley: Hoboken, N.J., 2009.
(36) Jakubovics, J. P. *Magnetism and Magnetic Materials*; Institute of Materials: London, 1994.

(37) Phenrat, T.; Saleh, N.; Sirk, K.; Tilton, R. D.; Lowry, G. V. Aggregation and Sedimentation of Aqueous Nanoscale Zerovalent Iron Dispersions. *Environ. Sci. Technol.* **2007**, *41* (1), 284–290.
(38) Climent, E.; Maxey, M. R.; Karniadakis, G. E. Dynamics of Self-Assembled Chaining in Magnetorheological Fluids. *Langmuir* **2004**, *20* (2), 507–513.
(39) Yavuz, C.; Mayo, J.; Yu, W.; Prakash, A.; Falkner, J.; Yean, S.; Cong, L.; Shipley, H.; Kan, A.; Tomson, M.; et al. Low-Field Magnetic Separation of Monodisperse Fe3O4 Nanocrystals. *Science* **2006**, *314* (5801), 964–967.
(40) Lekkerkerker, H. N. W.; Tuinier, R. *Colloids and the Depletion Interaction*; Springer: Dordrecht; New York, 2011.
(41) De Las Cuevas, G.; Faraudo, J.; Camacho, J. Low-Gradient Magnetophoresis through Field-Induced Reversible Aggregation. *J. Phys. Chem. C* **2008**, *112* (4), 945–950.
(42) Faraudo, J.; Camacho, J. Cooperative Magnetophoresis of Superparamagnetic Colloids: Theoretical Aspects. *Colloid. Polym. Sci.* **2010**, *288* (2), 207–215.
(43) Faraudo, J.; Andreu, J. S.; Camacho, J. Understanding Diluted Dispersions of Superparamagnetic Particles under Strong Magnetic Fields: A Review of Concepts, Theory and Simulations. *Soft Matt.* **2013**.
(44) Faure, B.; Salazar-Alvarez, G.; Bergström, L. Hamaker Constants of Iron Oxide Nanoparticles. *Langmuir* **2011**, *27* (14), 8659–8664.
(45) Butt, H.-J. *Physics and Chemistry of Interfaces*, 2nd., rev. and enl. ed.; Physics textbook; Wiley-VCH: Weinheim, 2006.
(46) Bhattacharjee, S.; Elimelech, M.; Borkovec, M. DLVO Interaction between Colloidal Particles: Beyond Derjaguin's Approximation. *Croat. Chem. Acta* **1998**, *71* (4), 883–903.
(47) Tsouris, C.; Scott, T. C. Flocculation of Paramagnetic Particles in a Magnetic Field. *J. Colloid Interface Sci.* **1995**, *171* (2), 319–330.
(48) Mandel, K.; Hutter, F. The Magnetic Nanoparticle Separation Problem. *Nano Today* **2012**, *7* (6), 485–487.
(49) Jung, J. H.; Lee, J. H.; Shinkai, S. Functionalized Magnetic Nanoparticles as Chemosensors and Adsorbents for Toxic Metal Ions in Environmental and Biological Fields. *Chem. Soc. Rev.* **2011**, *40* (9), 4464–4474.
(50) Tang, S. C. N.; Lo, I. M. C. Magnetic Nanoparticles: Essential Factors for Sustainable Environmental Applications. *Water Res.* **2013**, *47* (8), 2613–2632.
(51) Lim, J.; Lanni, C.; Evarts, E. R.; Lanni, F.; Tilton, R. D.; Majetich, S. A. Magnetophoresis of Nanoparticles. *ACS Nano* **2011**, *5* (1), 217–226.
(52) Faraudo, J.; Andreu, J. S.; Camacho, J. Understanding Diluted Dispersions of Superparamagnetic Particles under Strong Magnetic Fields: A Review of Concepts, Theory and Simulations. *Soft Matter* **2013**, *9* (29), 6654–6664.
(53) Ma, W.-F.; Zhang, Y.; Li, L.-L.; You, L.-J.; Zhang, P.; Zhang, Y.-T.; Li, J.-M.; Yu, M.; Guo, J.; Lu, H.-J.; et al. Tailor-Made Magnetic Fe3O4@mTiO2 Microspheres with a Tunable Mesoporous Anatase Shell for Highly Selective and Effective Enrichment of Phosphopeptides. *ACS Nano* **2012**, *6* (4), 3179–3188.
(54) Leshuk, T.; Everett, P.; Krishnakumar, H.; Wong, K.; Linley, S.; Gu, F. Mesoporous Magnetically Recyclable Photocatalysts for Water Treatment. *J. Nanosci. Nanotechnol.* **2013**, *13* (4), 3127–3132.
(55) Stevens, P. D.; Fan, J.; Gardimalla, H. M. R.; Yen, M.; Gao, Y. Superparamagnetic Nanoparticle-Supported Catalysis of Suzuki Cross-Coupling Reactions. *Org. Lett.* **2005**, *7* (11), 2085–2088.

(56) Ge, J.; Huynh, T.; Hu, Y.; Yin, Y. Hierarchical Magnetite/Silica Nanoassemblies as Magnetically Recoverable Catalyst–Supports. *Nano Lett.* **2008**, *8* (3), 931–934.
(57) Xuan, S.; Wang, Y.-X. J.; Yu, J. C.; Leung, K. C.-F. Preparation, Characterization, and Catalytic Activity of Core/Shell Fe3O4@Polyaniline@Au Nanocomposites. *Langmuir* **2009**, *25* (19), 11835–11843.
(58) Zeng, T.; Zhang, X.; Ma, Y.; Niu, H.; Cai, Y. A Novel Fe3O4–graphene–Au Multifunctional Nanocomposite: Green Synthesis and Catalytic Application. *J. Mater. Chem.* **2012**, *22* (35), 18658–18663.
(59) Kavanagh, R. J.; Frank, R. A.; Oakes, K. D.; Servos, M. R.; Young, R. F.; Fedorak, P. M.; MacKinnon, M. D.; Solomon, K. R.; Dixon, D. G.; Van Der Kraak, G. Fathead Minnow (Pimephales Promelas) Reproduction Is Impaired in Aged Oil Sands Process-Affected Waters. *Aquat. Toxicol.* **2011**, *101* (1), 214–220.
(60) Kamaluddin, M.; Zwiazek, J. J. Naphthenic Acids Inhibit Root Water Transport, Gas Exchange and Leaf Growth in Aspen (Populus Tremuloides) Seedlings. *Tree Physiol.* **2002**, *22* (17), 1265–1270.
(61) Rogers, V. V.; Wickstrom, M.; Liber, K.; MacKinnon, M. D. Acute and Subchronic Mammalian Toxicity of Naphthenic Acids from Oil Sands Tailings. *Toxicol. Sci.* **2002**, *66* (2), 347–355.
(62) Martin, J. W.; Han, X.; Peru, K. M.; Headley, J. V. Comparison of High- and Low-Resolution Electrospray Ionization Mass Spectrometry for the Analysis of Naphthenic Acid Mixtures in Oil Sands Process Water. *Rapid Commun. Mass Spectrom.* **2008**, *22* (12), 1919–1924.
(63) Tailings Ponds http://www.oilsandstoday.ca/topics/Tailings/Pages/default.aspx (accessed Sep 19, 2014).
(64) Grewer, D. M.; Young, R. F.; Whittal, R. M.; Fedorak, P. M. Naphthenic Acids and Other Acid-Extractables in Water Samples from Alberta: What Is Being Measured? *Sci. Total Environ.* **2010**, *408* (23), 5997–6010.
(65) Frank, R. A.; Fischer, K.; Kavanagh, R.; Burnison, B. K.; Arsenault, G.; Headley, J. V.; Peru, K. M.; Kraak, G. V. D.; Solomon, K. R. Effect of Carboxylic Acid Content on the Acute Toxicity of Oil Sands Naphthenic Acids. *Environ. Sci. Technol.* **2009**, *43* (2), 266–271.
(66) Rowland, S. J.; Scarlett, A. G.; Jones, D.; West, C. E.; Frank, R. A. Diamonds in the Rough: Identification of Individual Naphthenic Acids in Oil Sands Process Water. *Environ. Sci. Technol.* **2011**, *45* (7), 3154–3159.
(67) Misiti, T. M.; Tezel, U.; Pavlostathis, S. G. Effect of Alkyl Side Chain Location and Cyclicity on the Aerobic Biotransformation of Naphthenic Acids. *Environ. Sci. Technol.* **2014**, *48* (14), 7909–7917.
(68) Crittenden, J. C.; Zhang, Y.; Hand, D. W.; Perram, D. L.; Marchand, E. G. Solar Detoxification of Fuel-Contaminated Groundwater Using Fixed-Bed Photocatalysts. *Water Environ. Res.* **1996**, *68* (3), 270–278.
(69) Headley, J. V.; Du, J.-L.; Peru, K. M.; McMartin, D. W. Electrospray Ionization Mass Spectrometry of the Photodegradation of Naphthenic Acids Mixtures Irradiated with Titanium Dioxide. *J. Environ. Sci. Health, Part A* **2009**, *44* (6), 591–597.
(70) Mishra, S.; Meda, V.; Dalai, A. K.; McMartin, D. W.; Headley, J. V.; Peru, K. M. Photocatalysis of Naphthenic Acids in Water. *J. Water Resour. Prot.* **2010**, *02* (07), 644–650.
(71) Chatterjee, D.; Dasgupta, S. Visible Light Induced Photocatalytic Degradation of Organic Pollutants. *J. Photochem. Photobiol., C* **2005**, *6* (2–3), 186–205.
(72) Zhang, Y.; Chen, Z.; Liu, S.; Xu, Y.-J. Size Effect Induced Activity Enhancement and Anti-Photocorrosion of Reduced Graphene Oxide/ZnO Composites for Degradation of Organic Dyes and Reduction of Cr(VI) in Water. *Appl. Catal., B* **2013**, *140–141*, 598–607.

(73) Yang, M.-Q.; Zhang, Y.; Zhang, N.; Tang, Z.-R.; Xu, Y.-J. Visible-Light-Driven Oxidation of Primary C–H Bonds over CdS with Dual Co-Catalysts Graphene and TiO2. *Sci. Rep.* **2013**, *3*.
(74) Current Readings for UW Weather Station http://weather.uwaterloo.ca/ (accessed Dec 16, 2014).
(75) Jivraj, M. N.; MacKinnon, M.; Fung, B. *Naphthenic Acid Extraction and Quantitative Analysis with FT-IR Spectroscopy*; Technical Report; Syncrude Canada Ltd.: Edmonton, Alberta, 1995.
(76) Holowenko, F. M.; MacKinnon, M. D.; Fedorak, P. M. Naphthenic Acids and Surrogate Naphthenic Acids in Methanogenic Microcosms. *Water Res.* **2001**, *35* (11), 2595–2606.
(77) Headley, J. V.; Peru, K. M.; McMartin, D. W.; Winkler, M. Determination of Dissolved Naphthenic Acids in Natural Waters by Using Negative-Ion Electrospray Mass Spectrometry. *J. AOAC Int.* **2002**, *85* (1), 182–187.
(78) Allen, E. W. Process Water Treatment in Canada's Oil Sands Industry: I. Target Pollutants and Treatment Objectives. *J. Environ. Eng. Sci.* **2008**, *7* (2), 123–138.
(79) McMartin, D. W.; Headley, J. V.; Friesen, D. A.; Peru, K. M.; Gillies, J. A. Photolysis of Naphthenic Acids in Natural Surface Water. *J. Environ. Sci. Health, Part A* **2004**, *39* (6), 1361–1383.
(80) Lea, J.; Adesina, A. A. The Photo-Oxidative Degradation of Sodium Dodecyl Sulphate in Aerated Aqueous TiO2 Suspension. *J. Photochem. Photobiol., A* **1998**, *118* (2), 111–122.
(81) Lair, A.; Ferronato, C.; Chovelon, J.-M.; Herrmann, J.-M. Naphthalene Degradation in Water by Heterogeneous Photocatalysis: An Investigation of the Influence of Inorganic Anions. *J. Photochem. Photobiol., A* **2008**, *193* (2–3), 193–203.
(82) He, Y.; Wiseman, S. B.; Hecker, M.; Zhang, X.; Wang, N.; Perez, L. A.; Jones, P. D.; Gamal El-Din, M.; Martin, J. W.; Giesy, J. P. Effect of Ozonation on the Estrogenicity and Androgenicity of Oil Sands Process-Affected Water. *Environ. Sci. Technol.* **2011**, *45* (15), 6268–6274.
(83) Klamerth, N.; Moreira, J.; Li, C.; Singh, A.; McPhedran, K. N.; Chelme-Ayala, P.; Belosevic, M.; Gamal El-Din, M. Effect of Ozonation on the Naphthenic Acids' Speciation and Toxicity of PH-Dependent Organic Extracts of Oil Sands Process-Affected Water. *Sci. Total Environ.* **2015**, *506–507*, 66–75.
(84) Garrett, R. M.; Pickering, I. J.; Haith, C. E.; Prince, R. C. Photooxidation of Crude Oils. *Environ. Sci. Technol.* **1998**, *32* (23), 3719–3723.
(85) Fathalla, E. M.; Andersson, J. T. Products of Polycyclic Aromatic Sulfur Heterocycles in Oil Spill Photodegradation. *Environ. Toxicol. Chem.* **2011**, *30* (9), 2004–2012.
(86) Griffiths, M. T.; Da Campo, R.; O'Connor, P. B.; Barrow, M. P. Throwing Light on Petroleum: Simulated Exposure of Crude Oil to Sunlight and Characterization Using Atmospheric Pressure Photoionization Fourier Transform Ion Cyclotron Resonance Mass Spectrometry. *Anal. Chem.* **2014**, *86* (1), 527–534.
(87) Shankar, R.; Shim, W. J.; An, J. G.; Yim, U. H. A Practical Review on Photooxidation of Crude Oil: Laboratory Lamp Setup and Factors Affecting It. *Water Res.* **2015**, *68*, 304–315.
(88) Lemkau, K. L.; McKenna, A. M.; Podgorski, D. C.; Rodgers, R. P.; Reddy, C. M. Molecular Evidence of Heavy-Oil Weathering Following the M/V Cosco Busan Spill: Insights from Fourier Transform Ion Cyclotron Resonance Mass Spectrometry. *Environ. Sci. Technol.* **2014**, *48* (7), 3760–3767.
(89) Martin, J. W.; Barri, T.; Han, X.; Fedorak, P. M.; El-Din, M. G.; Perez, L.; Scott, A. C.; Jiang, J. T. Ozonation of Oil Sands Process-Affected Water Accelerates Microbial Bioremediation. *Environ. Sci. Technol.* **2010**, *44* (21), 8350–8356.
(90) Bobinger, S.; Andersson, J. T. Photooxidation Products of Polycyclic Aromatic Compounds Containing Sulfur. *Environ. Sci. Technol.* **2009**, *43* (21), 8119–8125.

(91) Pérez-Estrada, L. A.; Han, X.; Drzewicz, P.; Gamal El-Din, M.; Fedorak, P. M.; Martin, J. W. Structure–Reactivity of Naphthenic Acids in the Ozonation Process. *Environ. Sci. Technol.* **2011**, *45* (17), 7431–7437.
(92) D'Auria, M.; Emanuele, L.; Racioppi, R.; Velluzzi, V. Photochemical Degradation of Crude Oil: Comparison between Direct Irradiation, Photocatalysis, and Photocatalysis on Zeolite. *J. Hazard. Mater.* **2009**, *164* (1), 32–38.
(93) Fujishima, A.; Zhang, X.; Tryk, D. TiO2 Photocatalysis and Related Surface Phenomena. *Surf. Sci. Rep.* **2008**, *63* (12), 515–582.
(94) Grebel, J. E.; Pignatello, J. J.; Mitch, W. A. Effect of Halide Ions and Carbonates on Organic Contaminant Degradation by Hydroxyl Radical-Based Advanced Oxidation Processes in Saline Waters. *Environ. Sci. Technol.* **2010**, *44* (17), 6822–6828.
(95) Hirakawa, T.; Nosaka, Y. Properties of O2•- and OH• Formed in TiO2 Aqueous Suspensions by Photocatalytic Reaction and the Influence of H2O2 and Some Ions. *Langmuir* **2002**, *18* (8), 3247–3254.
(96) Daimon, T.; Hirakawa, T.; Kitazawa, M.; Suetake, J.; Nosaka, Y. Formation of Singlet Molecular Oxygen Associated with the Formation of Superoxide Radicals in Aqueous Suspensions of TiO2 Photocatalysts. *Appl. Catal., A* **2008**, *340* (2), 169–175.
(97) Shiraishi, Y.; Hirai, T. Selective Organic Transformations on Titanium Oxide-Based Photocatalysts. *J. Photochem. Photobiol., C* **2008**, *9* (4), 157–170.
(98) Cermenati, L.; Dondi, D.; Fagnoni, M.; Albini, A. Titanium Dioxide Photocatalysis of Adamantane. *Tetrahedron* **2003**, *59* (34), 6409–6414.
(99) Esterbauer, H.; Schaur, R. J.; Zollner, H. Chemistry and Biochemistry of 4-Hydroxynonenal, Malonaldehyde and Related Aldehydes. *Free Radical Biol. Med.* **1991**, *11* (1), 81–128.
(100) Guéraud, F.; Atalay, M.; Bresgen, N.; Cipak, A.; Eckl, P. M.; Huc, L.; Jouanin, I.; Siems, W.; Uchida, K. Chemistry and Biochemistry of Lipid Peroxidation Products. *Free Radic. Res.* **2010**, *44* (10), 1098–1124.
(101) Betancor, C.; Francisco, C. G.; Freire, R.; Suárez, E. The Reaction of Enols with Superoxide Anion Radicals: Preparation of Tertiary α-Ketols. *J. Chem. Soc., Chem. Commun.* **1988**, No. 14, 947–948.
(102) Pichat, P. Photocatalytic Degradation of Aromatic and Alicyclic Pollutants in Water: By-Products, Pathways and Mechanisms. *Water Sci. Technol.* **1997**, *35* (4), 73–78.
(103) Antunes, C. S. A.; Bietti, M.; Salamone, M.; Scione, N. Early Stages in the TiO2-Photocatalyzed Degradation of Simple Phenolic and Non-Phenolic Lignin Model Compounds. *J. Photochem. Photobiol., A* **2004**, *163* (3), 453–462.
(104) Wen, B.; Li, Y.; Chen, C.; Ma, W.; Zhao, J. An Unexplored O2-Involved Pathway for the Decarboxylation of Saturated Carboxylic Acids by TiO2 Photocatalysis: An Isotopic Probe Study. *Chem. Eur. J.* **2010**, *16* (39), 11859–11866.
(105) Kraeutler, B.; Bard, A. J. Photoelectrosynthesis of Ethane from Acetate Ion at an N-Type Titanium Dioxide Electrode. The Photo-Kolbe Reaction. *J. Am. Chem. Soc.* **1977**, *99* (23), 7729–7731.
(106) Yuan, R.; Ramjaun, S. N.; Wang, Z.; Liu, J. Photocatalytic Degradation and Chlorination of Azo Dye in Saline Wastewater: Kinetics and AOX Formation. *Chem. Eng. J.* **2012**, *192*, 171–178.
(107) Yuan, R.; Ramjaun, S. N.; Wang, Z.; Liu, J. Concentration Profiles of Chlorine Radicals and Their Significances in •OH-Induced Dye Degradation: Kinetic Modeling and Reaction Pathways. *Chem. Eng. J.* **2012**, *209*, 38–45.

(108) Shu, Z.; Li, C.; Belosevic, M.; Bolton, J. R.; El-Din, M. G. Application of a Solar UV/Chlorine Advanced Oxidation Process to Oil Sands Process-Affected Water Remediation. *Environ. Sci. Technol.* **2014**, *48* (16), 9692–9701.
(109) McCullagh, C.; Skillen, N.; Adams, M.; Robertson, P. K. J. Photocatalytic Reactors for Environmental Remediation: A Review. *J. Chem. Technol. Biotechnol.* **2011**, *86* (8), 1002–1017.
(110) *Oil Sands Mining Operators - Water Allocation and Water Use by Year*; OSIP Data Library; Government of Alberta, 2015.
(111) Lacaze, E.; Devaux, A.; Bruneau, A.; Bony, S.; Sherry, J.; Gagné, F. Genotoxic Potential of Several Naphthenic Acids and a Synthetic Oil Sands Process-Affected Water in Rainbow Trout (Oncorhynchus Mykiss). *Aquat. Toxicol.* **2014**, *152*, 291–299.
(112) Mohseni, P.; Hahn, N. A.; Frank, R. A.; Hewitt, L. M.; Hajibabaei, M.; Van Der Kraak, G. Naphthenic Acid Mixtures from Oil Sands Process-Affected Water Enhance Differentiation of Mouse Embryonic Stem Cells and Affect Development of the Heart. *Environ. Sci. Technol.* **2015**, *49* (16), 10165–10172.
(113) Morandi, G. D.; Wiseman, S. B.; Pereira, A.; Mankidy, R.; Gault, I. G. M.; Martin, J. W.; Giesy, J. P. Effects-Directed Analysis of Dissolved Organic Compounds in Oil Sands Process-Affected Water. *Environ. Sci. Technol.* **2015**, *49* (20), 12395–12404.
(114) Barrow, M. P.; Witt, M.; Headley, J. V.; Peru, K. M. Athabasca Oil Sands Process Water: Characterization by Atmospheric Pressure Photoionization and Electrospray Ionization Fourier Transform Ion Cyclotron Resonance Mass Spectrometry. *Anal. Chem.* **2010**, *82* (9), 3727–3735.
(115) Headley, J. V.; Barrow, M. P.; Peru, K. M.; Fahlman, B.; Frank, R. A.; Bickerton, G.; McMaster, M. E.; Parrott, J.; Hewitt, L. M. Preliminary Fingerprinting of Athabasca Oil Sands Polar Organics in Environmental Samples Using Electrospray Ionization Fourier Transform Ion Cyclotron Resonance Mass Spectrometry. *Rapid Commun. Mass Spectrom.* **2011**, *25* (13), 1899–1909.
(116) Barrow, M. P.; Peru, K. M.; Fahlman, B.; Hewitt, L. M.; Frank, R. A.; Headley, J. V. Beyond Naphthenic Acids: Environmental Screening of Water from Natural Sources and the Athabasca Oil Sands Industry Using Atmospheric Pressure Photoionization Fourier Transform Ion Cyclotron Resonance Mass Spectrometry. *J. Am. Soc. Mass Spectrom.* **2015**, 1–14.
(117) Wang, N.; Chelme-Ayala, P.; Perez-Estrada, L.; Garcia-Garcia, E.; Pun, J.; Martin, J. W.; Belosevic, M.; Gamal El-Din, M. Impact of Ozonation on Naphthenic Acids Speciation and Toxicity of Oil Sands Process-Affected Water to Vibrio Fischeri and Mammalian Immune System. *Environ. Sci. Technol.* **2013**, *47* (12), 6518–6526.
(118) Drzewicz, P.; Perez-Estrada, L.; Alpatova, A.; Martin, J. W.; Gamal El-Din, M. Impact of Peroxydisulfate in the Presence of Zero Valent Iron on the Oxidation of Cyclohexanoic Acid and Naphthenic Acids from Oil Sands Process-Affected Water. *Environ. Sci. Technol.* **2012**, *46* (16), 8984–8991.
(119) Leshuk, T.; Wong, T.; Linley, S.; Peru, K. M.; Headley, J. V.; Gu, F. Solar Photocatalytic Degradation of Naphthenic Acids in Oil Sands Process-Affected Water. *Chemosphere* **2016**, *144*, 1854–1861.
(120) Damasceno, F. C.; Gruber, L. D. A.; Geller, A. M.; Campos, M. C. V. de; Gomes, A. O.; Guimarães, R. C. L.; Péres, V. F.; Jacques, R. A.; Caramão, E. B. Characterization of Naphthenic Acids Using Mass Spectroscopy and Chromatographic Techniques: Study of Technical Mixtures. *Anal. Methods* **2014**, *6* (3), 807–816.
(121) Zheng, X.; Li, D.; Li, X.; Chen, J.; Cao, C.; Fang, J.; Wang, J.; He, Y.; Zheng, Y. Construction of ZnO/TiO2 Photonic Crystal Heterostructures for Enhanced Photocatalytic Properties. *Appl. Catal., B* **2015**, *168–169*, 408–415.

(122) Zheng, X.; Li, D.; Li, X.; Yu, L.; Wang, P.; Zhang, X.; Fang, J.; Shao, Y.; Zheng, Y. Photoelectrocatalytic Degradation of Rhodamine B on TiO2 Photonic Crystals. *Phys. Chem. Chem. Phys.* **2014**, *16* (29), 15299–15306.
(123) Gao, E.; Wang, W. Role of Graphene on the Surface Chemical Reactions of BiPO4–rGO with Low OH-Related Defects. *Nanoscale* **2013**, *5* (22), 11248–11256.
(124) Ishibashi, K.; Fujishima, A.; Watanabe, T.; Hashimoto, K. Quantum Yields of Active Oxidative Species Formed on TiO2 Photocatalyst. *J. Photochem. Photobiol., A* **2000**, *134* (1–2), 139–142.
(125) Hirakawa, T.; Nosaka, Y. Properties of O2•- and OH• Formed in TiO2 Aqueous Suspensions by Photocatalytic Reaction and the Influence of H2O2 and Some Ions. *Langmuir* **2002**, *18* (8), 3247–3254.
(126) Chakraborti, R. K.; Atkinson, J. F.; Van Benschoten, J. E. Characterization of Alum Floc by Image Analysis. *Environ. Sci. Technol.* **2000**, *34* (18), 3969–3976.
(127) Lee, C.; Kramer, T. A. Prediction of Three-Dimensional Fractal Dimensions Using the Two-Dimensional Properties of Fractal Aggregates. *Adv. Colloid Interface Sci.* **2004**, *112* (1–3), 49–57.
(128) Ehrl, L.; Soos, M.; Lattuada, M. Generation and Geometrical Analysis of Dense Clusters with Variable Fractal Dimension. *J. Phys. Chem. B* **2009**, *113* (31), 10587–10599.
(129) de Martín, L.; Fabre, A.; Ruud van Ommen, J. The Fractal Scaling of Fluidized Nanoparticle Agglomerates. *Chem. Eng. Sci.* **2014**, *112*, 79–86.
(130) Schmitt, C. G.; Heymsfield, A. J. Total Surface Area Estimates for Individual Ice Particles and Particle Populations. *Journal of Applied Meteorology* **2005**, *44* (4), 467–474.
(131) Montgomery, D. C. *Design and Analysis of Experiments*, Eighth edition.; John Wiley & Sons, Inc: Hoboken, NJ, 2013.
(132) Myers, R. H.; Montgomery, D. C.; Anderson-Cook, C. M. *Response Surface Methodology: Process and Product Optimization Using Designed Experiments*, 3rd ed.; Wiley series in probability and statistics; Wiley: Hoboken, N.J, 2009.
(133) Katz, A.; McDonagh, A.; Tijing, L.; Shon, H. K. Fouling and Inactivation of Titanium Dioxide-Based Photocatalytic Systems. *Crit. Rev. Environ. Sci. Technol.* **2015**, *0* (ja), 00–00.
(134) Carp, O.; Huisman, C.; Reller, A. Photoinduced Reactivity of Titanium Dioxide. *Progress in Solid State Chemistry* **2004**, *32* (1–2), 33–177.
(135) Miller, C. J.; Rose, A. L.; Waite, T. D. Hydroxyl Radical Production by H2O2-Mediated Oxidation of Fe(II) Complexed by Suwannee River Fulvic Acid Under Circumneutral Freshwater Conditions. *Environ. Sci. Technol.* **2013**, *47* (2), 829–835.
(136) Li, Y.; Bachas, L. G.; Bhattacharyya, D. Selected Chloro-Organic Detoxifications by Polychelate (Poly(Acrylic Acid)) and Citrate-Based Fenton Reaction at Neutral PH Environment. *Ind. Eng. Chem. Res.* **2007**, *46* (24), 7984–7992.
(137) Sjogren, J. C.; Sierka, R. A. Inactivation of Phage MS2 by Iron-Aided Titanium Dioxide Photocatalysis. *Appl. Environ. Microbiol.* **1994**, *60* (1), 344–347.
(138) Ohno, T.; Haga, D.; Fujihara, K.; Kaizaki, K.; Matsumura, M. Unique Effects of Iron(III) Ions on Photocatalytic and Photoelectrochemical Properties of Titanium Dioxide. *J. Phys. Chem. B* **1997**, *101* (33), 6415–6419.
(139) Domínguez, C.; García, J.; Pedraz, M. A.; Torres, A.; Galán, M. A. Photocatalytic Oxidation of Organic Pollutants in Water. *Catal. Today* **1998**, *40* (1), 85–101.
(140) Franch, M. I.; Ayllón, J. A.; Peral, J.; Domènech, X. Enhanced Photocatalytic Degradation of Maleic Acid by Fe(III) Adsorption onto the TiO2 Surface. *Catal. Today* **2005**, *101* (3–4), 245–252.

(141) Marugán, J.; López-Muñoz, M.-J.; Gernjak, W.; Malato, S. Fe/TiO2/PH Interactions in Solar Degradation of Imidacloprid with TiO2/SiO2 Photocatalysts at Pilot-Plant Scale. *Ind. Eng. Chem. Res.* **2006**, *45* (26), 8900–8908.
(142) Marugán, J.; Aguado, J.; Gernjak, W.; Malato, S. Solar Photocatalytic Degradation of Dichloroacetic Acid with Silica-Supported Titania at Pilot-Plant Scale. *Catal. Today* **2007**, *129* (1–2), 59–68.
(143) Yu, H.; Irie, H.; Shimodaira, Y.; Hosogi, Y.; Kuroda, Y.; Miyauchi, M.; Hashimoto, K. An Efficient Visible-Light-Sensitive Fe(III)-Grafted TiO2 Photocatalyst. *J. Phys. Chem. C* **2010**, *114* (39), 16481–16487.
(144) Haarstrick, A.; Kut, O. M.; Heinzle, E. TiO2-Assisted Degradation of Environmentally Relevant Organic Compounds in Wastewater Using a Novel Fluidized Bed Photoreactor. *Environ. Sci. Technol.* **1996**, *30* (3), 817–824.
(145) Sirota, T. V. Involvement of Carbonate/Bicarbonate Ions in the Superoxide Generating Reaction of Adrenaline Autooxidation. *Biochem. Moscow Suppl. Ser. B* **2014**, *8* (4), 323–330.
(146) Haygarth, K. S.; Marin, T. W.; Janik, I.; Kanjana, K.; Stanisky, C. M.; Bartels, D. M. Carbonate Radical Formation in Radiolysis of Sodium Carbonate and Bicarbonate Solutions up to 250 °C and the Mechanism of Its Second Order Decay. *J. Phys. Chem. A* **2010**, *114* (5), 2142–2150.
(147) Xu, A.; Li, X.; Xiong, H.; Yin, G. Efficient Degradation of Organic Pollutants in Aqueous Solution with Bicarbonate-Activated Hydrogen Peroxide. *Chemosphere* **2011**, *82* (8), 1190–1195.
(148) Quinlan, P. J.; Tam, K. C. Water Treatment Technologies for the Remediation of Naphthenic Acids in Oil Sands Process-Affected Water. *Chem. Eng. J.* **2015**, *279*, 696–714.
(149) Daneshvar, N.; Rabbani, M.; Modirshahla, N.; Behnajady, M. A. Kinetic Modeling of Photocatalytic Degradation of Acid Red 27 in UV/TiO2 Process. *J. Photochem. Photobiol., A* **2004**, *168* (1–2), 39–45.
(150) Pettibone, J. M.; Cwiertny, D. M.; Scherer, M.; Grassian, V. H. Adsorption of Organic Acids on TiO2 Nanoparticles: Effects of PH, Nanoparticle Size, and Nanoparticle Aggregation. *Langmuir* **2008**, *24* (13), 6659–6667.
(151) Bekbölet, M.; Balcioglu, I. Photocatalytic Degradation Kinetics of Humic Acid in Aqueous TiO2 Dispersions: The Influence of Hydrogen Peroxide and Bicarbonate Ion. *Water Sci. Technol.* **1996**, *34* (9), 73–80.
(152) Liu, S.; Lim, M.; Fabris, R.; Chow, C.; Chiang, K.; Drikas, M.; Amal, R. Removal of Humic Acid Using TiO2 Photocatalytic Process – Fractionation and Molecular Weight Characterisation Studies. *Chemosphere* **2008**, *72* (2), 263–271.
(153) Tang, P.; Greenwood, J.; Raper, J. A. A Model to Describe the Settling Behavior of Fractal Aggregates. *J. Colloid Interface Sci.* **2002**, *247* (1), 210–219.
(154) Wu, R. M.; Lee, D. J.; Waite, T. D.; Guan, J. Multilevel Structure of Sludge Flocs. *J. Colloid Interface Sci.* **2002**, *252* (2), 383–392.
(155) Huang, Y.; Li, K.; Chen, Y. Temperature Effect on the Aggregation Kinetics of CeO2 Nanoparticles in Monovalent and Divalent Electrolytes. *J. Environ. Anal. Toxicol.* **2012**, *02* (07).
(156) Raj, K.; Viswanathan, B. Effect of Surface Area, Pore Volume and Particle Size of P25 Titania on the Phase Transformation of Anatase to Rutile. *Indian J. Chem., Sect. A* **2009**, *48* (10), 1378–1382.
(157) Suttiponparnit, K.; Jiang, J.; Sahu, M.; Suvachittanont, S.; Charinpanitkul, T.; Biswas, P. Role of Surface Area, Primary Particle Size, and Crystal Phase on Titanium Dioxide Nanoparticle Dispersion Properties. *Nanoscale Res. Lett.* **2010**, *6* (1), 27.

(158) Yu, J.; Yu, H.; Cheng, B.; Zhou, M.; Zhao, X. Enhanced Photocatalytic Activity of TiO2 Powder (P25) by Hydrothermal Treatment. *J. Mol. Catal. A* **2006**, *253* (1–2), 112–118.
(159) Chen, D.; Ray, A. K. Photodegradation Kinetics of 4-Nitrophenol in TiO2 Suspension. *Water Res.* **1998**, *32* (11), 3223–3234.
(160) Machado, A. E. H.; de Miranda, J. A.; de Freitas, R. F.; Duarte, E. T. F. M.; Ferreira, L. F.; Albuquerque, Y. D. T.; Ruggiero, R.; Sattler, C.; de Oliveira, L. Destruction of the Organic Matter Present in Effluent from a Cellulose and Paper Industry Using Photocatalysis. *J. Photochem. Photobiol., A* **2003**, *155* (1–3), 231–241.
(161) Herrmann, J.-M. Heterogeneous Photocatalysis: State of the Art and Present Applications. *Top. Catal.* **2005**, *34* (1–4), 49–65.
(162) Jassby, D.; Farner Budarz, J.; Wiesner, M. Impact of Aggregate Size and Structure on the Photocatalytic Properties of TiO2 and ZnO Nanoparticles. *Environ. Sci. Technol.* **2012**.
(163) Xu, Y.; Schoonen, M. The Absolute Energy Positions of Conduction and Valence Bands of Selected Semiconducting Minerals. *Am. Mineral.* **2000**, *85* (3–4), 543–556.
(164) Nosaka, Y.; Nosaka, A. Y. Identification and Roles of the Active Species Generated on Various Photocatalysts. In *Photocatalysis and Water Purification*; Pichat, P., Ed.; Wiley-VCH Verlag GmbH & Co. KGaA, 2013; pp 1–24.
(165) Gerischer, H.; Heller, A. The Role of Oxygen in Photooxidation of Organic Molecules on Semiconductor Particles. *J. Phys. Chem.* **1991**, *95* (13), 5261–5267.
(166) Gerischer, H.; Heller, A. Photocatalytic Oxidation of Organic Molecules at TiO2 Particles by Sunlight in Aerated Water. *J. Electrochem. Soc.* **1992**, *139* (1), 113–118.
(167) Ohko, Y.; Hashimoto, K.; Fujishima, A. Kinetics of Photocatalytic Reactions under Extremely Low-Intensity UV Illumination on Titanium Dioxide Thin Films. *J. Phys. Chem. A* **1997**, *101* (43), 8057–8062.
(168) Iliev, V.; Tomova, D.; Bilyarska, L.; Eliyas, A.; Petrov, L. Photocatalytic Properties of TiO2 Modified with Platinum and Silver Nanoparticles in the Degradation of Oxalic Acid in Aqueous Solution. *Appl. Catal., B* **2006**, *63* (3–4), 266–271.
(169) Chatzitakis, A.; Berberidou, C.; Paspaltsis, I.; Kyriakou, G.; Sklaviadis, T.; Poulios, I. Photocatalytic Degradation and Drug Activity Reduction of Chloramphenicol. *Water Res.* **2008**, *42* (1–2), 386–394.
(170) Liu, M.; Qiu, X.; Miyauchi, M.; Hashimoto, K. Energy-Level Matching of Fe(III) Ions Grafted at Surface and Doped in Bulk for Efficient Visible-Light Photocatalysts. *J. Am. Chem. Soc.* **2013**, *135* (27), 10064–10072.
(171) Talapin, D. V.; Lee, J.-S.; Kovalenko, M. V.; Shevchenko, E. V. Prospects of Colloidal Nanocrystals for Electronic and Optoelectronic Applications. *Chem. Rev.* **2010**, *110* (1), 389–458.
(172) You, H.; Yang, S.; Ding, B.; Yang, H. Synthesis of Colloidal Metal and Metal Alloy Nanoparticles for Electrochemical Energy Applications. *Chem. Soc. Rev.* **2013**, *42* (7), 2880–2904.
(173) Howes, P. D.; Chandrawati, R.; Stevens, M. M. Colloidal Nanoparticles as Advanced Biological Sensors. *Science* **2014**, *346* (6205), 1247390.
(174) Qu, X.; Alvarez, P. J. J.; Li, Q. Applications of Nanotechnology in Water and Wastewater Treatment. *Water Res.* **2013**, *47* (12), 3931–3946.
(175) Holmes, A. B.; Gu, F. X. Emerging Nanomaterials for the Application of Selenium Removal for Wastewater Treatment. *Environ. Sci.: Nano* **2016**, *3* (5), 982–996.
(176) Gottschalk, F.; Nowack, B. The Release of Engineered Nanomaterials to the Environment. *J. Environ. Monit.* **2011**, *13* (5), 1145–1155.

(177) Kim, J.; Van der Bruggen, B. The Use of Nanoparticles in Polymeric and Ceramic Membrane Structures: Review of Manufacturing Procedures and Performance Improvement for Water Treatment. *Environ. Pollut.* **2010**, *158* (7), 2335–2349.
(178) Ma, Z.; Yin, X.; Ji, X.; Yue, J.-Q.; Zhang, L.; Qin, J.-J.; Valiyaveettil, S.; Adin, A. Evaluation and Removal of Emerging Nanoparticle Contaminants in Water Treatment: A Review. *Desalin. Water Treat.* **2016**, *57* (24), 11221–11232.
(179) Troester, M.; Brauch, H.-J.; Hofmann, T. Vulnerability of Drinking Water Supplies to Engineered Nanoparticles. *Water Res.* **2016**, *96*, 255–279.
(180) Wang, J.; Munir, A.; Zhu, Z.; Zhou, H. S. Magnetic Nanoparticle Enhanced Surface Plasmon Resonance Sensing and Its Application for the Ultrasensitive Detection of Magnetic Nanoparticle-Enriched Small Molecules. *Anal. Chem.* **2010**, *82* (16), 6782–6789.
(181) Wang, Y.; Wang, G.; Xiao, Y.; Yang, Y.; Tang, R. Yolk–Shell Nanostructured Fe3O4@NiSiO3 for Selective Affinity and Magnetic Separation of His-Tagged Proteins. *ACS Appl. Mater. Interfaces* **2014**, *6* (21), 19092–19099.
(182) Hsing, I.-M.; Xu, Y.; Zhao, W. Micro- and Nano- Magnetic Particles for Applications in Biosensing. *Electroanalysis* **2007**, *19* (7–8), 755–768.
(183) Paleček, E.; Fojta, M. Magnetic Beads as Versatile Tools for Electrochemical DNA and Protein Biosensing. *Talanta* **2007**, *74* (3), 276–290.
(184) Liang, R.-P.; Yao, G.-H.; Fan, L.-X.; Qiu, J.-D. Magnetic Fe3O4@Au Composite-Enhanced Surface Plasmon Resonance for Ultrasensitive Detection of Magnetic Nanoparticle-Enriched α-Fetoprotein. *Analytica Chimica Acta* **2012**, *737*, 22–28.
(185) Lim, C. W.; Lee, I. S. Magnetically Recyclable Nanocatalyst Systems for the Organic Reactions. *Nano Today* **2010**, *5* (5), 412–434.
(186) Horak, D.; Babic, M.; Mackova, H.; Benes, M. J. Preparation and Properties of Magnetic Nano- and Microsized Particles for Biological and Environmental Separations. *J. Sep. Sci.* **2007**, *30* (11), 1751–1772.
(187) Hu, Y.-R.; Wang, F.; Wang, S.-K.; Liu, C.-Z.; Guo, C. Efficient Harvesting of Marine Microalgae Nannochloropsis Maritima Using Magnetic Nanoparticles. *Bioresour. Technol.* **2013**, *138*, 387–390.
(188) Wang, S.-K.; Wang, F.; Hu, Y.-R.; Stiles, A. R.; Guo, C.; Liu, C.-Z. Magnetic Flocculant for High Efficiency Harvesting of Microalgal Cells. *ACS Appl. Mater. Interfaces* **2014**, *6* (1), 109–115.
(189) Kim, J.; Lee, J. E.; Lee, J.; Jang, Y.; Kim, S.-W.; An, K.; Yu, J. H.; Hyeon, T. Generalized Fabrication of Multifunctional Nanoparticle Assemblies on Silica Spheres. *Angew. Chem.* **2006**, *118* (29), 4907–4911.
(190) Ge, J.; Zhang, Q.; Zhang, T.; Yin, Y. Core–Satellite Nanocomposite Catalysts Protected by a Porous Silica Shell: Controllable Reactivity, High Stability, and Magnetic Recyclability. *Angewandte Chemie International Edition* **2008**, *47* (46), 8924–8928.
(191) Jiang, J.-Q. The Role of Coagulation in Water Treatment. *Curr. Opin. Chem. Eng.* **2015**, *8*, 36–44.
(192) Lee, C. S.; Robinson, J.; Chong, M. F. A Review on Application of Flocculants in Wastewater Treatment. *Proc. Safety Env. Protect.* **2014**, *92* (6), 489–508.
(193) Verma, A. K.; Dash, R. R.; Bhunia, P. A Review on Chemical Coagulation/Flocculation Technologies for Removal of Colour from Textile Wastewaters. *J. Environ. Manage.* **2012**, *93* (1), 154–168.
(194) Liu, N.; Liu, C.; Zhang, J.; Lin, D. Removal of Dispersant-Stabilized Carbon Nanotubes by Regular Coagulants. *J. Environ. Sci.* **2012**, *24* (8), 1364–1370.

(195) Popowich, A.; Zhang, Q.; Le, X. C. Removal of Nanoparticles by Coagulation. *J. Environ. Sci.* **2015**, *38*, 168–171.
(196) Duan, L.; Hao, R.; Xu, Z.; He, X.; Adeleye, A. S.; Li, Y. Removal of Graphene Oxide Nanomaterials from Aqueous Media via Coagulation: Effects of Water Chemistry and Natural Organic Matter. *Chemosphere* **2017**, *168*, 1051–1057.
(197) Srinivasan, P. T.; Viraraghavan, T.; Subramanian, K. S. Aluminium in Drinking Water: An Overview. *Water SA* **1999**, *25* (1), 47–55.
(198) Kimura, M.; Matsui, Y.; Kondo, K.; Ishikawa, T. B.; Matsushita, T.; Shirasaki, N. Minimizing Residual Aluminum Concentration in Treated Water by Tailoring Properties of Polyaluminum Coagulants. *Water Res.* **2013**, *47* (6), 2075–2084.
(199) Hall, W. S.; Mirenda, R. J. Acute Toxicity of Wastewater Treatment Polymers to Daphnia Pulex and the Fathead Minnow (Pimephales Promelas) and the Effects of Humic Acid on Polymer Toxicity. *Res. J. Water Pollut. Control Fed.* **1991**, *63* (6), 895–899.
(200) Rowland, C. D.; Burton, G. A.; Morrison, S. M. Implication of Polymer Toxicity in a Municipal Wastewater Effluent. *Environ. Toxicol. Chem.* **2000**, *19* (8), 2136–2139.
(201) Harford, A. J.; Hogan, A. C.; Jones, D. R.; van Dam, R. A. Ecotoxicological Assessment of a Polyelectrolyte Flocculant. *Water Res.* **2011**, *45* (19), 6393–6402.
(202) Lee, C. S.; Chong, M. F.; Robinson, J.; Binner, E. A Review on Development and Application of Plant-Based Bioflocculants and Grafted Bioflocculants. *Ind. Eng. Chem. Res.* **2014**, *53* (48), 18357–18369.
(203) Yang, R.; Li, H.; Huang, M.; Yang, H.; Li, A. A Review on Chitosan-Based Flocculants and Their Applications in Water Treatment. *Water Res.* **2016**, *95*, 59–89.
(204) Morrissey, K. L.; He, C.; Wong, M. H.; Zhao, X.; Chapman, R. Z.; Bender, S. L.; Prevatt, W. D.; Stoykovich, M. P. Charge-Tunable Polymers as Reversible and Recyclable Flocculants for the Dewatering of Microalgae. *Biotechnol. Bioeng.* **2015**, *112* (1), 74–83.
(205) Leshuk, T.; de Oliveira Livera, D.; Peru, K. M.; Headley, J. V.; Vijayaraghavan, S.; Wong, T.; Gu, F. Photocatalytic Degradation Kinetics of Naphthenic Acids in Oil Sands Process-Affected Water: Multifactorial Determination of Significant Factors. *Chemosphere* **2016**, *165*, 10–17.
(206) Ozaki, M.; Kratohvil, S.; Matijević, E. Formation of Monodispersed Spindle-Type Hematite Particles. *J. Colloid Interface Sci.* **1984**, *102* (1), 146–151.
(207) Stober, W.; Fink, A.; Bohn, E. Controlled Growth of Monodisperse Silica Spheres in Micron Size Range. *J. Colloid Interface Sci.* **1968**, *26* (1), 62–69.
(208) Ohmori, M.; Matijevic, E. Preparation and Properties of Uniform Coated Colloidal Particles .7. Silica on Hematite. *J. Colloid Interface Sci.* **1992**, *150* (2), 594–598.
(209) Caruso, F.; Caruso, R. A.; Möhwald, H. Nanoengineering of Inorganic and Hybrid Hollow Spheres by Colloidal Templating. *Science* **1998**, *282* (5391), 1111–1114.
(210) Caruso, F.; Lichtenfeld, H.; Donath, E.; Möhwald, H. Investigation of Electrostatic Interactions in Polyelectrolyte Multilayer Films: Binding of Anionic Fluorescent Probes to Layers Assembled onto Colloids. *Macromolecules* **1999**, *32* (7), 2317–2328.
(211) Verma, M. S.; Chen, P. Z.; Jones, L.; Gu, F. X. Branching and Size of CTAB-Coated Gold Nanostars Control the Colorimetric Detection of Bacteria. *RSC Adv.* **2014**, *4* (21), 10660–10668.
(212) Turkevich, J.; Stevenson, P. C.; Hillier, J. A Study of the Nucleation and Growth Processes in the Synthesis of Colloidal Gold. *Discuss. Faraday Soc.* **1951**, *11* (0), 55–75.
(213) Frens, G. Controlled Nucleation for the Regulation of the Particle Size in Monodisperse Gold Suspensions. *Nature* **1973**, *241* (105), 20–22.

(214) Sui, Z.; Chen, X.; Wang, L.; Chai, Y.; Yang, C.; Zhao, J. An Improved Approach for Synthesis of Positively Charged Silver Nanoparticles. *Chem. Lett.* **2005**, *34* (1), 100–101.
(215) Sui, Z. M.; Chen, X.; Wang, L. Y.; Xu, L. M.; Zhuang, W. C.; Chai, Y. C.; Yang, C. J. Capping Effect of CTAB on Positively Charged Ag Nanoparticles. *Physica E* **2006**, *33* (2), 308–314.
(216) Xiong, Y.; Chen, J.; Wiley, B.; Xia, Y.; Aloni, S.; Yin, Y. Understanding the Role of Oxidative Etching in the Polyol Synthesis of Pd Nanoparticles with Uniform Shape and Size. *J. Am. Chem. Soc.* **2005**, *127* (20), 7332–7333.
(217) Herricks, T.; Chen, J.; Xia, Y. Polyol Synthesis of Platinum Nanoparticles: Control of Morphology with Sodium Nitrate. *Nano Lett.* **2004**, *4* (12), 2367–2371.
(218) Sanuki, S.; Arai, K.; Kojima, T.; Nagaoka, S.; Majima, H. Photocatalytic Reduction of Selenate and Selenite Solutions Using TiO2 Powders. *Metall. Mater. Trans., B* **1999**, *30* (1), 15–20.
(219) Tan, T. T. Y.; Beydoun, D.; Amal, R. Photocatalytic Reduction of Se(VI) in Aqueous Solutions in UV/TiO2 System: Importance of Optimum Ratio of Reactants on TiO2 Surface. *J. Mol. Catal., A* **2003**, *202* (1–2), 73–85.
(220) Mohamed, M. H.; Wilson, L. D.; Headley, J. V.; Peru, K. M. Screening of Oil Sands Naphthenic Acids by UV-Vis Absorption and Fluorescence Emission Spectrophotometry. *J. Environ. Sci. Health, Part A* **2008**, *43* (14), 1700–1705.
(221) Leshuk, T.; Krishnakumar, H.; Gu, F. Size-Tunable Fe3O4 Spherical Nanoclusters Through a One-Pot Hydrothermal Synthesis. *J. Nanosci. Nanotechnol.* **2015**, *15* (7), 5378–5383.
(222) de Grooth, J.; Haakmeester, B.; Wever, C.; Potreck, J.; de Vos, W. M.; Nijmeijer, K. Long Term Physical and Chemical Stability of Polyelectrolyte Multilayer Membranes. *J. Membrane Sci.* **2015**, *489* (Supplement C), 153–159.
(223) Dunlop, D. J. Magnetite: Behavior near the Single-Domain Threshold. *Science* **1972**, *176* (4030), 41–43.
(224) Bolto, B.; Gregory, J. Organic Polyelectrolytes in Water Treatment. *Water Res.* **2007**, *41* (11), 2301–2324.
(225) Naldoni, A.; Shalaev, V. M.; Brongersma, M. L. Applying Plasmonics to a Sustainable Future. *Science* **2017**, *356* (6341), 908–909.
(226) Chavez, S.; Linic, S.; Aslam, U. Controlling Energy Flow in Multimetallic Nanostructures for Plasmonic Catalysis. *Nat. Nano.* **2017**, *12* (10), 1000.
(227) Crock, C. A.; Tarabara, V. V. Pd and Pd–Au Nanocatalysts Supported on Exfoliated Graphite for High Throughput Dehalogenation by Nanocomposite Membranes. *Environ. Sci.: Nano* **2016**, *3* (2), 453–461.
(228) Biswas, P.; Bandyopadhyaya, R. Synergistic Antibacterial Activity of a Combination of Silver and Copper Nanoparticle Impregnated Activated Carbon for Water Disinfection. *Environ. Sci.: Nano* **2017**.
(229) Wei, H.; Abtahi, S. M. H.; Vikesland, P. J. Plasmonic Colorimetric and SERS Sensors for Environmental Analysis. *Environ. Sci.: Nano* **2015**, *2* (2), 120–135.
(230) Cornelis, G.; Forsberg-Grivogiannis, A. M.; Sköld, N. P.; Rauch, S.; Perez-Holmberg, J. Sludge Concentration, Shear Rate and Nanoparticle Size Determine Silver Nanoparticle Removal during Wastewater Treatment. *Environ. Sci.: Nano* **2017**, *4* (11), 2225–2234.
(231) King, S. M.; Jarvie, H. P.; Bowes, M. J.; Gozzard, E.; Lawlor, A. J.; Lawrence, M. J. Exploring Controls on the Fate of PVP-Capped Silver Nanoparticles in Primary Wastewater Treatment. *Environ. Sci.: Nano* **2015**, *2* (2), 177–190.

(232) Louie, S. M.; Tilton, R. D.; Lowry, G. V. Critical Review: Impacts of Macromolecular Coatings on Critical Physicochemical Processes Controlling Environmental Fate of Nanomaterials. *Environ. Sci.: Nano* **2016**, *3* (2), 283–310.
(233) Menne, D.; Üzüm, C.; Koppelmann, A.; Wong, J. E.; Foeken, C. van; Borre, F.; Dähne, L.; Laakso, T.; Pihlajamäki, A.; Wessling, M. Regenerable Polymer/Ceramic Hybrid Nanofiltration Membrane Based on Polyelectrolyte Assembly by Layer-by-Layer Technique. *J. Membrane Sci.* **2016**, *520* (Supplement C), 924–932.
(234) *Final Criterion: Aquatic Life Ambient Water Quality Criterion for Selenium- Freshwater 2016*; EPA 822-R-16-006; United States Environmental Protection Agency: Washington, DC, 2016.
(235) Lemly, A. D. Symptoms and Implications of Selenium Toxicity in Fish: The Belews Lake Case Example. *Aquat. Toxicol.* **2002**, *57* (1–2), 39–49.
(236) Lemly, A. D. Aquatic Selenium Pollution Is a Global Environmental Safety Issue. *Ecotoxicol. Environ. Saf.* **2004**, *59* (1), 44–56.
(237) Kannel, P. R.; Gan, T. Y. Naphthenic Acids Degradation and Toxicity Mitigation in Tailings Wastewater Systems and Aquatic Environments: A Review. *J. Environ. Sci. Health, Part A* **2012**, *47* (1), 1–21.
(238) Yue, S.; Ramsay, B. A.; Wang, J.; Ramsay, J. Toxicity and Composition Profiles of Solid Phase Extracts of Oil Sands Process-Affected Water. *Sci. Total Environ.* **2015**, *538*, 573–582.
(239) Han, X.; Scott, A. C.; Fedorak, P. M.; Bataineh, M.; Martin, J. W. Influence of Molecular Structure on the Biodegradability of Naphthenic Acids. *Environ. Sci. Technol.* **2008**, *42* (4), 1290–1295.
(240) Valencia, S.; Marín, J.; Restrepo, G. Photocatalytic Degradation of Humic Acids with Titanium Dioxide Embedded into Polyethylene Pellets to Enhance the Postrecovery of Catalyst. *Env. Eng. Sci.* **2017**.
(241) Tu, W.; Lin, Y.-P.; Bai, R. Removal of Phenol in Aqueous Solutions by Novel Buoyant Composite Photocatalysts and the Kinetics. *Sep. Purif. Technol.* **2013**, *115*, 180–189.
(242) Lu, Z.; Zhou, W.; Huo, P.; Luo, Y.; He, M.; Pan, J.; Li, C.; Yan, Y. Performance of a Novel TiO2 Photocatalyst Based on the Magnetic Floating Fly-Ash Cenospheres for the Purpose of Treating Waste by Waste. *Chem. Eng. J.* **2013**, *225*, 34–42.
(243) Halász, G.; Gyüre, B.; Jánosi, I. M.; Szabó, K. G.; Tél, T. Vortex Flow Generated by a Magnetic Stirrer. *Am. J. Phys.* **2007**, *75* (12), 1092–1098.
(244) Jackson, N. B.; Wang, C. M.; Luo, Z.; Schwitzgebel, J.; Ekerdt, J. G.; Brock, J. R.; Heller, A. Attachment of TiO2 Powders to Hollow Glass Microbeads: Activity of the TiO2 - Coated Beads in the Photoassisted Oxidation of Ethanol to Acetaldehyde. *J. Electrochem. Soc.* **1991**, *138* (12), 3660–3664.
(245) Espino-Estévez, M. R.; Fernández-Rodríguez, C.; González-Díaz, O. M.; Navío, J. A.; Fernández-Hevia, D.; Doña-Rodríguez, J. M. Enhancement of Stability and Photoactivity of TiO2 Coatings on Annular Glass Reactors to Remove Emerging Pollutants from Waters. *Chemical Engineering Journal* **2015**, *279*, 488–497.
(246) Lim, L. L. P.; Lynch, R. J.; In, S.-I. Comparison of Simple and Economical Photocatalyst Immobilisation Procedures. *Applied Catalysis A: General* **2009**, *365* (2), 214–221.
(247) Wang, G.; Xu, L.; Zhang, J.; Yin, T.; Han, D. Enhanced Photocatalytic Activity of TiO2 Powders (P25) via Calcination Treatment. *Int. J. Photoenergy* **2012**, *2012*, 1–9.
(248) Velásquez, J.; Valencia, S.; Rios, L.; Restrepo, G.; Marín, J. Characterization and Photocatalytic Evaluation of Polypropylene and Polyethylene Pellets Coated with P25 TiO2 Using the Controlled-Temperature Embedding Method. *Chem. Eng. J.* **2012**, *203*, 398–405.

(249) Fabiyi, M. E.; Skelton, R. L. Photocatalytic Mineralisation of Methylene Blue Using Buoyant TiO2-Coated Polystyrene Beads. *J. Photochem. Photobiol., A* **2000**, *132* (1–2), 121–128.
(250) Magalhães, F.; Moura, F. C. C.; Lago, R. M. TiO2/LDPE Composites: A New Floating Photocatalyst for Solar Degradation of Organic Contaminants. *Desalination* **2011**, *276* (1–3), 266–271.
(251) Zhao, X. u; Li, Z.; Chen, Y.; Shi, L.; Zhu, Y. Solid-Phase Photocatalytic Degradation of Polyethylene Plastic under UV and Solar Light Irradiation. *Journal of Molecular Catalysis A: Chemical* **2007**, *268* (1–2), 101–106.
(252) Shang, J.; Chai, M.; Zhu, Y. Photocatalytic Degradation of Polystyrene Plastic under Fluorescent Light. *Environ. Sci. Technol.* **2003**, *37* (19), 4494–4499.
(253) Tennakone, K.; Kottegoda, I. R. M. Photocatalytic Mineralization of Paraquat Dissolved in Water by TiO2 Supported on Polythene and Polypropylene Films. *J. Photochem. Photobiol., A* **1996**, *93* (1), 79–81.
(254) Faramarzpour, M.; Vossoughi, M.; Borghei, M. Photocatalytic Degradation of Furfural by Titania Nanoparticles in a Floating-Bed Photoreactor. *Chem. Eng. J.* **2009**, *146* (1), 79–85.
(255) Wang, B.; Li, Q.; Wang, W.; Li, Y.; Zhai, J. Preparation and Characterization of Fe3+-Doped TiO2 on Fly Ash Cenospheres for Photocatalytic Application. *Appl. Surf. Sci.* **2011**, *257* (8), 3473–3479.
(256) Hosseini, S. N.; Borghei, S. M.; Vossoughi, M.; Taghavinia, N. Immobilization of TiO2 on Perlite Granules for Photocatalytic Degradation of Phenol. *Appl. Catal., B* **2007**, *74* (1–2), 53–62.
(257) Matthews, R. W. Photooxidative Degradation of Coloured Organics in Water Using Supported Catalysts. TiO2 on Sand. *Water Res.* **1991**, *25* (10), 1169–1176.
(258) Pozzo, R. L.; Giombi, J. L.; Baltanás, M. A.; Cassano, A. E. The Performance in a Fluidized Bed Reactor of Photocatalysts Immobilized onto Inert Supports. *Catalysis Today* **2000**, *62* (2–3), 175–187.
(259) Hurum, D. C.; Agrios, A. G.; Gray, K. A.; Rajh, T.; Thurnauer, M. C. Explaining the Enhanced Photocatalytic Activity of Degussa P25 Mixed-Phase TiO2 Using EPR. *J. Phys. Chem., B* **2003**, *107* (19), 4545–4549.
(260) Lawrence, G. A.; Ward, P. R. B.; MacKinnon, M. D. Wind-Wave-Induced Suspension of Mine Tailings in Disposal Ponds – a Case Study. *Can. J. Civ. Eng.* **1991**, *18* (6), 1047–1053.
(261) Lawrence, G. A.; Tedford, E. W.; Pieters, R. Suspended Solids in an End Pit Lake: Potential Mixing Mechanisms. *Can. J. Civ. Eng.* **2015**, *43* (3), 211–217.
(262) Dompierre, K. A.; Barbour, S. L. Characterization of Physical Mass Transport through Oil Sands Fluid Fine Tailings in an End Pit Lake: A Multi-Tracer Study. *J. Contam. Hydrol.* **2016**, *189*, 12–26.
(263) Holowenko, F. M. Methanogenesis and Fine Tailings Waste from Oil Sands Extraction: A Microcosm-Based Laboratory Examination. MSc Thesis, University of Alberta: Edmonton, Alberta, 2000.
(264) Barrow, M. P.; Peru, K. M.; Headley, J. V. An Added Dimension: GC Atmospheric Pressure Chemical Ionization FTICR MS and the Athabasca Oil Sands. *Anal. Chem.* **2014**, *86* (16), 8281–8288.
(265) Barrow, M. P.; Peru, K. M.; McMartin, D. W.; Headley, J. V. Effects of Extraction PH on the Fourier Transform Ion Cyclotron Resonance Mass Spectrometry Profiles of Athabasca Oil Sands Process Water. *Energy Fuels* **2016**, *30* (5), 3615–3621.
(266) Morandi, G. D.; Wiseman, S. B.; Guan, M.; Zhang, X. W.; Martin, J. W.; Giesy, J. P. Elucidating Mechanisms of Toxic Action of Dissolved Organic Chemicals in Oil Sands Process-Affected Water (OSPW). *Chemosphere* **2017**, *186* (Supplement C), 893–900.

(267) Rowland, S. J.; West, C. E.; Jones, D.; Scarlett, A. G.; Frank, R. A.; Hewitt, L. M. Steroidal Aromatic 'Naphthenic Acids' in Oil Sands Process-Affected Water: Structural Comparisons with Environmental Estrogens. *Environ. Sci. Technol.* **2011**, *45* (22), 9806–9815.
(268) Pereira, A. S.; Bhattacharjee, S.; Martin, J. W. Characterization of Oil Sands Process-Affected Waters by Liquid Chromatography Orbitrap Mass Spectrometry. *Environ. Sci. Technol.* **2013**, *47* (10), 5504–5513.
(269) Marshall, A. G.; Rodgers, R. P. Petroleomics: Chemistry of the Underworld. *Proc. Natl. Acad. Sci. U.S.A.* **2008**, *105* (47), 18090–18095.
(270) McKenna, A. M.; Nelson, R. K.; Reddy, C. M.; Savory, J. J.; Kaiser, N. K.; Fitzsimmons, J. E.; Marshall, A. G.; Rodgers, R. P. Expansion of the Analytical Window for Oil Spill Characterization by Ultrahigh Resolution Mass Spectrometry: Beyond Gas Chromatography. *Environ. Sci. Technol.* **2013**, *47* (13), 7530–7539.
(271) Morandi, G. D.; Zhang, K.; Wiseman, S. B.; Pereira, A. dos S.; Martin, J. W.; Giesy, J. P. Effect of Lipid Partitioning on Predictions of Acute Toxicity of Oil Sands Process Affected Water to Embryos of Fathead Minnow (Pimephales Promelas). *Environ. Sci. Technol.* **2016**, *50* (16), 8858–8866.
(272) Headley, J. V.; Peru, K. M.; Mohamed, M. H.; Frank, R. A.; Martin, J. W.; Hazewinkel, R. R. O.; Humphries, D.; Gurprasad, N. P.; Hewitt, L. M.; Muir, D. C. G.; et al. Chemical Fingerprinting of Naphthenic Acids and Oil Sands Process Waters—A Review of Analytical Methods for Environmental Samples. *J. Environ. Sci. Health, Part A* **2013**, *48* (10), 1145–1163.
(273) Frank, R. A.; Roy, J. W.; Bickerton, G.; Rowland, S. J.; Headley, J. V.; Scarlett, A. G.; West, C. E.; Peru, K. M.; Parrott, J. L.; Conly, F. M.; et al. Profiling Oil Sands Mixtures from Industrial Developments and Natural Groundwaters for Source Identification. *Environ. Sci. Technol.* **2014**, *48* (5), 2660–2670.
(274) Sun, C.; Shotyk, W.; Cuss, C. W.; Donner, M. W.; Fennell, J.; Javed, M.; Noernberg, T.; Poesch, M.; Pelletier, R.; Sinnatamby, N.; et al. Characterization of Naphthenic Acids and Other Dissolved Organics in Natural Water from the Athabasca Oil Sands Region, Canada. *Environ. Sci. Technol.* **2017**, *51* (17), 9524–9532.
(275) McQueen, A. D.; Hendrikse, M.; Gaspari, D. P.; Kinley, C. M.; Rodgers Jr., J. H.; Castle, J. W. Performance of a Hybrid Pilot-Scale Constructed Wetland System for Treating Oil Sands Process-Affected Water from the Athabasca Oil Sands. *Ecol. Eng.* **2017**, *102*, 152–165.
(276) Liu, J.; Wang, L.; Tang, J.; Ma, J. Photocatalytic Degradation of Commercially Sourced Naphthenic Acids by TiO2-Graphene Composite Nanomaterial. *Chemosphere* **2016**, *149*, 328–335.
(277) Allain, E.; Besson, S.; Durand, C.; Moreau, M.; Gacoin, T.; Boilot, J.-P. Transparent Mesoporous Nanocomposite Films for Self-Cleaning Applications. *Adv. Funct. Mater.* **2007**, *17* (4), 549–554.
(278) Nair, M.; Luo, Z.; Heller, A. Rates of Photocatalytic Oxidation of Crude Oil on Salt Water on Buoyant, Cenosphere-Attached Titanium Dioxide. *Ind. Eng. Chem. Res.* **1993**, *32* (10), 2318–2323.
(279) Berry, R. J.; Mueller, M. R. Photocatalytic Decomposition of Crude Oil Slicks Using TiO2 on a Floating Substrate. *Microchem. J.* **1994**, *50* (1), 28–32.
(280) Magalhães, F.; Lago, R. M. Floating Photocatalysts Based on TiO2 Grafted on Expanded Polystyrene Beads for the Solar Degradation of Dyes. *Sol. Energy* **2009**, *83* (9), 1521–1526.
(281) Singh, S.; Mahalingam, H.; Singh, P. K. Polymer-Supported Titanium Dioxide Photocatalysts for Environmental Remediation: A Review. *Appl. Catal. A* **2013**, *462–463*, 178–195.
(282) Qiu, W.; Zheng, Y. A Comprehensive Assessment of Supported Titania Photocatalysts in a Fluidized Bed Photoreactor: Photocatalytic Activity and Adherence Stability. *Appl. Catal. B* **2007**, *71* (3–4), 151–162.

(283) Hughes, S. A.; Huang, R.; Mahaffey, A.; Chelme-Ayala, P.; Klamerth, N.; Meshref, M. N. A.; Ibrahim, M. D.; Brown, C.; Peru, K. M.; Headley, J. V.; et al. Comparison of Methods for Determination of Total Oil Sands-Derived Naphthenic Acids in Water Samples. *Chemosphere* **2017**, *187* (Supplement C), 376–384.
(284) Huang, R.; McPhedran, K. N.; Sun, N.; Chelme-Ayala, P.; Gamal El-Din, M. Investigation of the Impact of Organic Solvent Type and Solution PH on the Extraction Efficiency of Naphthenic Acids from Oil Sands Process-Affected Water. *Chemosphere* **2016**, *146*, 472–477.
(285) Islam, M. S.; Moreira, J.; Chelme-Ayala, P.; Gamal El-Din, M. Prediction of Naphthenic Acid Species Degradation by Kinetic and Surrogate Models during the Ozonation of Oil Sands Process-Affected Water. *Sci. Total Environ.* **2014**, *493*, 282–290.
(286) Soana, F.; Sturini, M.; Cermenati, L.; Albini, A. Titanium Dioxide Photocatalyzed Oxygenation of Naphthalene and Some of Its Derivatives. *J. Chem. Soc., Perkin Trans. 2* **2000**, No. 4, 699–704.
(287) Bui, T. D.; Kimura, A.; Higashida, S.; Ikeda, S.; Matsumura, M. Two Routes for Mineralizing Benzene by TiO2-Photocatalyzed Reaction. *Appl. Catal., B* **2011**, *107* (1–2), 119–127.
(288) Grabowska, E.; Reszczyńska, J.; Zaleska, A. Mechanism of Phenol Photodegradation in the Presence of Pure and Modified-TiO2: A Review. *Water Res.* **2012**, *46* (17), 5453–5471.
(289) Meshref, M. N. A.; Chelme-Ayala, P.; Gamal El-Din, M. Fate and Abundance of Classical and Heteroatomic Naphthenic Acid Species after Advanced Oxidation Processes: Insights and Indicators of Transformation and Degradation. *Water Research* **2017**, *125* (Supplement C), 62–71.
(290) Alharbi, H. A.; Saunders, D. M. V.; Al-Mousa, A.; Alcorn, J.; Pereira, A. S.; Martin, J. W.; Giesy, J. P.; Wiseman, S. B. Inhibition of ABC Transport Proteins by Oil Sands Process Affected Water. *Aquat. Toxicol.* **2016**, *170*, 81–88.
(291) Quesnel, D. M.; Oldenburg, T. B. P.; Larter, S. R.; Gieg, L. M.; Chua, G. Biostimulation of Oil Sands Process-Affected Water with Phosphate Yields Removal of Sulfur-Containing Organics and Detoxification. *Environ. Sci. Technol.* **2015**, *49* (21), 13012–13020.
(292) Mapolelo, M. M.; Stanford, L. A.; Rodgers, R. P.; Yen, A. T.; Debord, J. D.; Asomaning, S.; Marshall, A. G. Chemical Speciation of Calcium and Sodium Naphthenate Deposits by Electrospray Ionization FT-ICR Mass Spectrometry. *Energy Fuels* **2009**, *23* (1), 349–355.
(293) Sutton, P. A.; Smith, B. E.; Rowland, S. J. Mass Spectrometry of Polycyclic Tetracarboxylic ('ARN') Acids and Tetramethyl Esters. *Rapid Commun. Mass Spectrom.* **2010**, *24* (21), 3195–3204.
(294) Lewis, A. T.; Tekavec, T. N.; Jarvis, J. M.; Juyal, P.; McKenna, A. M.; Yen, A. T.; Rodgers, R. P. Evaluation of the Extraction Method and Characterization of Water-Soluble Organics from Produced Water by Fourier Transform Ion Cyclotron Resonance Mass Spectrometry. *Energy Fuels* **2013**, *27* (4), 1846–1855.
(295) Rowland, S. J.; Pereira, A. S.; Martin, J. W.; Scarlett, A. G.; West, C. E.; Lengger, S. K.; Wilde, M. J.; Pureveen, J.; Tegelaar, E. W.; Frank, R. A.; et al. Mass Spectral Characterisation of a Polar, Esterified Fraction of an Organic Extract of an Oil Sands Process Water. *Rapid Commun. Mass Spectrom.* **2014**, *28* (21), 2352–2362.
(296) Sun, J.; Peng, H.; Alharbi, H. A.; Jones, P. D.; Giesy, J. P.; Wiseman, S. B. Identification of Chemicals That Cause Oxidative Stress in Oil Sands Process-Affected Water. *Environ. Sci. Technol.* **2017**, *51* (15), 8773–8781.
(297) Zhang, K.; Pereira, A. S.; Martin, J. W. Estimates of Octanol–Water Partitioning for Thousands of Dissolved Organic Species in Oil Sands Process-Affected Water. *Environ. Sci. Technol.* **2015**, *49* (14), 8907–8913.

(298) Zhang, K.; Wiseman, S.; Giesy, J. P.; Martin, J. W. Bioconcentration of Dissolved Organic Compounds from Oil Sands Process-Affected Water by Medaka (Oryzias Latipes): Importance of Partitioning to Phospholipids. *Environ. Sci. Technol.* **2016**, *50* (12), 6574–6582.
(299) Wang, C.; Huang, R.; Klamerth, N.; Chelme-Ayala, P.; Gamal El-Din, M. Positive and Negative Electrospray Ionization Analyses of the Organic Fractions in Raw and Oxidized Oil Sands Process-Affected Water. *Chemosphere* **2016**, *165*, 239–247.
(300) Dobson, K. D.; McQuillan, A. J. In Situ Infrared Spectroscopic Analysis of the Adsorption of Aliphatic Carboxylic Acids to TiO2, ZrO2, Al2O3, and Ta2O5 from Aqueous Solutions. *Spectrochim. Acta, A.* **1999**, *55* (7), 1395–1405.
(301) Janković, I. A.; Šaponjić, Z. V.; Čomor, M. I.; Nedeljković, J. M. Surface Modification of Colloidal TiO2 Nanoparticles with Bidentate Benzene Derivatives. *J. Phys. Chem. C* **2009**, *113* (29), 12645–12652.
(302) Frank, R. A.; Kavanagh, R.; Kent Burnison, B.; Arsenault, G.; Headley, J. V.; Peru, K. M.; Van Der Kraak, G.; Solomon, K. R. Toxicity Assessment of Collected Fractions from an Extracted Naphthenic Acid Mixture. *Chemosphere* **2008**, *72* (9), 1309–1314.
(303) Dong, T.; Zhang, Y.; Islam, M. S.; Liu, Y.; Gamal El-Din, M. The Impact of Various Ozone Pretreatment Doses on the Performance of Endogenous Microbial Communities for the Remediation of Oil Sands Process-Affected Water. *Int. Biodeterior. Biodegrad.* **2015**, *100*, 17–28.
(304) Brown, L. D.; Pérez-Estrada, L.; Wang, N.; El-Din, M. G.; Martin, J. W.; Fedorak, P. M.; Ulrich, A. C. Indigenous Microbes Survive in Situ Ozonation Improving Biodegradation of Dissolved Organic Matter in Aged Oil Sands Process-Affected Waters. *Chemosphere* **2013**, *93* (11), 2748–2755.
(305) Chow, K. L.; Man, Y. B.; Tam, N. F. Y.; Liang, Y.; Wong, M. H. Removal of Decabromodiphenyl Ether (BDE-209) Using a Combined System Involving TiO2 Photocatalysis and Wetland Plants. *J. Hazard. Mater.* **2017**, *322* (Part A), 263–269.
(306) Araña, J.; Garriga i Cabo, C.; Fernández Rodríguez, C.; Herrera Melián, J. A.; Ortega Méndez, J. A.; Doña Rodríguez, J. M.; Pérez Peña, J. Combining TiO2-Photocatalysis and Wetland Reactors for the Efficient Treatment of Pesticides. *Chemosphere* **2008**, *71* (4), 788–794.
(307) Cermenati, L.; Albini, A.; Pichat, P.; Guillard, C. TiO2 Photocatalytic Degradation of Haloquinolines in Water: Aromatic Products GM-MS Identification. Role of Electron Transfer and Superoxide. *Res. Chem. Intermed.* **2000**, *26* (3), 221–234.
(308) Jones, D.; Scarlett, A. G.; West, C. E.; Rowland, S. J. Toxicity of Individual Naphthenic Acids to Vibrio Fischeri. *Environ. Sci. Technol.* **2011**, *45* (22), 9776–9782.
(309) Holowenko, F. M.; MacKinnon, M. D.; Fedorak, P. M. Characterization of Naphthenic Acids in Oil Sands Wastewaters by Gas Chromatography-Mass Spectrometry. *Water Res.* **2002**, *36* (11), 2843–2855.
(310) Nicholls, E. M.; Carey, S. K.; Humphreys, E. R.; Clark, M. G.; Drewitt, G. B. Multi-Year Water Balance Assessment of a Newly Constructed Wetland, Fort McMurray, Alberta. *Hydrol. Process.* **2016**, *30* (16), 2739–2753.
(311) Chen, X.; Liu, L.; Yu, P. Y.; Mao, S. S. Increasing Solar Absorption for Photocatalysis with Black Hydrogenated Titanium Dioxide Nanocrystals. *Science* **2011**, *331* (6018), 746–750.
(312) Wang, Z.; Yang, C.; Lin, T.; Yin, H.; Chen, P.; Wan, D.; Xu, F.; Huang, F.; Lin, J.; Xie, X.; et al. Visible-Light Photocatalytic, Solar Thermal and Photoelectrochemical Properties of Aluminium-Reduced Black Titania. *Energy Environ. Sci.* **2013**, *6* (10), 3007–3014.

(313) Lin, T.; Yang, C.; Wang, Z.; Yin, H.; Lü, X.; Huang, F.; Lin, J.; Xie, X.; Jiang, M. Effective Nonmetal Incorporation in Black Titania with Enhanced Solar Energy Utilization. *Energy Environ. Sci.* **2014**, *7* (3), 967–972.
(314) Liu, P.; Zhao, Y.; Qin, R.; Mo, S.; Chen, G.; Gu, L.; Chevrier, D. M.; Zhang, P.; Guo, Q.; Zang, D.; et al. Photochemical Route for Synthesizing Atomically Dispersed Palladium Catalysts. *Science* **2016**, *352* (6287), 797–800.
(315) Wan, J.; Chen, W.; Jia, C.; Zheng, L.; Dong, J.; Zheng, X.; Wang, Y.; Yan, W.; Chen, C.; Peng, Q.; et al. Defect Effects on TiO2 Nanosheets: Stabilizing Single Atomic Site Au and Promoting Catalytic Properties. *Adv. Mater.* **2018**, n/a-n/a.
(316) Liu, M.; Inde, R.; Nishikawa, M.; Qiu, X.; Atarashi, D.; Sakai, E.; Nosaka, Y.; Hashimoto, K.; Miyauchi, M. Enhanced Photoactivity with Nanocluster-Grafted Titanium Dioxide Photocatalysts. *ACS Nano* **2014**, *8* (7), 7229–7238.
(317) Niasar, H. S.; Li, H.; Kasanneni, T. V. R.; Ray, M. B.; Xu, C. (Charles). Surface Amination of Activated Carbon and Petroleum Coke for the Removal of Naphthenic Acids and Treatment of Oil Sands Process-Affected Water (OSPW). *Chem. Eng. J.* **2016**, *293*, 189–199.
(318) Mohamed, M. H.; Wilson, L. D.; Shah, J. R.; Bailey, J.; Peru, K. M.; Headley, J. V. A Novel Solid-State Fractionation of Naphthenic Acid Fraction Components from Oil Sands Process-Affected Water. *Chemosphere* **2015**, *136*, 252–258.
(319) Chen, L.; Wang, X.; Lu, W.; Wu, X.; Li, J. Molecular Imprinting: Perspectives and Applications. *Chem. Soc. Rev.* **2016**, *45* (8), 2137–2211.
(320) Mohamed, M. H.; Wilson, L. D.; Headley, J. V. Tunable Polymeric Sorbent Materials for Fractionation of Model Naphthenates. *J. Phys. Chem. B* **2013**, *117* (13), 3659–3666.
(321) Rivas, G.; Carra, I.; García Sánchez, J. L.; Casas López, J. L.; Malato, S.; Sánchez Pérez, J. A. Modelling of the Operation of Raceway Pond Reactors for Micropollutant Removal by Solar Photo-Fenton as a Function of Photon Absorption. *Appl. Catal., B* **2015**, *178*, 210–217.
(322) Hreiz, R.; Sialve, B.; Morchain, J.; Escudié, R.; Steyer, J.-P.; Guiraud, P. Experimental and Numerical Investigation of Hydrodynamics in Raceway Reactors Used for Algaculture. *Chem. Eng. J.* **2014**, *250*, 230–239.